

Università dell'Insubria
Dipartimento di Matematica e Fisica

INAF-OAB Istituto Nazionale di Astrofisica, Osservatorio Astronomico di Brera

Doctor of Philosophy Dissertation

DEVELOPMENT OF THE GLASS SLUMPING TECHNOLOGY FOR THE PRODUCTION OF THE X-RAY MIRRORS ABOARD THE INTERNATIONAL X-RAY OBSERVATORY OPTICAL MODULE

Author: **Laura Proserpio**
(Mat.: 708041)

Supervisors: Dr. Mauro Ghigo,
Dr. Giovanni Pareschi



XXIII ciclo di Dottorato di Ricerca – Astronomia ed Astrofisica
Como, 2011

Contents

Contents	i
List of acronyms	v
Introduction.....	1
1 Astronomical X-ray Telescopes	7
1.1 History of X-ray Astronomy.....	7
1.2 X-ray Focusing systems: the principle of Grazing Incidence	10
1.3 Manufacturing techniques.....	15
1.3.1 Direct polishing of mirror shells.....	17
1.3.2 Mirror shells replication by electroformed Nickel.....	18
1.3.3 Aluminum thin-foil mirror shells.....	21
2 The International X-ray Observatory.....	23
2.1 IXO mission overview.....	23
2.2 IXO Science case	25
2.2.1 Matter under extreme conditions	28
2.2.2 Large Scale Structure	31
2.2.3 Life cycle of matter and energy	38
2.3 IXO Optical payload	41
2.3.1 Technical requirements and goals	42
2.3.2 IXO X-ray manufacturing challenge: the need of a new technology	45
2.3.3 ESA base-line for IXO telescope manufacturing: the Pore Optics technology	48
3 IXO back-up optic study.....	53
3.1 The ESA <i>IXO back-up optic</i> project	53

3.2	IXO optical design based on the glass technology	55
3.3	Aim of the present research	66
4	The slumping technology for making mirrors.....	67
4.1	Slumping technology basic concepts.....	67
4.2	Different slumping approaches.....	70
4.2.1	The hot direct slumping with pressure at INAF-OAB, Italy	71
4.2.2	The direct slumping at NASA-Goddard and Columbia University, USA.....	75
4.2.3	The Indirect slumping at MPE, Germany	77
4.2.4	The hybrid slumping approach at the Academy of Science of Prague, Czech Republic	78
4.3	Mould and glass properties to consider during material selection.....	80
4.4	Slumping thermal cycle parameters.....	84
5	Design of experiments and preparatory activities.....	89
5.1	Rationale of the carried out experiments.....	89
5.2	Preparatory activities to the experiments conduction.....	91
5.2.1	Assessment and improvements on the available tools and instruments	91
5.2.2	Selection of the metrological systems to be employed for results analyses	98
5.2.3	Procurement of glass and mould for the slumping technology assessment	101
6	Results on the application of the slumping technology to the IXO case.....	109
6.1	Modification of past INAF-OAB slumping procedure	110
6.1.1	Modification in the process environment conditions: from vacuum to Ar controlled atmosphere	111
6.1.2	Modifications in cleaning procedures: elimination of First Contact.....	114
6.1.3	Selection of a reliable antisticking layer	115
6.2	Cylindrical slumping on procured moulds	127
6.2.1	Cylindrical slumping moulds characterization.....	127
6.2.2	Schott glass D263 characterization.....	137
6.2.3	Slumping thermal cycle optimization	149
6.2.4	Slumping results in terms of plates shape	150

6.2.5	Slumping results in terms of roughness	165
6.3	Analyses and understanding of still open questions	168
6.3.1	Thermal origin of the edge shape deformations	168
6.3.2	Simulation of glass edges cutting	171
6.3.3	Investigation on the effects of the pressing membrane	173
6.3.4	Summary of open questions and proposed solutions for follow up studies.....	177
7	Conclusions and final remarks	179
8	Annex A: Surface morphology parameters.....	183
9	Annex B: Characterization instruments.....	189
	Shape characterization instruments	189
	Surface roughness characterization.....	194
	Summary of the characterization instruments.....	200
10	Annex C: List of experiments	201
11	Annex D: Slumping procedure	207
	List of publications	209
	Bibliography.....	213

List of acronyms

Acronym	Meaning
AFM	Atomic Force Microscope
AGN	Active Galactic Nuclei
AIV	Assembling Integration Verification
AO	Adaptive Optic
AS&E	American Science and Engineering
BH	Black Hole
BN	Boron Nitride
CC	Core Collapse
CCC	Channel Cut Crystal
CDR	Critical Design Review
CTE	Coefficient of Thermal Expansion
CT	Central thickness
CUP	Characterization Universal Profilometer
CXO	Chandra X-ray Observatory
DGP	Dvali Gabadadze Porrati (model of gravity proposed in 2000)
DLC	Diamond Like Coating
EDS	Energy Dispersion Spectroscopy
EOB	Extensible Optical Bench
EOS	Equation Of State
FEA	Finite Element Analysis
FEM	Finite Element Model
FMA	Flight Mirror Assembly
FOS	Factor Of Safety
FOV	Field Of View
FS	Fused Silica
GBH	Galactic Black Hole
GI	Grazing Incidence
GR	General Relativity
HEW	Half Energy Width
HDOS	Hughes Danbury Optical Systems
HP	Hertzsprung-Russell diagram
HPD	Half Power Diameter
HPO	High Performance Pore Optic
HTRS	High Time Resolution Spectrometer
HW	Hardware

HXI	Hard X-ray Imager
ICM	Intra Cluster Medium
I/F	Interface
IGM	Inter Galactic Medium
IM	Instruments Module
INAF	National Institute for Astrophysics (Istituto Nazionale di Astrofisica)
ISM	Inter Stellar Medium
IXO	International X-ray Observatory
KOM	Kick Off Meeting
LCDM	Lambda Cold Dark Matter (current standard model of cosmology)
LSF	Line Spread Function
LTP	Long Trace Profilometer
MA	Mirror Assembly
MDP	Minimum Detectable Polarization
MHD	Magneto-Hydro Dynamic
MIP	Movable Instruments Platform
MM	Mirror Module
MOB	Mirror Optical Bench
MOS	Margin of safety
MP	Mirror Plate
MPE	Max Planck Institut für Extraterrestrische Physik
M-R	Mass-Radius
MS	Mirror Shell
NA	Not Available
NF	Numerical File
NS	Neutron Star
OAB	Brera Astronomical Observatory (Osservatorio Astronomico di Brera)
PDR	Preliminary Design Review
PLC	Programmable Logic Controller (oven controller)
P.O.C.	Proof Of Concept (HW output of the contract)
PP	Plate Pair
PS	Petal Structure
PSD	Power Spectral Density
PSF	Point Spread Function
P-V	Peak to Valley
QCD	Quantum Chromodynamics
QED	Quantum Electrodynamics
ROC	Radius Of Curvature
RMS	Root Mean Square
RT	Room Temperature
SEM	Scanning Electron Microscope
SGO	Segmented Glass Optic
SGT	Segmented Glass Technology
SMBH	Super Massive Black Hole

SN	Supernovae
SNR	Supernovae Remnant
SoW	Statement of Work
SPO	Silicon Pore Optic
SVM	Service Module
TBA	To Be Agreed
TBC	To Be Confirmed
TBD	To Be Determined
TES	Transition Edge Sensor
TN	Technical Note
TR	Test Review
TRL	Technology Readiness Level
TRR	Test Readiness Review
WFI	Wide Field Imager
WHIM	Warm Hot Intergalactic Medium
wrt	with respect to
XEUS	X-ray Evolving Universe Spectroscopy
XGS	X-ray Grating Spectrometer
XMM	X-ray Multi Mirror Mission (XMM-Newton)
XMS	X-ray imaging Microcalorimeter Spectrometer
XOU	X-ray Optical Unit
XOU BB	X-ray Optical Unit Bread Board (HW output of the contract)
XPOL	X-ray Polarimeter
XRR	X-ray reflectivity
XRS	X-ray scattering

Introduction

The study of the Universe in the X-ray band of the electromagnetic spectrum is important to answer contemporary astrophysical questions about the origin of the cosmos and its evolution. As X-ray cannot penetrate Earth's atmosphere, X-ray telescopes and detectors require being launched in space aboard balloons, sounding rockets, and satellites, hence one of their main requirement is to be lightweight. Because of the nature of interaction of X-ray with the surface of focusing systems, high precision in X-ray mirror shape and surface finishing is required. In general, the shape must be controlled at sub-micron level while the roughness needs to be in the Å level. Due to their high energy, X-ray can be focalized only following the principle of Grazing Incidence: an X-ray mirror shows a tube-like configuration and X-photons are reflected by the inner surface when they are incident with angle smaller than 1 degree. Since the advent of space era in the 50s, many X-ray instruments have been launched above atmosphere, starting from simple detectors to focusing imaging systems. The great majority of X-ray telescopes launched so far follows the optical design called Wolter I (or its approximation), that focalizes the X-photons with a double reflection on a first paraboloid and a second hyperboloid mirror surfaces. State of the art in X-ray telescopes is represented by the US Chandra satellite and by the European XMM-Newton satellite, launched into space in the 1999 and still operative. To further improve the scientific knowledge of the X-ray sky, the next generation X-ray telescopes will require a larger collecting area combined with higher angular resolution with respect to them. The current production technologies cannot meet such demanding requirements; they will result in too heavy systems to be launched on orbit; hence the need to develop a new manufacturing technology for the X-ray telescopes of the future.

This dissertation describes the research performed on the assessment and the development of the slumping technology, based on the thermal shaping of glass materials, as a candidate technology for the realization of next generation X-ray telescopes that require being lightweight, large and with a high angular resolution. The work realized by the author at the Astronomical Observatory of Brera (INAF-OAB) during a Ph.D program, covering a time frame of three years, is reported. The majority of the performed research is part of an ESA contract for the development of a back-up technology for the realization of the International X-ray Observatory (IXO – former XEUS) optical payload. For this reason, the IXO project is described. However, it has to be considered as a case study since the

technology itself can be applied to other missions and even for the production of items with different end-scope, such as for example thin mirrors for adaptive optics or lightweight segmented mirrors.

Chapter 1 provides an introduction to X-ray astronomy. X-ray telescopes Grazing Incidence principle is described, together with the manufacturing techniques so far employed for the realization of X-ray telescopes to give an overview of the state of the art in the field.

Chapter 2 describes the International X-ray Observatory mission. The requirements for the X-ray optical payload, as derived by the main scientific goals, are presented together with the challenge the astronomers and engineers community has to face for the manufacturing of such demanding system. The current European base-line design, based on Silicon Pore Optics, is also described to show where the need for a risk mitigation back-up technology for the X-ray mirrors production comes from.

Chapter 3 reports on the “IXO back-up optics study”, the context in which the majority of the presented research works has been performed. The proposed optical design for IXO telescope making use of the back-up glass mirror plates technology is presented.

Chapter 4 discusses the slumping technology under assessment by INAF-OAB for the manufacturing of X-ray segmented mirrors made by glass. A general introduction to the slumping technology is given to familiarize the reader with the terminology and the many process parameters that have to be considered. A comparison with the Pore Optics technology and with different approaches of the slumping technology under development by other research groups in the world for the production of X-ray telescopes is reported, showing advantages and disadvantages of the proposed technique with respect to them.

Chapter 5 goes in the details of the tests implementation, giving a description of the items and tools employed during the experiments realization and the analyses of results. In particular, the oven laboratory upgrades realized during the study are reported. The procurement of necessary tools, primarily moulds and glass foils, is described, following the explanation on the selected materials and geometrical properties.

Chapter 6 might be considered the core of this work, reporting the main results obtained during the research activities performed from spring 2008 to spring 2011. Particular attention is dedicated to the results in terms of shape and of micro-roughness of the slumped mirror plates. Important improvements in the slumping process steps and related analyses are also given space.

The work is still on-going: upcoming activities will be presented, together with future improvements proposed on the base of the gained experience.

Chapter 7 closes the present dissertation, summarizing the main results and the future steps of the development proposed for the next phases of this project or for other projects that require large and lightweight optical systems composed by a number of equal elements.

Annexes have been added to the text to help the reader in the understanding of the exposed research. Annex A gives a brief description of the surface topography to introduce the definition of shape and micro-roughness. Annex B provides the description of the metrological instrumentation operating principle. Annex C lists all the carried out experiments and their main goals. Annex D shows the current hot direct slumping procedure developed during the study.

A lot of people did not directly work on this project, but indirectly supported it (and me) in a million of different ways: many many thanks to all of them, whose help was crucial. A lot of people even did not know of the existence of this project: thanks to all of them for their curious questions (and their attention to the answers). A lot of people worked on this project: many thanks to all of them, which make the research possible. A lot of people still work, and many other will start to, on this research topic: to all of them... good luck! (and have the same fun that I had).

The author

Merate, September 2011

1 Astronomical X-ray Telescopes

This chapter provides an introduction to X-ray astronomy and in particular to the X-ray optical systems necessary to focus X-photons. Their production technologies are presented to give an overview of the state of the art in this field.

1.1 History of X-ray Astronomy

X-ray astronomy is the study of astronomical objects at almost the highest energies of the electromagnetic spectrum. It is a relatively new branch of astronomy that dates back to only few decades ago, in late 1940s, when the first Geiger counts carried aloft German V-2 rocket were able to discover X-ray emission from the Sun. Since 1930s there was evidence that the outer regions of the solar atmosphere were much hotter than the known surface temperature of about 6000 K, making them a possible source of X-ray; but it was only when the first payload could be lift above most of the atmosphere (more than 99%) that the first experimental evidence for that could be recorded. Only the advent of space era, in fact, allowed to study X-ray emissions coming from astronomical object in the Universe since the Earth atmosphere is highly opaque to the X-ray band of the electromagnetic spectrum, as depicted in Fig. 1.1. Balloons, sounding rockets and satellites are essential to perform X-ray astronomy.

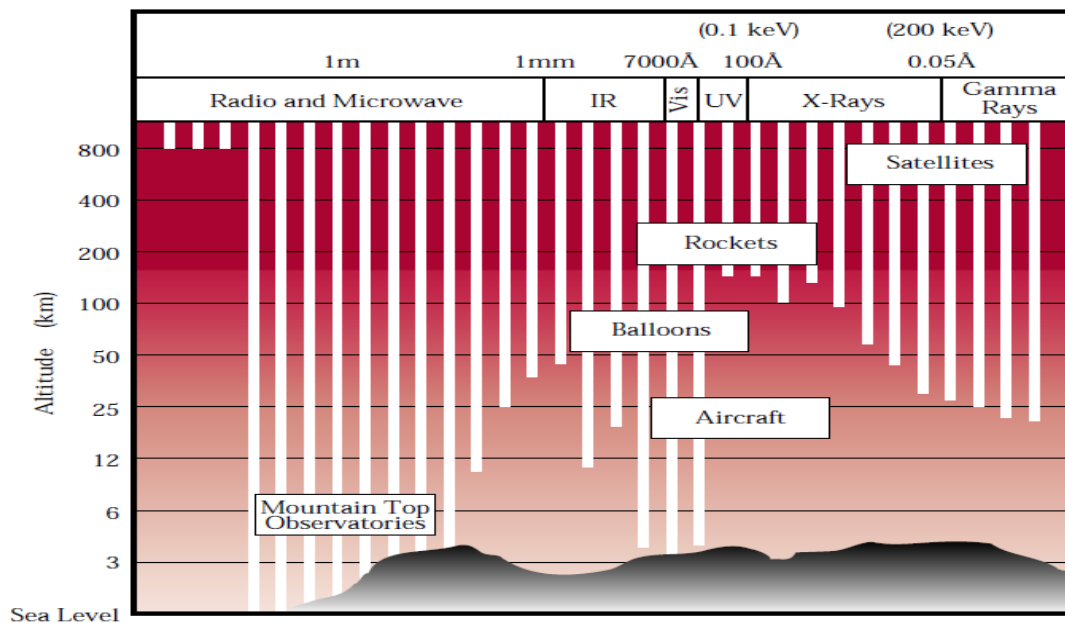


Fig. 1.1: Earth atmosphere is opaque to the X-ray band of the electromagnetic spectrum. Balloons, sounding rockets and satellites are essential to lift detection systems above it and perform X-ray astronomy [1].

Even if the first launches did not allow discovering any X-ray radiation other than that coming from the Sun, they contributed in spreading scientific considerations on the high potential that X-ray observations could bring to the astronomical community: X-ray were the lower energy radiation in the high-energy domain that could reach Earth unimpeded over cosmological distances and therefore they would have provide the highest photon flux in the emission from high-energies processes. The fluxes that astronomers could predict from extra-solar sources, however, were quite small: while the Sun produced at Earth a flux of 10^6 photons/cm² s, the fluxes expected from other celestial sources were order of magnitudes smaller. For example, a Sun-like star at a distance of one light year would have produced 2.5×10^{-4} photons/cm² s (for comparison, consider that the cosmic-ray background was of about 1 count/cm² s, in the Geiger counters used at that time). Since the total X-ray output from the Sun was so small, despite the fact that the Sun is so close to Earth in terms of interstellar distances, many scientists believed that no other sources would have been found in the sky. In this context, a group of determined researches at American Science and Engineering (AS&E), including Riccardo Giacconi, Herb Gursky, Frank Paolini, and Bruno Rossi, started thinking of a way to concentrate the X-ray radiation from a large area collector onto a small detector, in order to increase the signal to noise in proportion to the ratio of the area of the collector to that of the resolution element. They tried several materials and techniques before coming out with the manufacturing of the first real flight-worthy X-ray telescope [2]. In 1962, they were successful in recording, along with a diffuse background coming from all directions, the first cosmic source of X-ray emission: Sco X-1, in the constellation of Scorpius. In 1965, they obtained the first scientifically useful image of the Sun in the X-ray band. The X-ray astronomy was born. For “its pioneering contributions to astrophysics, which have led to the discovery of cosmic X-ray sources”, Riccardo Giacconi was awarded a share of the Nobel Prize in Physics in 2002 [3].

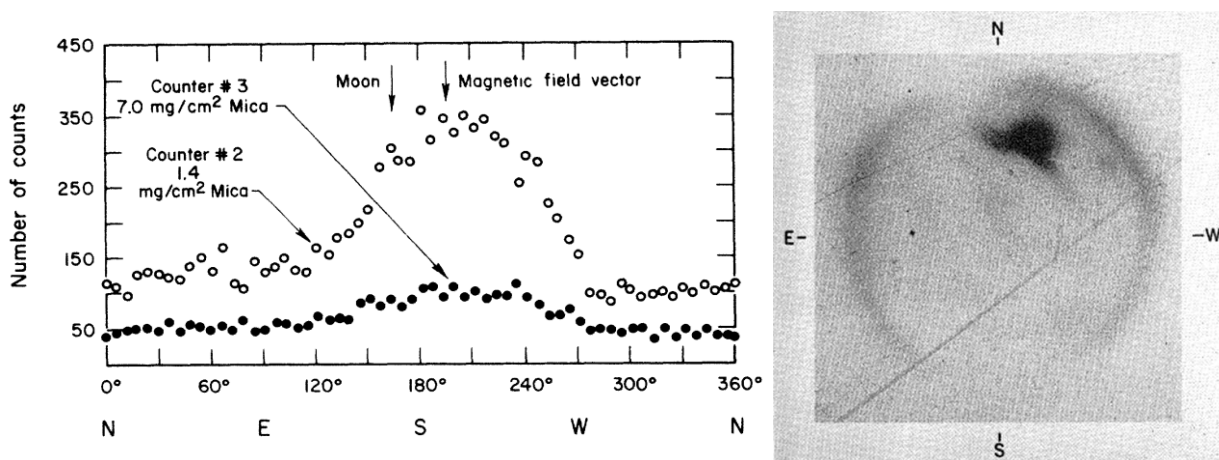


Fig. 1.2: (Left Side) Azimuthal distribution of X-rays from the photon Geiger counters on a sounding rocket in 1962. The numbers represent counts accumulated in 350 sec in each 6° angular interval. These data revealed the existence of a discrete celestial X-ray source (Sco X-1) around 195° azimuth and the diffuse X-ray background. [4]. (Right Side): Solar X-ray photograph: first scientifically useful image of the Sun taken with an X-ray telescope in 1965 [5].

Since that time, a number of rockets, balloons, and satellites have been launched in space carrying X-ray telescopes and photons detectors and this field of astronomy has been developed at an astounding pace [6], [7]. Among the largest and most productive X-ray missions are Uhuru, launched in 1970 [8]; Einstein, operative from 1978 to 1981 [9]; EXOSAT, operative from 1983 to 1986 [10]; Rosat, launched in 1990 [11]; BeppoSAX, launched in 1996 [12], Chandra and XMM, operative since 1999 [13], [14]; and Suzaku, launched in 2005 [15]. Tens to thousands of X-ray sources are presently known in the sky. Many of these sources are orders of magnitude brighter than the Sun, now recognized to be relatively quiet in the X-ray band of electromagnetic spectrum. X-rays provides a unique window on some of the hottest and most violent phenomenon in the Universe [16]. Among the wide variety of X-ray sources there are:

1) X-ray Binaries: X-ray Binaries are close binary systems in which gas from one star falls onto its companion, heats up, and emits X-rays. The emission is especially bright when the companion is a compact object, such as a Neutron Star or a Black Hole. In fact in this case the enormous gravitational field compresses and heats up the falling gas causing it to emit at X-ray wavelengths, whose study is fundamental to understand the processes at the base of this behavior. 2) X-ray Background: The sky is not dark in the X-ray wavelength region: a diffuse background is detectable. Its origin is still not known, although it is believed to be the results of many individual, unresolved sources. The collection of X-photons in high-resolution and sharp images will help in explain this phenomenon. 3) Supernova Remnant: The X-ray spectra of stars explosions show traces of the heavy elements that are formed, giving important data to study the origins of the elements in the Universe. 4) Active Galactic Nuclei: Quasars and Active Galactic Nuclei are among the most energetic cosmic objects. They are believed to be composed by a Supermassive Black Hole surrounded by an accretion disk of in-falling gas at millions of degrees: the study of the enormous quantity of radiation that they emit at X-ray wavelength is fundamental to discriminate between several models and finally understand the process at the base of their formation. 5) Sun, Planets, Stars and Comets: practically all the objects in the sky have emissions in the X-ray band, including our planetary neighbors, the Sun and the planets of the Solar System.

Data collected so far have been of fundamental importance for the understanding of the nature of these sources and the mechanisms by which X-ray are emitted. Meantime, they opened new outstanding questions on the physics of our Universe that requires even larger and more challenging instrumentations to found answers. The next generation of X-ray observatories is currently under consideration. Among the proposed future missions there are IXO [17] and GEN-X [18]. One thing connects them: the necessity of new technologies for the production of their X-ray telescopes.

1.2 X-ray Focusing systems: the principle of Grazing Incidence

A typical X-ray telescope assumes the configuration reported in Figure 1.3 and 1.4, composed by several co-axial and confocal mirrors¹ (called shells) having the shape of concentric surfaces of revolution nested one inside the others. The particular geometry is dictated by the principle of Grazing Incidence (GI): X-ray are reflected and focalized only when they hit a solid surface with very small angles, in the range of few tenths of degree [19].

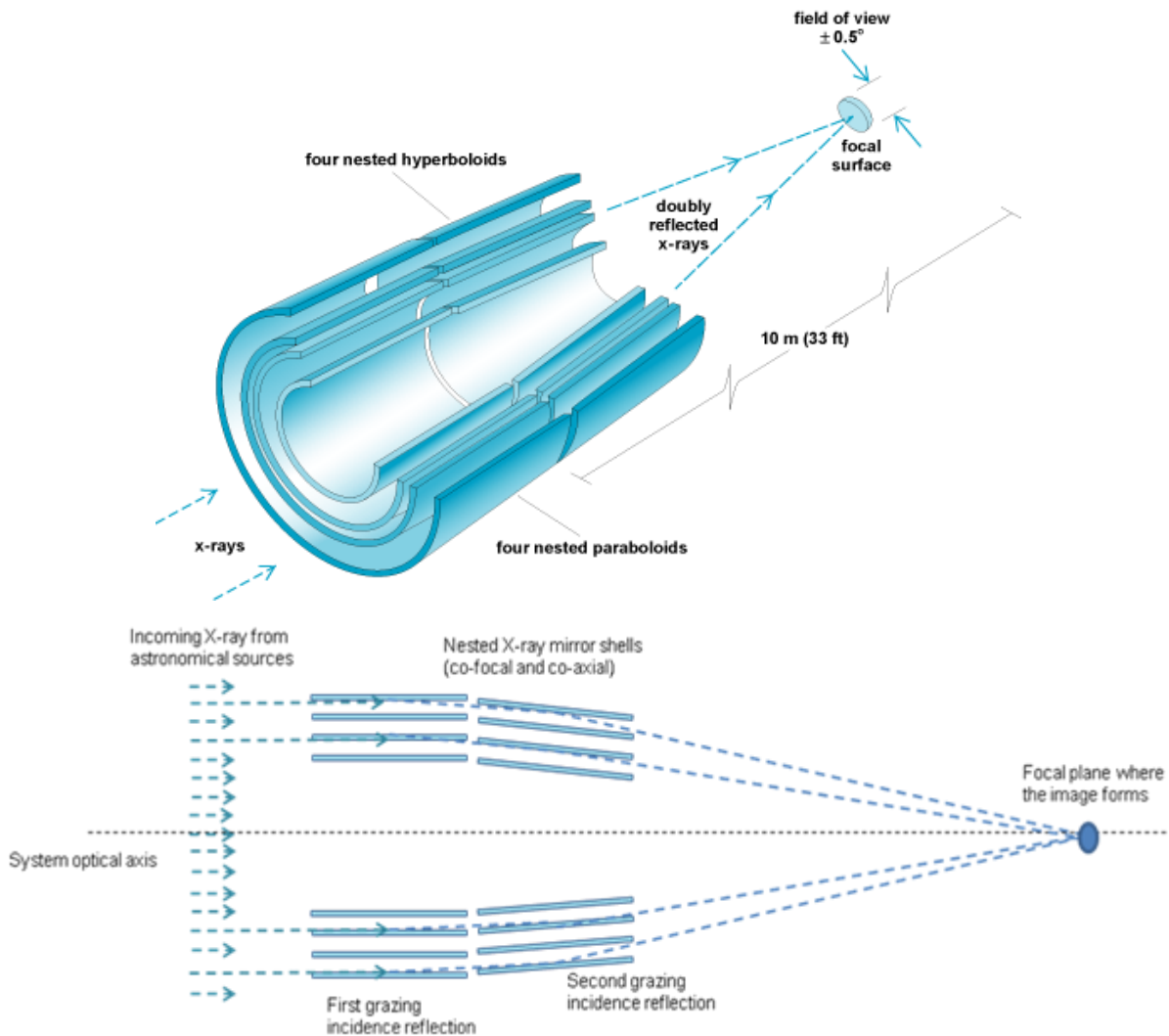


Fig. 1.3: Configuration of a typical X-ray telescope employed in the detection of X-ray sources in the sky. The Grazing Incidence principle is clearly depicted: X-ray coming from a virtually infinitely distant source (left side of the picture) are incident consecutively on two co-axial and confocal surfaces with very small incidence angles and are focalized into the focal plane where the detector is positioned (right side of the image). Picture above refers to Rosat X-ray telescope composed by four nested mirror shells, having a focal of 10 m and a Field of View of 1 degree. A number of shells are nested in order to fully exploit the available geometric area.

¹ In practice X-ray optics have to be *reflective* since *refractive* optics would result in too long focal lengths to be implemented on-board space systems and thick lenses are not employable due to the absorption coefficient.

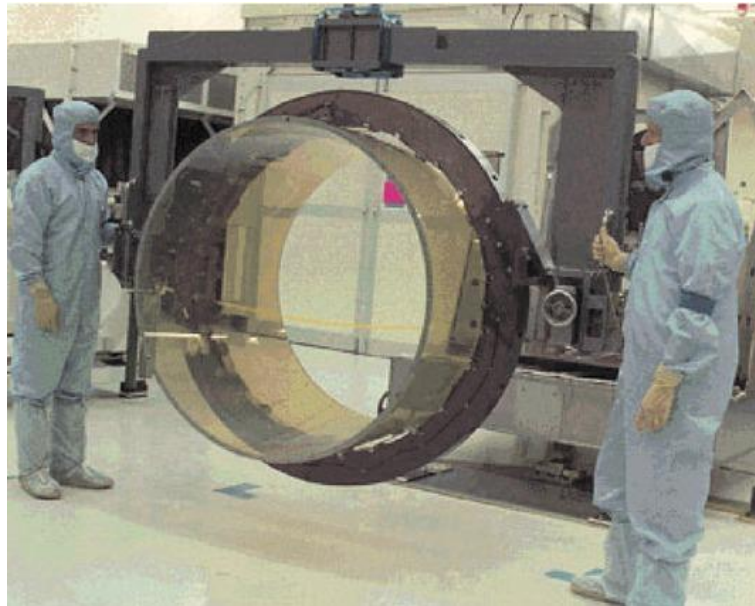


Fig. 1.4: Example of an X-ray mirror. The tube-like configuration due to the principle of grazing incidence is clearly visible in the center of the image. The 1 m long and 1.2 m wide paraboloidal Zerodur mirror which makes up the biggest mirror of the 0.5 arcsec resolution Chandra telescope is shown. To date, it represents the biggest existing X-ray mirror. Next generation ones will have diameters in the order of several meters (at least 3X). (Image credit: NASA/CXC/SAO [20])

A critical angle α_t exists, above which no reflection happens; this is proportionally dependent on the square-root of the reflecting material density (ρ) and on the energy of the X-ray photons being reflected. This behavior of X-ray is connected to the interaction of light with matter, which can be expressed by the complex index of refraction describing the change of the properties of the incident electromagnetic wave when crossing the boundary between the two materials involved. This index expresses the material behavior to reflection, absorption, and transmission and can be written as:

$$n = 1 - \delta - i \cdot \beta$$

where δ describes the phase change and β accounts for the absorption. The components of the index of refraction for vacuum-matter transition are often called the optical constants of the material: they are function of the wavelength, that is to say the energy, of the incident photons. In the optical wavelength range, for instance, the real part of the index of refraction is always greater than 1, but with decreasing wavelength it becomes less than 1, which changes the interaction of light with matter dramatically. The refractive index of all materials in the X-ray band is only slightly less than 1 (being exactly 1 in vacuum [21]); X-rays act in a completely different way than the visible light does, when they encounter a reflecting surface. The reflectivity at normal incidence drops so rapidly with decreasing wavelength that for observations at wavelengths shorter than about 15 nm, Grazing

Incidence is the only choice². By applying the Snell law³, it turns out that in the X-ray band total external reflection can occur only for Grazing Incidence angles $\alpha \leq \alpha_t$. For heavy elements (e.g. Gold or Platinum)⁴ for which the ratio between the atomic number and weight is $Z/A \approx 0.5$, the incidence angle of total reflection (i.e. index of refraction $\delta \ll 1$) can be estimated to: $\alpha_t = 5.6 \lambda \sqrt{\rho}$ with α_t in arcmin, λ in Å and ρ in g/cm^3 . For X-rays, with λ of a few Å, α_t is about one degree. The same can be expressed in terms of energy as: $\alpha_t = 6.9 \sqrt{\rho/E}$, with E in keV [22], [23]. The most used configuration for X-ray systems is called Wolter I, from the name of the German physicist that first proposed it in 1952; Hans Wolter demonstrated the possibility to focalize X-rays, without focal distortions, utilizing two Grazing Incidence reflections in succession on confocal and coaxial surfaces of revolution [24]. He proposed three optical designs, shown in Fig. 1.5 and named Wolter I, Wolter II, and Wolter III⁵. These configurations allow the Abbe sine condition⁶ to be nearly satisfied. Wolter also showed that any odd number of co-axial conic sections will not form an image, while any even number can. In practice, the only even number considered is 2 for the enhanced difficulties in integrating and correctly aligning more than two elements and because any system with four or more mirror elements would result in increased scattering and reflection losses. In particular, in the Wolter I geometry, the double reflection happens on a first paraboloid mirror followed by a coaxial hyperboloid one. This solution offers the advantage of reducing the focal length of a factor of two with respect to the other Wolter solutions, a parameter very important for optics that require to operate in space, i.e. to be lift by a launcher. It also offers the great advantage of a simpler mechanical configuration, hence easier practical realization. The great majority of X-ray imaging systems launched so far is realized with the Wolter I configuration, or with one of its approximations (such as the double cone approximation) because of the possibility it allows of nesting several mirror shells, increasing the filling factor (i.e. the ratio of usable to total aperture) of the geometrical area available for the optical system. The effective area of a single Grazing Incidence X-ray mirror is in fact very modest: for an X-ray telescope, the effective photon collecting area is the product of the mirror surface reflectivity times the geometric area of the primary mirror projected on the front aperture.

² X-rays ranges from 0.01 to 10 nm in terms of wavelength, which is from 3×10^{16} Hz to 3×10^{19} Hz in terms of frequency, which is from 120 eV to 120 keV in terms of Energy.

³ The Snell Law is the formula describing the relationship between the angle of incidence and the angle of refraction of a wave passing through a boundary between two different materials; it states that the ratio of the sines of the angles of incidence and refraction is equivalent to the opposite ratio of the indices of refraction of the two materials.

⁴ Since the critical angle of reflection is proportional to the density of the reflecting material, X-ray mirrors are usually coated with heavy materials, such as Ni, Au, Ir and Pt, to increase the allowed angle. Since several years, multilayer coatings are under study to reflect more energetic (shorter λ) photons. They are not described here since out of the scope of this work.

⁵ Wolter systems are not the only existing systems. Other two-mirror configurations exist to focalize X-ray, such as Kirkpatrick-Baez type systems, and the focusing collimator or 'lobster-eye' systems.

⁶ An optical system has to meet the Abbe sine condition to produce sharp images of on-axis as well as off-axis objects; this condition states that the sine of the output angle of the light rays (relative to the optical axis of the system) should be proportional to the sine of the input angle.

Being r the radius of curvature, l the length, and f the focal length of the X-ray mirror element, the projected geometric collecting area is given by:

$$a \approx 2\pi r \times l \sin \alpha$$

that for small angles α can be written as:

$$a \approx 0.5\pi r^2 \times l/f$$

As stated before, the mirror surface reflectivity is a function of the photon wavelength. Different reflective materials can be considered in dependence on the wavelength range of X-rays to be focused and detected: Au, Pt, Ir can be used for energies up to 10 keV; for higher energies the use of multilayer coatings is necessary [25]. As previously explained, in order to increase the effective area of the telescope, a number of these tube-like co-axial and confocal mirrors are nested one inside the others decreasing the radii. The number of shells nested one inside the other is different from time to time and it is strictly related to the methods adopted for their production (see later § 1.3). The maximum effective area reached with nowadays instruments is in the order of 4500 cm^2 , obtained with the XMM Newton optical payload, composed by 3 identical modules of 58 nested shells each. Next generation X-ray telescopes, such us for example IXO, will require at least 5 times this value. So far, only few solar X-ray telescopes, when nesting could be renounced, have been produced with the Wolter II configuration, or its Wolter_Schwarzschild approximation [26] because of its compactness; no X-ray astronomy telescopes have been to date realized following the Wolter III design.

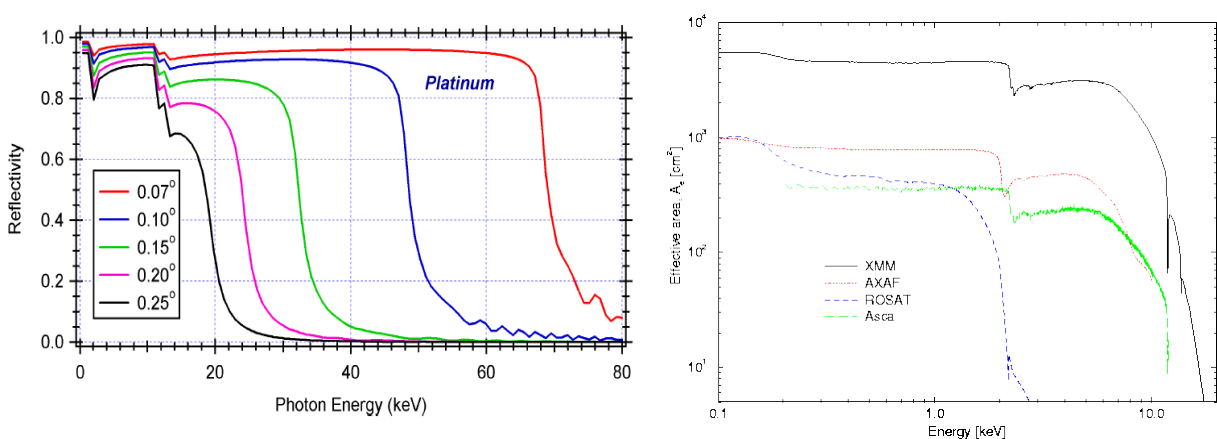


Fig. 1.5: Example of Reflectivity and Effective area of X-ray mirrors as a function of photons Energy. The reflectivity is good in Grazing Incidence up to a critical cut-off angle, above which the reflection drops; this angle depends on the reflecting material density and on the energy of the X-ray photons being reflected.

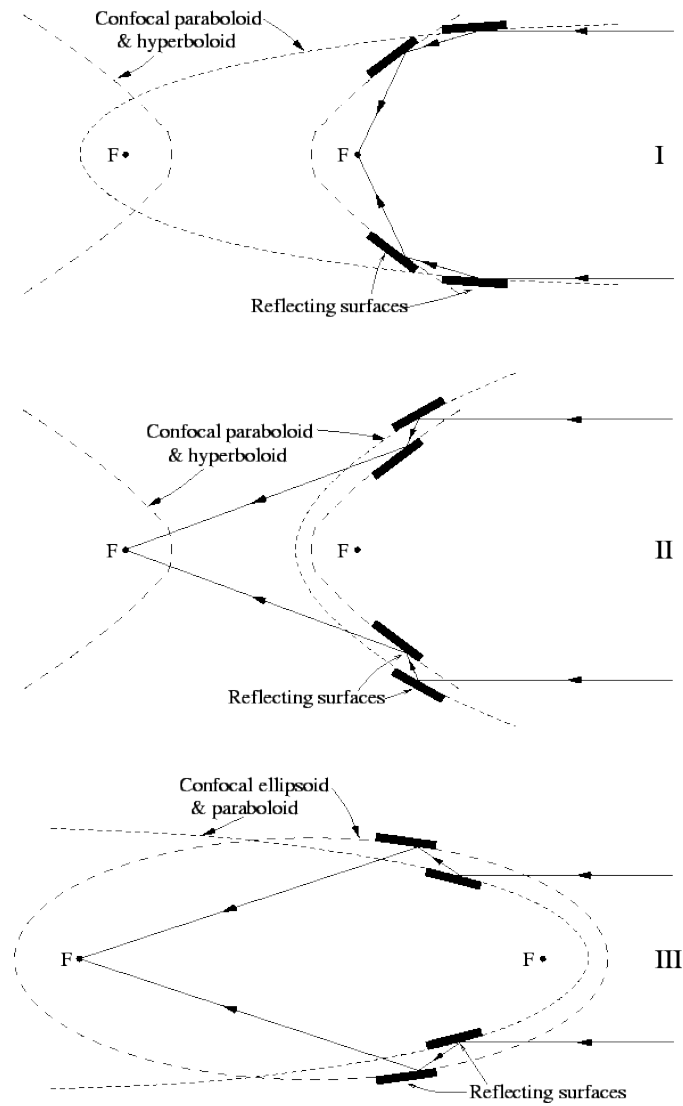


Fig. 1.6: Wolter geometries for X-ray optical systems, based on the fact that X-rays are reflected by smooth surfaces under small angle of incidence. Wolter I and Wolter II are composed of a paraboloid and a hyperboloid. Wolter III is composed of a paraboloid and an ellipsoid.

In addition to the effective area, one other important parameter to keep in mind when describing a telescope is its angular resolution, which describes the smallest details of the observed object distinguishable on the obtained image. The value of angular resolution is governed by the accuracy of the X-ray mirror figure, described in terms of roundness and slope errors with respect to the theoretical shape, and by its surface texture finishing (see Annex A for explanation). Long-wave deformation effects can be described by the geometrical optic laws, while at higher spatial frequencies scattering interference effects dominate the image quality [27]. Both the phenomena influence the Point Spread Function (PSF) of the optical system, and thus its angular resolution. The PSF is the bi-dimensional distribution on the focal plane of the photons coming from an object located at infinite distance; its mono-dimensional integral is the Line Spread Function (LSF). The fraction of focused photons as a function of the angular distance from the optical axis is defined as

the Encircled Energy. The angular resolution is obtained from this definition as the Half Energy Width (HEW) or the Half Power Diameter (HPD) of the focal plane image, which are the angular diameter including the 50% of the focused photons. The HEW and HPD are normally expressed in arcsec. The maximum value reached for nowadays X-ray mirrors is of 0.5 arcsec HEW for on-axis performances, obtained for the relatively small effective area shells of Chandra. The goal value for the future IXO mission taken as example is of 5 arcsec, anyway combined with an almost 50X effective area with respect to that of Chandra, whose value is around 800 cm^2 . Also this parameter is strictly related to the method of production employed for the manufacturing of the optics, as described in the next paragraphs.

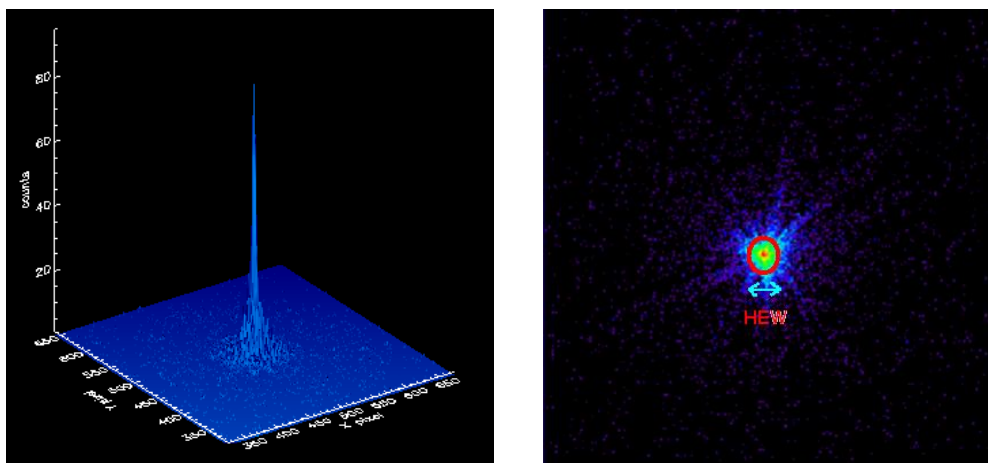


Fig. 1.7: *The Point Spread Function (PSF) describes the imaging system response to a point input, i.e. it describes how the focused intensity is spread around the focal spot. The HEW (or HPD) is the angular diameter including 50% of focused photons, normally expressed in arcsec (Credits: MPE/PANTER) [28].*

1.3 Manufacturing techniques

The state of the art for X-ray mirrors production comprises essentially three methods, adopted for the realization of past and present X-ray observatories: the production by direct polishing of single mirror shells, the production by replica of mirror shells made in Electroformed Nickel, and the realization of aluminum thin foil mirror shells [29]. The variety of angular resolution and effective area obtainable with the different technologies is reported in Table 1.1. The different techniques have been adopted in the past for the realization of several missions, for which, from time to time, one specific requirement was favored over the other in dependence on the specific scientific aim of the mission. The same compromise might not be accepted for next generation X-ray telescopes for which both the angular resolution and the effective area should have a relatively high value, compared with the previous X-ray mission, although respecting the mass limits imposed by the launchers.

Table 1.1: Main characteristics of a selection of past, present, and future X-ray optical systems

Mission	Status	Launch	Telescope module #	Max module diameter (mm)	Diam. of Total geometric covered area (mm)	Telescope Focal length (m)	Module Eff. Area (m ²)	Angular Res. HEW (arcsec)	Module Mass (kg)	Thickness of shells (mm)	Mirror Technology
Einstein	Non operative	1978	1	580	> 580	3.45	0.04	~ 10	--	~ 20	Glass Directly polished shells
ROSAT	Non operative	1990	1	835	> 835	2.4	0.10	< 5	~ 600	16-25	Zerodur Directly polished shells
Chandra	Operation	1999	1	1200	> 1200	10	0.08	0.5	1000	~ 35	Zerodur directly polished shells
Beppo/Sax	Non operative	1996	4	162	> 325	1.8	0.0123	60	~ 90	0.2-0.4	Replicated Ni shells
JET-X/Swift	Operation	2004	1	300	--	3.5	0.011	15	~ 67	0.6-1.1	Replicated Ni shells
XMM-Newton	Operation	1999	3	700	> 1400	7.5	0.15	15	420-437	0.47-1.1	Replicated Ni shells
ASCA	Non operative	1993	4	350	> 700	3.5	0.041	200	--	0.125	Thin Al foil
Suzaku (ASTRO-E)	Operation	2005	5	400	> 800	4.75	0.04	120	12	0.155	Thin Al foil
HEFT	Balloon experiment	2005	1	240	--	6.5	0.025	60	~ 90	0.300	Thin glass foil
NuSTAR	Under construction	2012	2	382	--	10	0.05	40	~ 25	0.200	Thin glass foil*
IXO	Develop-ment	> 2020	1	3500	> 3500	20	2.5	5	800 - 1200	0.4	Thermally formed glass segments*
Gen-X	Concept	> 2030	1 (TBC)	30 m (TBC)	30 m (TBC)	300m(TBC)	50	0.1	12300	< 0.4	Actively adjustable segments

*note that the two techniques here indicated with two different words "thin glass foil" and "thermally formed glass" might appear to be substantially the same technique. They are, however, called in different ways to highlight the fact that current thin glass foil resolution results are not sufficient for the next generation telescopes, for which a big step forward in the technology is necessary.

1.3.1 Direct polishing of mirror shells

The direct polishing of glass shells has been used for the production of the first astronomical X-ray satellites (such as Einstein and ROSAT) [30], [31]. It foresees the realization of each single monolithic shell by the direct polishing and figuring of the substrate material, realized with the mechanical action of a special tool in contact with the mirror shells. The materials utilized are usually Quartz or Zerodur and to withstand each step of the production, and possess the necessary rigidity to maintain the intrinsic shape without suffering from deformations, their thickness necessitates to be in the order of 20-30 mm. This allows obtaining high precision in the geometrical profiles of the shells (which means high angular resolution hence sharp images) but relatively small collecting area since only few shells can be nested one inside the other. The two reflective surfaces (parabola and hyperbola of the Wolter I design) are normally machined separately and consequently aligned during the integration process. The best result in the application of this technology is represented by the satellite Chandra, whose angular resolution reached 0.5 arcsec HEW. This type of optics is aimed at the observation of extended X-ray source or of the cosmic X-ray background (throughout long observation time) for which the angular resolution is a fundamental parameter rather than the effective area.

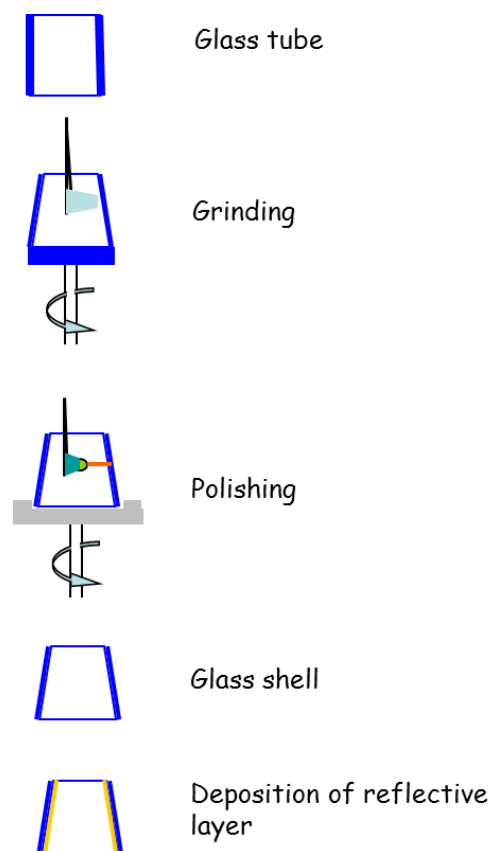


Fig. 1.8: Schematic of X-ray mirror shells production by direct polishing.

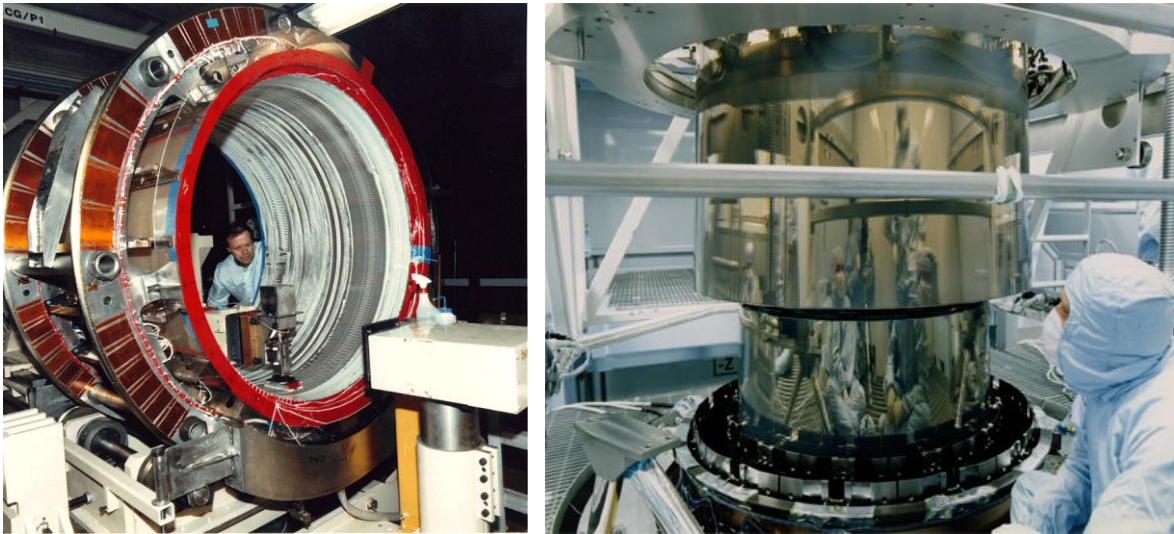


Fig. 1.9: Example of mirror shells produced by direct polishing: the case of Chandra satellite is shown. (Left Side) Optical direct polishing of large Zerodur mirror shells of Chandra realized at HDOS. While the glass shell rotates, the polishing tool moves back and forth to polish it (Credits: Raytheon Company). (Right Side): Chandra mirror being assembled at Eastman-Kodak. One of the four hyperbola shells is being aligned and integrated with respect to the others, visible in the bottom of the image. (Credits: Eastman-Kodak).

1.3.2 Mirror shells replication by electroformed Nickel

The technique based on electroformed Nickel was the one employed for the very first X-ray telescope in 1965 [32]. In late 1980s, INAF-OAB improved it for the realization of the Italian satellite Beppo-Sax [33]. The same technique has been then employed for the realization of Jet-X/Swift and XMM-Newton X-ray optics. It provides good effective area, due to the possibility of nesting several relatively thin shells one inside the other, coupled with pretty good angular resolution. It foresees the realization of Nickel optics by electroforming them on a precisely figured mandrel in an electrogalvanic bath. A layer of evaporated gold is used both as release agent and reflective coating. This type of optics offer a major flexibility in the choice of shells thickness, selected as compromise between effective area, angular resolution, and mass. This approach permits the deposition of a range of Nickel thicknesses, in dependence on the process time set for the deposition in the electrogalvanic bath during the process of replica. Normally, low thicknesses are used to limit the system mass; this is possible since no direct mechanical machining is foreseen on the mirrors: the typical range is from 0.2 mm to 1 mm. Thinner mirror shells will result in floppy structures subject to any type of deformations, because of the low value of rigidity, and so extremely demanding in terms of integration requirements; thicker mirror shells do not suffer for this problem but might not

respect the mass budget located for the satellite payload, resulting in too heavy structures. The compromises adopted till now gave good results with the possibility to realize mirrors with high effective area and high filling factor. One of the main characteristics which make the technology attractive resides in the fact that it is a replication technology, i.e. with one figured mandrel it is possible to obtain several identical mirror shells that can be assembled in identical mirror modules. This characteristic is very important in the industrialization phase, in the case several identical pieces have to be realized. Other replication approaches have been studied, with substrate materials that cannot be electroformed, like Silicon Carbide, Alumina, and Beryllium. They are based on the replication by epoxy: the figured mandrel with an evaporated reflecting layer is positioned inside a pre-machined substrate that has been produced with a diameter slightly bigger than that of the mandrel to leave a gap in the order of 100 μm . This gap between the mandrel and the pre-figured substrate is filled with epoxy and the reflective layer adheres on the shells with the replicated shape of the precisely figured mandrel [34].

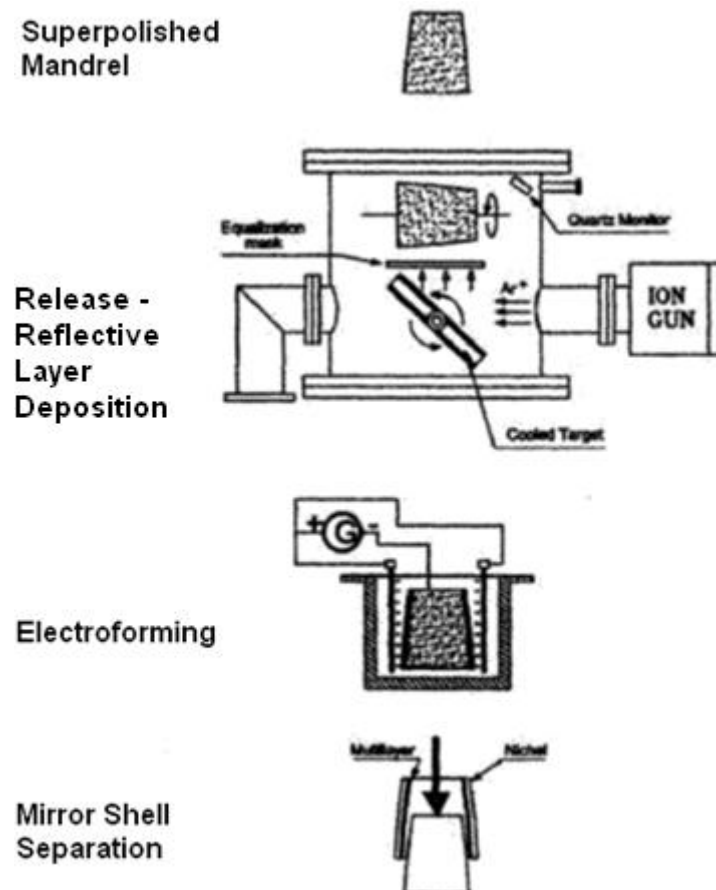


Fig. 1.10: Schematic of X-ray mirror shells production method based on the direct replication by Nickel electroforming [35].

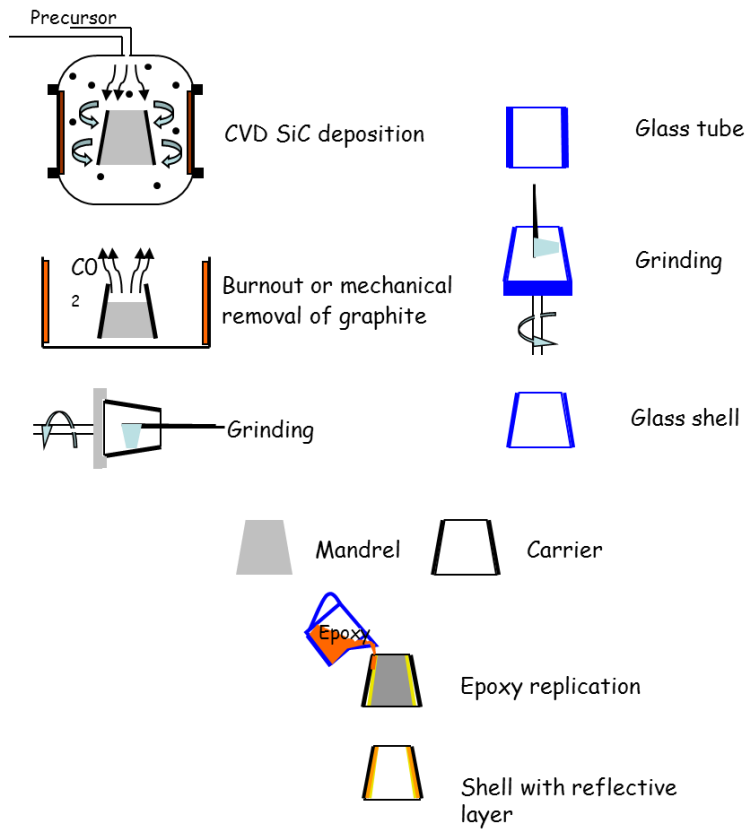


Fig. 1.11: Schematics of X-ray mirror shells production by epoxy replication. The reflective layer, that replicates the shape of a precisely figured mandrel, adheres because of the epoxy application on a pre-machined carrier that can be manufactured in different materials, for example SiC or Quartz.

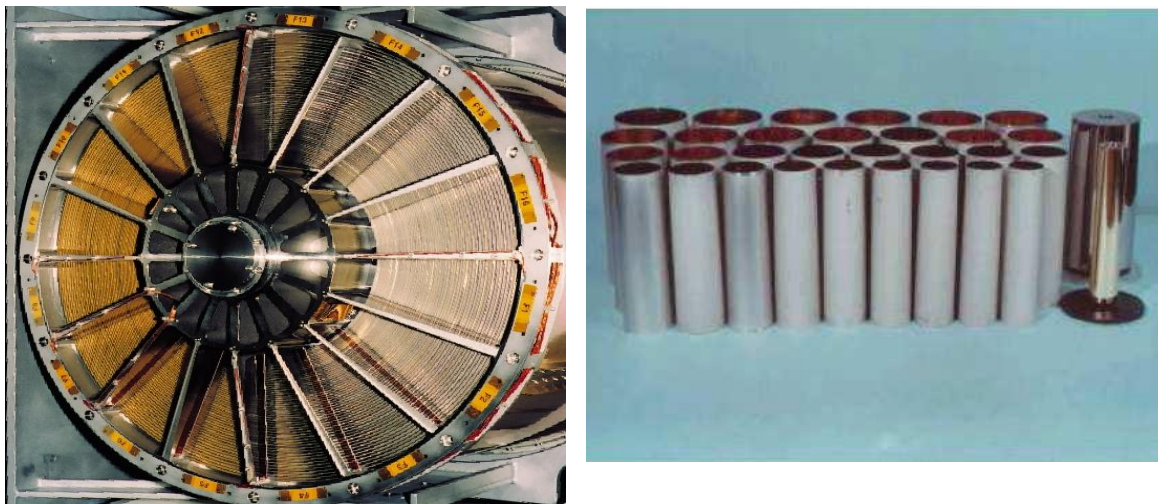


Fig. 1.12: Example of X-ray mirror shells realized with the electroforming of Nickel on a suitably figured mandrel. (Left Side): One of the XMM-Newton modules, containing 58 shells with thickness ranging from 0.47-1.1 mm. (Right Side): The entire series of shells for one of the four modules of Beppo-Sax together with two of the mandrels employed in the replication process for their production.

1.3.3 Aluminum thin-foil mirror shells

The method of thin foil has been implemented in the past for the construction of X-ray segmented optics: instead of building a close tube-like structure, the X-ray mirror shell is realized by integrating together a number of curved segments with the same radius of curvature in such a way to reconstruct the close cylindrical symmetry of the optical design. The obtained angular resolution is quite poor, in the range of few arcmins. Nevertheless, it allowed the close packaging of up to 200 thin segments (100-400 micron in thickness) in a single optical module, with good performances in terms of mass/geometric area ratio. The method has been adopted for example for ASCA and ASTRO-E2 missions [36], [37]. It makes use of thin aluminum foil shaped to conical profile (approximation of Wolter I design). This type of optics is aimed at application of spectroscopy, polarimetry and timing for which the effective area is more important rather than the angular resolution. Few years ago, an alternative method was studied for the realization of Polyethylene Terephthalate (PET) substrates to enhance the angular resolution utilizing thin substrates, which in this case were made by plastic [38].

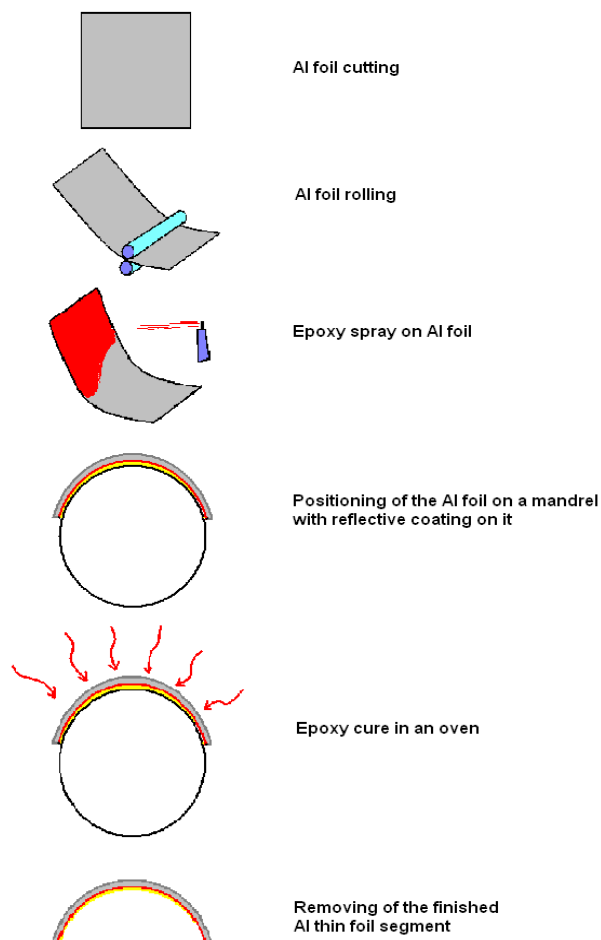


Fig. 1.13: Schematic of X-ray mirror shells production by Aluminum thin foils method [39].

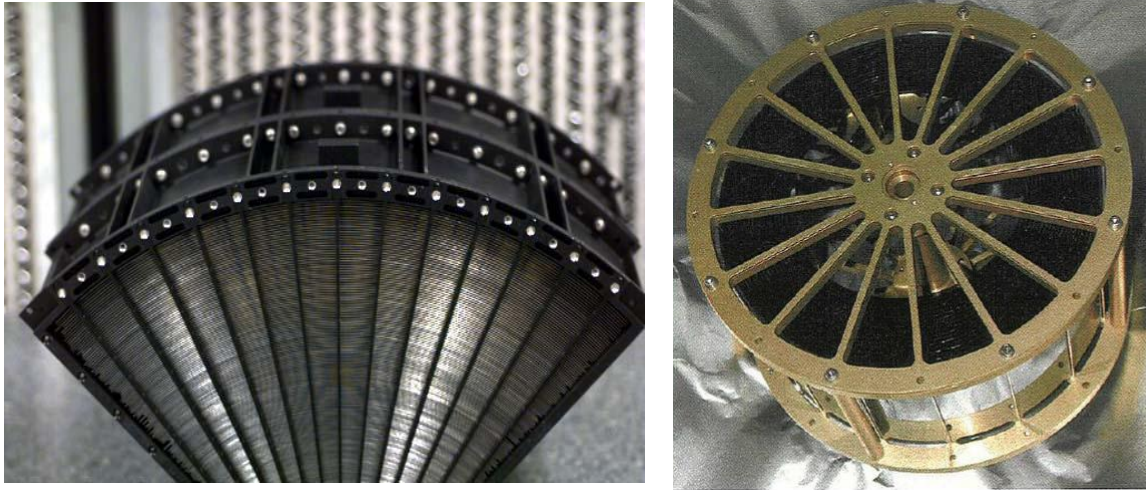


Fig. 1.14: Example of X-ray telescopes realized by thin-foil method. (Left Side): One of the four 90° modules realized for ASTRO-E mission. By integrating and align 4 identical modules it is possible to reconstruct the cylindrical symmetry of the X-ray telescope design. In this case, each module consists of 175 mirror segments made in aluminium. (Right Side): Prototype realized with 20 PET nested thin-foil shells [38]

2 The International X-ray Observatory

The International X-ray Observatory (IXO) is a proposed mission specifically dedicated to the exploration of high-energy phenomena of the Universe in the X-ray band, which characterize the evolution of cosmic structure on both large and small scales. The IXO space segment will consist of a single spacecraft accommodating the scientific instruments and an Extendible Optical Bench containing the X-ray telescope. The launch is foreseen for the year 2022. The realization of the mission has been assessed feasible both by Space Agencies and by industrial studies. The IXO spacecraft bus can be built with established hardware and technologies fully mature today and with substantial flight heritage while critical-subsystems and scientific payload instruments necessitate technology development activities in order to meet the necessary Technology Readiness Level (TRL, [40]). In particular, the large IXO X-ray telescope presents the main technological challenges.

In this chapter, an overview of the entire IXO mission and its main scientific goals is provided to present the requirements posed to the X-ray optical system. The present ESA base-line design, based on Silicon Pore Optics, is also described.

2.1 IXO mission overview

The International X-ray Observatory mission was under development in the context of ESA Cosmic Vision as one of the three candidates for the L-Class missions and in the context of US Decadal Survey (Astro2010) as a high scientific interest mission [41], [42]. In summer 2008, an ESA-NASA-JAXA coordination started, with the intent of join the efforts and expertise of the three agencies in the development of a future International X-ray Observatory: the previous ESA-JAXA XEUS study and NASA Constellation-X study merged together addressing the recommendation to seek international cooperation to maintain costs to affordable funds and to consolidate science goals [43]. The key technologies of the mission are under development to reach the necessary Technology Readiness Level (TRL = 5) by the end of 2012, when the final selection of candidate missions is foreseen. IXO is aimed to study the high-energy Universe detecting and performing spectroscopy of faint astrophysical sources located at high red-shift with unprecedented instrumental capabilities, far beyond the current generation of X-ray observatories (e.g. Chandra, XMM-Newton, RXTE, and Suzaku). IXO data will allow the scientific community to answer outstanding astrophysical questions on the origin and evolution of stars, galaxies and the Universe as a whole. IXO science operations are

expected for the decade 2022-2032 since the launch is foreseen by 2022 and the design assumes a five-year mission lifetime, with a goal of ten being all consumables dimensioned for at least ten years of operation. The satellite will be launch with an Ariane V or with an Atlas V/551 launcher and placed on an halo orbit around the second Lagrangian point of the Earth-Sun system (L2), which provides uninterrupted viewing, an ideal stable thermal environment, and freedom from Low Earth Orbit radiation belt problems. With its 6.5 tons (mass at launch), IXO satellite will be one of the biggest scientific satellites ever launched. The heart of the satellite will be the optical payload, consisting of a single large X-ray telescope, and two instruments platforms (one fixed and one movable) to locate the detectors. The telescope will have a diameter of about 3.5 m and focal length of 20 m (see § 3 for details). The peak of power consumption during operations is estimated to be about 5.5 kW. The power will be generated by triple-junction GaAs solar arrays and stored in Li-ion batteries. Communications will be guaranteed mainly by high speed and low speed X-band antennas. The attitude determination and control will be realized with star trackers and on board metrology (for the Extensible Optical Bench) and with five reaction wheels and thrusters [45]. The IXO system design has been realized both by industry and by Space Agencies (NASA & ESA): despite inevitable small differences, the studies converged to similar solutions. An example is shown in Fig. 2.1.

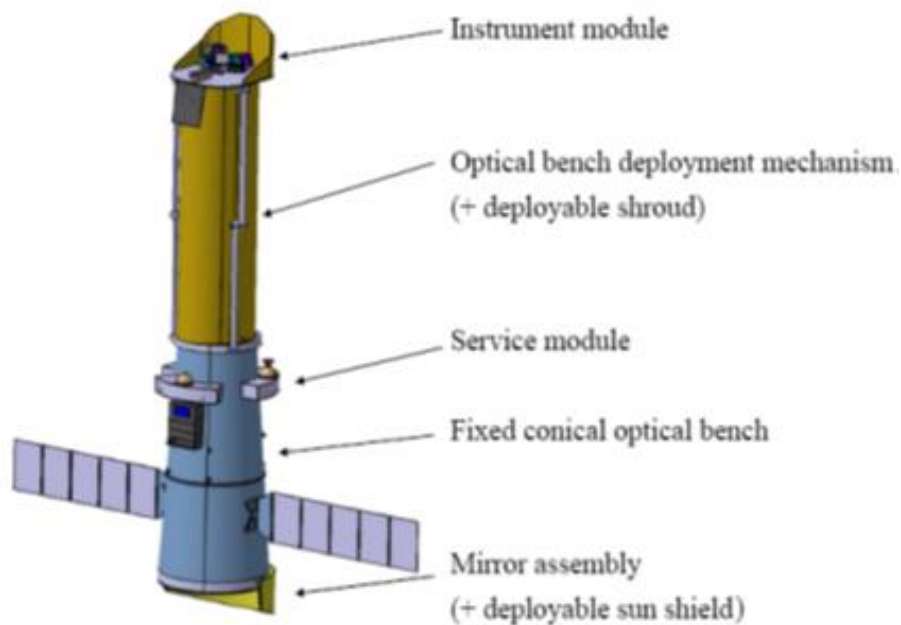


Fig. 2.1: *The IXO system design was carried out by Space Agencies and industry which, despite inevitable differences, came out with similar solutions. The IXO spacecraft is composed by three main modules: the Instruments Module (IM), the Service Module (SVM), and the Mirror Assembly module (MA). The result of a design study carried out in Europe is shown in the figure [46].*

In particular, the spacecraft can be divided into three main functional modules:

- **The Mirror Assembly (MA):** The MA is located inside the fixed telescope metering structure (part of the Service Module) and contains the X-ray optics, the associated supporting structures and thermal control hardware.
- **The Service Module (SVM):** The SVM includes the fixed telescope structure, the deployment mechanism, the deployable shroud and the actual S/C service platform.
- **The Instrument Module (IM):** The IM accommodates the focal plane instruments and includes the moving platform, the focusing mechanism and the X-ray imaging Micro-calorimeter spectrometer Instruments cryogenic chain, with dedicated thermal radiators.

2.2 IXO Science case

IXO mission is foreseen to address some of the most fundamental issue in contemporary astrophysics and cosmology; it will undoubtedly play a significant role in answering a wide range of the science questions listed in both Cosmic Vision 2015-2025 and Astronet documents [47], [48]. Table 2.1 shows a list of the open questions as derived by ESA Cosmic Vision program for the decade 2015-2025 and highlights the fields in which IXO will provide the data necessary to enhance our knowledge.

Table 2.1: Main present astrophysical open questions (Credit: ESA, CV15-25 program) and fields where IXO can help in finding an answer (underlined sentences).

<p>1. PLANETS AND LIFE</p> <p>What are the conditions for planet formation and the emergence of life?</p> <p>From gas and dust to stars and planets From exo-planets to biomarkers Life and habitability in the Solar System</p>
<p>2. THE SOLAR SYSTEM</p> <p>How does the Solar System work?</p> <p>From the Sun to the edge of the Solar System Gaseous giants and their moons Asteroids and other small bodies</p>
<p>3. FUNDAMENTAL LAWS</p> <p>What are the fundamental physical laws of the Universe?</p> <p>Explore the limits of contemporary physics The gravitational wave Universe <u>Matter under extreme conditions</u></p>
<p>4. THE UNIVERSE</p> <p>How did the Universe originate and what is it made of?</p> <p>The early Universe <u>The Universe taking shape</u> <u>The evolving violent Universe</u></p>

Given that almost all astrophysical objects emit X-ray, the study of this band of the electromagnetic spectrum is of great importance for a wide range of astrophysical research. High-energy phenomena in the X-ray band characterize the evolution of cosmic structures on both large and small scales; X-ray images reveals hot spots and sources in the sky, associated with the different phases of stellar evolution and with regions where particles have been energized or raised to very high temperatures by intense gravitational forces, strong magnetic fields or violent explosions. X-ray observations are crucial for the astronomers to better understand the history and evolution of matter and energy, visible and dark, as well as their interplay during the formation of the largest structures. Also, they might give important hints on planetary formation and on the influence of the central star on solar-systems objects. With the help of IXO and its improved instrumental capabilities in X-ray imaging, timing, and spectroscopy order-of-magnitude beyond the current generation of X-ray observatories instrumentations (e.g. XMM-Newton, Chandra and Suzaku), in the next decade X-ray astronomy will leap into a deeper comprehension of all the above mentioned physical processes. IXO also shows an unrivalled potential for breakthrough and serendipitous discoveries that cannot be predicted now and might even surpass the posed questions. IXO instruments foresee for each single detected photon the recording of its position, energy, arrival time and polarization so that spectrum and time-data of variable source will be available in addition to X-ray images of the sky. These capabilities, some of which are shown as an example in Fig. 2.3 [49], constitute the potentiality of the IXO observatory in answering the unsolved questions of nowadays astrophysics.

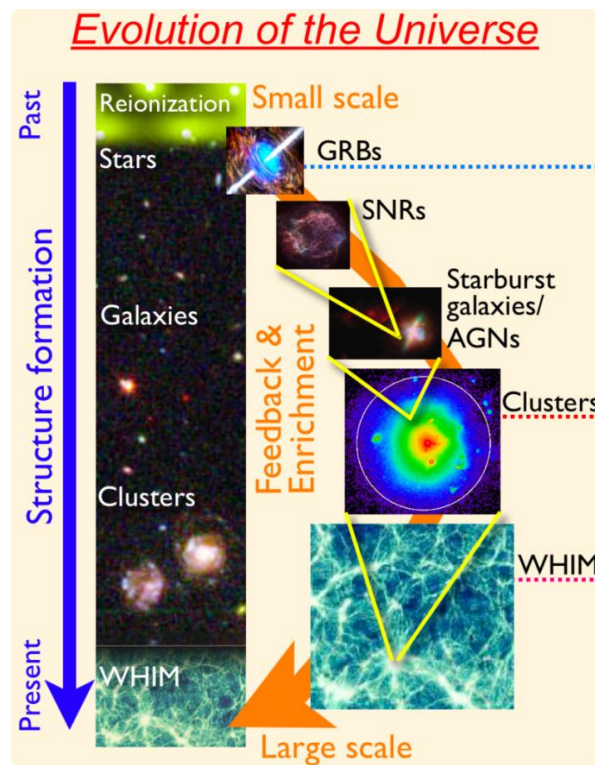


Fig. 2.2: IXO will collect data on the X-ray emission of almost all the objects in the Universe, allowing for a deeper understanding of its evolution history [50].

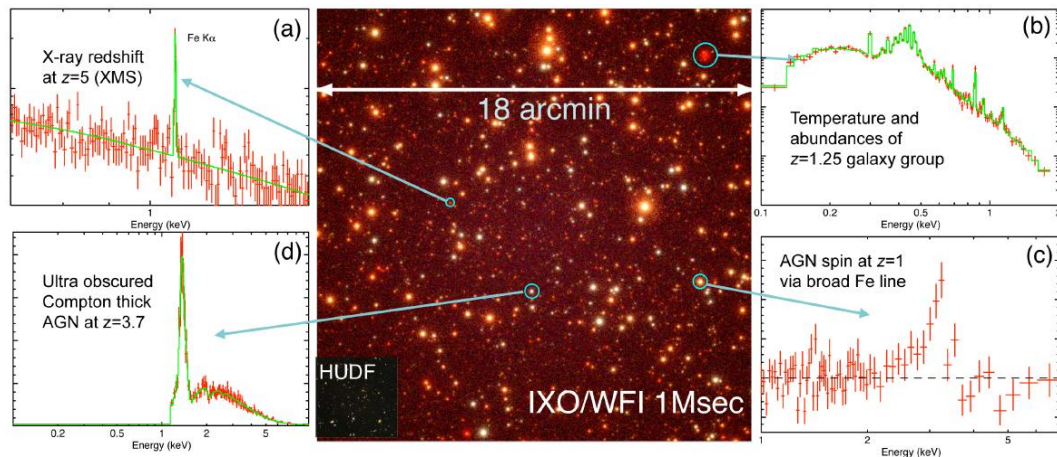


Fig. 2.3: Example of the potential capabilities of IXO. The picture shows an IXO Wide Field Imager simulation of the Chandra Deep Field South with Hubble Ultra Deep Field in inset. The shown simulated spectra illustrates the foreseen ability of IXO: (a) to determine redshift in the X-ray band; (b) to determine temperatures and abundances even for low luminosity groups to $z > 1$; (c) make spin measurements of AGN to redshift around 1; (d) to uncover the most heavily obscured, Compton-thick AGN.

IXO scientific goals are summarized in Table 2.2: a complete and exhaustive description of all of them is out of the scope of this text; however, a selection of major science cases is briefly presented hereafter [51]. Following the Table, the arguments are divided in short paragraphs for easiness in reading, although if many of the topics are connected each other's.

Table 2.2: Main scientific question that IXO will address (Credit: NASA and IXO collaboration).

1. Black Holes and Matter Under Extreme Conditions

a. Supermassive Black Hole Growth

How do Supermassive Black Holes grow?
Does this change over cosmic time?

b. Matter Orbiting a Black Hole (Strong Gravity)

What are the demographics of BH spin, and what do they tell on BH formation and growth?

c. Neutron Star Equation of State

What is the Equation Of State of matter in neutron stars?

2. Formation and Evolution of Galaxies, Clusters, and Large Scale Structures

a. Nature of Dark Matter and Dark Energy

How does galaxy cluster evolution constrain the nature of dark matter and dark energy?

b. Cosmic Feedback

How does cosmic feedback work and influence galaxy formation?

c. Missing Baryons

Where are the missing baryons and do they form a cosmic web in the nearby Universe?

3. Life Cycles of Matter and Energy

a. Origin and Dispersion Elements

When and how were the elements created and dispersed?

b. Particle Acceleration

How are particles accelerated to extreme energies producing shocks, jets and cosmic rays?

c. Planet Formation

How do high-energy processes effect planetary formation and habitability?

d. Stellar Magnetic Field

How do magnetic fields shape stellar exteriors and the surrounding environment?

2.2.1 Matter under extreme conditions

Black Holes (BH) and Neutron Stars (NS) possess the strongest density, gravitational field, and magnetic field in the Universe. The properties of matter in such extreme conditions, very far from being reproduced in terrestrial laboratories, are governed by two main theories: the Quantum Chromodynamics (QCD) and the Quantum Electrodynamics (QED). The only experimental possibility to test them is through the direct study of Neutron Stars and Black Holes, which also represents a test bench for General Relativity (GR) in intense gravity field.

2.2.1.1 Black Holes evolution

One of the driving goals of IXO is to understand the evolution of Black Holes and the properties of their extreme environment. Black Holes create the strongest gravitational fields in the Universe. Matter trapped in the gravitational potential of such objects is spun and heated and emits X-ray, revealing the presence of the huge gravitational field. The observation and study of these X-ray emissions is of fundamental importance for the comprehension of the originating phenomena and of the physics behind the subsequent events. The details might be different in the case of stellar-mass or Super Massive Black Holes (SMBH); however, in both cases the spin of a Black Hole can be adopted as the parameter to probe their formation and growth history. So the measurement of spin is important because in Active Galactic Nuclei (AGN), it can discriminate between different growth histories (since the spin is mainly acquired during the SMBH evolution); while in Galactic Black Holes (GBHs), it gives information about the origin of the BH (since in this case the spin is mainly pristine). The study of X-ray emission emitted by the accreting disk around Black Holes is a valuable means to derive their spin. Current studies have been limited to only few objects mainly because of the limited instrumental signal-to-noise ratio: high signal-to-noise spectra across a wide band-pass are required to obtain robust spin measurements since it will enable the disk spectrum decomposition in a completely unambiguous manner. With the unique time and spectral-resolution capabilities foreseen for IXO, it will be possible to measure the spin distribution of SMBH up to $z \sim 1$ and utilize the data to test different growing models (see Fig. 2.4). IXO will make measurements of Black Holes spin a matter of routine: it offers five independent methods to this aim, which can be cross-calibrated and checked to enhance the reliability of the measurements: Fe line spectroscopic profiles, reverberation, accretion disk spectral continuum fitting, quasi-periodic oscillations and polarimetry. Also, the combination of high effective area, good angular resolution and large field of view will allow for the first time to characterize SMBH up to $z \sim 7$, reaching the Chandra's limiting sensitivity 20 times faster.

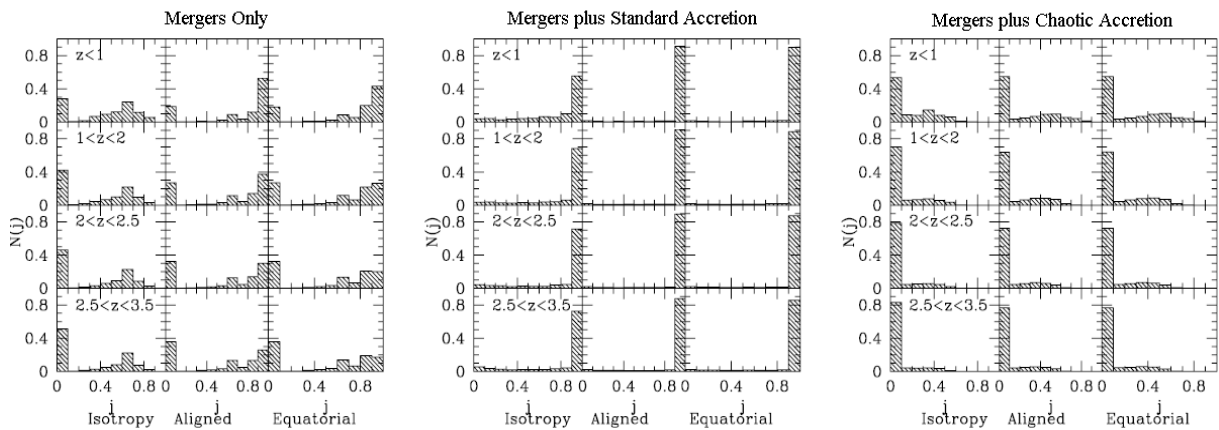


Fig. 2.4: The spin of Super Massive Black Holes is a parameter probing their growth history. The three pictures show the different predicted distribution of spin evolution of all BHs in a scenario where pure merging, merging plus standard accretion, or merging plus chaotic accretion is present. The three columns in each picture correspond to different possible scenarios. The spin value j and its distribution $N(j)$ are reported on the plot axes. The data collected by IXO will allow the discrimination between the different growth models [52].

2.2.1.2 Strong Gravity

X-ray observation of accretion and ejection phenomena around Active Galactic Nuclei (AGN) or Super Massive Black Holes (SMBH) offers a unique opportunity to test the laws of General Relativity in intense gravity fields. Close to the event horizon, its extreme effects are evident in the form of gravitational redshift, light bending and frame dragging. Irradiation of the inner accretion disk area by hard X-rays produces emission lines and a characteristic disk “reflection” spectrum, which is the signature of the physical phenomena, happening closed to the Black Holes. In luminous BH systems, the accretion flow is in the form of a thin disk of gas orbiting the Black Hole; at first order approximation, each parcel of gas within the disk follows a circular test-particle orbit. By observing the geometric and dynamic features of the accretion disks, a number of clues to probe the General Relativity in the strong field limit are collected through the evaluation of BH potential. Current studies are limited by the available collecting area that forces the integration of signal for many orbits of the accretion disk to collect enough photons for the definition of the disk reflection spectrum. In this way, dynamical information is lost. IXO high throughput⁷ will allow to overcome the limitation. For example, non-axisymmetry and variability in the emission of the iron line will be detected through “arcs” features in the time-energy plane, as shown in Fig. 2.5. The form of these arcs is associated with the turbulence in the disk and is predicted from General Relativity in

⁷ The throughput characterized the ability to collect light. It is a fraction that expresses the flux of electrons detected on the detectors divided by the incoming flux of photons. For X-ray telescopes it dependent on the filling factor.

dependence on the mass and the spin of the Black Hole so their recording is a mean to test General Relativity.

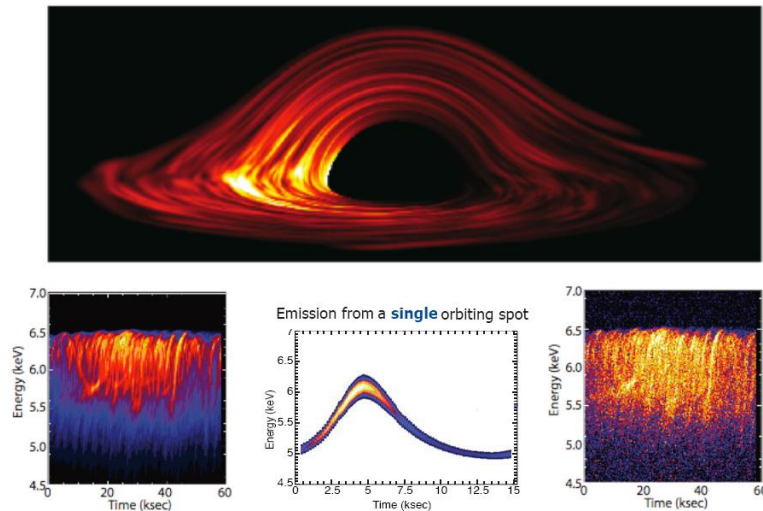


Fig. 2.5: This picture shows a simulation (Top and Bottom Left) of X-ray radiation from a highly-inclined (80°) Magneto Hydrodynamic (MHD) turbulent accretion disk around a Schwarzschild Black Hole [53]. In the time-energy plane, the emission from resolved hot spots appears as arcs (Bottom Center) and can be directly mapped through IXO observations (simulated in the Bottom Right) to test-particle like orbital motion and probe a number of predictions from General Relativity in the strong field limit.

2.2.1.3 Neutron Star Equation Of State

X-ray data can be used to constrain the Equation Of State of Neutron Stars. NSs have the highest known matter densities in nature and the measurement of their fundamental properties represent a direct method to test the relationship between pressure and density of cold nuclear matter. This relationship is determined by the physics of the strong interaction between the particles that constitute the star. The principal way to determine Neutron Stars properties is by measuring the gravitational redshift of spectral lines produced in their photosphere that provides a constraint on the Mass-to-Radius ratio [54]. This ratio is of fundamental importance to derive the Equation Of State of Neutron Stars for which several models exists: some of them foresee the NSs composed by normal nuclear matter; some others foresee the appearance of exotic excitations and phase transitions to strange matter. The knowledge of Mass-Radius relation is one of the open astrophysical questions and allows the selection among the possible models, as shown in Fig. 2.6. IXO will determine the Mass-Radius relation for dozens of NS with four different complementary methods: the gravitational red-shift; Doppler shift and broadening of atmospheric absorption lines; pulse timing distortions due to gravitational lensing; and pressure broadening of line profiles. All these measurements will be possible thanks to high spectral resolution and high count rate capabilities.

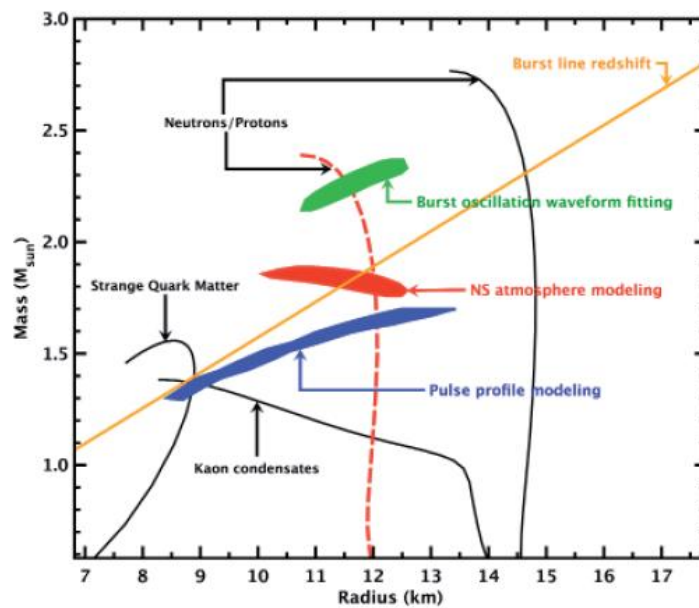


Fig. 2.6: The Mass-Radius (M - R) relationship of Neutron Stars reflects the Equation Of State of cold superdense matter, for which several models exist. IXO will permit a selection among them proving the necessary data for probing them. In the plot, trajectories for typical EOS are shown in black and refer to standard nucleonic matter, self-bound quark, and Kaon condensates. IXO measurements will provide several constraints on the Mass-Radius relationship employing evaluation methods. These constraints are illustrated in the plot as colored areas, which have only representative purposes. In the shown example, only one M - R relation would match the IXO constraints, leading to the conclusion that matter at supra-nuclear densities is made of standard nucleonic matter [55].

2.2.2 Large Scale Structure

The formation and evolution of the large-scale structure of the Universe are central issues of cosmology. Nowadays, it is known that around 95% of the total mass-energy content of the Universe is represented by Dark Energy and Dark Matter, whose distribution has been derived by the evolution of initial density fluctuations. Regarding the $\sim 5\%$ of ordinary matter, its evolution is yet not understood and a large fraction (around $1/3$) of it is even not “seen”. Present observations and theoretical models suggest that the evolution of the baryonic content of the Universe derives from complex interplay and interconnection between gravitational and non-gravitational multi-scale processes: galaxy formation depends on the large scale environment and on the physical and chemical properties of the intergalactic gas from which they form, which in turn is affected by galaxy influence through energy released from star explosion and active nuclei accreting matter from their environment. The remarkable link between the two phenomena, named “feedback” (see Fig. 2.7 [56]), is the key element to comprehend both of them. IXO data will help in finding an answer to open questions, such as: how does cosmic feedback work? How did large scale structures evolve? What is the nature of Dark Energy? Where are the missing baryons in the Universe?

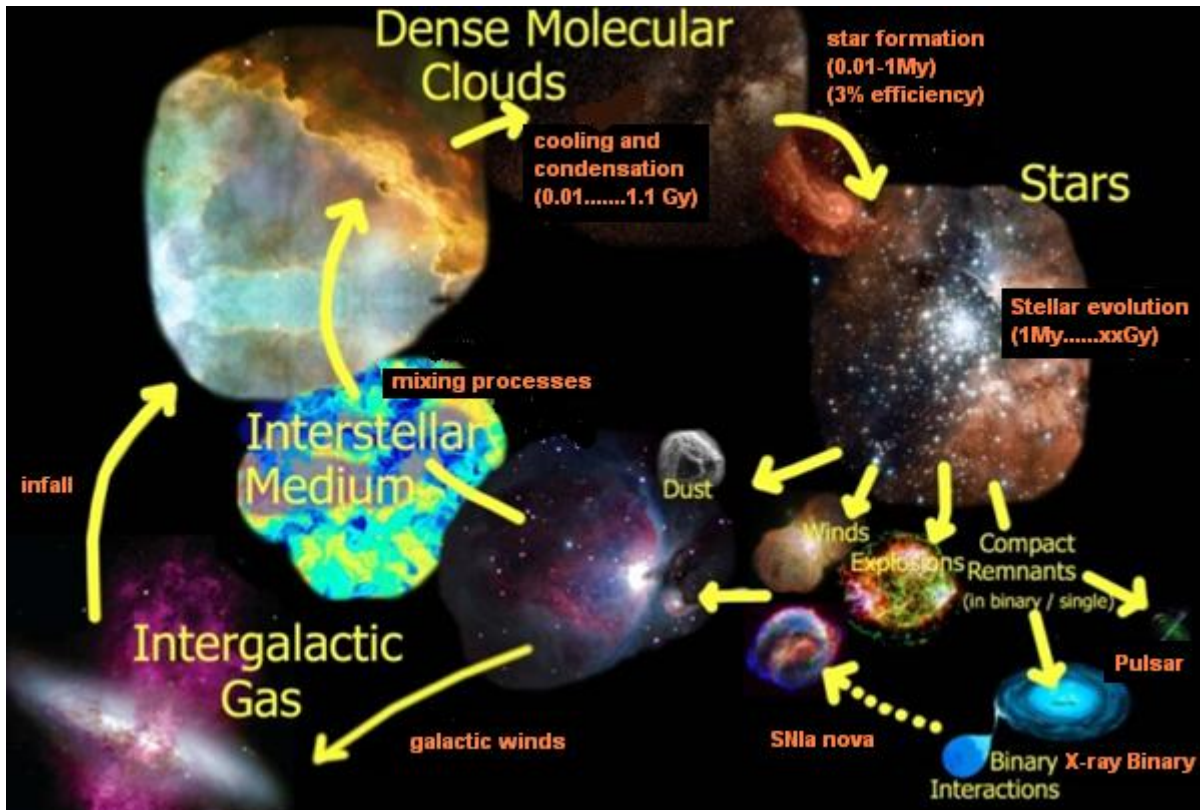


Fig. 2.7: Representation of the many forms of interconnection present in the Universe between small and large scale structures.

2.2.2.1 Cosmic Feedback

Feedback phenomena, of radiative or mechanical form, are extremely important in the evolution of Universe and their understanding represents one of the main topics of modern astrophysics. Fig. 2.8, adapted from [57], illustrate a simplified scheme and few examples of feedback, which is responsible of the chemical enrichment and the energy and momentum flows among the main elements of the Universe: stars, Super Massive Black Holes, Inter-Stellar Medium (ISM) and Inter-Galactic Medium (IGM). The first step of feedback is related to the Nucleosynthesis of elements that happens in stars in the final stages of their life, e.g. in Supernovae explosions (SN). The second step consists in the enrichment and circulation of the produced elements in clusters of galaxies, through Ram pressure stripping (the mechanical form of feedback, mostly evident in cluster cores), Galactic wind, Galaxy-Galaxy interaction, and outflows from active galaxies.

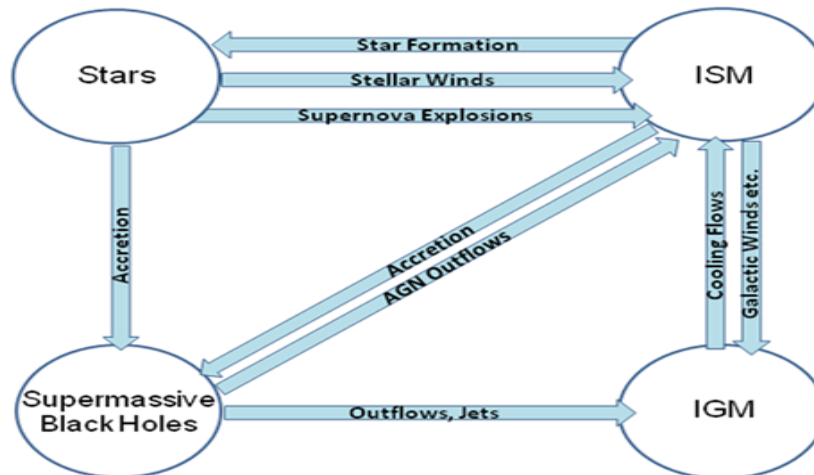


Fig. 2.8: The scheme shows the feedback phenomena responsible for the chemical enrichment and the energy and momentum flows among the elements in the Universe (adapted from [71]).

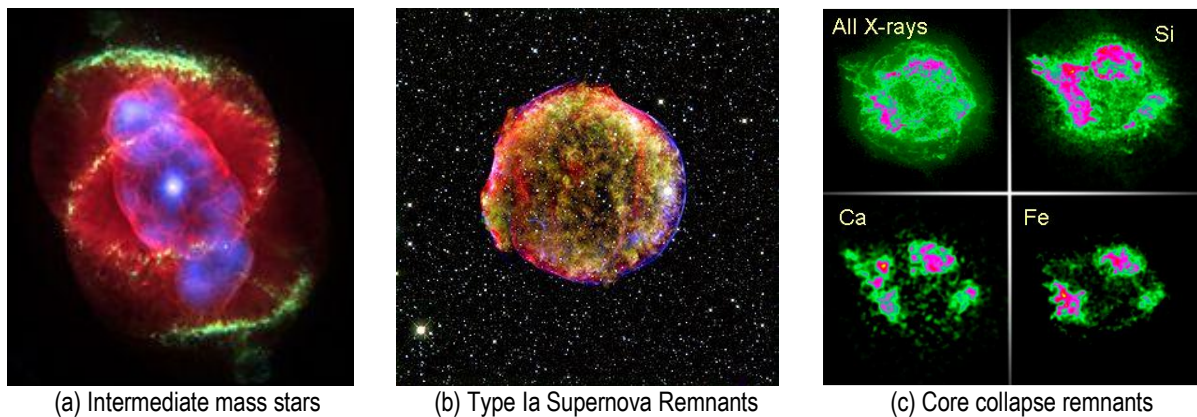


Fig. 2.9: Example of images related to the first step of feedback, i.e. Nucleosynthesis of elements. (a) example of a star with mass $< 8 M_{\text{solar}}$; in the late stages of its life it collapses into a white dwarf and ejects a planetary nebula; (b) Cassiopeia B, remnant of Tycho SN1572 that ejected metals (mainly heavier like Si, Fe, Ni) into the interstellar medium; (c) Cassiopeia A, remnant of SN1680 that ejected metals (mainly lighter like O, Ne, Si) into the Interstellar Medium and during the explosions produced heavy elements (up to U).

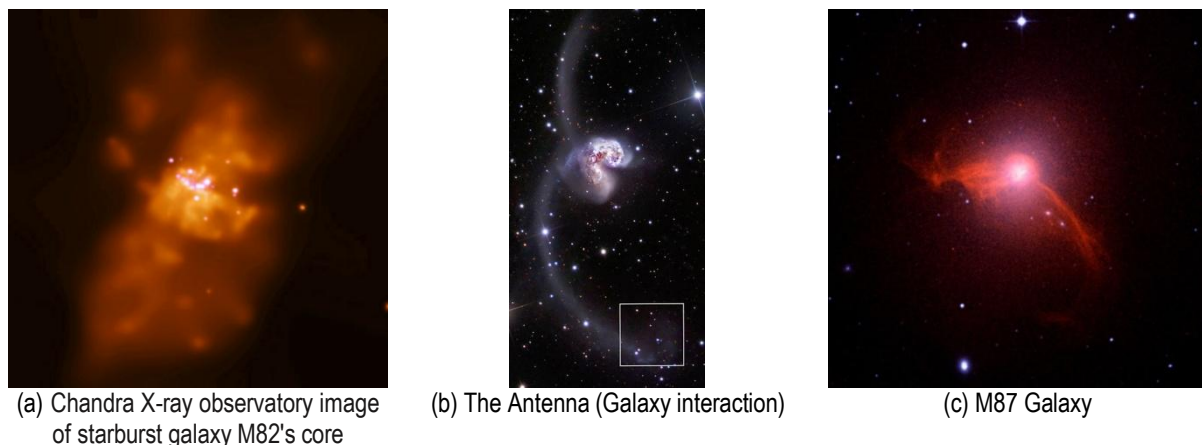


Fig. 2.10: Example of images related to the second step of feedback, i.e. the enrichment and circulation of the produced elements in clusters of galaxies. (a) Galactic wind blow gas from SN explosions out of galaxy; (b) example of galaxy close encounter that might cause tidal tails of stars and enriched gas entering the intergalactic space; example of a giant outflows from active galaxies (c).

SMBH influencing its surrounding environment is a typical example of feedback. Energetic disk accretion processes around Black Hole results in huge radiative and mechanical outputs, like winds and relativistic jets, which dramatically affect its environment at large scale, i.e. on surrounding galaxies, clusters and Inter-Galactic Medium. To understand the physics that drives these processes and the connections between them, high X-ray resolution spectra on relevant orbital and even sub-orbital timescales are needed, as shown in Fig. 2.11. They can be obtained through a combination of high spectral resolution and large collecting area, both characteristics foreseen for IXO.

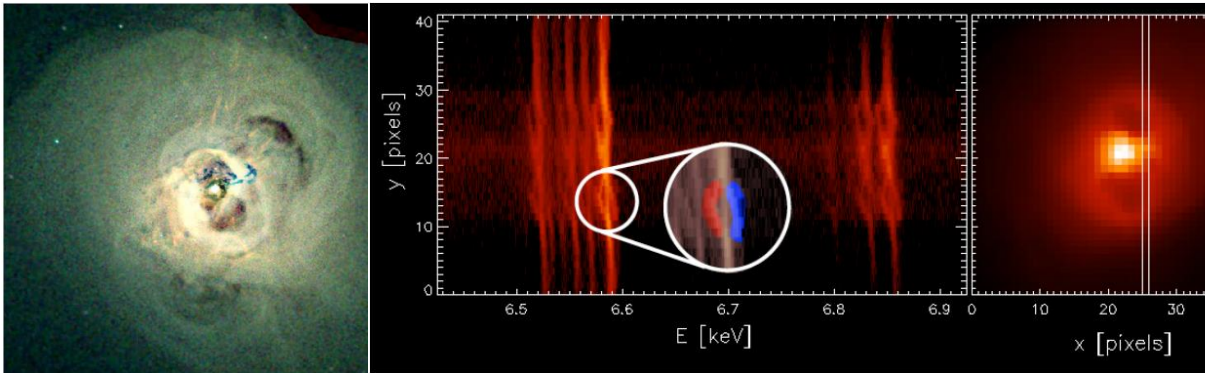


Fig. 2.11: (Left Side) Chandra X-ray observation of the Perseus cluster revealing the indelible imprinting of AGN on the hot gas in the core. Radiative and mechanical heating and pressure from Black Holes has a profound influence not only on the hot baryons, but on the evolution of all galaxies, whether or not they are in clusters. (Central Side) Simulated high-resolution X-ray spectrum of the K-alpha lines (both lines are multiplets) from Fe XXV and Fe XXVI of Perseus cluster as will be detected by IXO. Each of the lines splits into three components (approaching, restframe, and receding) from which the velocity and age, and therefore the power of the jet, can be derived. (Right Side) X-ray image that reports the used spectral slit.

2.2.2.2 Galaxy Cluster physics and evolution

Clusters of galaxies are the largest collapsed structures in the Universe; their baryonic content is concentrated in galaxies and in diffuse hot-T plasma, i.e. the Intra-Cluster Medium (ICM), that radiate primarily in the X-ray band. Our current knowledge of the interplay of the hot and cold components of the baryonic matter and the dark matter comes primarily from detailed studies of clusters in the nearby Universe, $z < 0.5$. It is known from XMM-Newton and Chandra data that the hot atmosphere of local clusters have much more entropy than expected from gravitational heating alone [59], [60], [61]. Determining when and how this non-gravitational excess energy was acquired is crucial in the comprehension of the Universe evolution. Measuring the evolution of the gas entropy and metallicity from the epoch of cluster formation to nowadays is the key information required to disentangle and understand the role of each feedback process. Early clusters of few elements are of interest not only because they are the building blocks of today massive clusters, but also because the non-gravitational effects are easier to be observed. Hence, new development in this research field

requires high throughput, high spectral and spatial resolution X-ray observations of the first low mass clusters emerging at $z \sim 2$, and directly trace their thermodynamic and energetic evolution to the present epoch. Thermodynamic properties and metal content can be derived from IXO by measuring gas density and temperatures profiles (thus entropy and mass profiles) in groups and clusters out to $z=2$. Examples of the potentiality of the IXO instrumentation are shown in Fig. 2.12 and 2.13.

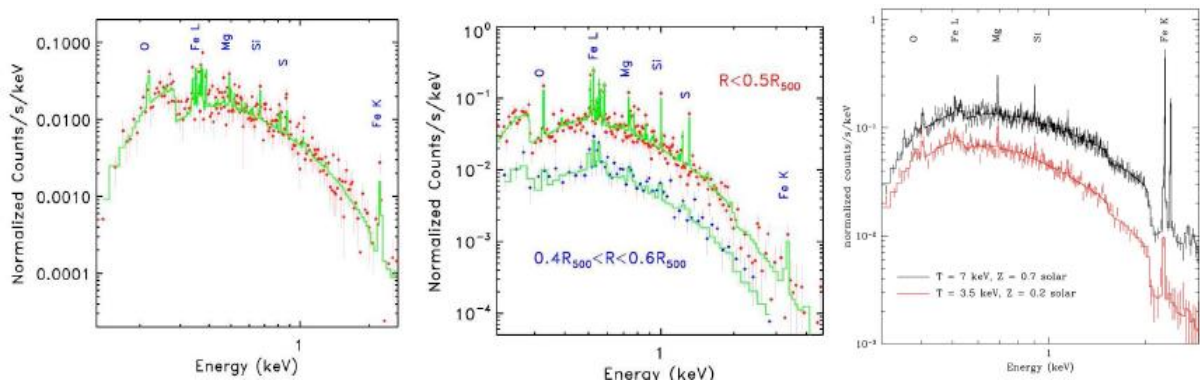


Fig. 2.12: X-ray spectra of high redshift clusters and groups obtained with IXO will yield gas densities, temperatures and metallicities profile in all clusters up to $z=2$, key parameters to understand the role of each feedback process. In the reported plot, the simulated spectra of low-mass galaxy clusters are reported, as derived from [62].

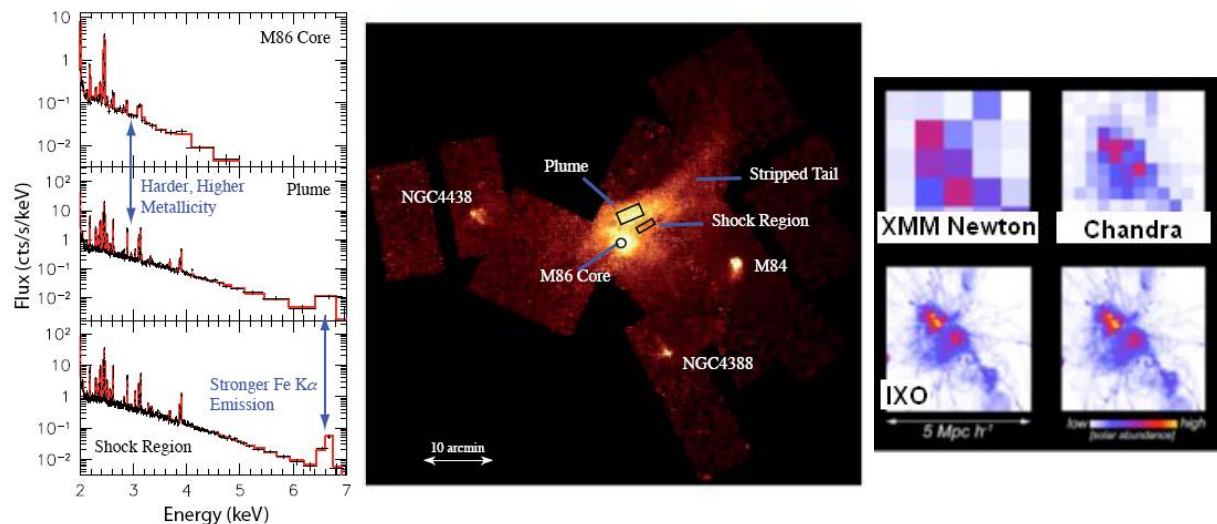
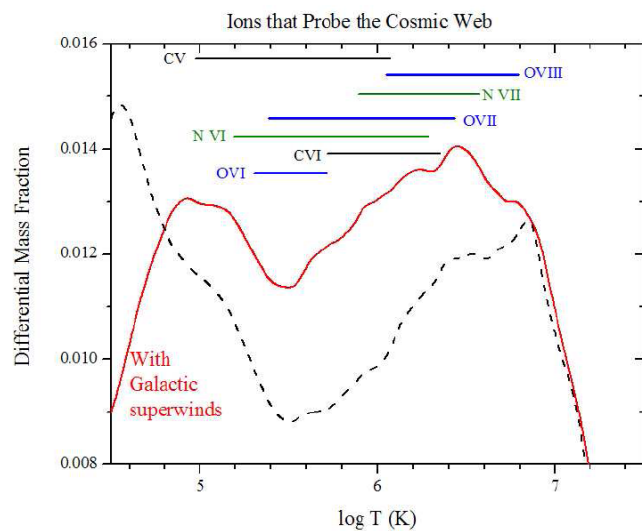
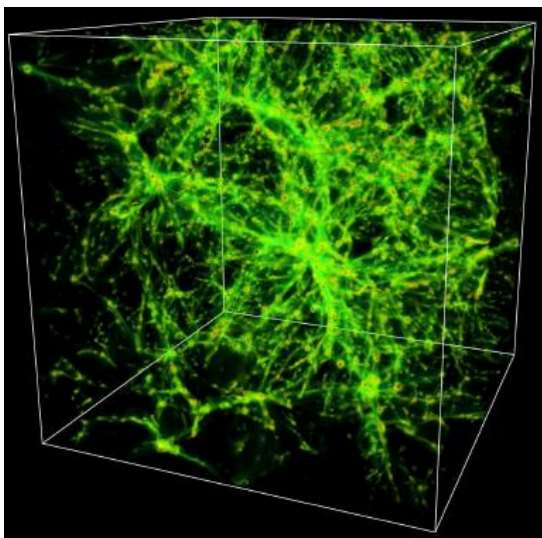


Fig. 2.13: In the center of the picture a mosaic of Chandra (0.5-2 keV) images is reported, showing the X-ray emission from the Virgo elliptical galaxy M86 and its 380 kpc Ram pressure stripped tail. IXO, with its improved capabilities in terms of sensitivity and resolution, will allow to measure the metallicity along the tail and the gas around the cluster with unprecedented resolution, as evidenced in the right panel of the figure, which shows Chandra, XMM-Newton and IXO simulations of the metal abundance and distribution in a merging cluster [63], [64]. The left panel of the picture shows examples of the IXO obtainable spectra in different positions of the X-ray image, which will be useful to distinguish among the possible enrichment scenarios.

2.2.2.3 The Cosmic Web of Baryons

Ordinary matter (baryons) represents 4.6% of the total mass/energy density of the Universe. Only 10% of these baryonic elements lies in collapsed objects, like galaxies or stars; theoretical predictions foresee that the majority is contained in vast unvirialized filaments that connect galaxy group and cluster, forming the so called the Cosmic Web (Fig. 2.14). Clusters of galaxies represent the nodes of the cosmic web. Absorption line studies detect warm baryons, but more than 50% is still missing since out of the current X-ray observatories capabilities. High throughput and high spectral resolution is required to IXO for the determination of the missing baryons existence in the predicted hot phase. Additional goals consist in the definition of cosmic web filaments connections to galaxy groups and clusters, through the assessment of galactic superwind mechanism or the chemical mixing process, as shown in Fig. 2.15. These goals are achieved by measuring the He-like and H-like X-ray resonance lines of Carbon (C V, C VI), Nitrogen (N VI, N VII), and Oxygen (O VII, O VIII) [65].



(Left Side): Fig. 2.14: Simulation of the density distribution of baryons at low redshift: most of the mass of the WHIM (Warm Hot Intergalactic Medium) lies within the filaments that connect the higher density regions.

(Right Side): Fig. 2.15: The plot reports the Differential Mass Fraction as a function of temperature derived from cosmological simulations. Solid red line refers to the situation in the presence of galactic superwinds; while the dashed black line refers to the case in which galactic superwinds are not present. Being the plotted distribution sensitive to the presence of galactic superwinds, its definition acts as a probe for the existent models, all of which predict that most of the baryonic mass resides in gas that can only be seen through X-rays: hence the importance of IXO.

2.2.2.4 Cosmology

All above mentioned studies are of fundamental importance for cosmological research. Observations of galaxy clusters in X-ray are very promising tools to probe the structure and mass-energy content of

the Universe and to assess the different existing cosmological models. IXO observations will be complementary to other planned cosmological experiments at different wavelengths to enable a leap forward in the understanding of the Universe. Precise measurements of the hot intra-cluster gas X-ray brightness and temperature allow two independent types of cosmological tests: the observation of the expansion history (through distance-redshift combination) and the collection of data on the growth of matter density perturbations. The first type of cosmological tests is primarily a geometric method and it is based on precise measurements of the distance-redshift relation. The constraints for the selection between several models on the expansion history of the Universe are given by measurements of the X-ray emitting gas mass fraction in high-redshift clusters. The second one poses constraints in the growth models of cosmic structures, primarily providing accurate measurements of high-redshift galaxies, i.e. their spatial distribution and main properties (mass, X-ray brightness, temperature, metallicity, and velocity structure). Both approaches are necessary to select between the actual models for the explanation of the accelerated cosmic expansion, i.e. between quintessence type models or modified General Relativity ones. Fig. 2.16 shows how a combination of the data acquired with the two methods poses constraints on the Dark Energy Equation Of State.

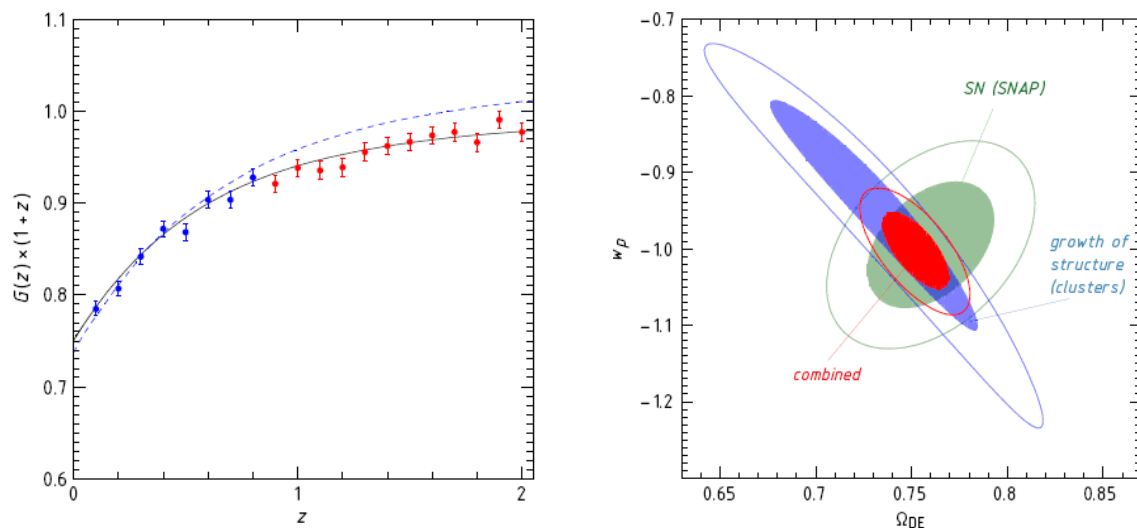


Fig. 2.16: (Left Side): simulation of IXO observation of 2000 clusters at redshift z from 0 to 2. Measurements at redshift higher than 0.8 are possible only with the high sensitivity of IXO. The normalized growth factor of structure is plot in dependence of the redshift. IXO data are crucial for testing non-GR models of cosmic acceleration. In the plot, the dashed line represents the expected growth in the case of a non-GR DGP model of cosmic acceleration; while the solid line refers to the case of the quintessence LCDM model in case of the same expansion history [66], [67]. (Right Side): the combination of distance-redshift based techniques (projected results shown for the SNAP SNIa experiment) and X-ray structure growth methods (possible with IXO) reduced the equation of state uncertainties by a factor of approximately 2.5.

2.2.3 Life cycle of matter and energy

Additional relevant questions for contemporary Astrophysics are related to the life cycle of both matter and energy in the Universe. IXO will be a key element for these studies, which derive from the observation of Supernovae (SN) and their Remnants (SNR) performed to understand their explosion mechanism and their nucleosynthesis products; the characterization of the Inter-Stellar Medium (ISM); and the evaluation of the influence of stars on their local environments. Examples of these issues are given in the following paragraphs.

2.2.3.1 Cosmic rays in Supernovae

The most abundant massive elements in the Universe are released by Supernova explosions. These processes are the most important source of energy for the Interstellar Medium, as kinetic/thermal energy or in the form of cosmic rays. The explosions can be study directly by observing X-ray emission from extra-galactic Supernovae (SNe), or indirectly by studying Supernova Remnants (SNRs) in the Galaxy and the Local Group. For Core Collapse (CC) SNe, it is known the starting process of stellar core collapse, but the following process whereby the core rebounds and ejects the rest of the star is poorly understood. Two models are actually under evaluation: the neutrino-driven convection [68] and the jet induction [69]. Further precise data are needed to select between the models. For the thermonuclear SN (SN Ia), the situation is even worse since even the explosion process, i.e how the nuclear ignition starts and how the subsequent burning proceeds, is not known [70]. To understand these processes, the synthesis of the Fe-group elements in SNe and in SNRs is of fundamental importance. Because of the limited spectral resolution and effective area of present missions, the detection of the lower abundance Fe-group species in small spatial scale features is not affordable at the moment. IXO will overcome current limitation, allowing the interpretation of the explosion processes.

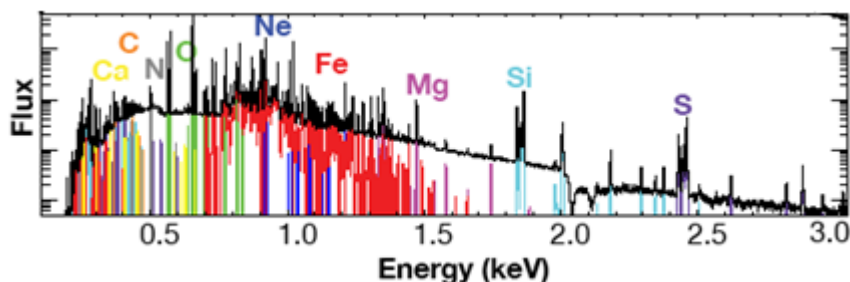


Fig. 2.17: A simulated IXO spectrum that shows (picks in the black curve) how the enhanced spectral resolution of IXO with respect to previous mission allows for the individuation of K-line transitions of 25 elements (from Carbon to Zinc. The enhanced IXO capability allow to detect the presence of F, Na, Al, P, Cl, K, Ti, V, Cr, Mn, Co, Cu, Zn in addition to the element nowadays detectable, i.e. C, N, O, Ne, Mg, Si, S, Ar, Ca, Fe, Ni).

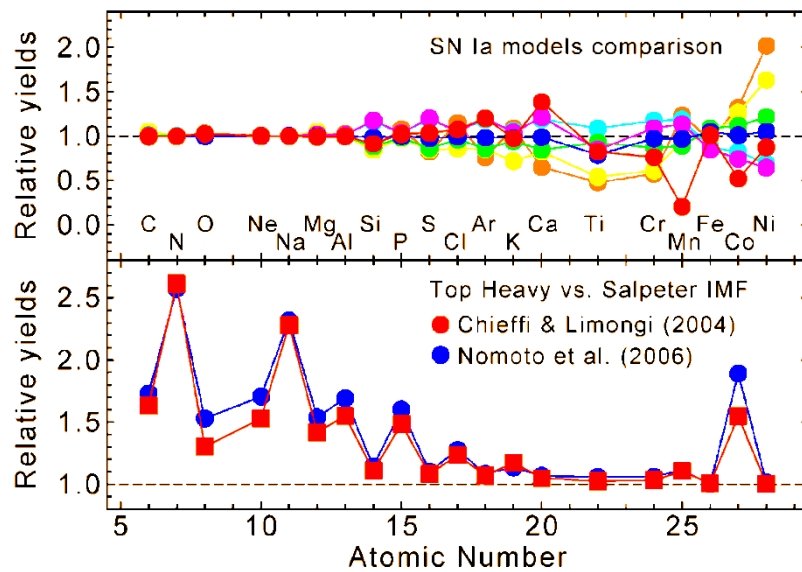


Fig. 2.18: The simultaneous direct abundance determination of the elements allows, for example, the selection between different SN existing models [71].

2.2.3.2 Stellar mass loss

Stellar mass loss is a key parameter that drives stellar evolution in the HR diagram. How rapidly stars lose mass and angular momentum, and how the phenomenon is influenced by the star rotation and magnetic field, are open questions in nowadays stellar astrophysics. Observations of X-ray wind line profiles offer the opportunity of resolving the uncertainties currently present in the determination of mass loss, mainly derived from the moderate time and spectral resolution of present instruments. Indeed, actual knowledge is limited to a very small number of brightest objects. IXO high signal-to-noise of X-ray emission lines will allow detailed modelling of the distribution of hot plasma in the wind, the mass-loss rates, the degree of wind inhomogeneity, and even the geometrical shape of wind clumps. This kind of information, obtained for all types of hot stars, allows to derive wind properties and inputs for stellar evolution codes. The data on mass loss are important not only for the understanding of stellar evolution, but also for the determination of the interaction between the star and the surrounding environments (e.g. to understand how it shapes the circumstellar medium and its effects on the formation and evolution of planets).

2.2.3.3 Studies of the Interstellar Medium in the Galaxy

The abundances of gas and dust (solids and complex molecules) in the Inter-Stellar Medium as well as their composition and structures impact practically any astrophysical process, from galaxy evolution to star formation to stellar or AGN outflow. Hence, it is essential to determine the elemental abundances in both the gas and the dust phase of the ISM. X-ray spectral observations are a powerful way for mapping elemental distribution and abundances, free of any model uncertainties

that affect measurements in optical or UV range. Further, X-ray studies give the possibility to penetrate into giant molecular clouds, opaque to UV and optical light. Current available data are limited because of the available effective area at high spectral resolution of past or operational X-ray observatories. High spectral resolution and high effective area are essential for this kind of research. IXO capabilities meet those requirements, as shown in the example reported in Fig. 2.19, from which it appears clear how the IXO's grating capability of performing spectroscopy of bright X-ray sources enable to reveal the physical aggregation state (i.e. molecular, atomic or metallic) of ion species in the ISM of the Galaxy. This is possible because of the great resolution in the edges of their absorption spectra.

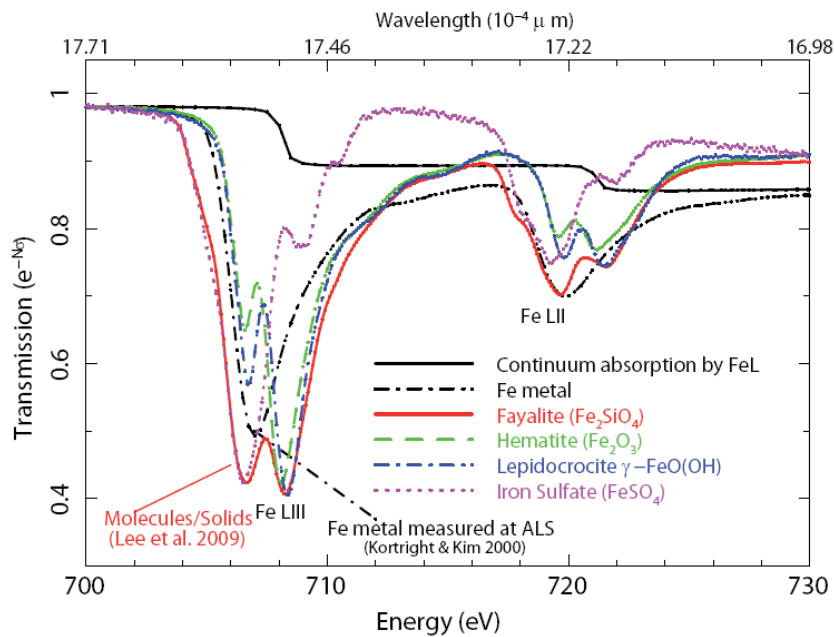


Fig. 2.19: Simulation of an absorption curve obtainable with the high resolution of IXO, whose data will allow to distinguish between Fe in molecules (solid red line), various type of metals (dot-dashed lines), and continuum absorption (solid black line). The plot is derived from [72].

2.2.3.4 Star and planet formation

Stars have influence on their local environment affecting the formation of planets and the habitable zone. The magnetized surface of the stars divert a small fraction of the stellar energy into high energy products that range from coronal UV and X-ray, flare X-ray and energetic particle, and a high-velocity stellar wind. These components interact with the cool orbiting bodies or proto-planetary disk gases and solids and produce X-ray through various processes like charge-exchange between ionized and neutral components. Regarding our Solar System, the resulting X-ray emission gives unique insights into the solar activity, planetary atmosphere, cometary comae, charge exchange physics, and space weather. Regarding Young Stellar Objects, the resulting X-ray emission gives indication on the influence of the star on the proto-planetary disk, hence on the planet formation processes. Today

instruments capabilities can achieve only a small percentage of the potentiality envisaged for X-ray investigations related to planetary science. High-throughput and high-spectral resolution observatory is essential to study the faint X-ray emission of the involved objects, variable in time and with lots of spectral components that need to be resolved. The IXO mission possesses a high potentiality to enhance knowledge in this almost new research field. Fig. 2.20 reports an example of research that will be allowed in this field thanks to IXO.

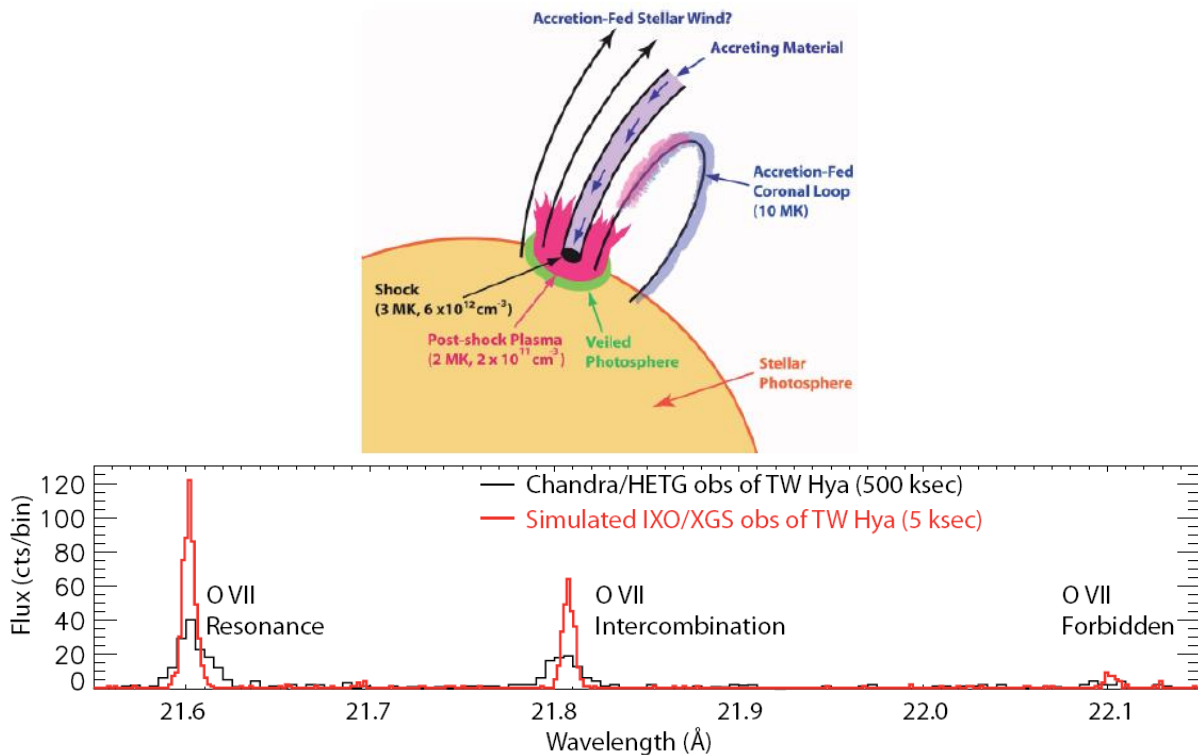


Fig. 2.20: (Top): The scheme illustrate the accretion shock for T Tauri star as derived from [73]: it is shown as an example of the influence that a star can have on its surrounding environments through X-ray emissions. (Bottom): A spectrum derived by Chandra data (black line) is compared with a simulated spectrum obtainable with IXO (red line); thanks to its high throughput, IXO will enable dynamical studied of the emitting plasma to be conducted through sequences of short exposures contributing in the progress of this current astrophysical field.

2.3 IXO Optical payload

The key element of IXO mission is represented by the scientific payload. While no particular show-stoppers have been individuated for the focal plane instrumentations, the X-ray telescope requires challenging efforts in the improvement of its manufacturing technology. If the mirror manufacturing technique is not demonstrated to reach a TRL ≥ 5 by spring 2012, this can be a show-stopper for the further steps in the development of this mission. The present section gives an overview of the baseline for IXO payload implementation (as for summer 2011).

2.3.1 Technical requirements and goals

The technical requirements for IXO payload, summarized in Table 2.3, derive directly from the demanding science objectives. The goals can be met with an X-ray telescope with collecting area at 1 keV of at least 2.5m^2 and a spatial resolution of 5 arcsec for energies up to 7 keV (a value already met by present observatories but with very modest area compared to that required for IXO). The effective area required for higher energies is of at least 0.65m^2 at 6 keV, and 150cm^2 at 30 keV, with an angular resolution of 30 arcsec HPD. These technical requirements on the X-ray telescope foresee the realization of a huge optical system, at least 5 times larger than any previous X-ray telescope, i.e. showing a bigger collecting area almost maintaining (or even improving) the image resolution of past and present systems, as graphically shown in Fig. 2.21. Such large dimension poses several engineering challenges.

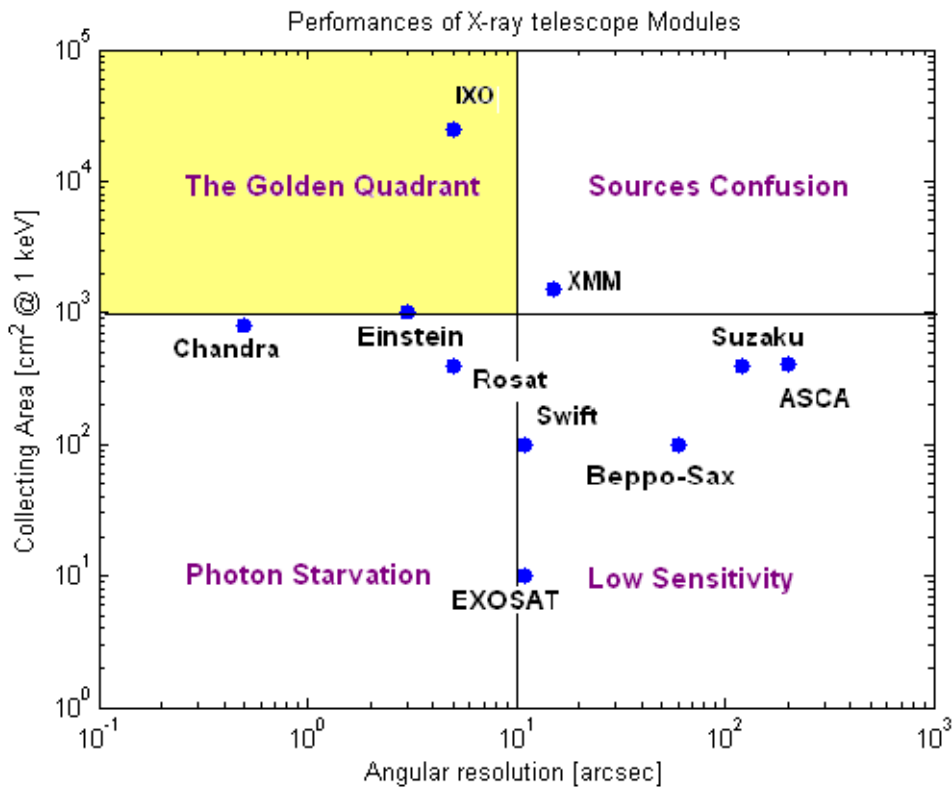


Fig. 2.21: Collecting area and angular resolution of IXO compared with present or past X-ray missions.

Preliminary feasibility studies have identified that the requirements can be met with a telescope having diameter in the order of 3.5 m and focal length around 20 m. The diameter is mainly coming from the limitation posed by the diameter of the launcher fairing: no available or planned launcher has a fairing bigger than this in diameter. For a similar limitation this time coming from the height of existing launcher fairings, the nominal focal length, necessary due to the photon energy range, is only

obtainable with an Extendable Optical Bench (EOB). The deployment by mast or boom structures has already been demonstrated on Shuttle radar instruments and on JAXA missions so it is more reliable than formation flying systems [74]. Furthermore, the requirement in terms of deployment and fixation accuracy in 3D for IXO is of circa 1 mm, relatively easy to achieve.

Table 2.3: Key performances parameter for IXO and main associated science drivers [75].

Parameter	Value	Science Driver
Mirror Effective Area	2.5 m ² @ 1.25 keV 0.65 m ² @ 6 keV 150 cm ² @ 30 keV	Black Hole evolution; large scale structure; cosmic feedback; EOS; Strong Gravity; cosmic acceleration
Spectral Resolution/FOV E _{bp} = 0.3–12 keV E _{bp} = 0.1–15 keV	ΔE = 2.5 eV (@6keV) within 2x2 arcmin ≤ 10 eV (@6keV) within 5x5 arcmin ≤ 150 eV (@6keV) within 18 arcmin ∅ = 1keV (10-40 keV) within 8x8 arcmin E/ΔE=3000 (0.3-1keV) with an A=1000 cm ²	Black Hole evolution and cosmic feedback; large scale structure; missing baryons using tens of background AGN
Mirror Angular Resolution	≤ 5 arc sec HPD (0.1-7 keV) ≤ 30 arc sec HPD (7-40 keV)	Large scale structure; cosmic feedback; Black Hole evolution; missing baryons
Count Rate	1 crab with > 90% throughput ΔE < 200 eV @ 6keV (0.3-15 keV)	Strong gravity; Equation Of State
Polarimetry	1% MDP on 1 mCrab in 200 ksec (2 – 6 keV)	AGN geometry; Strong Gravity
Astrometry	1.5 arcsec at 3σ confidence	Black Hole evolution
Absolute Timing	100 μsec	Neutron Star studies

A single focal plane instrument cannot meet all the requirements in terms of spatial resolution, field of view, energy range and resolution, quantum efficiency, count rate capability, and polarisation sensitivity. Different focal plane instruments are envisaged, comprising:

- An X-ray imaging Microcalorimeter Spectrometer (XMS)
- A Wide Field Imager (WFI)
- A confocal Hard X-ray Imager (HXI)
- A non-imaging High Time resolution Spectrometer (HTRS)
- An imaging X-ray Polarimeter (XPOL)
- An X-ray Grating Spectrometer (XGS)

Table 2.4: Brief description of the scientific instruments envisaged for IXO.

- **An X-ray imaging Microcalorimeter Spectrometer (XMS)**

The XMS is mainly dedicated to provide revolutionary new capabilities for plasma diagnostics. It covers the energy range from 0.3 to 12 keV with energy resolution never experienced in past or present X-ray missions, a FoV of 5×5 arcmin², and a relatively low count rate capability. The key element for the XMS is the detector that works by sensing the increase in temperature generated by X-ray photons when they are absorbed and thermalized causing a change in the electrical resistance of the sensor. Transition Edge Sensors (TES) are the studied base-line for this instrument: they already match the requirements in arrays of modest dimension. Developments are on-going to increase the size of the array. One other important element of the XMS is the cooling system since the above mentioned sensors operate at 50 mK. To guarantee the highest TRL, the base-line consists on an extension of the cryogenic system in development for the ASTRO-H mission, planned to be launched in 2014.

- **A Wide Field Imager (WFI)**

This instrument is mainly dedicated to provide images simultaneously with spectrally and time resolved photon counting. It covers the energy range from 0.1 to 15 keV and offers a large FoV with a diameter of 18 arcmin. The spatial resolution, energy resolution, count rate capability, and efficiency are excellent and can be easily met with mature technologies derived from XMM-Newton EPIC and from developments performed for BepiColombo.

- **A confocal Hard X-ray Imager (HXI)**

The HXI is mainly dedicated to provide images simultaneously with spectrally and time resolved photon counting, extending the energy range of observation of the WFI: in fact it covers the energy range from 10 to 40 keV. The HXI capability is essential in understanding reflection phenomena and obscuration around supermassive Black Holes. The instrument FoV is 8×8 arcmin². Its performances in terms of spatial and energy resolution, efficiency, and count rate are very good and based on technology items with high TRL, based on the heritage of ASTRO-H, Simbol-X and Nustar project.

- **A non-imaging High Time Resolution Spectrometer (HTRS)**

This instrument is mainly dedicated to the observation of the strongest (i.e. brightest) X-ray sources in the sky. It covers an energy range from 0.3 to 15 keV and offers an ultra-high count rate capability, i.e. sub-millisecond timing, low dead time and low pile-up. Its technology is mature from high energy physics applications and does not require major developments.

- **An imaging X-ray Polarimeter (XPOL)**

This instrument is dedicated to provide IXO with the capability of performing polarimetric measurements to 1% Minimum Detectable Polarization (3σ) for a 1mCrab source. It covers an energy range from 2 to 10 keV, offering an excellent sensitivity to polarization although if the FoV and the energy resolution are relatively low. The instrument is based on mature technologies that require only finalization and optimization studies.

- **An X-ray Grating Spectrometer (XGS)**

This instrument is dedicated to the high-resolution spectroscopy of point sources: one main goal is the detection of the hottest phase of the missing baryons. It covers an energy range from 0.3 to 1 keV and offers a resolving power of > 3000 , with an effective area of 1000 cm^2 . The XGS is complementary to XMS: it offers higher spectral resolution at longer wavelengths. The instrument is based on gratings and a camera. Two concepts are under development for the XGS, both based on past X-ray mission experiences and not requiring fundamental development to meet the necessary TRL. The X-ray Grating Spectrometer is positioned on an instruments platform permanently illuminated, aligned with the fixed dispersive grating placed between the X-ray mirror and its camera. All the other four scientific instruments (the XMS, the combination of WFI/HXI, the HTRS, and the XPOL) are located on a Movable focal plane Instruments Platform (MIP) that allows their consecutive position on demand, in the focus into the optical path.

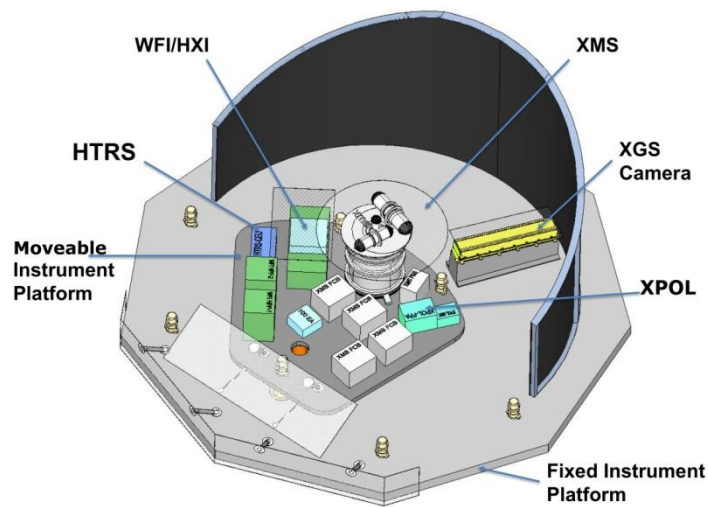


Fig. 2.22: Drawing of the IXO Instruments Module (IM) including one fix and one moveable platform housing the focal plane instruments [image credit: <http://ixo.gsfc.nasa.gov>].

Most of the scientific focal plane instruments envisaged for IXO are at an advanced stage of development and parts of them already meet the required TRL. No show-stoppers for further design and development have been identified between the scientific instruments payload.

The key element of IXO is represented by the X-ray telescope, which poses the main technological challenge for the mission to be realized. It can be a show-stopper if improvements in the technology for X-ray optics manufacturing are not demonstrated by spring 2012. This problem is important not only for the IXO mission but also for other next generation X-ray missions (for example GEN-X) for which this study should be taken in consideration.

2.3.2 IXO X-ray manufacturing challenge: the need of a new technology

Due to the large dimensions envisaged for IXO X-ray telescope (diameter of 3.5 m), the construction of its mirror shells as monolithic structures is not feasible. Segmented X-ray Optic has to be considered. In practice, the entire aperture of the telescope is azimuthally divided in sectors, like slides of a cake, and the circular symmetry of the telescope design is reconstructed by suitable alignment and integration of a number of mirror segments. In this way, it is possible to produce optical segments of reasonable dimension despite a more complex integration procedure. The concept has already been applied for the past missions ASCA and ASTRO-E2 for which the production technique (Al thin-foil method) did not allow the realization of close shells. The concept is described in more details in sections § 2.3.3 and § 3.2, dedicated to the present ESA base-line and back-up design for the IXO optical payload. Re-calling back from chapter § 1 the different existing methods of

production (i.e. direct polishing, Ni electroforming, and thin Al foils), it easy to understand that they are not suitable for IXO, and that a new technology needs to be developed. All the three technologies have been successfully applied in the past, but cannot be employed for the production of the segmented optics envisaged for the IXO telescope mainly for two factors: the combination of their mass/geometric area ratio and of the optical performances that they are able to deliver: optics for IXO made with such techniques will result too heavy and expensive and not capable to give the necessary effective area or the required angular resolution. It has to be considered that the mass budget for the IXO optics is of about 2000 kg (including mounting structures and thermal control elements), only about 35% larger than that of XMM-Newton but with more than 5X the effective area. This requires a mirror technology with a very high area-to-mass ratio, in the order of 20 cm²/kg (50 times larger than that of Chandra). Looking at Fig. 2.23, the situation appears immediately clear; low mass usually goes at the expenses of the optical performances, and vice-versa. That's not acceptable for IXO that requires high levels for both the parameters.

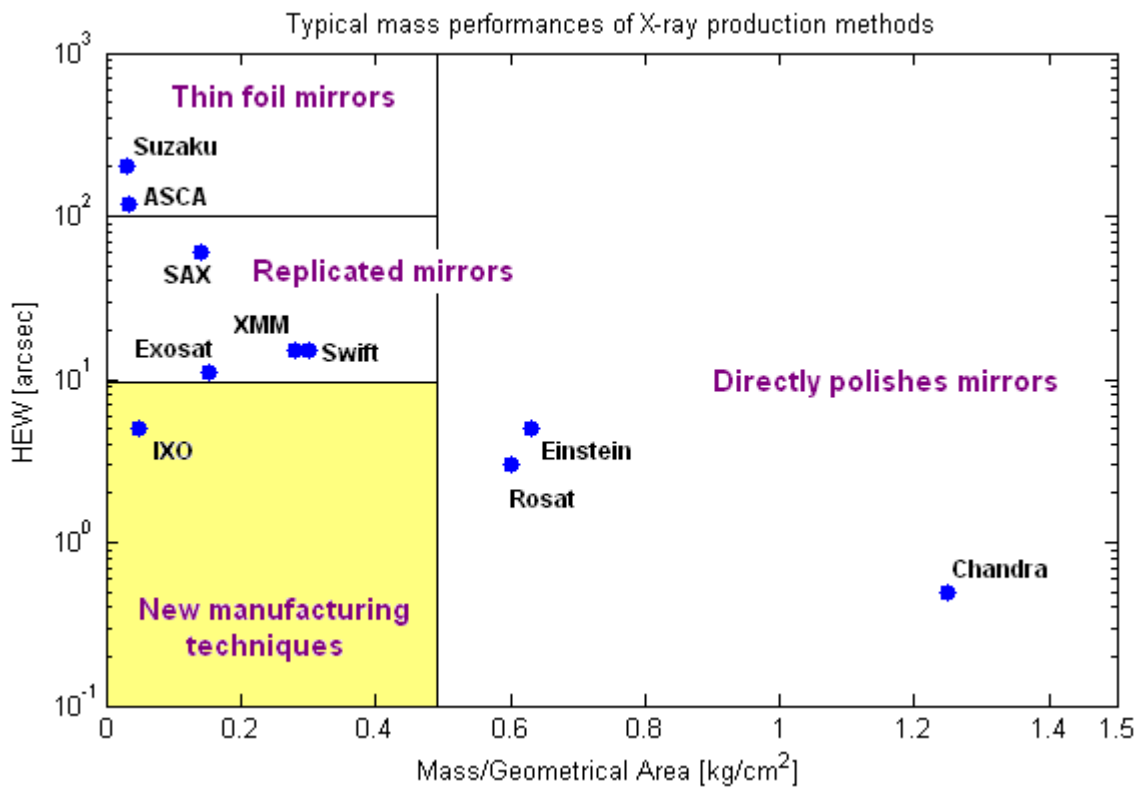


Fig. 2.23: Angular resolution (HEW) as a function of the mass/geometric area ratio of the mirrors for a number of past and present X-ray missions: the plot area is divided in three parts, considering the state of the art methods of production. The requirement of IXO is positioned in the area that requires the development of new technology rather than a mere evolution of existing techniques.

Going a little bit more in details, the problems associated with the existing technologies for their application to the IXO case are hereafter summarized:

- **DIRECT POLISHING:** Even if developments are ongoing to improve the technique for the direct polishing of thin mirror shells, of thickness 1-2 mm [76], this technology is not applicable to the IXO case because of the big diameters envisaged for the IXO telescope. The direct polishing of thin monolithic shells is realized starting from a raw quartz tube. Market available tubes have a maximum diameter in the order of 900-1000mm; no bigger tubes are nowadays produced. Further, it has to be considered the difficulty of handling and machining a tube/shell of such eventually large dimensions required by the IXO optical design (up to 3.5m diameter). In principle, one possibility to overcome this difficulty could be the application of the direct polishing technique for the realization of X-ray segmented optics. However, the huge quantity of shell segments that will be needed and their small thickness (<1mm) makes this solution impossible: it is unthinkable to produce thousands of thin glass segments by directly polishing each one of them at a time. The operation will be too time-consuming and risky, which means too expensive to be realized.
- **Ni ELECTROFORMING:** The Nickel technology has been employed so far for the manufacturing of close monolithic shells. Its extension for segmented optics is in principle applicable and relatively easy. Even so, it cannot be adopted for the IXO case primarily because of mass constraint. The specific weight of Nickel is such that the resulting optical system with the effective area required for IXO will be, in any case, too heavy for the launcher. Also the other replication techniques, based on Silicon Carbide, Alumina, or Beryllium, will result in too heavy systems if applied to the IXO case.
- **ALUMINUM THIN FOILS:** The aluminum thin-foil technique cannot be applied to the IXO case because of the difficulty in precisely shaping and integrating the aluminum foils to the required precision: the mechanical deformation and the poor assembling precision of so thin structures cause optical degradation too high in the case of IXO to meet its challenging goals. This technique does not present the potentiality of meeting IXO specifications.

A simple evolution of the already used existing techniques is not enough for the IXO telescope manufacturing; one new technology needs to be developed, able to lower the mass/effective area ratio while delivering a high angular resolution. Also, it necessitates being a replication technique to be compatible with the industrial production of big numbers of equal optical segments.

Nowadays, there are two techniques under evaluation to solve the issue, both based on the use of lightweight material [77]: the Silicon Pore Optics (SPO), under study by ESA since early 2000, and the Slumping Technology (or Segmented Glass Technology -SGT-), under development by several groups

in the world. The first one is hereafter described. The last one is discussed in the following completely dedicated chapters.

2.3.3 ESA base-line for IXO telescope manufacturing: the Pore Optics technology

The Silicon Pore Optics technology (SPO) is under development by ESA in collaboration with the Cosine Research Company since more than 10 years. At the moment, it is assumed by ESA as base-line for the production of IXO telescope. The Silicon Pore Optics technology is based on the use of Silicon as substrate material for the mirror shells. The selection of this material is mainly related to its low density if compared to traditional material ($\rho_{\text{Si}} = 2.32 \text{ g/cm}^3$ compared to $\rho_{\text{Ni}} = 8.9 \text{ g/cm}^3$) that ensures the potentiality to deliver mass/geometric area ration as low as 200 kg/m^2 . A segmented X-ray telescope design has to be considered since large monolithic structure cannot be realized in Silicon: this substrate material is available on the market in wafers of dimension up to 315 mm in diameter. Silicon has the great advantage to be a very well-known material because of its large use in the semiconductor industry, from where many technologies have been harnessed for the wafers preparation and shaping into the complex structures required to reflect X-rays. In practice, the Silicon Pore Optics foresees the realization of the segmented X-ray optics by stacking and hydrophilic bonding together several suitably etched Silicon plates with the aim of forming a monolithic block of segmented mirror shells, called High Performance Pore Optic (HPO). Two such HPO stacks are then aligned and assembled into a Mirror Module (MM) to produce the double reflection required by the Wolter I design of X-ray telescope. However, their actual shape is not that of a theoretical Wolter I (first reflection on a parabolic mirror and second reflection on a hyperbolic one) but a conical approximation of it: when stacked the mirrors remain flat along the pores. The achievable angular resolution is then limited by the height of a single pore: this leads in a lower limit of about $3''$ HEW for the current design that foresees pore height of 0.6 mm. Fig. 2.24 displays each step of the production of Silicon Pore optics: Silicon wafers are cut into paper-thick square plates and 'ribs' are diced into them to facilitate their stacking. They are then tapered into a wedge shape to direct X-rays along the desired optical path, and a metal reflective layer is added. An industrial robot performs their precision stacking and mounting. A large number of MMs are then aligned and isostatically mounted in the telescope structure. The maximum dimensions of a Silicon Pore Optics module are mainly dictated from the availability of substrate material and from the possibility to conform them to the required shape. The present considered dimensions for the Silicon plate are 66 mm x 66 mm, with an original thickness of 0.775 mm. After the wedging and ribbing, the square mirror has a membrane thickness of 0.17 mm, the same as the circa 1 mm spaced ribs. Tens of plates can be stacked in each single module. The overall small size of the SPO modules allows compact production

equipment, ensuring the cost-effective implementation of mass production lines in clean room environment. A summary of the main characteristics of currently produced SPO is provided in Table 2.5. For the entire telescope, the mirror module size will be determined by its radial position within the X-ray aperture (plate length), meaning that outer plates will be shorter than inner ones, according to the design reported in Fig. 2.25 and dictated by the conical approximation of Wolter I geometry [78]. The limits on circumferential radius will be instead imposed by both the Si wafer size and the ability to curve it. The technique is called ‘Silicon Pore Optics’ because the massed stacks of ribbed Silicon appears porous: each pore in the assembled Silicon stack directs X-rays into the focal plane of the system. The present Mirror Assembly based on Silicon Pore Optics is composed by 8 so-called petal structures that contain 236 mirror modules each, for a total mass of around 1929 kg (accounting for one Al pre-collimator⁸). They are assembled together in the Optical Bench to cover the entire available area. The around 2000 MMs necessary to fill them will require a total of 200000 Silicon plates overall [79].

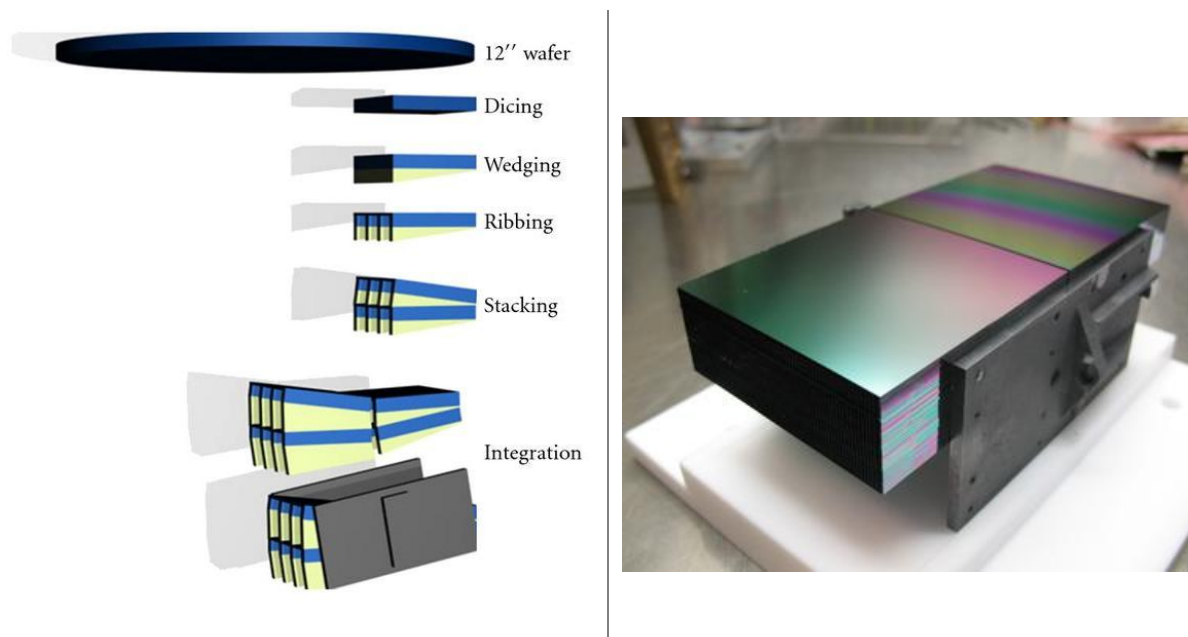


Fig. 2.24: (Left Side): The production of SPO modules starts with commercial Silicon wafers and utilises, as far as possible, existing methods and processes. The stacking is done automatically using a stacking robot, [80], [80b]. (Right Side): Picture of a complete SPO module. It is composed by two High Performance Pore Optics (HPO), stacks of ribbed Silicon wafers. They are aligned to arc second accuracy using pencil beam X-rays and then joined by mounting CeSiC brackets, which offers the I/F to attach the mirror module to the petal structure (Credits: ESA-COSINE Research).

⁸ A pre-collimator is an element which blocks stray light that otherwise would enter the detector at a larger angle than intended fouling the focal plane photon detection.

Table 2.5: Summary of the basic characteristics of the SPO realized up to now (adapted from [81]).

Specific mass	35 gr per cm ² geometric collecting area
Collecting area per unit	9 cm ²
Module mass	140 gr
Module thickness	54 mm
Module number of mirror plates	Demonstrate up to 45
Mirror plate material	Silicon
Mirror plate dimension	66 mm x 66 mm
# ribs for plate	64
Ribs separation	0.85 mm
Ribs pitch	1 mm
Ribs thickness	170 μm
Membrane thickness	170 μm
Mirror plate shape	Conical approximation of Wolter I design
Surface roughness	< 0.6 nm
Grazing angle	0.5 deg
Image resolution	15 arcsec
Focal length	20 m
Reflective coating	Iridium

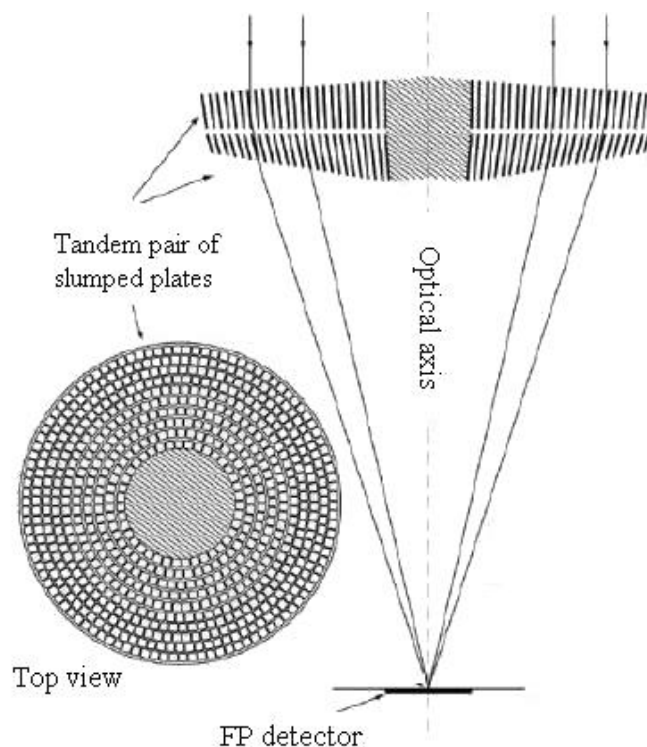


Fig. 2.25: Current design of the IXO X-ray telescope based on SPO: it is an approximation of the Wolter-I optic, realized through conical surfaces, implemented by using a large number of rectangular SPO modules in concentric circles [CREDIT://sci.esa.int/science-e].

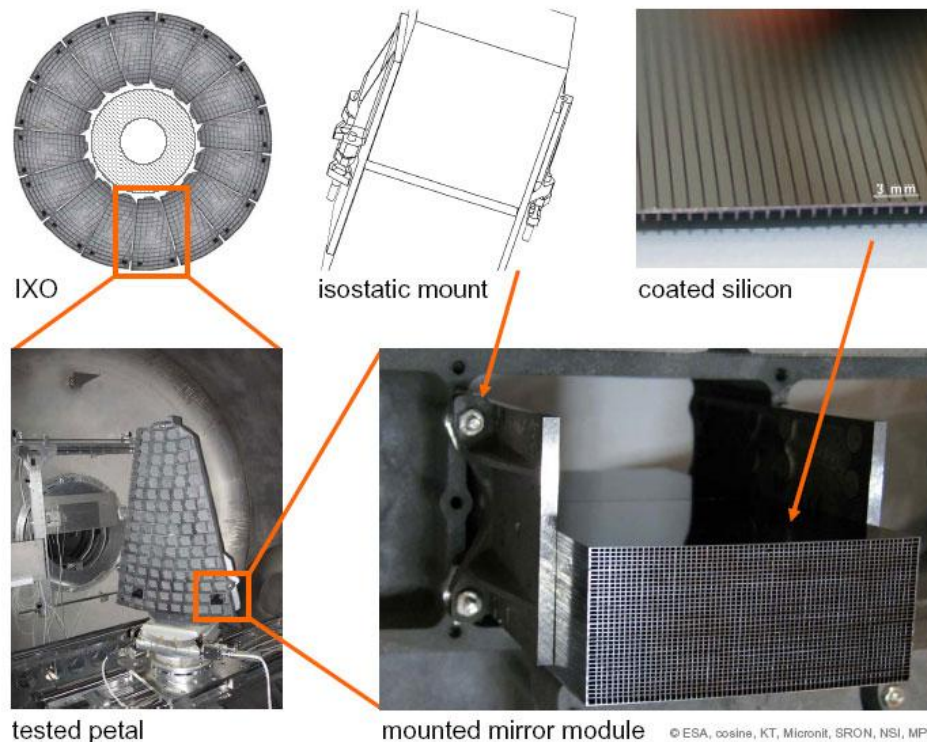


Fig. 2.26: Representation of the entire production chain of the IXO telescope based on SPO: single Silicon mirror plates are ribbed, wedged, Ir coated and stacked together to form a basic optical module. A number of optical modules are then integrated and aligned in the petal structures that mounted together will compose the X-ray telescope. Note that the upper left figure is only representative of the concept: the current design foresees 8 petals. In the lower right picture the pore structure from which the technology gets its name is clearly visible [82].

For the purposes of the SPO development for IXO mission various breadboards have been built. Demonstration of 17 arcsec angular performance over a stack height of 4 plates was achieved in 2007, for a 50 m focal length optic. In 2008 the attention was shifted to upgrading the stacking system, in particular improving the cleaning control. To date, a complete module up to 45 mirrors has been assembled and its performances verified with representative X-ray tests. The results are quite encouraging, showing an HEW of 16.6 arcsec at 3keV (7,5 arcsec if only the first 4 mirror plates are considered). However, the next step requires streamlining the assembly process for mass production and further improving quality, to reach the TRL of 5 expected at the first down-selection from three to two L class mission by spring 2012 (the actual TRL is around 4). To reach the required 5 arcsec it is necessary to improve the conical approximation to true Wolter-1 geometry and demonstrate the technology application also for the inner radius of IXO aperture, which is more challenging. The technological feasibility of this step has not been proven yet and might become of fundamental importance in the case of a revision of the IXO optical design. It has to be mentioned in

fact that at the moment of writing (summer 2011) the US Decadal Survey commission decided not to rank IXO as “high priority mission” because of budgetary reason [44]. After this choice, that delays the launch after 2030, ESA started to assess the study of a new ESA-lead mission with no USA participation to try maintaining the launch prevision around 2022. The mission will probably took the new name of Athena and will be probably smaller than IXO to stay in the budget ESA reserved for L-class mission (850 M€). A European scientific commission is currently verifying the possibility to achieve the goals set for IXO also with a smaller mission (eventually changing the observation procedures and data analyses in addition to the change of the optical design). Due to the rapid evolution of the project, it was decided to freeze the design as it was in April 2011, considering that eventual changes do not have implication on the results of the presented activities, which can be applied independently from the specific details of the final design. For this reason throughout the entire document the IXO design as for early summer 2011 is considered.

3 IXO back-up optic study

The Slumping Technology, also known as the Segmented Glass Optic technology (SGO), is under development by ESA as a back-up technology for IXO. The reason why ESA decided a different technology needs to be explored originates from considerations on the reduction of any contingency effects in terms of mission feasibility: the technique is investigated as a risk mitigation measure in case the SPO base-line does not meet the necessary TRL. Also, it has to be considered that the slumping technology can be useful for other applications (for example adaptive optics). For these reasons it is important and of interest for ESA to explore it.

The slumping technology foresees the realization of the single X-ray optical segments by thermally shaping thin glass sheets onto a suitable mould. A number of slumped plates are then integrated and aligned into basic modules, characterized by stiffening structures that allow their handling and integration into the Mirror Assembly (MA) structure to completely fill the telescope aperture. The first step in the development of the slumping technology for the realization of IXO X-ray telescope is to demonstrate the feasibility of the mirror plate and of the basic module production within the required specifications. With this goal, the INAF-OAB is working since more than 2 years under ESA contract for the development of the technique. The activities will finish in spring 2012 with the delivery of two prototypes, aimed at demonstrating the technology feasibility. This section presents the project in the context of which the majority of the research activities was realized. The optical design of the IXO mirror telescope based on the glass technology is described, to derive the requirements for the slumping technology development. All the details of the slumping technology itself are left for the following dedicated chapter § 4. This section is closed with a summary diagram that highlights the areas in which the author brings contributions.

3.1 The ESA IXO back-up optic project

In response to an ESA call for the study of “Back-up IXO (former XEUS) Optics Technology, Phase 1”, INAF-OAB prepared a plan for the assessment of the slumping technology to be applied to the IXO case based on its past experience with this technique [83]. The contract has been won and it formally started in September 2009 (ESA contract #22545), even if researches and preliminary investigations already began the year before with internal funds. The study is led by the Astronomical Observatory of Brera and involves the collaboration of other institutes and small enterprises: Max Planck Institut für Extraterrestrische Physik -MPE- (Garching, Germany), BCV-Progetti (Milano, Italy), ADS-

International (Lecco, Italy), and Media Lario Technologies (Bosisio Parini, Italy). The activities follow the flow proposed in the Statement of Work [84], reported in Fig. 3.1. Due to time constrain reason, mainly originated from the ESA Cosmic Vision selection process [85], the study should have been finished in a relatively short period (14 months) and so it was necessary to plan activities in parallel. Some delays have been experienced and the end of the project is actually expected for the middle of next year 2012.

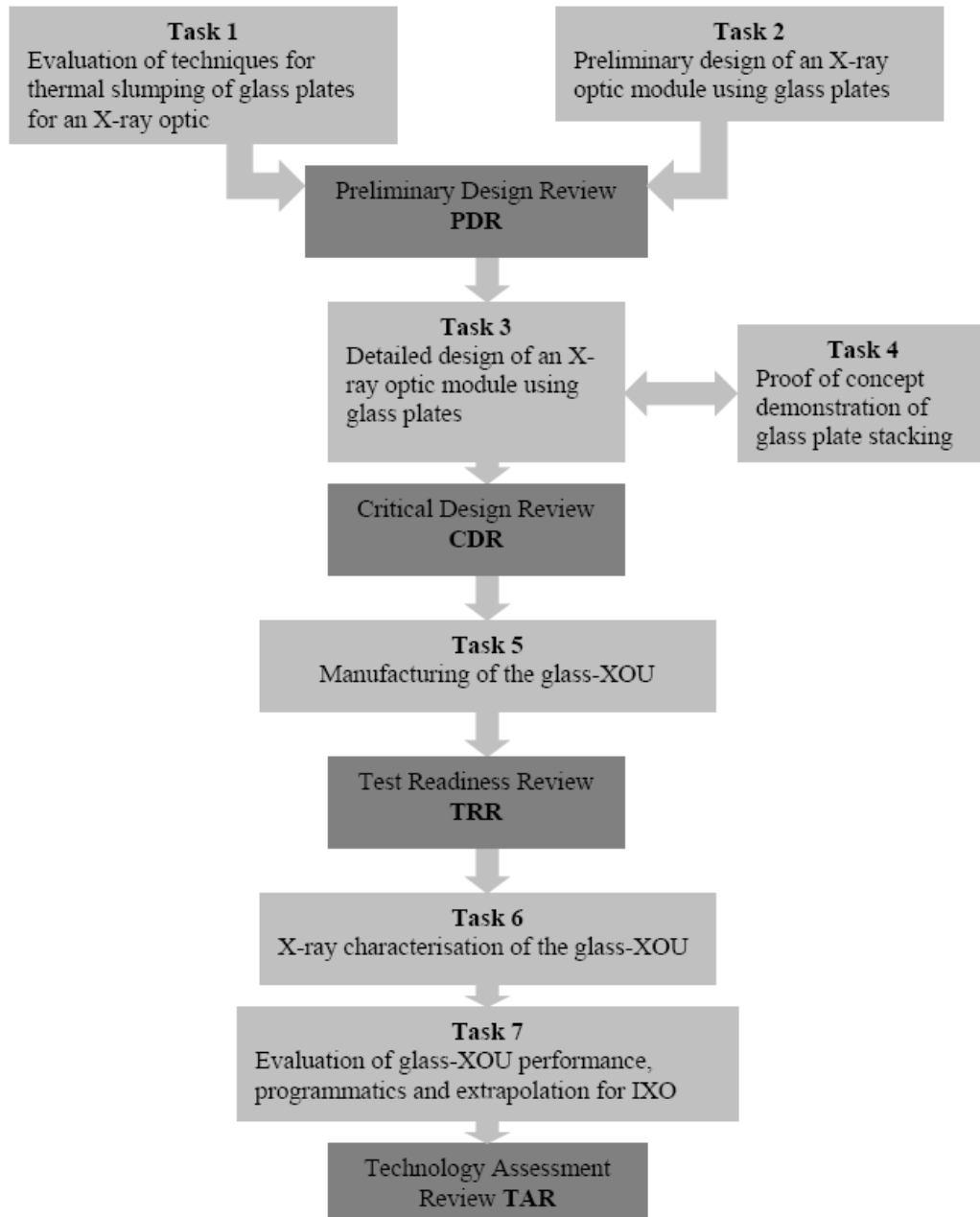


Fig. 3.1: Project workflow diagram as derived by the Statement of Work document. Due to programmatic constraints, the activities required the execution of tasks in parallel.

The entire project was divided in two main phases:

- **PHASE 1:** from Kick Off Meeting (KOM) in September 2009 to the Preliminary Design Review (PDR) in August 2010

The first phase has been **dedicated to the assessment of the slumping technology** for its application to the IXO case. It was devoted to individuate the most relevant parameters and their influence on the process results and to demonstrate its potentiality in meeting the IXO requirements. In particular, two different slumping approaches have been considered: the direct slumping approach, investigated by the INAF-OAB and the indirect slumping approach, investigated by MPE. The main scope of phase one was to individuate the slumping approach to pursue during phase two, i.e. the one that presents the higher potentiality to meet IXO demanding requirements. This thesis regards the direct approach.

- **PHASE 2:** from September 2010 till the end of the project (presently set for the first half of 2012)

The second phase of the project is mainly dedicated to the assessment of the integration procedure, an essential part of the slumping technology⁹. To this end, **the realization of two prototypes is foreseen**, whose assembly and characterization required the development of ad-hoc designed machines. While working on these topics, slumping activities are still on going to further improve the process performances and deliver the numerous optical segments to be integrated in the prototypes.



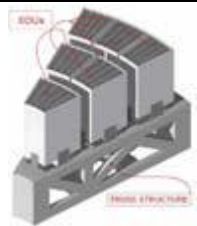
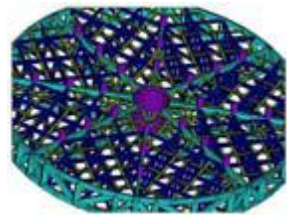

3.2 IXO optical design based on the glass technology

The design of the IXO X-ray telescope based on the use of glass slumping technology is presented and considered in this section. It follows a Wolter I geometry, with a focal length of 20 m, a Field of View of 18 arcmin, and radius of the shells comprises between 0.25 and 1.70 m. This design is developed together with BCV, partner of INAF-OAB in this study. As already mentioned previously, it represents a snapshot of the situation at the moment of writing (Spring-Summer 2011) and will probably suffer from changes in the future, also in consideration of the Athena mission proposal. However, the basic concept will remain the same and so the current optical design is described for clarity and completeness reasons also if it has not to be considered definitive. Because of the maximum

⁹ A perfectly slumped plate is in fact useless if there is no capability of aligning and integrating it with the necessary accuracies.

aperture of the IXO telescope, the shells composing the X-ray telescope are azimuthally divided into segments: basically the telescope mirror is partitioned into petals and each petal is further divided in smaller segments of circular coronas whose dimensions can be optimized to reduce the obscuration area. Substantially, a principle of hierarchical integration is adopted for the realization of the Mirror Assembly, as summarized in Table 3.1 and in Fig. 3.2. The current design for the IXO telescope comprises 8 petals, populated by 200 basic optical modules (25 each petal, arranged in 8 nested rings) and supported by the Optical Bench through spokes. Within a petal the basic Mirror Modules are arranged in rows (i.e. identical radii) which ensure the mirror modules within a row are optically identical (good for industrial production and eventual substitution of defective modules). The basic optical module is called X-ray Optical Unit (XOU) and is composed by glass segments called Mirror Plates (MP): two of them in Wolter I configuration (one parabolic and the other hyperbolic) form a Plate Pair (PP). Several Plate Pairs, up to 55, are assembled together to form any single XOU, following a stacking approach that makes use of reinforcing glass spacers, called ribs, and stiffening structures, called back plates. The ribs are glued on the mirror plates with the aim of maintaining them in their mutual correct position, meanwhile solving a structural function. A total of more than 16000 slumped mirror plates will be necessary for the assembling of the entire IXO telescope. As an example, let's consider the XOU at a radius around 1000 mm: the two independent stacks of parabolic and hyperbolic mirror segments are composed by 40 MPs each, of dimensions around 200 mm x 200 mm x 0.4 mm. Each glass foil is connected to the adjacent ones by 6 glued ribs equally spaced along azimuthal direction. The ribs width ranges from 4 to 5 mm for the outermost ribs, while it is of 1-2 mm for the innermost ones. Their thickness follows the MS separation according to the optical design, and ranges from 1 to 5 mm going outward. Parabola and hyperbola stacks are made monolithic by two back plates placed at top and at bottom of the stacks. Two options have been until now considered for the back plates: a sandwich back plate with glass skins and internal Ti honeycomb; or a solid glass ribbed back plate. A metallic casing surrounds the XOU allowing for its connection to the petal structure through three quasi-isostatic mounts by screws. This frame is composed by three separate frames, two of which are connected by adhesive pads to both back plates, while the intermediate one houses the interfaces with the petal structures. The three frames are connected by flexures which decouple the petal structure from the optical XOU components.

Table 3.1: Principle of hierarchical integration of the IXO Mirror Assembly: starting from the single slumped glass plate, all the components are shown and definitions given, to arrive at the assembly of the whole optical payload.

Mirror Plate (MP)	Individual glass plate with parabolic or hyperbolic surface in accordance to the Wolter I optical scheme.	
Plate Pair (PP)	Pair of MPs, one parabolic and one hyperbolic.	
X-ray Optical Unit (XOU)	Elemental optical unit composed by a stack of glass PP connected each other through glued glass ribs. An outer structure, composed by two back plates, allows for handling, calibration and assembly into higher level structures.	
Mirror Petal Structure (PS)	Intermediate level structure containing a number of XOUs and supporting them with the required alignment accuracy and stability. Several PSs are needed to azimuthally cover the entire aperture of the telescope.	
Mirror Optical Bench (MOB)	Mechanical structure that supports all the PSs, iso-statically mounted on it, with the required alignment accuracy and stability.	
Mirror Thermal Baffles	Low mass baffling element supported by the mirror petals and located in front of the mirror basic modules (sky side), allowing to heat the optics by radiative exchange.	
Mirror Contamination covers	Dedicated, removable, protection covers, located in close proximity of the optics having the function to minimise the contamination of the sensitive reflective surface of the XOUs.	
Mirror grating Arrays	Two grating assembly used by the Critical Angle Transmission Gratings Spectrometer (CAT-XGS) and accommodated on two symmetric petals, facing the focal plane side of the mirror assembly.	
Mirror Assembly (MA)	The entire optics assembly of the satellite, i.e. all the optical and structural part that compose the telescope payload.	

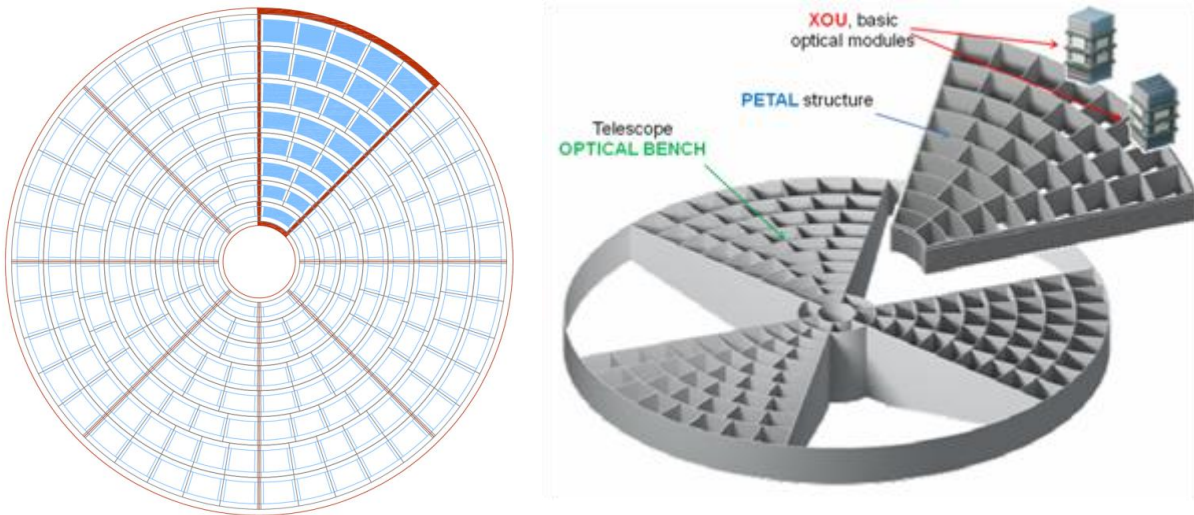


Fig. 3.2: Schematization of the proposed principle of hierarchical integration. (Left Side): the sketch of the Mirror Assembly layout with optical units arranged in 8 petals, one of which is evidenced. Cyan areas in the picture represent the net optical available area, not shielded or vignette by structures. Parts between optical areas are occupied by structural back-plates, interface frames and petal walls. (Right Side): Three different levels of structure are envisaged for IXO: the single slumped mirror segments are integrated to form the elemental X-ray Optical Unit, called XOU; the XOUs are integrated on the petal structure through isostatic mounts; a number of petals are then iso-statically mounted onto the telescope Optical Bench to fill the entire geometric area restoring the circular symmetry of the telescope Wolter I design. Note that only six petals are shown in the sample scheme; the actual number is eight.

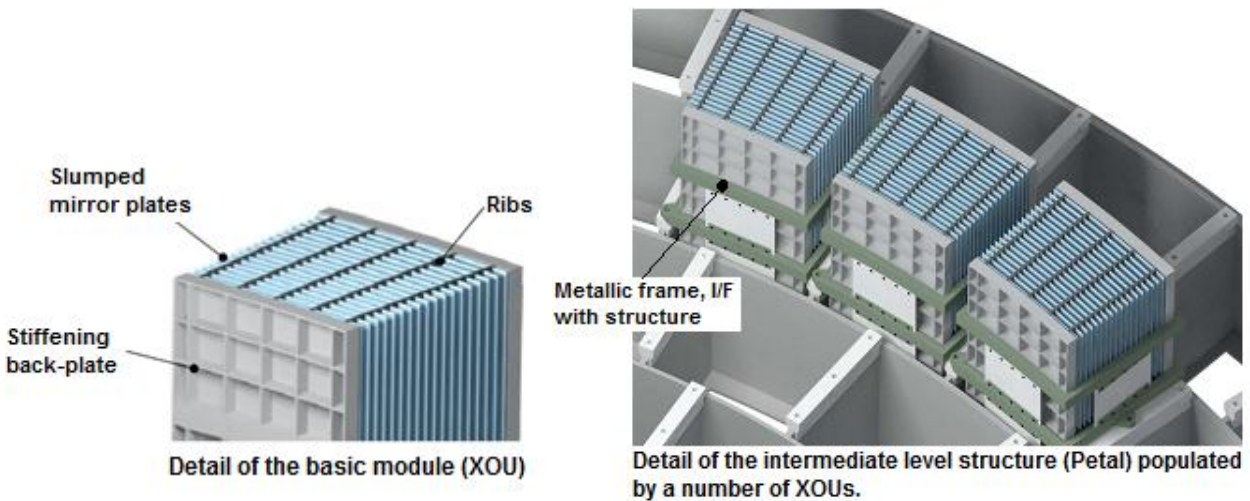


Fig. 3.3: Details of XOU and Petal structure; the optical units are embedded into the Petal Structure through a metallic frame, useful for handling and I/F purposes. The hyperbola part of the Mirror Plates stack is completely accommodated into the proper volume delimited by the Petal walls. The Petal structure offers three isostatic points of connection to the Optical Bench structure; it consists of a multi-connected box, without top and bottom covers, spanning on an azimuthal sector 45° wide. External walls delimiting the sector are stiffened with ribs. A previous version of the optical design is here reported: the current one makes use of six ribs instead of the five visible in the pictures. The case of solid glass ribbed back plate is depicted.

Table 3.2: Characteristics of the current optical design based on the SGT (Segmented Glass Technology) able to verify the IXO requirements, as clear from the design values reported on the right [86].

Ring	XOUs per ring	MS per XOUs	R med inner MS [m]	R med outer MS [m]	MS foil arc length [m]	XOU net angular [degrees]	Number of MP
1	8.	55	0.31383	0.38216	0.200	30.0	880
2	16.	50	0.44960	0.52884	0.160	17.3	1600
3	16.	45	0.59543	0.68304	0.200	16.8	1440
4	24.	45	0.75080	0.85640	0.180	12.0	2160
5	24.	40	0.92446	1.03518	0.200	11.1	1920
6	32.	40	1.10254	1.23139	0.190	8.8	2560
7	40.	40	1.30248	1.45168	0.180	7.1	3200
8	40.	35	1.52137	1.66989	0.220	7.5	2800

Wolter I geometry

Focal length = 20 m

Field of View = 18 arcmin

Eff. Area = 2.58m²@1 keV

Eff. Area = 1.17m²@4 keV

Eff. Area = 0.70m²@6 keV

HEW = 5 arcsec

Such a modular approach for the production of the IXO MA (Mirror Assembly), although calling for additional mass with respect to monolithic systems due to the intermediate level structures, i.e. XOUs and petal structures (see Fig. 3.4), is aimed to consent and facilitate the fabrication and AIV (Assembling Integration Verification) activities, and is justified by four main reasons:

- The difficulties associated with the handling, integration and calibration of the full telescope aperture, with a diameter of about 3.5 m. In practice, the production of such a large monolithic telescope is not possible (or at least not easy and highly risky) with present production techniques and existent production and test facilities.
- The need to reduce the risk associated with the integration and alignment of a single mirror structure. In the case of monolithic structure, if something get wrong the risk of lose the entire telescope assembly is very high. In the case of a modular approach, if one module is broken or suffer from some defects, it can be easily substituted with no impact on the other modules. Furthermore, all the modules located at the same radius in the Mirror Assembly aperture are equal and present the same interface to the petal. Therefore the modules of the same line are interchangeable and a single back up module might be considered for a number of them.
- The need to reduce the schedule constraints allowing for parallel activities on separate elemental XOUs modules and petals.
- The easiness in maintaining the stringent cleanliness requirements: it is simpler to guarantee the cleaning of a relatively small and manageable structure with respect to a big one that cannot fit inside standard cleaning apparatus.

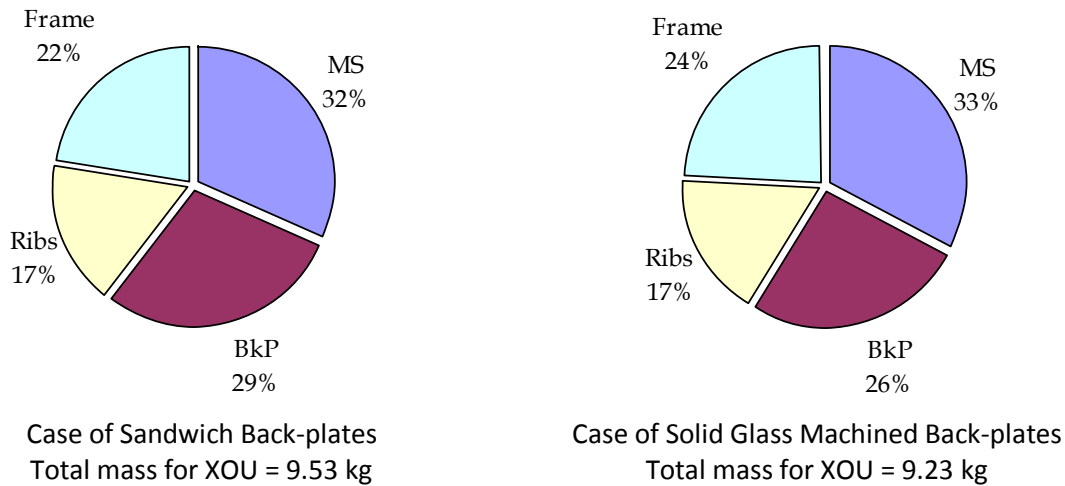


Fig. 3.4: A preliminary mass estimation for the present design has been conducted. Considering for example an XOU located in ring 5 (i.e. having Radius Of Curvature around 1m) the various parts of the optical unit participate to the global mass with the following ratios: Mirror Shells represent slightly more than 30% of the XOU global mass; approximately the same percentage of MS mass is represented by glass ribs; remaining contributions are provided by structural back-plates and I/F frames. The slumping technology has the potential to meet IXO mass budget¹⁰, even if the structural parts account for higher percentage with respect to the traditional X-ray telescopes (for which it is generally around 30% of the telescope mass). The two possibilities of Sandwich or solid glass machined back plates are compared.

The current design requires the geometry, dimensions, and materials reported in Table 3.3, coming from optimization analyses based on the present knowledge of loads conditions and technology performances. An exhaustive knowledge of the mechanical parameters of the material and of the strength of the elements, together with a more detailed definition of environmental conditions, could allow further design optimizations. Works in this direction are envisaged for the next steps of the present study. Due to the importance of the strength parameter in the mechanical design of the system, few activities already started in this area and are reported in chapter § 6.

Further optimization activities are ongoing (the project evolves in time and the optical design is not definitive), improving the simulation models with the latest laboratory results. Under study at the moment of writing (summer 2011) are: 1) the number of ribs for each single mirror plate and their geometric dimensions; 2) the structural configuration of the back-plates; 3) the exact glass material for structural parts; 4) the total number of XOUs and petals. The basic concept does not change and these parameters have no dramatic impact on the slumping technology under evaluation. It is worth nothing that the telescope design is conceptually similar in the case of slumping technology or Pore Optics technology. Even if the names and the geometrical/physical realization of the components might be (and actually are) different, the hierarchical approach for the segmented X-ray optic

¹⁰ The mass budget of the entire IXO spacecraft is of 6500 kg, with almost 2000 reserved for the optical payload. The present design is of about 2200 kg, accounting for design margins. Further optimization analyses, planned for the next steps of the project, such as structural optimization of ribs and back-plates, will guarantee the full reaching of the requirement.

manufacturing is always the same: single mirror elements are stacked together to form many basic optical modules that assembled together form the telescope. This is extremely important as both the SGT and the SPO design are compatible and fits in the same satellite bus with no major changes: only the MA module is different, the SVM and IM are identical. This fact allows ESA to effectively consider the slumping technology as a back-up for the SPO one and develop them in parallel until 2012, when a down-selection base on the reached TRL might be done.

Table 3.3: List of materials and main characteristics envisaged for the manufacturing of each component of the IXO telescope optics.

Component	Foreseen material	Characteristics	Dimensions and #
XOU Mirror Segments	Structural glass: Schott D263	Young Modulus E = 72900 Mpa Poisson ratio $\nu = 0.208$ CTE $\alpha = 7.2 \times 10^{-6} / ^\circ\text{C}$ (20-300°C) Density $\rho = 2510 \text{ Kg/m}^3$ Thermal Conductivity $k = 0.960 \text{ W/(m}\times\text{K)}$	> 16000 200x200mm on average 0.4 mm thickness 0.25 ÷ 1.90 m ROC Par & Hyp profile shape
XOU Ribs	Structural glass: Schott BK7	N-BK7TM borosilicate Glass Young Modulus E = 82000 Mpa Poisson ratio $\nu = 0.206$ CTE $\alpha = 7.1 \times 10^{-6} / ^\circ\text{C}$ (-30-70°C) Density $\rho = 2510 \text{ Kg/m}^3$ Thermal Conductivity $k = 1.144 \text{ W/(m}\times\text{K)}$	6 for each MP 200 mm long 1.5 ÷ 5 mm thickness 1÷2 mm width (innerm.) 4÷5 mm width (outerm.) Tapered shape
XOU Backplate	Structural glass: Schott BK7	Same as above	2 for each XOU = 400 (200 XOU in total) Par & Hyp profile shape
Adhesive for XOU integration	Master Bond Polymer System EP30-2	Young Modulus E = 2760 Mpa Poisson ratio $\nu = 0.34$ CTE $\alpha = 45 \times 10^{-6} / ^\circ\text{C}$ (24°C) Density $\rho = 1400 \text{ Kg/m}^3$ Ultimate Compr. Strength = 69Mpa Ultimate Tensile Strength = 78Mpa Tensile lap shear strength = 19MPa Cure shrinkage 0.0003	25-100 μm thickness
XOU Case ad I/F (bolts included)	Titanium Alloy Ti-15Mo-3Nb-3Al-0.2Si* Data derived from TIMETALTM datasheet (TIMET)	Young Modulus E = 85000 MPa Poisson ratio $\nu = \text{N/A}$ (value 0.3 adopted) CTE $\alpha = 7.07 \times 10^{-6} / ^\circ\text{C}$ (temp. +38°C) Density $\rho = 4930 \text{ Kg/m}^3$ Thermal Cond. $k = 7.6 \text{ W/(m}\times\text{K)}$ (T.=33°C) Yielding Stress (0.2%) 759-1338 Mpa depending on aging treatment Ultimate Tensile Strength 793-1427 Mpa depending on aging treatment	External Titanium frame with flexures I/F frame is supposed bolted to a stiff sub-structure in 3 points
Petal structure	SUPERSiC-SiCTM from Poco Graphite Inc.	Young Modulus E = 379000 MPa Poisson ratio $\nu = 0.15$ CTE $\alpha = 2.4 \times 10^{-6} / ^\circ\text{C}$ Density $\rho = 3070 \text{ Kg/m}^3$ Ultimate Tensile Strength 138MPa	8 petals in total 240 mm total height 250 ÷ 1892mm Radius 5÷8mm Walls thickness

The two prototypes that will be realized during the second phase of the project with the aim of demonstrating the suitability of the slumping and integration approach to meet the requirements of

IXO, derive directly from the above presented BCV design and are fully representative of a real IXO XOU.

- **The Proof Of Concept (P.O.C.):**

The Proof Of Concept demonstrator (P.O.C.) is a first breadboard, considered an intermediate step in prototypes development, and mainly dedicated to the demonstration of the appositely designed Integration Machine (IMA) to meet the necessary assembling and aligning accuracies of slumped glasses (see Table 3.4) rather than to obtain a definitive XOU. It is composed by a back-plate and two integrated glass Plate Pairs (PP#1 and PP#2) stacked through the use of glass ribs, six for each mirror plate, and aligned in order to have a common focus. Its general scheme is reported in Figure 3.5, while Table 3.5 lists the components and items that will be utilized for its realization [87]. Without considering handling provision, the overall dimension of the P.O.C. will be of 430 mm x 210 mm x 38 mm, for a mass of around 6,350 kg \pm 5%. The P.O.C. optical plates will be a double cone approximation of the Wolter I configuration envisaged for the final XOU. This design allows for a faster realization while giving the possibility to test the IMA before its employment in the final prototype manufacturing.

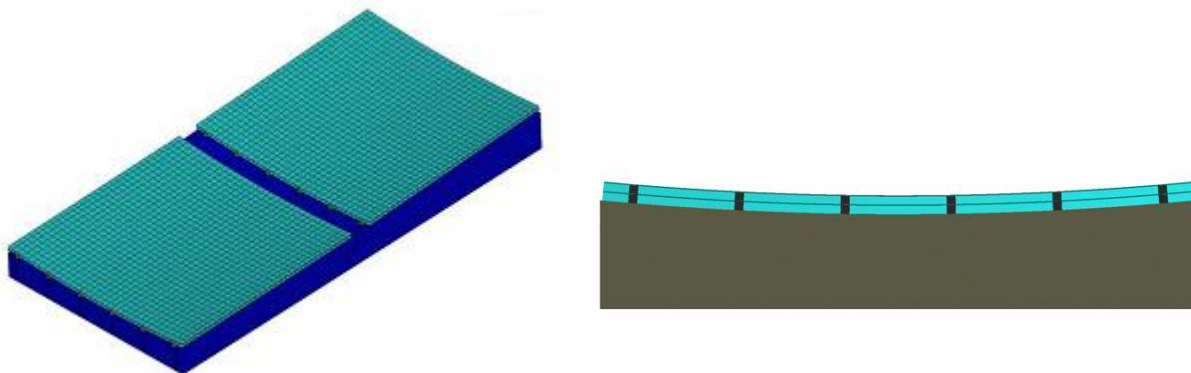


Fig. 3.5: Schematic layout of the P.O.C. demonstrator: top view and side view.

The slumped plates necessary for the integration of P.O.C. have a dimension of 200 mm x 200 mm x 0.4 mm Radius of Curvature on 1 m. To be representative of the IXO project, they should fulfill the following requirements:

- Shape of plates so that the inferred HEW for the integrated single plate is less than 15'';
- The roughness of the optical surface must be better than 10 Å (WYKO 20X, 660 – 10 mm wavelengths range) and equal to that of the starting glass foil in the AFM range (3-4 Å rms).

Table 3.4: Tolerances on plate positioning and tilt. The reference system has origin in the intersection between the intersection plane of the two conical surfaces with the optical axis; Z is the optical axis pointing toward the source; X is orthogonal to Z pointing toward the plates; and Y completes the orthogonal system. On the right the focal spot as composition of PP#1 and PP#2 when aligned with the required tolerances to have the same barycenter.

ITEM	D.o.F.	Reference item	Value
HYP+PAR	X	Backplane	$\pm 5 \mu\text{m}$
HYP+PAR	Y	Backplane	$\pm 5 \mu\text{m}$
HYP+PAR	Z	Backplane	$\pm 5 \mu\text{m}$
HYP+PAR	Rx	Backplane	$\pm 5''$
HYP+PAR	Ry	Backplane	$\pm 5''$
HYP+PAR	Rz	Backplane	$\pm 5''$
PAR	X	HYP	$\pm 5 \mu\text{m}$
PAR	Y	HYP	$\pm 20 \mu\text{m}$
PAR	Z	HYP	$\pm 20 \mu\text{m}$
PAR	Rx	HYP	$\pm 1''$
PAR	Ry	HYP	$\pm 0.25''$
PAR	Rz	HYP	$\pm 10''$

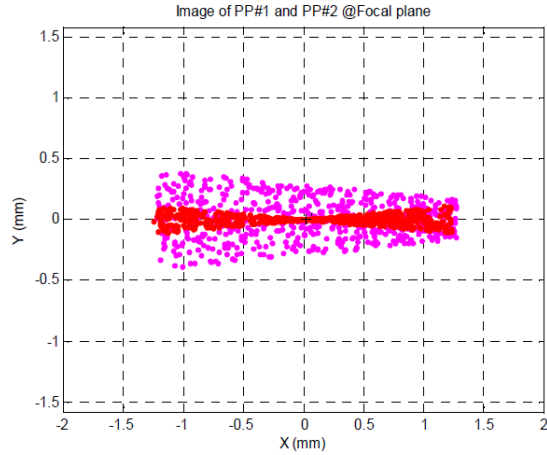


Table 3.5: Lists of the components and items that will be utilized for the realization of P.O.C.

Item/ component	#	Material	Dimension [mm]	Comment
Back plate	1	Ohara S-BSL7	430 \pm 0.2 (l) x 210 \pm 0.2 (w) x 30 \pm 1 (h)	Concave double cone design Radius at intersection= 1006 \pm 3 mm Front inclination = 2590 \pm 10'' Rear inclination = 7783 \pm 10'' Flatness of top surface = $\pm 5 \mu\text{m}$ Lateral side orthogonality to top surface = $\pm 30''$
Ribs	24	BK7	198 \pm 0.2 (l) x 2.4 \pm 0.2 (w) x 2.8 (indicat. h)	12 ribs parallelepiped for PAR side Average thickness = 2.804 \pm 0.01 mm Flatness = $\pm 10 \mu\text{m}$ 12 ribs trapezoidal for HYP side Average thickness = 2.786 \pm 0.01 mm Wedge shape max-min thickness = 25 \pm 5 μm Flatness = $\pm 10 \mu\text{m}$
Glue		Masterbond EP30-02	Thickness 75 \pm 25 μm	Low viscosity, two component epoxy resin compound with low shrinkage and outgassing Curing T = Room Temperature Curing time = 24h
Glass Plates	4	Schott D263	200 x 200 x 0.4	Slumped by using cylindrical moulds Roto-translation center along X and slope: Front #1: 1001.373mm, 2572.63'' Rear #1: 995.875mm, 7732.06'' Front #2: 1004.727mm, 2581.24'' Rear #2: 999.211mm, 7757.92''
I/F to IMA	3	Al pads	Diam. 30mm	Flexures interfaced glued to the backplane with glue Dow Corning RTV Q3-6093, 200 μm thickn.
IMA	1	ADS	1.5x1.2m base 1.2 m h	Appositely design for the integration of glass slumped plates into XOUs

- **The X-ray Optical Unit (XOU_BB):**

The XOU_BB is the final demonstrator to be delivered at the end of this project with the main scope of demonstrating the suitability of the entire proposed production flow (slumping technology plus integration with IMA) to realized IXO XOUs. Therefore its design is fully representative of a real IXO XOU. It will be composed of 20 Plate Pairs (3 of them optically representative of the Wolter I design of IXO X-ray telescope and 17 considered as dummies, for which the Wolter shape is not required). These plates will be stacked with glued glass ribs between them (6 for each plate) on a backplate and a second one will be employed to close the mechanical structure in such a way to form a single monolithic unit, intrinsically stiff. The two back-plates are connected by a surrounding flange made in Titanium that provides the I/F with the external handling/mounting devices. The XOU_BB general scheme is reported in Fig. 3.6, while Table 3.6 lists the components and items that will be utilized for its realization [88]. The slumped plates necessary for the integration of XOU_BB have a dimension of 200 mm x 200 mm x 0.4 mm and Radius of Curvature on 1 m. All the plates will be integrated taking as reference the position and the orientation of the Wolter-I configuration. The overall XOU_BB predicted optical performance is around 4.5 arcsec HEW (fully compliant with IXO resolution requirement) and its evaluation at X-ray facilities will allow a feedback on the manufacturing and integration procedure. The 6 optically representative slumped plates to be integrated into the XOU_BB should fulfill the same requirements as those dictated for the P.O.C., i.e.:

- Shape of plates so that the inferred HEW for the integrated single plate is less than 15'';
- The roughness of the optical surface must be better than 10 Å (WYKO 20X, 660 – 10 mm wavelengths range) and equal to that of the starting glass foil in the AFM range (3-4 Å rms).

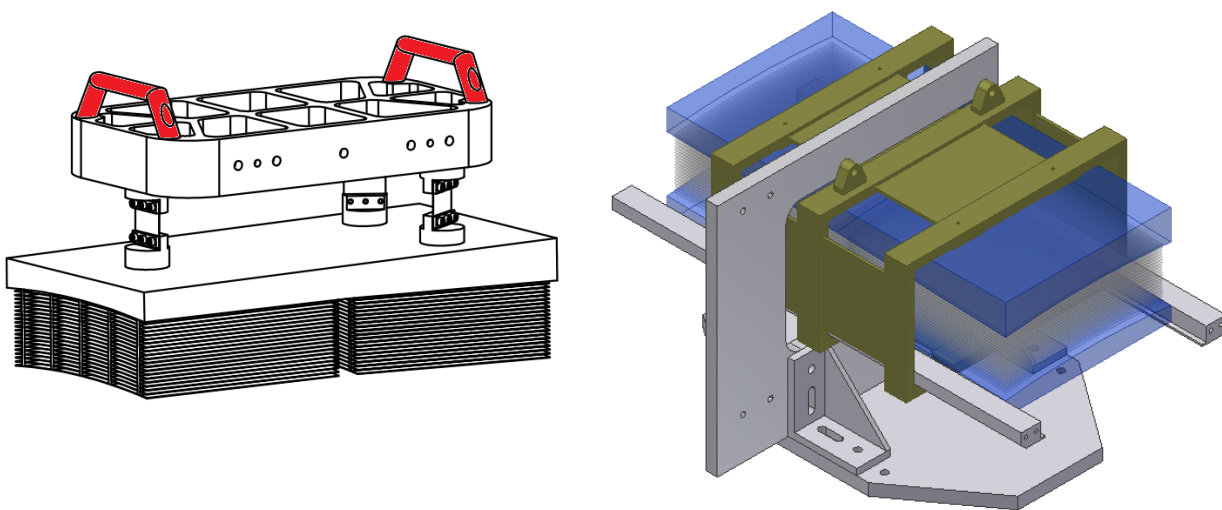


Fig. 3.6: Schematic layout of the XOU_BB prototype. (Left Side): still attached to the IMA interface; (Right Side): integrated in its final structure. The two extreme frames are glued to the glass back and top plates while the intermediate frame holds the connections to jigs and tools. In this case, the external structure necessary as support during X-ray characterization is shown.

For the 34 dummies plates, no particular requirements are given. For completeness in the descriptions of this project's activities, it is worth mentioning that a new dedicated machine is being realized, named CUP (Characterization Universal Profilometer – see Annex B –) for the characterization of slumped and integrated mirror plates, which adds to the state-of-the art instrumentation already available in the INAF-OAB laboratories.

Table 3.6: Lists of the components and items that will be utilized for the realization of XOU_BB.

Item/ component	#	Material	Dimension [mm]	Comment
Top Backplate	1	Ohara S-BSL7	430±0.2 (l) x 210±0.2 (w) x 30±1 (h)	Concave double cone design Radius at intersection= 1036.845±1mm Front inclination = 8016.369'±10" Rear inclination = 2667.342'±10" Flatness of top surface = ± 5 µm Lateral side orthogonality to top surface = ±30"
Closure Backplate	1	Ohara S-BSL7	430±0.2 (l) x 210±0.2 (w) x 30±1 (h)	Convex double cone design Radius at intersection= 1036.845±1mm Front inclination = 8016.369'±10" Rear inclination = 2667.342'±10"
Ribs	252	BK7	198±0.2 (l) x 2.4±0.1 (w) x 2.8 (indicat. h)	126 ribs parallelepiped for PAR side Average thickness = 2.805±0.01 mm Flatness = ±10 µm 126 ribs trapezoidal for HYP side Average thickness = 2.787±0.01 mm Wedge shape max-min thickness = 25±5 µm Flatness = ±5 µm
Glue	Masterbond EP30-02		Thickness 75±25 µm	Low viscosity, two component epoxy resin compound with very low shrinkage and no solvents or other volatiles content Curing T = Room Temperature Curing time = 24h
Glass Plates	40	Schott D263	200 x 200 x 0.4	Slumped by using cylindrical moulds Roto-translation center along X and slope adjustment wrt the nominal Wolter I design in order to have the same focus for all the 20 pairs
Interface to IMA	3	Al pads	Diam. 30mm	Flexures interfaced glued to the backplate with glue Dow Corning RTV Q3-6093, 200µm thickn.
Closure flanges	1	Ti outer metallic structure	TBD	Composed by three rectangular frames + 8 flexures (thin metallic plates) connecting them. The two extreme frames are glued to the glass back and top plates while the intermediate frame holds the connections to jigs and tools.
IMA	1	ADS	1.5x1.2m base 1.2 m h	Appositely design for the integration of glass slumped plates into XOU's

3.3 Aim of the present research

In the context of the above described project, the Petal structure and Optical Bench can be implemented base-lining state of the art technology, whereas the main technology demonstrations address the mirror modules. The research work presented in this dissertation fits in this area. The PhD-activities has been mainly dedicated to the first step of the feasibility demonstration of the proposed approach, as shown in the summary diagram on Fig. 3.7. The author's work has been mainly dedicated to the assessment and development of the slumping technology for the realization of IXO mirror plate able to deliver the necessary requirements both in terms of shape and surface finishing. In particular, she deeply analyzed the slumping process to individuate the main parameters and their influence on the final product. This has been achieved through the realization of slumping experiments and analysis of the taken measurements, as presented in the following of the test.

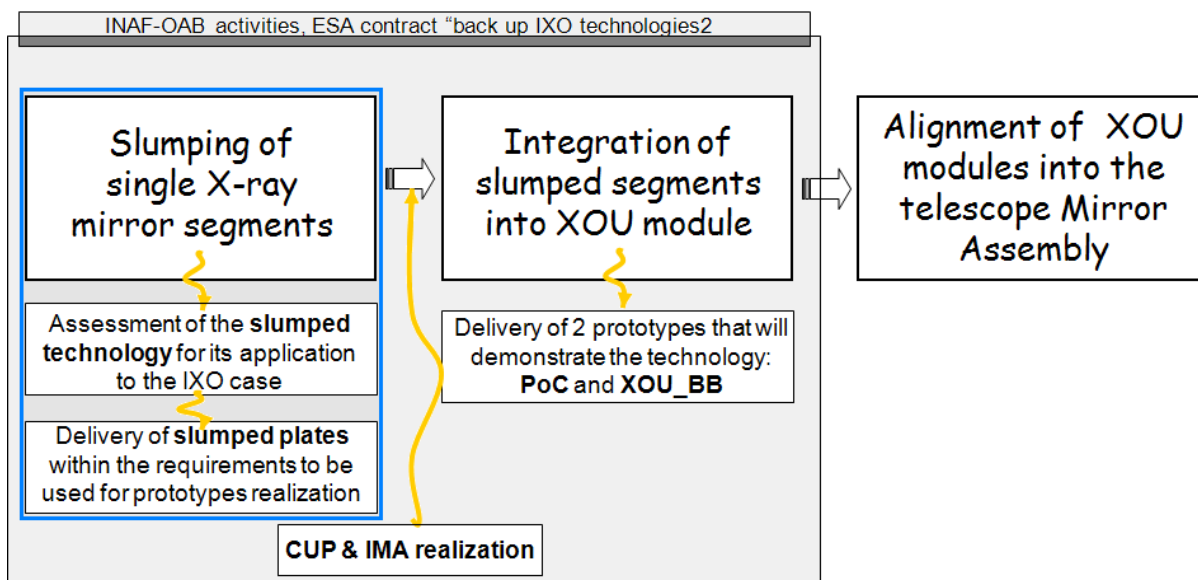


Fig. 3.7: Flow of production of IXO X-ray optic: single slumped plates are integrated to compose X-ray optical modules; a number of XOU are aligned to realize the entire telescope. In the grey box, all the activities carried out by INAF-OAB during this project are highlighted. Those represent the main steps to be developed in order to reach a TRL of 5. The alignment of single XOU into the mirror assembly is based on state of the art technology and no further improvements are required. The blue box highlights the contribution of the author to this project.

4 The slumping technology for making mirrors

The slumping technology is a technique that allows shaping a sheet of glass by applying a suitable thermal cycle. It can be considered for the manufacturing of glass optical components, i.e. lens and mirrors. It foresees the application of a thermal treatment inside an oven to a glass sheet lying over a mould having the desired shape; at high temperature, usually between the annealing point and the softening point of the glass, its viscosity is such that it slumps against the mould, replicating its shape within certain accuracies. Different combinations of mould materials and glass types can be considered to be employed in the slumping technique, in dependence on the requirements for the final application. Depending on the specific process procedure, two main families of slumping approaches exist: the direct slumping, in which the optical side of the mirror being produced is in contact with the mould surface, and the opposite indirect approach.

In this chapter, the basic concepts of the slumping technology are described, together with the main process parameters and the state of the art of its use in the field of X-ray astronomical mirrors production. Particular attention is reserved to the hot slumping approach followed during the PhD activities.

4.1 Slumping technology basic concepts

In the field of glass item production, the word slumping refers to techniques used to thermally form glass by applying heat: the decrease in viscosity, due to the applied heat, causes the glass to change its shape under the force of gravity (or other additionally applied force) and replicate that of a mould. The basic idea of the process is indeed simple: the glass, in the form of a sheet, is positioned onto or into a mould, with a desired shape, inside an oven. At the point where the glass becomes plastic, the force of gravity deforms it in dependence of the used mould or support form. Once the glass has achieved the desired shape, the heating is stopped and the temperature reduced to prevent further movement. The temperature is then stabilized at the glass annealing point to allow the relaxation of stresses inside the glass, if any (see § 4.4 for more details on annealing temperature and other characteristic temperatures of the glass). The process has long been used in the past for the production of open vessels, such as bowls and plates. The modern application derives from the

principle used in recent past (until the beginning of 19th century) to obtain a flat glass sheet starting from a cut blow cylinder¹¹ [89]. Nowadays, thanks to the invention of more reliable methods for the production of glass sheet, such as the float process¹² [90], the opposite process is widely utilized: a flat sheet of glass is bent laying it over a mould in a heated oven. Two main methods exist: the press-bending or the sag-bending, differing in the application of an additional force rather than solely gravity to shape the glass. These approaches are commonly used for the production of glass elements for architecture (like windows and doors) furnish elements (like basin, mirrors, hood, design elements), items for the automotive, marine, aviation industry (like windscreen or rear-view mirrors), and medical instrumentations. Since more than 30 years, it is in use in the green energy field for the production of solar thermal collectors employed in Concentrating Solar Power (CSP) plants¹³. Such systems mainly consist of concave parabolic mirrors with diameters from 3 to 25 meters (segmented systems) and are predominantly achieved via sag-bending. The method guarantees precision and optical quality acceptable for solar mirrors, whose current standard specifications for focus deviation is set to 8 mm or less, translating in a shape precision of few microns [91]. The application of this industrial well-known bending process to the astronomical field is not straightforward and necessitates optimization and development activities since the requirements in terms of shape and surface finishing accuracy of the final product are more rigorous. Nevertheless, some successful example exist: accurate parabolic mirror to image to a ring the light generated by the Cherenkov radiation have been manufactured in late 1980s by heat forming warm glass against moulds [92]; other application employed the slumping technique as the first step for shaping the mirror, followed by traditional grinding and polishing steps. The situation becomes even more demanding when referring to the field of X-ray optics, for which the mirrors can accept shape error of only fractions of microns with respect to the theoretical profile, and surface micro-roughness of fraction of nanometers. Since 10-15 years, the slumping technique is being evaluated for the production of X-ray telescopes reaching so far promising results, as later reported. A step forward is still necessary for the next generation X-ray telescopes that will combine large collecting area with high image angular resolution and low system mass. Table 4.1 summarized typical accuracy requirements in terms of shape and surface finishing for several applications of the slumping technology and immediately provides the feeling of the challenge that researchers and producers

¹¹ The cut blow cylinder was a method for the production of flat glass panel for windows: sheets of glass were made in the form of thin, walled, hollow cylinders, swinging a molten glass mass in a cylindrical trench. The glass was then allowed to cool before cutting and open out the cylinder, which was then re-heated and allowed to uncurl until it lied out flat on an iron plate.

¹² The float process, invented by Sir Pilkington in the 1950s, allows the realization of sheet of glass with uniform thickness and very flat surface by floating molten glass on a bed of molten metal, such us tin.

¹³ Solar thermal collectors, also known as parabolic panels or solar mirrors, are installed on the ground to reflect the solar energy towards tanks of water. The water heats up and produces steam, which turns turbines and generates electricity.

have to face before the slumping technology can be employed for the production of next generation X-ray optics.



Fig. 4.1: Example of nowadays utilization of curved glass and of the industrial slumping process to realize them.



Fig. 4.2: Example of solar thermal application of thermally bent glass sheets (Credits: Flabeg).

Table 4.1: Typical requirements, in terms of shape and surface finishing, of few traditional applications in which the slumping technology is employed. It is clear how the adoption of this technique for the production of X-ray optics cannot be straightforward but rather necessitates research and development activities.

Application	Shape accuracy requirements	Surface finishing quality
Decorative elements	Few mm	Visually smooth and free of bubbles and defects
Furnish elements	Fraction of mm	Visually smooth and free of bubbles and defects
Architecture elements	Fraction of mm	Visually smooth and free of bubbles and defects
Optical blanks	Few mm	Visually smooth and free of bubbles and defects
Solar industry	Few tens of μm	Smooth at nm level (average around 1 nm)
Cherenkov mirror	Fraction of mm	Smooth at nm level (average below 1 nm)
AO mirrors	Few μm	Smooth at nm level (average below 1 nm)
X-ray mirrors	Fraction of μm	Smooth at sub-nm level (average below 1 nm)

Many parameters have to be considered and analyzed to further develop the technology in order to meet the demanding requirements of X-ray mirrors. A precise and reliable production process able to deliver the necessary accuracies can be set only after an optimization work, including:

- Selection of the slumping approach to be followed;
- Selection of the materials, both for the mould and for the glass;
- Selection of the thermal cycle to be applied;
- Definition of the complete process procedures, taking into account all the necessary steps (including for example glass cutting, cleaning of all elements, assembly, alignment, integration, and handling).

These points are analyzed in the following sections of this chapter, mainly considering the application of the technology for the production of next generation X-ray segmented optics. It is worth noting that the basic theory and methods of the slumping technique are the same independently from the final application of the slumped item. Also if not explicitly considered in this work, other applications exist that can take advantage from this technology and many results of this study are applicable also to them with only minor adjustments.

4.2 Different slumping approaches

Depending on the specific process procedure, two main families of slumping approaches exist: the direct slumping and the indirect one. The direct slumping approach is characterized by the fact that the optical surface of the mirror being produced is the side of the glass sheet that comes in contact with the mould during the process. In this case, it is possible to consider or not the application of additional external forces to oblige the glass in full contact with the mould. If no force is applied, the glass slumps on the mould only because of its own weight, which is by gravity. In the indirect slumping, the optical surface of the mirror plate is the non-contact side of the glass. In this case, to enhance the contact between the glass and the mould, one possible solution might be the elimination of the air gap between the glass and the mould through vacuum suction. One third family of approaches can be considered, consisting in a mixing of the first two: the slumping realized with two moulds having complementary shapes and pressed one against the other to form the glass sheet in between them. All these approaches are nowadays under assessment by several groups in the world to develop a reliable and cheap method for the production of X-ray mirrors. In particular:

- A hot direct slumping approach with pressure is under assessment at the Astronomical Observatory of Brera (INAF-OAB), in Italy;

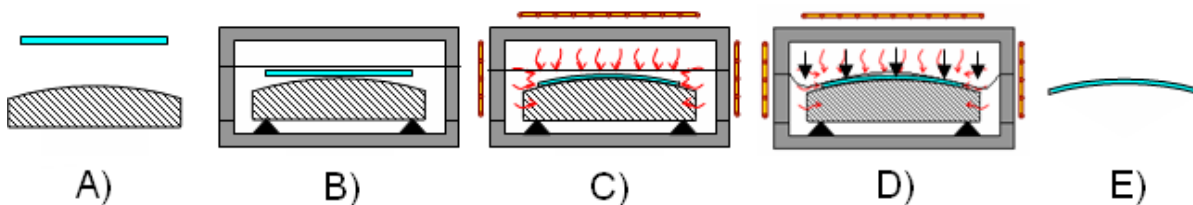
- A direct slumping approach with no pressure is under assessment by NASA-Goddard and the Columbia University, in USA;
- An indirect slumping approach is under assessment at Max-Planck-Institut für Extraterrestrische physic (MPE), in Germany;
- A hybrid slumping approach is under assessment at the Academy of science of Prague, in Czech Republic.

All these approaches are described in the following paragraphs and a comparison chart is provided on page 79.

4.2.1 The hot direct slumping with pressure at INAF-OAB, Italy

For the realization of IXO X-ray mirror segments, the Astronomical Observatory of Brera, in Italy, is developing a direct slumping approach that employs the active application of pressure to help the glass-mould contact. The institute know-how dates back to 2003: at the beginning only conceptually [94] and then also experimentally after the installation of the first oven in the laboratory [95]. In 2005 a project started to investigate the application of the slumping technique for the manufacturing of thin glass mirror for adaptive optics. The study was part of the OPTICON activities financed by the FP6 of the European Community and fit inside the international effort dedicated to the design of E-ELT [96]. The work was meant at the realization of a 500 mm diameter spherical mirror having thickness of 1.7 mm and radius of curvature of 5 m. It was based on glass Schott Borofloat 33 and mould in Zerodur K20 material. The project finished in early 2009, with very good and high-potentiality results: the shape of the mould has been replicated with an accuracy of 3 micron [97]. The technique is under further investigation for the realization of lightweight optics by applying the so called “cold slumping phase”, which foresees the shaping of thin sheets of glass at Room Temperature [98], [99]. In practice, the glass is forced through vacuum suction to adhere to the shape of a mould at Room Temperature taking advantage of its field of plastic deformation, however small. Stiffening structures might then be applied on the back side of the glass, freezing it in the current shape. At the vacuum and mould removal, the glass elastic energy stored during the previous phase tends to restore the original shape of the glass (a phenomenon named spring-back effect) but the stiffening structure opposes to that. At the end of the process the result is a mirror that has been shaped at Room Temperature, has the same shape of the adopted mould (apart of spring back effects) and contains stresses: the two last parameters can be controlled by acting on the process procedure to keep them at a low acceptable level. Throughout these projects, INAF-OAB had the opportunity to develop a relevant know how on the slumping technology and the issue that must be

taken into account to obtain good results. The logical subsequent step was to propose the application of the technology in the X-ray telescopes production, a field in which the institute possess a profound expertise dated back to the '80s with the realization of Beppo Sax telescope, followed by XMM_Newton and Swift XRT [100]. This is a very challenging task INAF-OAB has to face because of the severe requirements of X-ray optics that requires a 3X improvements with respect to the results obtained so far in the slumping technique. The gained experience allowed individuating a slumping procedure, whose main steps are sketched in Fig. 4.3. The glass sheets are procured on the market. A mould is specifically realized with the wanted shape and surface finishing. Then, after a characterization phase to check their properties, they undergo a deep cleaning step in a clean environment. The glass is then positioned over the mould and the thermal cycle can start with the appropriately set parameters. At high temperature, a force is applied to help the glass better replicate the shape of the mould, which it is in contact with. To have the possibility of applying pressure, the overall process takes place inside a stainless steel muffle, composed by a bottom part with a top lid. By inserting a very thin stainless steel sheet acting as a membrane between them, it is possible to separate the internal volume in two cavities so to have the possibility to obtain pressure difference. At the end of the thermal cycle, the slumped segment is removed from the mould and characterized, both in terms of shape and micro-roughness, to check the process results. After that, it is ready to be integrated in the optical system structure.



A) The mould is figured with the required shape and micro-roughness and treated in such a way to help the detachment of the glass at the end of the slumping process; thin glass sheets are procured from the market. **B)** The glass foil is placed above the mould in a stainless steel muffle where controlled atmosphere can be established. **C)** The thermal cycle is started. **D)** Once reached and maintained the maximum T of the cycle, a uniform pressure is applied on the plate, in order to constrain it against the mould. **E)** After the cooling of the oven, the slumped glass segment is released and it is ready to be characterized and integrated in the suitable structure.

Fig. 4.3: Schematic sketch and description of the main steps of the direct slumping technology with pressure under development at INAF-OAB.

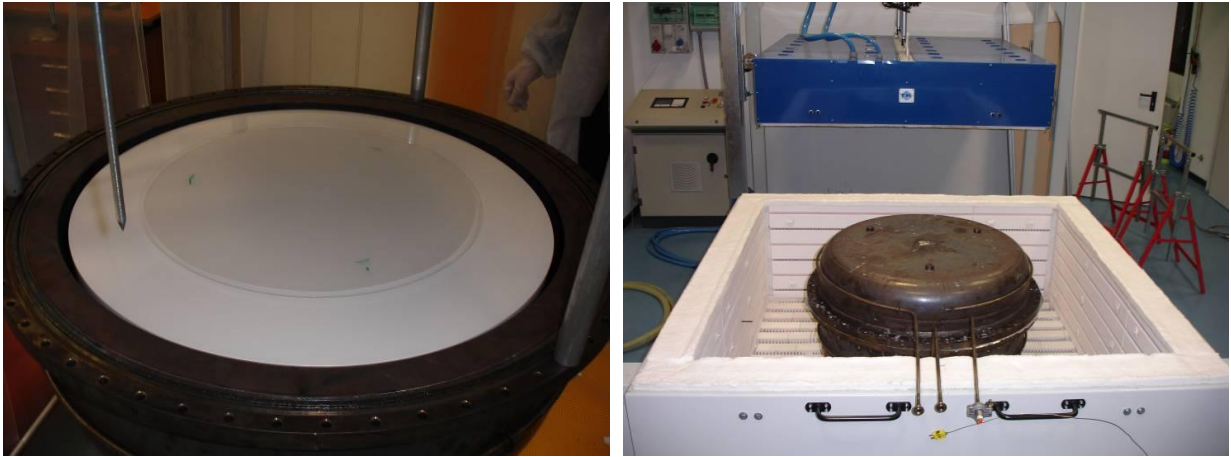


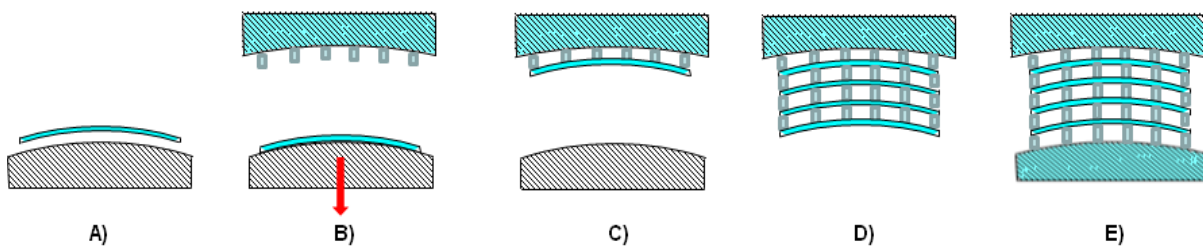
Fig. 4.4: Pictures showing the realization of the slumping process during the OPTICON activities financed by the FP6 of the European Community in the international contest of the E-ELT. This research allowed INAF-OAB to gain a valuable experience in the field of slumping technology.

The application of past know-how to the IXO case requires further improvements: Table 4.2 reports on the variation, with respect to the previous obtained results, necessary for the application of the slumping technology to the case of X-ray optics: they become the goal of the research. Notice that the goal in terms of shape was split in two different requirements, intended to be dependent on the results of the integration step. It is in fact of no meaning to slump a perfect glass plate if then there is no capability of integrating it free of stresses and deformations. For this reason, since the beginning, the slumping technology was considered as the close connection of the shaping phase plus the integration one. The objective in terms of shape was then split: the thermal slumping process should be able to guarantee the replication of the mould shape within an accuracy of few microns if the integration is able to confer the plates a further final cold shaping; or the thermal process should guarantee the replication of mould shape within sub-micron accuracy in case no correction can be realized during integration. The first possibility is of course to be preferred since it allows the relaxation of slumping mould procurement requirements and also a thermal process in principle easier that is to say cheaper. However, at the beginning of the project no information was available on the capability correction of the integration procedures and so the two cases had to be taken into account. For this reason the requirements on mould procurements were as good as they would have been if the shape replication had to be good at a sub-micron level (see chapter § 5). Regarding the requirements on the maintenance of the original micro-roughness of the glass, it was dictated by the consideration that the glass surface is in general as good as necessary to reflect X-ray. If it can be maintained during the process independently from the mould surface finishing, this allow procuring the slumping mould in a faster and easier way, giving also the possibility to consider as candidate mould materials the ones which could not be super-polished.

Table 4.2: The past INAF-OAB experience on the slumping technology needed to be assessed and improved for the new requirements posed by its application to the case of X-ray mirrors.

	Past experience	New goals
Shape	Replication of mould shape with 3 μm accuracy	Replication of mould shape with sub- μm accuracy or Replication of mould shape with few μm accuracy (in case the correction capability of integration is demonstrated)
Roughness	Replication of mould roughness	Maintenance of the glass original roughness

The integration method under development is based on the stacking of single slumped plates through the use of glued ribs between them, i.e. glass spacer that maintain the segments in their nominal relative position. A sketch of this approach is depicted in Fig. 4.5: the slumped foil is positioned on the integration mould and vacuum suction is applied in order for it to assume, via elastic deformation, the exact shape of the mould; during this step residual errors shape eventually present in the slumped foils after slumping are corrected. Glass ribs are glued on the slumped foil while the vacuum is maintained. The bonded connection partially freeze the correction that is maintained, except for spring back deformations related to the release of the elastic energy stored in the foil, also after the vacuum and integration mould removal, once the glue is cured. These steps are repeated several times in order to form the stack composing the XOUs. The stack is finally closed with a second plate to give rigidity to the elemental monolithic structure.



A) The slumped glass is positioned on the integration mould. **B)** Vacuum suction is applied to force the glass assuming the shape of the integration mould through elastic deformation. **C)** The plate is then glued through glass ribs to the stiffening back plate freezing it with the shape of integration mould (except for spring back effects that arise when vacuum suction is released). **D)** These steps are repeated for each plate of the stack. **E)** A second back plate closes the elemental X-ray Optical Unit, creating a stiff monolithic structure.

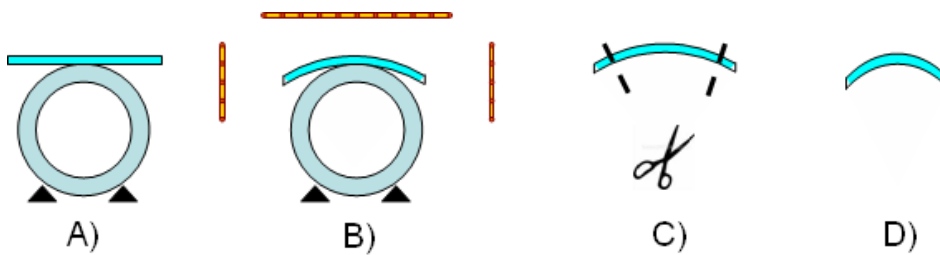
Fig. 4.5: Schematic representation of the adopted integration procedure that allow the correction of eventual residual errors in the slumped plates. It makes use of a precisely figured integration mould, glass spacers called ribs, and stiffening structures called back-plates.

The integration steps will be realized with ad-hoc designed Integration Machine (IMA) [101], under development at the time of writing. It makes use of specific integration moulds (different from those used for the slumping) precisely figured with the Wolter I shape required by the optical design (see § 5.2.3.2 for a detailed explanation). The most important assumption in the proposed integration concept is that the glass plate assumes the shape of the integration mould when vacuum suction is applied. This was demonstrated during phase one of the study (see § 6.2.4.2 for details). It is worth noting that this approach to mounting is completely innovative with respect to the traditional ones that rely on holding the individual X-ray mirror elements in a limited number of points, usually concentrated on the edges of the shells. This solution, instead, is more similar to the case of SPO, whose stacking structure is intrinsically very stiff and robust since based on a stronger inter-linkage between the mirrors plates. Also in the proposed integration approach for the slumped mirrors foils the same happens: individual mirror plates are connected to each other to form a stack structure in which the optical elements are given stiffness in the critical longitudinal direction parallel to the optical axis through the gluing of structural ribs. A further improvement with respect to the SPO mounting lies in the idea of mounting every couple together in the same time while checking the mutual alignment of the Plate Pair itself with respect to a fix reference (the XOU back plate). In this way errors are not accumulated during the integration, as it would be in the case the preceding integrated plates will serve as reference for the integration of the subsequent one, and the two plates mutual alignment is kept under control. The situation is different than the case of SPO mounting, in which two stacks (one for the cone-parabola and one for the cone-hyperbola side) are mounted separately and then assembled together by minimizing focal distortions [102].

4.2.2 The direct slumping at NASA-Goddard and Columbia University, USA

American researchers, mainly concentrated at NASA/Goddard Space Flight center and Centre for Astrophysics (CfA), with the collaboration of several Universities, are working since several years on the development of a slumping technology for the production of glass X-ray optics to be employed for next generation missions, such as IXO (formerly Constellation-X) [103] or Gen-X [104]. They employ a direct slumping approach in which the glass sheet slumps over the desired mould with the only action of gravity. The current considered dimensions for the segments are around 200 mm x 200 mm, with a thickness of 0.4 mm and Radius Of Curvature comprising in the range from few tens of centimeters up to one meter and an half. Their experience and know-how in this field dates back to late 1990s, when at California Institute of Technology they started investigating a new technique for the production of thin glass mirrors for hard X-ray focusing optics [105]. They came up with the launch of the balloon-mission HEFT (High-Energy Focusing Telescope) in 2005 [106]. Based on the

gained knowledge, a new hard X-ray space-mission, called NuSTAR, is presently under construction at the Columbia University, [107]. It mounts on board two X-ray telescopes realized with glass segments slumped at NASA's Goddard Space Flight Center in Greenbelt; the launch is presently planned for 2012. The current achieved accuracy in terms of X-ray imaging resolution is around an HEW value of 45-60 arcsec [108] far from IXO requirement of $\text{HEW} \leq 5$ arcsec; present researches are moving in the direction of improving slumping angular resolution. A sketch of this slumping approach is shown in Fig. 4.6 American researchers make use of close tube-like moulds (or half of it) with the external surface machined at the wanted Wolter I shape. During the slumping, the glass lies down on the mould for the only action of gravity. No additional forces are applied to help the glass-mould contact. At the end of the process the edges part of the glass are cut away to eliminate areas of not good contact or wrapped areas coming from thermal effects [109].



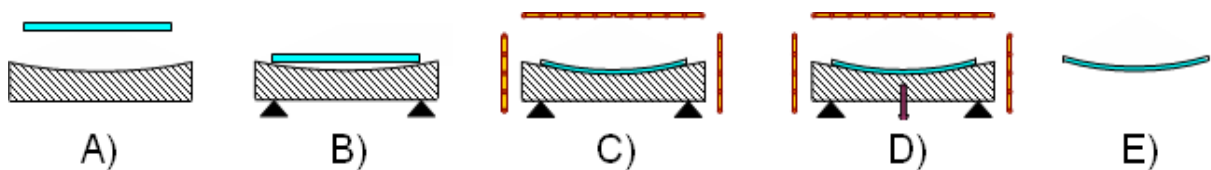
A) The mould is figured with the required shape and micro-roughness and treated in such a way to help the detachment of the glass at the end of the slumping; thin glass sheets are procured from the market. **B)** The glass foil is placed above the mould directly inside the oven where controlled atmosphere can be established and the thermal cycle is started. **C)** Once the slumping process is terminated, edges of the glass that didn't come in contact with the mould are cut away by means of a suitable cutting procedure that does not introduced defects or distortions in the plate. **D)** The slumped glass, released from the mould and cut at its edges is then ready to be characterized and integrated in the suitable structure.

Fig. 4.6: Schematic sketch and description of the main steps of the direct slumping technology under development at NASA-Goddard.

The American researchers are working on integration concepts based on single sustaining points at the glass edges areas. By gluing the glass edges in pre-computed positions to the structure, they demonstrated the capability of over-constrain the mirror segments without distorting their optical figure. The slumped plate is bond at 6 locations to a strong-back and in this way the flexible mirror segment is effectively converted into a rigid body that can be positioned and oriented using traditional alignment equipment and facilities. It is worth noting that this method is more similar to the traditional once and does not allow the slumped plate shape correction during integration [110].

4.2.3 The Indirect slumping at MPE, Germany

The Max-Planck-Institut für Extraterrestrische Physik (MPE), in Germany, is developing the indirect slumping technique, which involves the slumping of the glass sheets into a concave mould. The resulting optical surface is the surface not in contact with the mould so this method is not sensitive (even in principle) to the micro roughness of the mould surface; high frequency irregularities are damped by a factor of around 10 with the currently used glass thickness (0.4mm). No pressure is applied to get the glass in full contact with the mould, however due to the possible inclusion of air in the central part between the glass and the mould if the glass edges slump down first, a hole is needed in the center of the mould to enable the air to escape. This can be supported by a vacuum pump connected with the central hole of the mould, to ensure proper air escape and full contact of the glass with the mould surface. Thickness variations in the starting glass foil might affect the final figure of the optical surface; therefore an eventual phase of grinding and polishing to high quality might be required in order to ensure uniform thickness (less than 0.5-1 micron on large scales). The institute knowhow in this field dates back in time to 2005 when they started to assess the slumping technology for X-ray mirror production [111], [112]. Currently, they obtained some improvements and researches are still on-going to further enhance the performances of their process, not yet compliant with the requirements for the production of future X-ray telescopes [113]. A sketch of this slumping approach is shown in Fig. 4.7. No detailed study has been conducted by MPE on the integration of single slumped plates on the telescope structure.

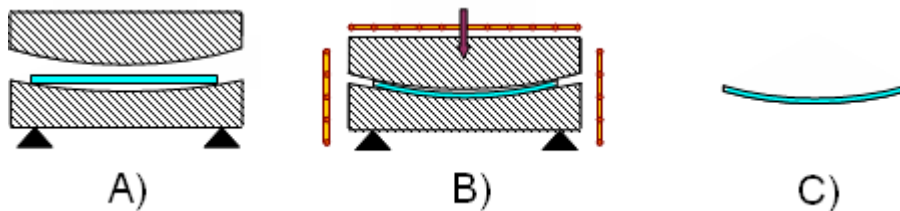


A) The mould is figured with the required shape and micro-roughness and treated in such a way to help the detachment of the glass at the end of the slumping; thin glass sheets are procured from the market. **B)** The glass foil is placed above the mould directly inside the oven. **C)** The thermal cycle is started. **D)** Once reached and maintained the maximum T of the cycle, vacuum suction can be applied through a hole in the center of the mould, which enables eventual air between the glass and the mould to escape. **E)** After the cooling of the oven, the slumped glass segment is released and it is ready to be characterized and integrated in the suitable structure.

Fig. 4.7: Schematic sketch and description of the main steps of the indirect slumping technology under development at MPE.

4.2.4 The hybrid slumping approach at the Academy of Science of Prague, Czech Republic

The Academy of Sciences of the Czech Republic, together with industrial partners located near Prague, is currently developing a thermal glass forming approach different from the others [114]. Together with the traditional direct and indirect one, they are investigating a hybrid approach, based on the use of two complementary moulds and on innovative materials [115]. Up to date, they obtained encouraging results (1 micron of process repeatability [115p]) and are actually working to further improve them, since also this approach does not present yet the necessary performance required for the production of next generation X-ray telescopes. A sketch of this slumping approach is shown in Fig. 4.8. No detailed study has been presented on the integration of slumped plates in the IXO mirror assembly by the Czech colleagues.

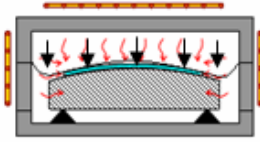
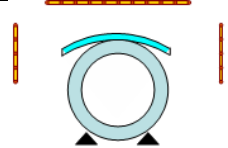
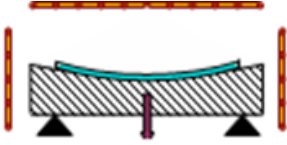
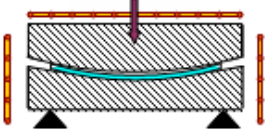


A) Two complementary moulds are figured with the required shape and micro-roughness. **B)** The glass foil is placed between them inside the oven and the thermal cycle is started. At some point during the thermal cycle the two moulds are pressed one against the other, forming the glass in between them. **C)** After the cooling of the oven, the slumped glass segment is released and it is ready to be characterized and integrated in the suitable structure.

Fig. 4.8: Schematic sketch and description of the main steps of the hybrid slumping approach under development in Czech Republic.

All the possible slumping approaches present advantages and drawbacks that need to be assessed before selecting the most reliable one for the production of future high resolution X-ray telescopes; they are summarized in the following table 4.2. Whatever the followed approach is, the nowadays state of the art of the slumping technology requires further development before meeting the requirements of future X-ray optics. All the efforts put in the slumping technology development are justified by the overall advantages that it offers, summarized in Table 4.2. The advantage of this technology is to be a replication process and so one single mould can be used several times to realize a number of equal optical elements, starting from commercially available glass materials. It also offers the advantage of directly machine with high accuracy only the mould, which is stiffer than the glass foils whose thickness is in general of the order of few mm, making it floppy and subject to deformations, hence difficult to machine with conventional contact techniques.

Table 4.3: Comparison between the different slumping approaches.

	Pro	Cons
	<ul style="list-style-type: none"> - No influence of the glass thickness inhomogeneity - The application of p guarantee the full glass-mould contact, preventing mid-frequencies deformations - The proposed integration approach allows for corrections 	<ul style="list-style-type: none"> - In principle the mould should be superpolished* - Relatively complicated set up - No possibility of visual inspection during the thermal cycle
	<ul style="list-style-type: none"> - Easy experiment set up 	<ul style="list-style-type: none"> - Necessity to cut the edges area that might suffer for not good contact - The proposed integration does not allow for corrections
	<ul style="list-style-type: none"> - Easy experiment set up - No need of superpolished mould - Possibility of visual inspection during the thermal cycle 	<ul style="list-style-type: none"> - Optical surface affected by thickness inhomogeneity (potential need of pre-polishing the glass to eliminate them before slumping)
	<ul style="list-style-type: none"> - Symmetry in the glass thermal conditions 	<ul style="list-style-type: none"> - Need of two coupled super-polished moulds - No possibility of visual inspection during the thermal cycle

* See later how the results of this study allowed relaxing this requirement.

Table 4.4: Main advantages of the slumping technology in general.

BEING A REPLICATION PROCESS	One single mould allows for the manufacturing of several equal optical elements
BEING CHEAPER THAN DIRECT TECHNIQUES	Only the mould needs to be directly figured and polished with high accuracy, while the final products derive from cheap market available glasses ¹⁴
REDUCTION OF PRODUCTION RISKS	If a slumping run experience some problems, only one glass foil and the work of few days is lost
EASINESS OF INDUSTRIALIZATION	Once the technology is validated, several industrial line can work in parallel

¹⁴ It is estimated that a slumping run costs around 200 euro, comprising the glass, the oven electrical consumption, the laboratory consumable for the process preparation (e.g. cleaning and handling). Only the cost of mould procurement is not considered here, however counting that a single mould can be employed for the production of a number of equal segments, the comparison with direct machining techniques is anyway winning.

4.3 Mould and glass properties to consider during material selection

Different materials might be considered for the production of the slumping mould, taking in mind at first its primary requirement to be able to withstand repeated thermal cycles without shape modification. Considering the selection of material for the realization of the integration mould, the situation is easier because it has not to withstand repeated thermal cycles at high temperatures: from this point of view more materials could be considered, such as for example Aluminum or porous ceramics. This section refers only to the case of slumping moulds. Several types of glasses are available on the market and their selection is mainly based on their characteristic temperatures. An initial comparison of the theoretical thermo-mechanical parameters of suitable materials for the mould and the glass is useful. The mechanical properties of the glass itself are twofold important: they are important to evaluate the behavior of the glass sheet during the process, but also to assess its performances in the final application. At this regards, it is essential to consider that glass properties might change after the slumping process due to the applied thermal cycle¹⁵. Table 4.5 reports the several parameters that have to be considered during the material selection process [116].

Table 4.5: Important parameters that need to be considered during the selection of the material for the mould and for the glass to be employed in a process of slumping. Notice that few of them are temperature dependent and also this dependency should be considered during the selection.

Mechanical	Physical	Structural	Fabrication	General
Young's modulus (T)	CTE (T)	Voids, inclusions	Machinability	Availability
Hardness (T)	CTE homogeneity	High T stability	Polishability	Scalability
	Thermal cond. (T)		Optical roughness	Mould cost
	Density		Mould character.	
	Glass adhesion (T)			
	Transparency			

It is important to take into account the dependence on temperature of some of the listed properties. A good choice of materials can be performed only considering the couple of glass and mould materials and the matching of their characteristics, mainly their thermal and chemical properties. Furthermore, the choice of material requires also general consideration, not strictly technical but anyway part of the entire process control, such as for example the availability of the material or its

¹⁵ Normally, market-available glasses have a superficial layer of compressive stresses, introduced through physical or chemical tempering to enhance their strength. The application of a thermal cycle might have influence on this pre-existent status of compressive stresses, causing a change in the glass strength (see chapter § 5 for further details).

costs. Taking in mind the importance of the couples, the main parameters listed in Table 4.5 are hereafter commented.

- **Coefficient of Thermal Expansion (CTE):** the more the mould CTE is equal to the glass CTE, the better it is. The linear Coefficient of Thermal Expansion expresses the relative change in linear dimension (elongation or shrinkage) experienced due to a unit variation in temperature. For the selection of materials to be utilized during the slumping, this parameter is not important separately for the mould and the glass but has to be considered in conjunction: ideally the best condition is to exactly match the two CTE. In this way the couple of material will expand and shrink together during the thermal cycle. If there is a mismatch in the two CTE, the slumped glass will experience in the end a change of Radius Of Curvature with respect to that of the mould [117]. This problem can be overcome by manufacturing the mould with a radius tailored to compensate the pre-computed change [118]. The homogeneity of CTE is also very important not to have random local deformations on the final mirror. When comparing two CTE values, attention has to be paid to the range of temperature in which they are evaluated; due to the dependence of the Coefficient of linear Thermal Expansion on temperature, two average linear CTE are usually given for the temperature range from -30°C to $+70^{\circ}\text{C}$ (normally listed as the relevant information for Room Temperature, RT) and for the range from RT (20°C) to $+300^{\circ}\text{C}$ (the last one is usually intended as the standard international value for comparison purposes and for orientation during melting processes and temperature change loading). A typical curve of the linear thermal expansion of glasses begins at an absolute zero point, with an obvious increase in slope to approximately Room Temperature. Then a nearly linear increase to the beginning of the noticeable plastic behavior follows. The transformation range is distinguished by a distinct bending of the expansion curve, which results from the increasing structural movement in the glass. Above this range the expansion again exhibits a nearly linear increase, but with a noticeably greater rate of increase. The curve is adopted to define characteristic temperatures for the particular glass as later reported in Fig. 4.11. Notice that this behavior is of particular relevance for the glass whose CTE changes in the range of T of relevance for the slumping. The abovementioned behavior is not usually encountered in the mould materials that show higher working T and high stability with temperature. Ideally, the best selection of mould and glass material is the one with the higher matching of the CTE curve in the temperature range interested by the process. This data are however difficult to be found in literature and need ad-hoc tests campaign for their evaluation.

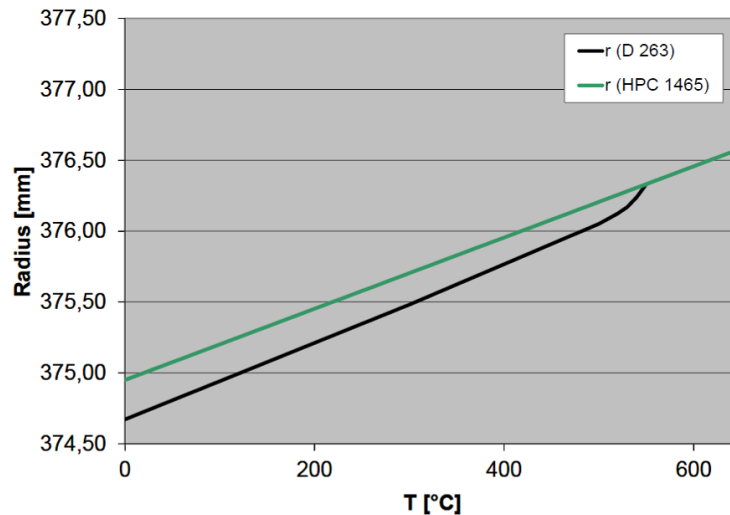


Fig. 4.9: Example of changes in radius of curvature between the mould and the slumped glass for the particular case of glass D263 ($CTE = 7.2 \times 10^{-6}/K$) and a High Porous Ceramic mould (with $CTE = 7 \times 10^{-6}/K$). The mould can be produced with a shape computed to take into account this effect. (Image credits by MPE).

- **Thermal conductivity:** the higher, the better. The thermal conductivity defines the material's ability to conduct heat. It is the quotient obtained dividing the heat quantity transferred through a unit area in a unit time, by the temperature difference per unit distance, and it is normally given in $W / (m \cdot K)$. It expresses the capability of the materials to quickly follow the temperature changes during the thermal cycle and reach a uniform temperatures distribution avoiding detrimental thermal gradients that might create stresses in the glass. If the selected materials present low thermal conductivity, longer thermal cycles should be employed to allow the necessary time required to have uniform temperatures distribution (meaning that the process is more time-consuming and expensive).

- **Glass adhesion:** it is important to take in mind that during the slumping process, at high temperatures, chemical reaction might happen between the two materials, which cause the glass sticking on the mould. The fact requires the application of a suitable antisticking or release layer between the mould and the glass surface; most of the time it is selected from empirical experimentation. In principle three possibilities exist: 1) apply the antisticking layer on the mould; in this case the application should be performed only once at the beginning of the operational life of the mould and the layer should need to sustain repeated thermal cycle without degradation; 2) apply the antisticking layer on the glass: in this case the layer could act also as reflective layer on the produced slumped mirror, hence it would need a high quality in terms of roughness; 3) apply the antisticking layer in between them: in this case the operation should need to be repeated at every cycle and the glass would have to be coated with reflective layer after the slumping.

- **Optical surfaces microroughness:** since the glass will finally become an X-ray mirror, its microroughness (defined as the glass topography, or surface finishing, at microscopic level) has to be very low. Glass sheets available on the market respect in general the requirement. It is important to set properly the parameters of the process so to avoid any degradation of the original microroughness of the glass. In principle, it is not strictly required that also the microroughness of the mould is as good as those needed for the mirror. However, in the case of direct slumping approach (with the optical surface of the glass in contact with the surface of the mould) the surface finishing of the mould is potentially important, since the microroughness of the mould could be partially transferred onto the slumped segments in dependence on which process parameters are set [119].

- **Maximum application temperature:** the lower the better, for what concern the glass material; the higher the better for what concern the mould material. The maximum temperature of the slumping thermal cycle depends on the type of glass selected for the process. A glass with low characteristic temperatures is preferable since it allows a shorter and easier (hence cheaper) process. Of course the material selected for the mould has to withstand at least the slumping temperature for the time required for the cycle. If its operational temperature is higher, it is even better since a major stability over repeated thermal cycles can be attended.

- **Elastic modulus:** the higher the better, considering the mould material, to limit the deformation that the mould will experience when laid on the supports in the oven. However, this does not represent a fundamental property since low values can be overpassed by a suitable mechanical design of the mould. The characteristic is much more important with regards to the glass since its value is one of the properties that guide the structural design of the final telescope. Attention should however be paid to the fact that the significant value is not the one stated in the glass datasheet but the one measured in the glass after it undergone the slumping thermal cycle. This value is not reported in literature and suitable test campaigns have to be conducted for its evaluation.

- **Knoop Hardness:** the hardness of the materials gives indication on the probability of scratch the surfaces during the handling, cleaning and all the other steps of the process. From this point of view, the higher the better. Anyway, referring to the mould material, it has to be considered that in general the grinding and polishing of hard surfaces is very costly because it requires long times.

- **Void, inclusions:** the less the better. Mould and glass must be made by homogeneous material with no bubbles or inclusions that might cause anomalous and not repeatable behaviour during the process.

- **Thickness variation:** the lower, the best. This parameter clearly refers only to the glass and is important because of its possible impact on the optical performances of the slumped mirror. The problem is of interest mainly in the case of indirect slumping approach since during the direct approach, all the thickness inconstancies are transferred on the back side of the mirror with no impact on its optical performances. The criticality can be overcome by pre-polishing both sides of the glass sheets before slumping it, increasing however costs and production time [spie-ultimo-teseschi].

4.4 Slumping thermal cycle parameters

The selection of the optimum thermal cycle is fundamental to obtain good slumping results that meet the requirements. It is of course strictly related to the couple of materials selected, and in particular to the glass, whose characteristic temperatures guide the maximum temperature of the thermal cycle [120], [121], [122]. The best thermal cycle is the one optimized to reach the wanted results in the fastest and cheapest way. Generally speaking, it always includes a number of ramps (increasing and decreasing in temperature) and plateaus at which the temperature is maintained constant. The heating can be relatively fast up to the required slumping temperature: then a holding time ensures that no detrimental temperature gradients are present and the glass has time to slump against the mould. The cooling down is done slowly to give the glass the possibility to reach the annealing point without internal stresses, since below this point the glass is no longer able to relax them. Fig. 4.10 shows an example of slumping thermal cycle, while Table 4.6 supply the definitions related to important phases of the process.

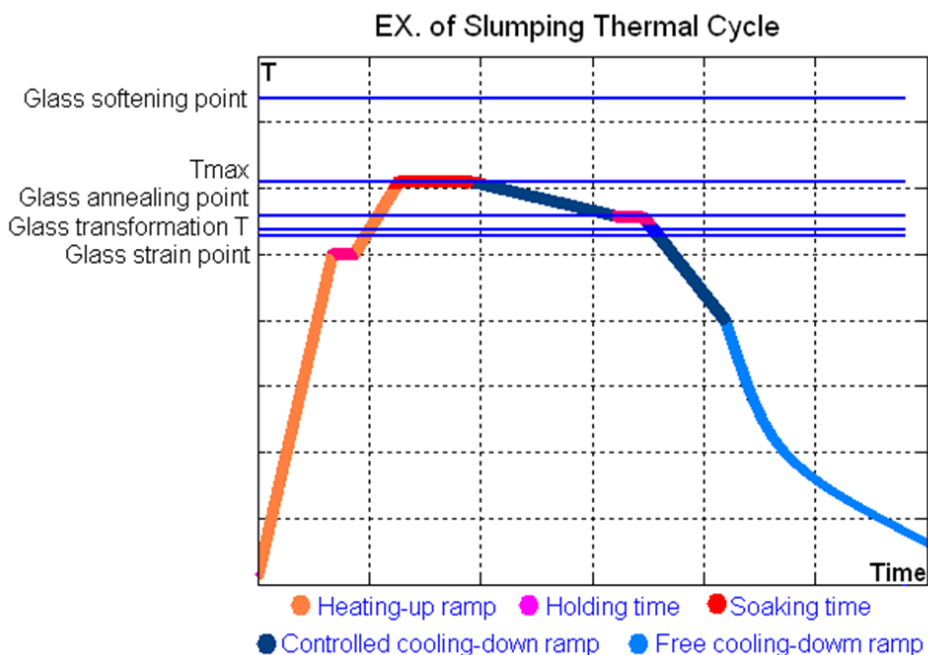


Fig. 4.10: Example of slumping thermal cycle, showing all the important phases of the process.

Table 4.6: Definitions of the main steps in the slumping thermal cycle.

-
- **Heating up ramp** (or phase): first step of the thermal cycle performed to reach the maximum temperature of the process

 - **Holding time**: step in the thermal cycle at which the temperature is set to a constant value to allow reaching good uniformity in the temperatures distribution

 - **Soaking time** or holding time at maximum T: period of wait at the maximum temperature of the cycle to allow the glass to sag against the mould and conform to its shape

 - **Cooling down ramp** (or phase): last step in the thermal cycle performed to cool down the glass. Normally, this phase is divided in two steps: one controlled step, performed in a slow controlled way so to avoid the introduction of unwanted stresses or deformations; and a free step, performed with the oven switch off and allowing for the natural cooling of the system.

The annealing point is one of the characteristic points of any glass material, together with the Transformation temperature (T_g), the Strain point and the Softening point, conventionally defined in dependence of the glass viscosity (see Table 4.7). In fact, glass behaves differently at various temperatures since its viscosity changes: as it is heated, it turns more fluid; when cooled it becomes more firm. This behavior is strictly connected to the key elements contained in the chemical composition of the glass and in part also on the production method (particularly the rate of cooling).

Table 4.7: Description of the main areas in the typical thermal expansion curve of a glass.

-
- **Brittle zone**: this zone refers to relatively low temperatures; let's say on average from Room Temperature to few hundreds degrees. If heated or cooled too quickly in this zone, the glass will break because of stresses or thermal shocks. In the brittle zone, glass swells when heated or shrinks when cooled. The glass shows an elastic behavior, also if very limited being a brittle material.

 - **Transition zone**: this zone is the most important one for the slumping process, since it is in this zone that the glass assumes a plastic behavior, which allows its shaping. The transition zone is delimited by the strain point (lower limit) and the softening point (upper limit). Glass is less sensitive to thermal shock in this zone, sometimes referred as annealing range since it contains the annealing point. When cooling down the glass, it is important to pass slowly through the annealing point to relieve internal stresses that might originate from the forming process.

 - **Fluid zone**: this is the high temperatures zone, where the glass becomes fluid and it will flow if not restricted. The fluid zone is of no interest for the slumping technology.
- In terms of viscosity, a transition from liquid to plastic state can be observed between 10^4 and 10^{13} dPa·s. The glass structure can be described as solidified or "frozen" above 10^{14} dPa·s. At this viscosity the internal stresses in glass equalized in about 15 minutes.
-

In general, three characteristic zones can be clearly individuated on glass temperature-elongation plot, the glass CTE diagram: this curve shows a nearly linear increase up to the beginning of the transition zone characterized by a plastic behavior and distinguished by a distinct bending of the expansion curve, which results from the increasing structural movement in the glass. Above this range the expansion again exhibits a nearly linear evolution, but with a noticeably greater rate of increase. The Transformation temperature (or Transition temperature) T_g is the parameter

describing this behavior: it can be considered for glasses what the melting point is for crystalline solids, referring to the temperature at which the glass transforms from a lower temperature glassy state to a higher temperature super-cooled liquid state. At temperatures higher than T_g , the structural units of the material are able to quickly reorganize themselves as a quasi-equilibrium liquid. At temperatures lower than the T_g , reorganization among the structural units virtually ceases and the resulting rigid material is what is known as glass. As illustrated in the Fig. 4.11, the Transformation temperature is determined by the intersection point of the two tangents of the high and low temperature ranges of the thermal expansion curve. The glass viscosity at T_g corresponds to about 10^{13} dPa•s. T_g serves as a useful benchmark for annealing.

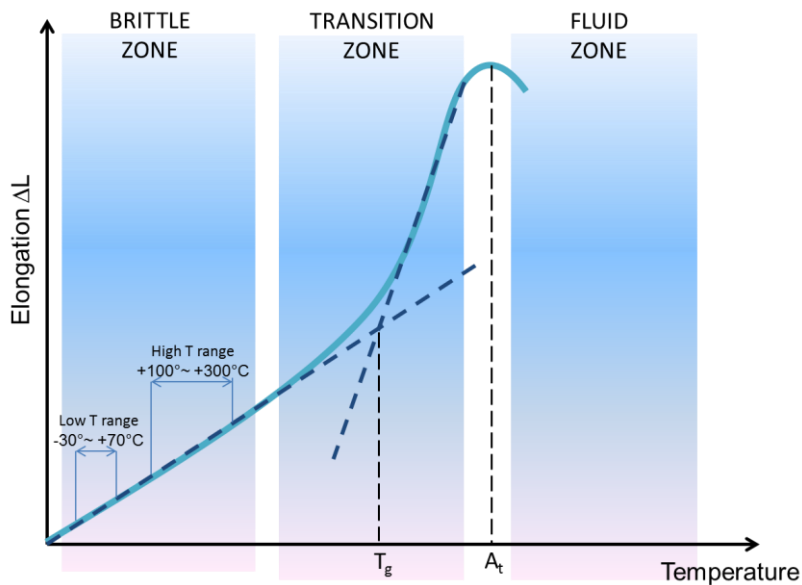


Fig. 4.11: Typical Thermal Expansion Curve for a glass.

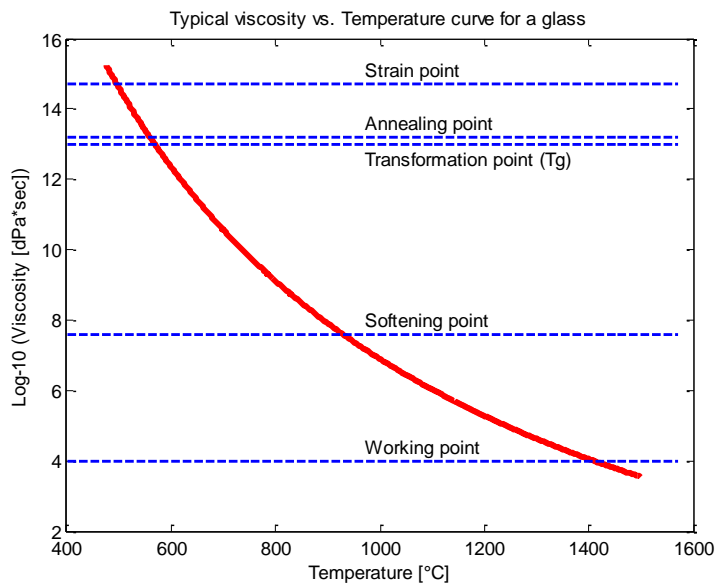


Fig. 4.12: Typical Temperature vs. Viscosity graph for a glass, showing the common viscosity points considered, in the glass item production field, to define the characteristics temperatures of the glass.

Table 4.8: Conventional definitions of the characteristic temperatures of glass in dependence on the viscosity value.

Characteristic Temperature	Viscosity	Description
Working Point	10^4 poise	The working point corresponds to the viscosity of 4 ($\text{Log}_{10}\text{Poise}$). It is contained in the glass forming region that span around viscosity values of 10^{6-5-4} poise: in this range of T the glass begins to soften up to the point where it is too soft to control.
Softening point Also called "Littleton Point"	$10^{7.6}$ poise	The softening point identifies the plastic range of temperatures at which glass begins to remarkably soften and deform under its own weight.
Yield point or Sag temperature	around 10^{10} to 10^{11} poise.	Yield point (A_t) or Sag Temperature (T_s) is defined as temperature at which thermal expansion stops increasing and actually begins to decrease with increasing temperature, or the point at which elongation becomes zero on the thermal expansion curve (Fig. 4.11). Actually this behaviour is not due to an intrinsic property of the glass but is rather due to deformation of the glass under the load applied in the standard measurement procedure.
Transformation T (Tg) also known as glass transition temperature	10^{13} poise	The transformation region (or Transition zone) is that temperature range in which a glass gradually transforms from its solid state into a "plastic" state. The Transformation temperature (Tg) can be determined from the thermal expansion curve (Fig. 4.11). It serves as useful benchmark for the annealing. In other words, this is the temperature at which the atoms, ions, and molecules become fixed in position without the mobility associated with a liquid but with the same disordered arrangement of the particles.
Annealing point	$10^{13.2}$ poise	The annealing point corresponds to the maximum temperature in the annealing range at which the internal strain of glass will be substantially eliminated. Internal stresses are relieved after few minutes.
Strain point	$10^{14.7}$ poise	The strain point corresponds to the lowest temperature in the annealing range at which viscous flow of glass will not occur. Internal stresses in the glass are relieved after few hours.

Note. 1 dPa•s = 1 poise

5 Design of experiments and preparatory activities

The majority of the slumping experiments has been performed at INAF-OAB site in Merate in the dedicated oven laboratory for what concern the realization of slumped plates, and in the metrology laboratories for what concern the characterization and analysis of results. In this chapter, the instruments, materials and tools used for the development of the *direct slumping with pressure assistance* are quickly presented, concentrating on the improvements specifically realized during the PhD activities.

5.1 Rationale of the carried out experiments

The main steps of the direct slumping approach developed during the study are summarized in Fig. 5.1. The author's contributions are spread in each one of them. It is here reminded that the aim of the research was to assess the application of the slumping technology to the case of X-ray segmented optics, with the goals reported in Table 5.1. These goals were meant to demonstrate the feasibility of the proposed method for the production of the elemental X-ray Optical Unit for the IXO mission and to show the potentiality of fully reaching its requirements. All the tests have been designed with the following topics and necessities in mind:

- To perform tests for the selection of glass and mould material;
- To test an antisticking (or release) layer;
- To check the process parameters for the selected couple of materials, eventually through flat samples: in particular, analyze the effect of the thermal cycle and pressure application on the glass surface finishing and strength;
- To slump on cylindrical sample;
- To verify the integration concept;
- To assess any new issue arising from time to time by the results of previous experiments.

Many of the experiments have been run in parallel. They all have been cataloged with an increasing number from test PS-IXO-1 to PS-IXO-131 up to now; the sequence is going on with the near future activities.

Table 5.1: Main goals considered during the technology study to be met for the slumped and integrated plates.

Requirement in terms of shape	Requirement in terms of micro-roughness
As a preliminary goal, the HEW of single integrated plates should reach a value of 15" (@1keV)	The roughness of the optical surface must be better than 10 Å (WYKO 20X, 660 – 10 µm wavelengths range) and equal to that of the starting glass foil in the AFM range (3-4 Å rms)

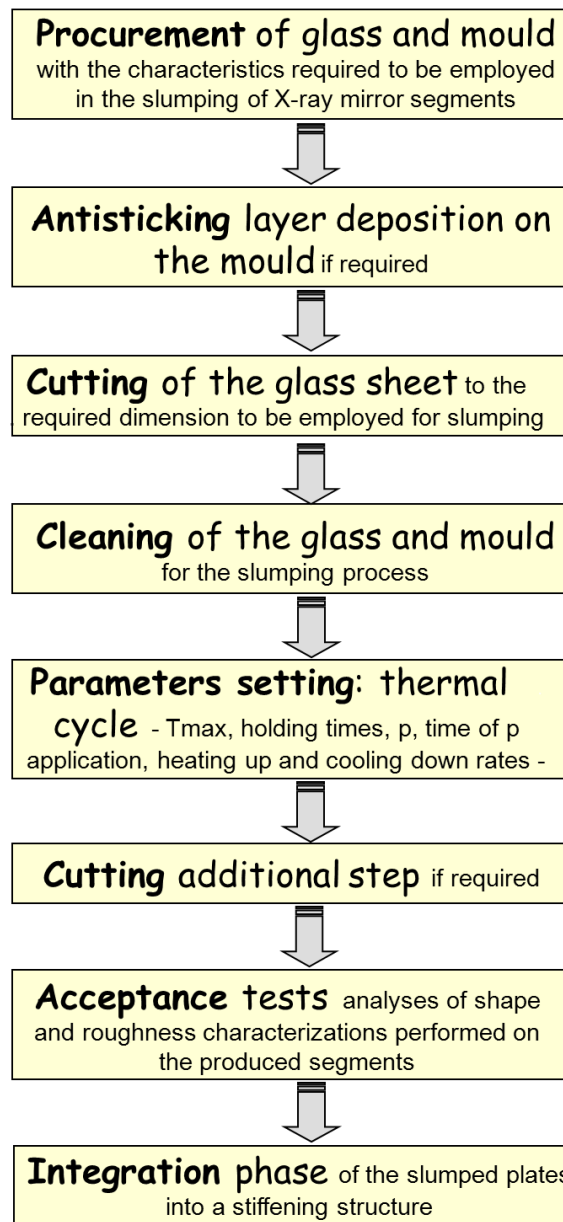


Fig. 5.1: Main steps of the direct slumping process with pressure developed by INAF-OAB. The author's contribution is spread in each one of them.

5.2 Preparatory activities to the experiments conduction

The activities started with an assessment of the instrumentations and tools available from INAF-OAB past experience in the slumping technique. Upgrades, that came up to be necessary for the application of the slumping technology to the IXO case, have been realized and the specifications for new necessary tools have been derived according to the research goals.

5.2.1 Assessment and improvements on the available tools and instruments

The oven laboratory installed at INAF-OAB was originally equipped with only two electrical ovens. A clean environment area, equipped with electrostatic system and sodium lamp, was added to take care of cleaning issue. The thermal behaviour of the ovens was deeply analysed and new muffles, moulds and glasses were procured with the characteristics imposed by their application for the IXO case.

5.2.1.1 Clean room environment

The whole process preparation procedure is presently realized in a clean room environment (ISO5 or class 100), appositely installed to take care of the dust contamination. Air filters guarantee that the laminar flow of incoming air does not contain more than 3520 particle/m³ bigger or equal to 0.5 microns. Overpressure is maintained in the environment so that dust cannot enter the area. The entire system of filters is switch on at least 12 hours before the utilization of the chamber to guarantee the cleaning. At the same time the laboratory doors and windows are closed and the room heating switch on to allow for environmental humidity to be eliminated. Inside the clean area the staff is dressed with Tyvek®-Coverall Classic. The zone is divided in two parts, one principally dedicated to the dressing of the personnel and the preparation of tools, the other for the slumping and integration activities. Dust contamination has to be avoid because a grain of dust between the mould and glass surfaces prevent the full contact of the two, introducing errors in the shape of the slumped plate, as shown in Fig. 5.2. An antistatic system has been installed in the clean room area to eliminate electrostatic charges that attract dust grains on the mould or glass surfaces. The initial idea of implementing such a system came from the necessity of eliminating antistatic charges that originated on the mould and glass after the removal of a peel-off paint used in the past as a last cleaning step. Deeper analyses showed that the peel-off paint left contaminants on the surfaces, not compatible with X-ray optics requirements, and so this product was eliminated by the cleaning procedure (see § 6. 1.2). However, the antistatic system utilization was maintained because it came up to be reliable for environmental static charges. Two sodium lamps are present in the laboratory, one portable and one in a fix position. They guarantee the possibility to check fringes and dust

presence between or on mould and glass surfaces. The intense light of the portable lamp allows the visual inspection of surfaces cleanliness. The Nomarski microscope (see Annex B) was located in the clean area to be utilized for the same scope. To better realize the tasks of cleaning and take care of dust contamination, a dedicated cleaning procedure has been study and implemented both for the moulds and for the glass foils. The entire procedure takes place in the clean environment: it consists of the following steps, which are repeated several times if necessary:

- Clean with bi-distilled water and optical soap;
- Abundantly rinse with bi-distilled water;
- Quickly dry with a flow of Nitrogen;
- Last cleaning with acetone and optical paper;
- Check with Nomarski microscope and intense light beam the results of the cleaning;
- If contaminants or dust are still present, repeat the procedure.



Fig. 5.2: The presence of dust prevents the full contact between mould and glass surface during the slumping process; even a small grain of dust has influence on a significant area, from few mm to cm. The use of sodium lamp shows this presence through the visualization of interference fringes between mould and glass surfaces. Picture above refers to an area about 150 mm wide: the impact of a dust grain is clearly visible.

5.2.1.2 Ovens

Two electrical industrial ovens are installed in the laboratory for the slumping technology assessment and development: one small oven and one big oven by Teknokilns [123]. They come from the glass and ceramic industry: their internal cavity is covered with isolating bricks and the heating elements consist of electrical resistances.



Fig. 5.3: *The two ovens available in the laboratory and largely used during the PhD work. (Left Side): The small oven utilized for preliminary tests. (Right Side): The big oven utilized for the slumping of the cylindrical plates to be integrated in the prototypes.*

The small oven has an internal volume of 0.5 m x 0.5 m x 0.3 m and the maximum power usage is of 9 kW. It can reach a max temperature of 950 °C using two sets of resistances located at the top and at the bottom of the oven cavity. One single internal thermocouple controls the temperature inside the oven. The big oven has internal size of 1.4 m x 1.4 m x 0.6 m and the maximum power usage higher than 80 kW. This value, however, has to be intended in the case all the heater elements are switch on contemporarily, a situation not very realistic and significant. The electrical grid line that serves the laboratory is dimensioned for a maximum power usage of 50 kW and so the five heater elements are never used all together in the same thermal cycle. This is not a problem or a limiting factor for the slumping process since three heaters are sufficient to guarantee the desired thermal conditions inside the oven, as demonstrated both by simulations and empirical data. The big oven can reach a maximum temperature of 950 °C and it has a more flexible internal PLC for precise thermal cycles control with respect to the small oven. To guarantee a good flexibility in the usage of the big oven, the electrical power can be applied on different sectors; in particular five different zones exist, each one of which is equipped with its own thermocouple. One sector consists of the lateral electrical resistance and the other sectors are represented by the upper and lower resistances, both composed by two separate heating elements, a central one and a lateral (external) one following the perimeter of the oven. Table 5.2 lists the specifications of the five heater elements contained in the big oven. Thermal simulations performed with ANSYS software evidenced that the mould temperature is more uniform in the big oven with respect to the small one because of the position of the heater elements. In fact, in the small oven the heater elements are only in the top and bottom part of it, causing a temperature gradient in the radial direction, especially during the cooling down phase when the edges of the mould cool down faster than its centre. Also, the limited internal volume of the small

oven is just enough to house the muffle, which is affected on the borders by high temperature gradients due to the oven aperture vicinity.

Table 5.2: Specifications of the heater elements of the big oven. Five electrical resistances are installed in the big oven to allow for flexibility in its use and better control of the inside volume for what concern the temperature uniformity.

Sector	Heater length [mm]	Power [kW]
Central Top	700	15.5
External Top	1300	16.5
Central Bottom	700	15.5
External Bottom	1300	16.5
Lateral	1300	19

Instead, in the big oven, lateral heater elements allow obtaining a more uniform distribution of temperature keeping smaller thermal gradients on the mould inside the muffle, also in reason of the fact that the muffle is more than 500 mm far from the oven walls and aperture. During the cooling down phase the lateral heater element is used to contrast the faster cooling down of the mould (and the glass) edges with respect to its central part, causing lower radial thermal gradients. Simulation results were confirmed by empirical data collected during the performed tests with additional K-type thermocouples inserted inside the oven and also inside the muffle. These additional thermocouples have been appositely procured and calibrated to measure the temperature gradients on the mould inside the muffle. Tests were also carried out to check the repeatability of thermal conditions inside the big oven. The following Fig. from 5.4 to 5.8 report a summary of the simulated and empirically recorded thermal behaviours of the ovens.

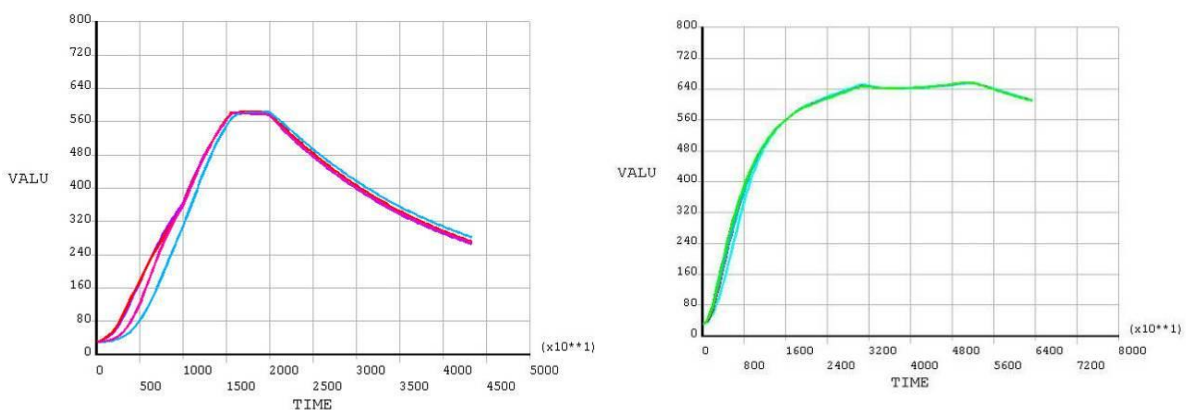


Fig. 5.4: Simulated temperature on mould during a thermal cycle in the small (Left Side) and big (Right Side) ovens. The Y-axis reports the temperature in °C, the X-axis the time from the beginning of the process in seconds. Several simulations have been performed changing the cycle time. The effect of shorter thermal cycle is that of enhancing the T gradients on the mould.

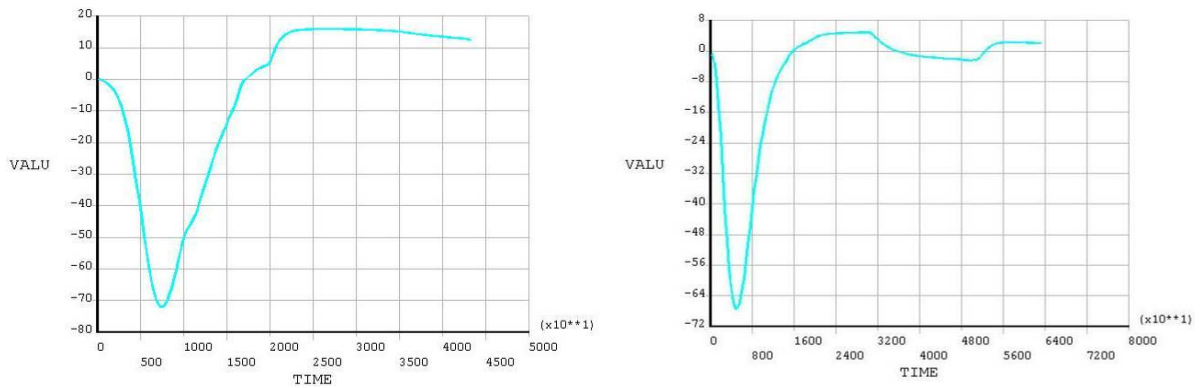


Fig. 5.5: Simulated thermal gradients on the mould in the small oven (Left Side) and in the big one (Right Side). The Y axis reports the temperature gradients in °C, the X-axis reports the time from the beginning of the process in sec. At equilibrium at maximum temperature, in the small oven the thermal gradients on the mould reach value of more than 15°C while in the big oven they can be maintained as low as 5°C or less.

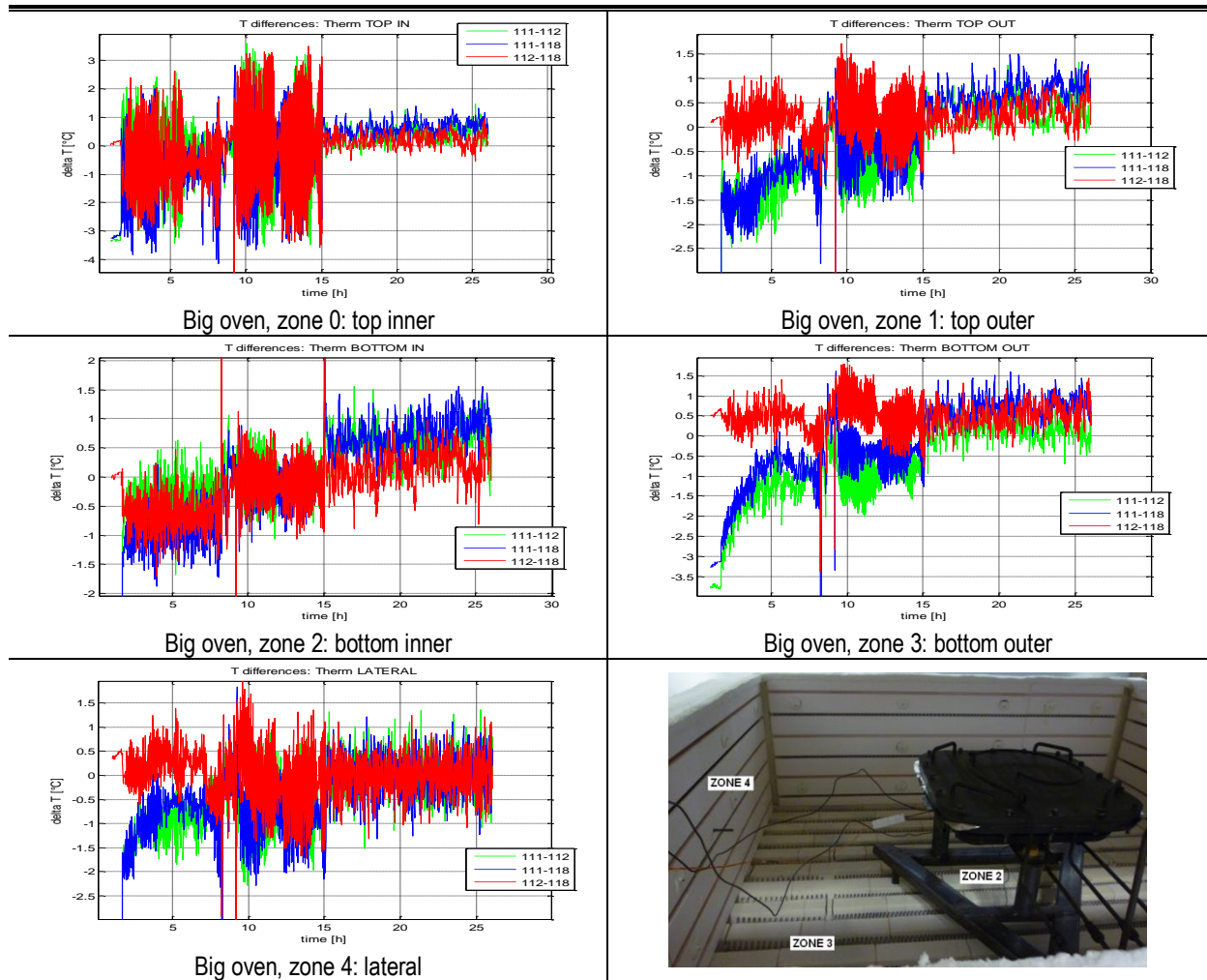


Fig. 5.6: Verification of the repeatability of the same thermal condition inside the big oven when the set parameters are not changed. During the critical cooling down phase (from 15h on), the recorded value differ of less than 2°C, the typical accuracy of the type of thermocouples present in the oven. This accuracy is good enough to repeat inside the muffle, at the center of the oven, the same thermal conditions from one cycle to the other.

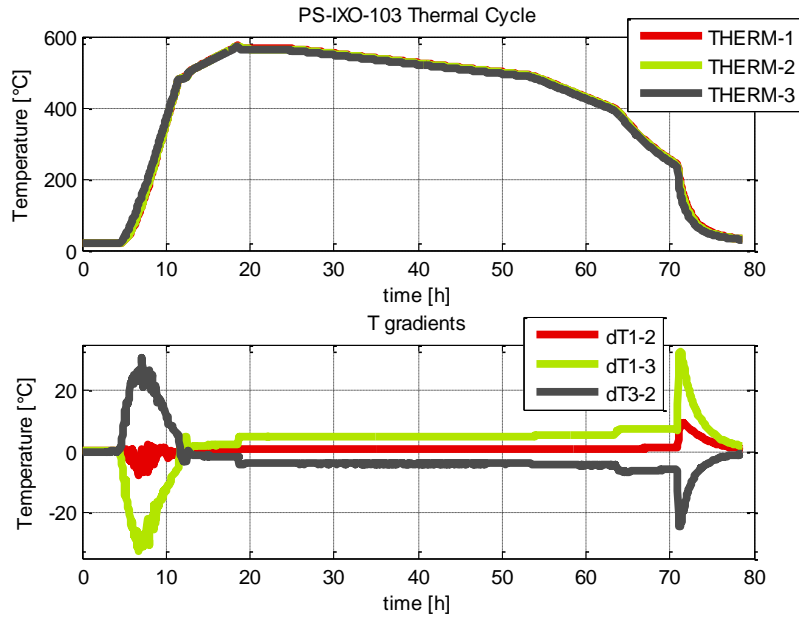


Fig. 5.7: Data recorded by additional thermocouples positioned inside the muffle. They verify the values expected by simulations and during the most critical phases of the process (the cooling down phase) are as low as 4°C.

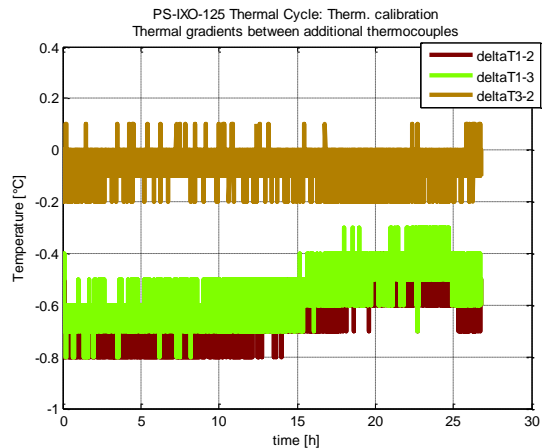


Fig. 5.8: Test of calibration performed on additional thermocouples to be positioned inside the muffle. A steel cylinder with holes toward its center has been employed. The thermocouples have been positioned as in the picture. Their resolution is of 0.1°C and their recorded values differ, in the worst case, for almost constant values of 0.6-0.7°C that is considered as corrective factor during the evaluation of T recording. Several of these tests have been performed both in the small and in the big oven and they always gave comparable results.

For the slumping of representative IXO mirror plates the big oven was considered. However, the small oven was largely used for preliminary tests whose scope could be met also with not optimal thermal gradients distribution. For example, it has been used for the realization of experiments aimed at the individuation of an antisticking layer (see § 6.1.3), for part of the tests performed to check the influence of pressure on the final micro-roughness of the plate (see § 6.2.5), and for the tests (in part performed and in part still on-going) to realize the huge number of samples necessary to check the glass strength after the slumping (see § 6.2.2.2).

5.2.1.3 Steel muffle

The direct slumping under investigation at INAF-OAB requires the application of pressure to help the glass coming in full contact with the mould during the slumping process in order to better replicate its shape without introducing undesired mid-frequencies (see Annex A for definition). The application of pressure is performed inside a steel muffle, a metal box able to withstand repeated thermal cycles, in which the entire slumping process takes place. It is made of AISI 310 stainless steel, a material well suited for high temperature applications and repeated thermal cycles, due to its low content of carbon. The muffle is divided in two chambers by mean of a thin stainless steel foil of 25 micron thickness, made in AISI 304. It acts as a membrane: by imposing a difference in the pressure between the two cavities the membrane forces the glass foil onto the mould surface. The CTE of the steel sheet is slightly larger than the steel AISI 310 of the muffle ($18.7 \times 10^{-6} / ^\circ\text{C}$ and $16.9 \times 10^{-6} / ^\circ\text{C}$ respectively). This guarantees the steel sheet expands more than the muffle when at high temperature, preventing any possibility of failure for internal stresses. The use of a steel muffle offers other advantages; it guarantees a uniform temperature distribution inside its volume: its walls act as shield from the direct heating generated by the resistances preventing localized overheating and spreading evenly the heat generated inside the oven. Furthermore, it guarantees a physical separation between the glass-mould couple and the oven environment, helping in the control and elimination of dust contamination. A circular muffle was already available at INAF-OAB with a diameter of 300 mm: it has been employed during the first period of activities for preliminary tests, while waiting for new tools. For the present study, two new muffles have been manufactured: one square-planar and one square-cylindrical. Both the new muffles are equipped with four pipes that allow to slump in a controlled atmosphere or in vacuum environment. They have respectively an overall dimension of 440 mm x 440 mm x 150 mm (the flat one) and 360 mm x 360 mm x 150 mm (the cylindrical one), to accommodate square moulds up to 300 mm side.

Old circular muffle already available, used at the beginning of activities for preliminary tests in the small oven.



Square-plane muffle, largely used for the realization of more than 50 experiments to validate the technique.

Square-cylindrical muffle, delivered by the producer in summer 2011.



Fig. 5.9: Images of the stainless steel muffles used during the activities reported in this text. Note the evolution in their shape and configuration, coming from improvement in the knowledge of the slumping process behavior.

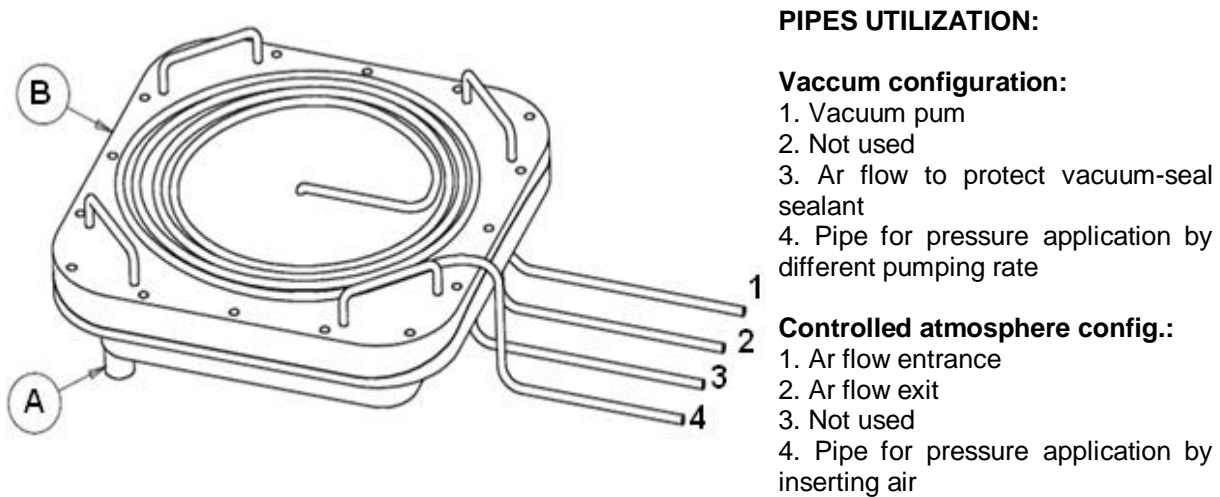


Fig. 5.10: Muffle drawing and explanation of the four pipes usage that allows both to slump in vacuum and in controlled atmosphere. A is the bottom part of the muffle; B is its cover. By inserting a metal membrane between them at the muffle closing, it is possible to divide the internal volume in two chambers, allowing for pressure application.

5.2.2 Selection of the metrological systems to be employed for results analyses

In order to characterize the goodness of the slumping process, the most important evaluation concerns the ability to replicate the mould shape without degrade to unacceptable level the original roughness of the glass substrate. State of the art instruments installed at INAF-OAB laboratories were chosen to be used for the characterization of the slumping process: measurements and analyses of the optical surfaces in terms of intrinsic shape and surface roughness at different spatial frequencies ranges (see Annex A), of both the moulds and the slumped plates, allowed the identification of the process potentialities and capabilities. It was however necessary the development of a dedicated machine (Characterization Universal Profilometer -CUP-) for the characterization of integrated plates (see Annex B). The measurement of shape and roughness parameters is an essential step in the evaluation of the process results. The characterization of the mould is essential to have a term of comparison for the slumped plate. But also to check the quality of the product delivered by the vendor and verify it meets the requirements. The measurements of these parameters on the slumped plates are twice important: first of all to be compared with that of the moulds and get hints on the replication capabilities of the process; and secondly also to know the goodness of the slumped plates in reflecting X-ray: the parameter *intrinsic shape* is necessary to guarantee that the X-rays are reflected following the wanted path into the focal plane, while the parameter *roughness* is critical from the scattering point of view, which might degrade the focal spot resolution. In order to determine the intrinsic shape, of both the glass foils and the moulds, characterizations were performed with:

1. A **3D Characterization Universal Profilometer (CUP)**, for a complete mapping of the slumped mirrors and moulds figure;
2. A **Long Trace Profilometer (LTP)**, for axial profiles figure characterization of moulds;
3. An optical sensor (**CHRocodile** sensor by Precitec) mounted on a precise linear stage, for 1D longitudinal or azimuthal profiles scans and thickness variation measurements;
4. A **Sodium Lamp**, for a qualitative evaluation of glass and mould shape difference through interference fringes.

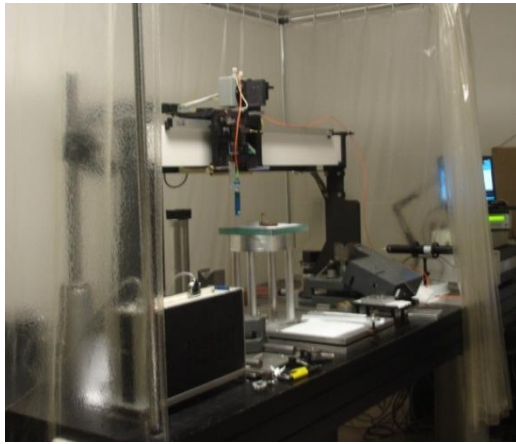
In order to determine the surface quality parameters, of both the glass foils and the moulds, characterizations were performed with a set of topographic and X-ray instrumentations, which allow obtaining the distribution of roughness over frequency windows (the Power Spectral Density – see Annex A for more details), giving useful indication on the presence of surface defects:

1. A **WYKO Optical Profilometer**, for mid-frequency roughness characterization of slumped samples and moulds;
2. An **Atomic Force Microscope (AFM)**, for high-frequency roughness characterization of slumped samples and moulds;
3. A **BEDE-D1 X-ray Diffractometer**, for indirect roughness PSD characterization of slumped samples;
4. Phase contrast **Nomarski Microscope**, for qualitative and cleanliness check of the surfaces at different magnifications.

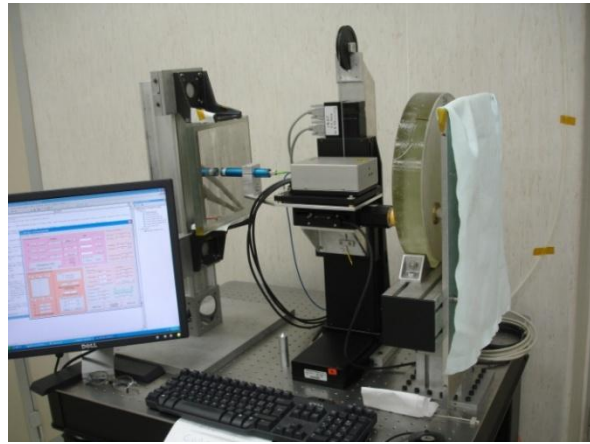
All the instruments are mounted on optical air-suspension self-stabilizing tables to avoid any ground vibration being introduced in the data. The majority of them is located in clean rooms where environmental conditions like temperature and humidity are checked and actively controlled. Whatever the adopted measurement method is, the following points have always to be taken into account:

- The surface parameters describe a sample (or a set of samples) of the surface, assumed as representative;
- Each measurement covers only a limited range of spatial frequencies, the limits being determined by the Nyquist criterion. That is the reason why the values of surface parameters are not unique and depends on the window sensitivity of the considered instruments;
- The accuracy and precision of the measured value are limited by instrumental and environmental noise.

Fig. 5.11 shows the main metrological instruments largely used during the development activities (details on their operative principles are provided in Annex B).



Long Trace Profilometer (LTP)



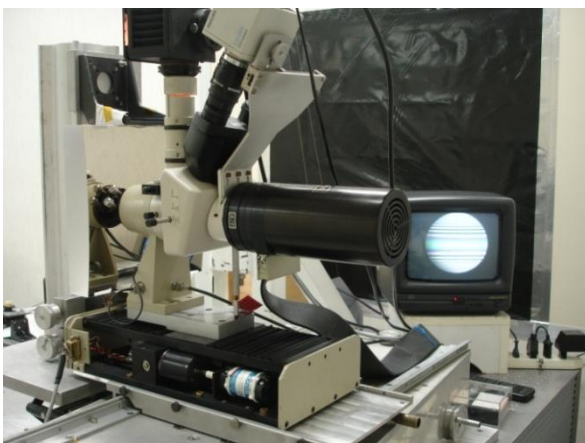
Characterization Universal Profilometer (CUP)



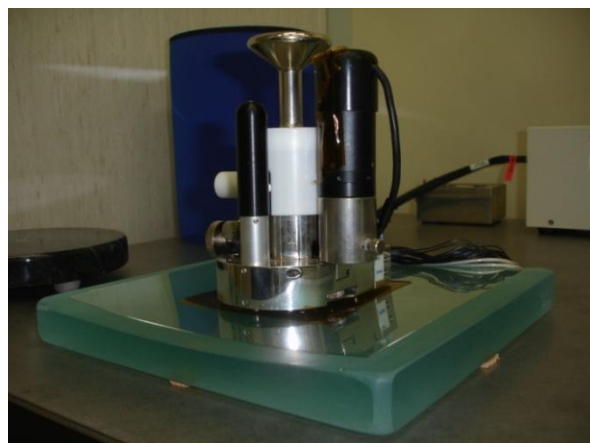
Nomarski microscope



Bede X-ray Diffractometer



WYKO profilometer



Atomic Force Microscope (AFM)

Fig. 5.11: Main metrological instrumentation available at the INAF-OAB laboratories in Merate site. All these instruments have been employed for the characterization of slumped plates in order to check the goodness of the process and assess its potentiality for the realization of X-ray segmented mirrors.

5.2.3 Procurement of glass and mould for the slumping technology assessment

The most important elements to be procured to start the experiments on the slumping for IXO segmented mirrors were, of course, the slumping mould and the glass.

5.2.3.1 Selection of the mould and glass materials

The selection of mould and glass material was fundamental. The choice was performed taking into account all the general considerations exposed in § 4.3. Table 5.3 shows a list of properties of materials that present good potentiality to be employed for slumping mould production in a slumping process for the production of X-ray mirrors. They have already been considered in the past or are currently under evaluation. These materials are: Alumina, Silicon Carbide, Quartz, Zerodur K20 [124], and Silicon.

Table 5.4 and 5.5 show a list of glass sheets available on the market together with their main properties: they might be considered for the application of the slumping technology for the production of X-ray segmented optics. The principal characteristic they have in common is their small thickness: this is an essential requirement, posed by the IXO optical design, mainly coming from mass and effective area constraints of X-ray space telescopes. All these glasses are available from the flat display market, where their entrance dates back in the last two decades. Other types of glass, which might be considered for the slumping technology of other items (for example Adaptive Optics), are available on the market but they are not reported here because they are not produced in the thickness range required for next generation X-ray optics (lower than 0.5 mm).

Table 5.3: Main properties of materials that possess a high potentiality to be employed for the production of mould to be used during a thermal slumping process.

	Alumina	SiC	Quartz	ZerodurK20	Silicon
Density (g/cc)	2.85	3.21	2.21	2.53	2.32
Elastic Modulus (GPa)	90	476	72	83	155.8
Knoop Hardn. (HK0.1/20)	1900	3000	580	620	1100
Max application T (°C)	1900	1450	1200	850	1400
High T stability	Very good	Very good	Very good	Very good	Very good
CTE (10⁻⁶/K)(RT1000°C)	8.2	4.0	0.5	2.0	2.6
Thermal Cond. (W/mK)	24	102	1.31	1.60	141.2
Polishing and figuring	Slow	Very slow	Fast	Medium	Slow
Microroughness (Å)	10-20	< 5	< 5	10-20	< 5
Voids, inclusions	NO	NO	Possible	NO	NO
Glass adhesion	YES	YES	YES	NO	YES

Table 5.4: Main properties of market available glasses that might be employed in a process of thermal slumping for the production of thin mirror segments.

	AF32	AF45	D263	0211	1737F	EagleXG	Gorilla
Manufacturer	Schott	Schott	Schott	Corning	Corning	Corning	Corning
Dimension (mm)	2.1x2.4m	440x360	440x360	406x432	355x457	1.1x1.2m	405x460
Thickness (mm)	0.1-1.1	0.05-0.5	0.03-1.1	0.05-0.5	0.7-1.1	0.4-0.7	0.7-2.0
t Constancy (μm)	± 50	< 10-30	$\pm 8-40$	--	--	± 20	--
Density (g/cm^3)	2.43	2.72	2.51	2.53	2.54	2.38	2.45
Young module (GPa)	74.8	66	72.9	75.9	71.4	73.6	73.3
Poisson's ratio	0.238	0.235	0.208	0.22	0.22	0.23	0.21
Shear Modulus (GPa)	30.2	26.7	30.1	30.9	28.8	30.1	30.1
CTE ($10^6/^\circ\text{C}$) 0-300°C	3.2	4.5	7.2	7.38	3.76	3.17	9.1
Th. Cond. ($\text{W/m}^2\text{K}$)	1.16	0.93-1.13	0.93-1.25	0.96	0.91-1.44	1.09-1.42	--

Table 5.5: Main characteristic temperatures of glasses that might be considered for the slumping of thin X-ray mirrors. All the temperatures in the table are expressed in degree Celsius [$^\circ\text{C}$].

	AF32	AF45	D263	0211	1737F	EagleXG	Gorilla
Softening point ($10^{7.6}$ poise)	969	883	736	720	975	971	843
Annealing point ($10^{13.2}$ poise)	728	663	557	550	721	722	609
Strain point ($10^{14.7}$ poise)	686	627	529	508	666	669	559
Forming T (10^{6-5-4} poise)	1090 1187 1309	1000 1098 1225	839 929 1051	--	--	--	--
Working Point (10^4 poise)	1309	1225	1051	1008	1312	1293	--
Transformation T (Tg)	715	662	557	--	--	--	--

The glass selected for this study was glass D263 by Schott [125]. The choice was mainly dictated by the relatively low values of characteristic temperatures of this glass with respect to the other thin glasses available on the market. In particular, low Transformation temperature (Tg) optical glasses have to be preferred for precision molding since they can be shaped at relatively lower temperatures, which means in a easier and shorter way, in terms of set up procedures and in terms of time (that is to say in a cheaper way). Furthermore, glass D263 was a well-known glass since already considered by other research groups for its application in space and so it has been already analyzed in the past [126]. This glass is produced with the thickness of 0.4 mm required by the optical design and it is available on the market in sheets up to 440 mm x 360 mm, so compliant with the necessary dimensions of 200 mm x 200 mm. Its original micro-roughness is of few Å, making it ideal for X-ray applications. Its procurement was not difficult: the glass was ordered to the producer

already cut in foils of 200 mm x 200 mm and was delivered in three separate production batches. The selection required more consideration for what concern the slumping mould material. Alumina or SiC would have been preferred because of their CTE, closer to that of the glass. However, the procurement of these materials is not always easy and requires long period, also because their figuring and polishing is very slow being them hard materials. In addition, Alumina cannot be polished to a level better than few nm and this could have been problematic for the direct slumping for which the behavior in terms of mould roughness replication in the glass was not known. Regarding SiC, it would have required many tests to select the type to be used and moreover it is very expensive. These two materials were not selected. Among the other three materials (Quartz, Zerodur K20 and Silicon), the choice was in favor of Quartz (or Fused Silica). Fused Silica is a well-known material for lenses, easily ground and figured. It can be super-polished and it is suitable to withstand very high temperatures. Besides, Fused Silica is a material already used for the moulds fabrication by the US groups involved in the glass slumping activities. Unfortunately, it has a low CTE, in the order of $0.5 \cdot 10^{-6} /K$, and a low thermal conductivity which requires low cooling down rates (that means longer thermal cycles) to avoid (or at least reduce) temperature gradients in the mould. Zerodur K20 was not selected at the beginning of the project because of the roughness level it can reach with polishing. Anyway, it was considered in the second phase, after the first phase results suggested that the micro-roughness of the glass can be maintained by fine tuning the process parameters (see § 6.2.5). Zerodur K20 is in fact a very attractive material since it does not need any antisticking layer. Also Silicon was considered in the second phase because of its higher thermal conductivity, when compared to those of other materials, and this will allow faster heat exchange and so faster processes. However, an antisticking layer is required to prevent glass adhesion. A trade-off between pro and cons of the Zerodur K20 and Silicon materials will be performed in the near future.

5.2.3.2 Characteristics of the glass and the mould

According to the IXO optical design, the geometrical parameters reported in Table 5.6 and in Fig. 5.13 were considered. While the glass procurement was not problematic, the situation was a little bit more difficult for the moulds since cylindrical or Wolter I optical elements of large dimensions are not commonly produced. A cylindrical shape was considered, instead of the Wolter I shape as it could have been expected due to the IXO design. The choice was dictated by programmatic reasons, mainly schedule and cost considerations: the procurement and measurement of a cylindrical shape mould is faster and cheaper than the realization of a Wolter I shape mould, still offering the possibility to evaluate the slumping technology capability. The 250 mm x 250 mm mould dimension was dictated

from the 200 mm x 200 mm dimensions of the glass foils coming from a trade-off considering the available materials on the market, FEA results on the XOu design and realization and handling issues (25 mm more per side were considered for thermal reason). It is worth nothing that these mould parameters were originally intended for the first phase of the project, whose main aim was to assess the technology potentiality and to compare the direct and indirect slumping approach in order to select the more reliable one to be followed during phase two. They were supposed to be upgraded during phase two of the project: in particular the original idea was to evolve from the cylindrical shape to the theoretical Wolter I shape of the telescope design. However, the results obtained in the first phase of the project suggested that these parameters could also be maintained for the subsequent activities. It was demonstrated, in fact, through FEM analyses before and then empirically (see later § 6.2.4.2) that the proposed integration procedure has the capability to correct low spatial frequencies shape errors of the slumped plates with acceptable spring back effects. And so the requirements on the slumping results can be relaxed. This is indeed a very important result that translates into two main effects: first of all, a lower grade of mould shape replication can be admitted (few microns instead of sub-micron level). Secondly, the requirements on the slumping mould can be relaxed with important gain in terms of cost and procurement time. This is fundamental in view of the industrialization of the whole manufacturing chain of the IXO optics. In principle, in fact, a different mould would be necessary for each IXO mirror shells with different Radius of Curvature and Wolter I shape. However, giving the possibility of shape correction during the integration through a phase of cold slumping, a single mould of cylindrical shape might be considered for the hot slumping of a number of near shells with slightly different radius and profile. Fig. 5.12 reports the HEW degradation expected by the application of this method.

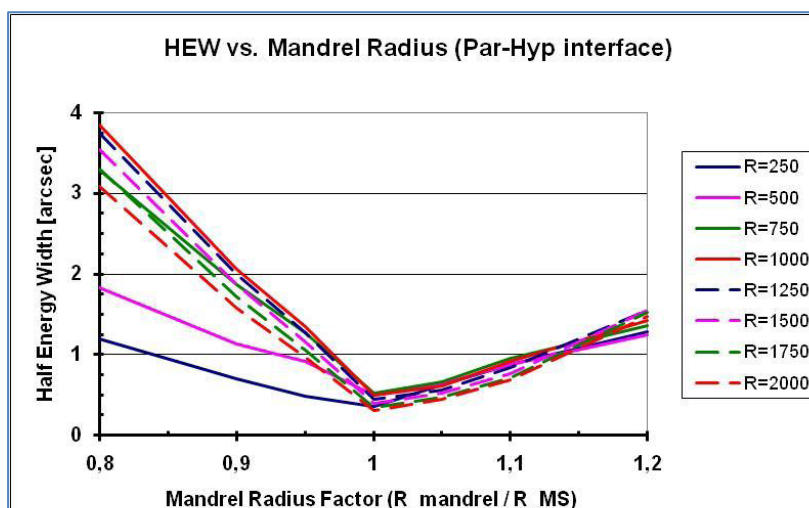


Fig. 5.12: Optical degradation related to the utilization of cylindrical slumping moulds (instead of par-hyp) having radii different with respect to the nominal one (R_{MS}) dictated by the Wolter I design. Different curves refer to different nominal MS radius at the par.-hyp. Interface [86]. For instance in the range $0.97 < R_{MANDREL}/R_{MS} < 1.1$ the final HEW is smaller than 1 arcsec in the whole range $250 < R_{MS} < 2000$ mm.

This lead, of course, to the need to produce integration moulds as precise as possible with Wolter I design. Anyway this is in principle less critical than slumping mould production since more materials could be considered because they do not have to withstand repeated thermal cycles at high temperature. Fig. 5.14 shows the drawing of the integration moulds currently under realization for their utilization in the prototypes manufacturing.

Table 5.6: Characteristics and geometrical parameters considered during the procurement of the slumping moulds and glass foils.

Glass foil dimension	200 mm x 200 mm	Selected from optical requirements and manufacturing consideration.
Glass foil thickness	0.4 mm	Selected as best compromise considering final telescope mass, strength and system requirements.
Glass roughness	Requirements for roughness (rms levels): Between 0.5 and 100 μm : $\sigma < 2.6 \text{ \AA}$ Between 100 μm and 1 mm: $\sigma < 5.5 \text{ \AA}$ Between 1 and 10 mm: $\sigma < 3 \text{ nm}$ Between 10 and 100 mm: $\sigma < 20 \text{ nm}$	Coming from X-ray reflection considerations to reach the final goal of 5" HEW (slightly relaxed for this first phase when $\sigma < 5 \text{ \AA}$ and $\sigma < 10 \text{ \AA}$ in AFM or WYKO range respectively can be accepted).
Glass thickness constancy	< 10 micron	As low as possible. Ideally a zero valued would be preferred.
Mould shape	Cylindrical plano-convex, with square base	Selected as the easier shape for manufacturing and testing although being representative of the optical design.
Mould RoC	+1000 \pm 5 mm	Representative of an intermediate mirror shells and XOUI in the present IXO optical design.
Mould dimension	250 mm x 250 mm (\pm 0.3)	Slightly bigger than the glass foil for thermal reason arising during the hot slumping process.
Mould central thickness	50 \pm 0.5 mm	Necessary to limit shape deformations of the optical surfaces due to gravity.
Mould Cylindrical shape accuracy	$\lambda/8$ on 50x70mm ² area	The requirement has been posed only on 50x70mm patches because of a limitation in measurement capability of the entire shape. This value guarantee on the entire surface a PV < $\lambda/2$, compliant with the theoretical Wolter I design.
Mould surface micro-roughness	As glass roughness	Since the replication of mould roughness was not known at the beginning of the project and had to be tested, it was decided for a super-polished mould.
Holes in the mould	3 holes diam. 4 \pm 0.2 mm	To insert thermocouples; they are positioned on the bottom centre of the mould and on one lateral surface. Their function is to allow the positioning of thermocouples to monitor the mould temperature during the slumping process.

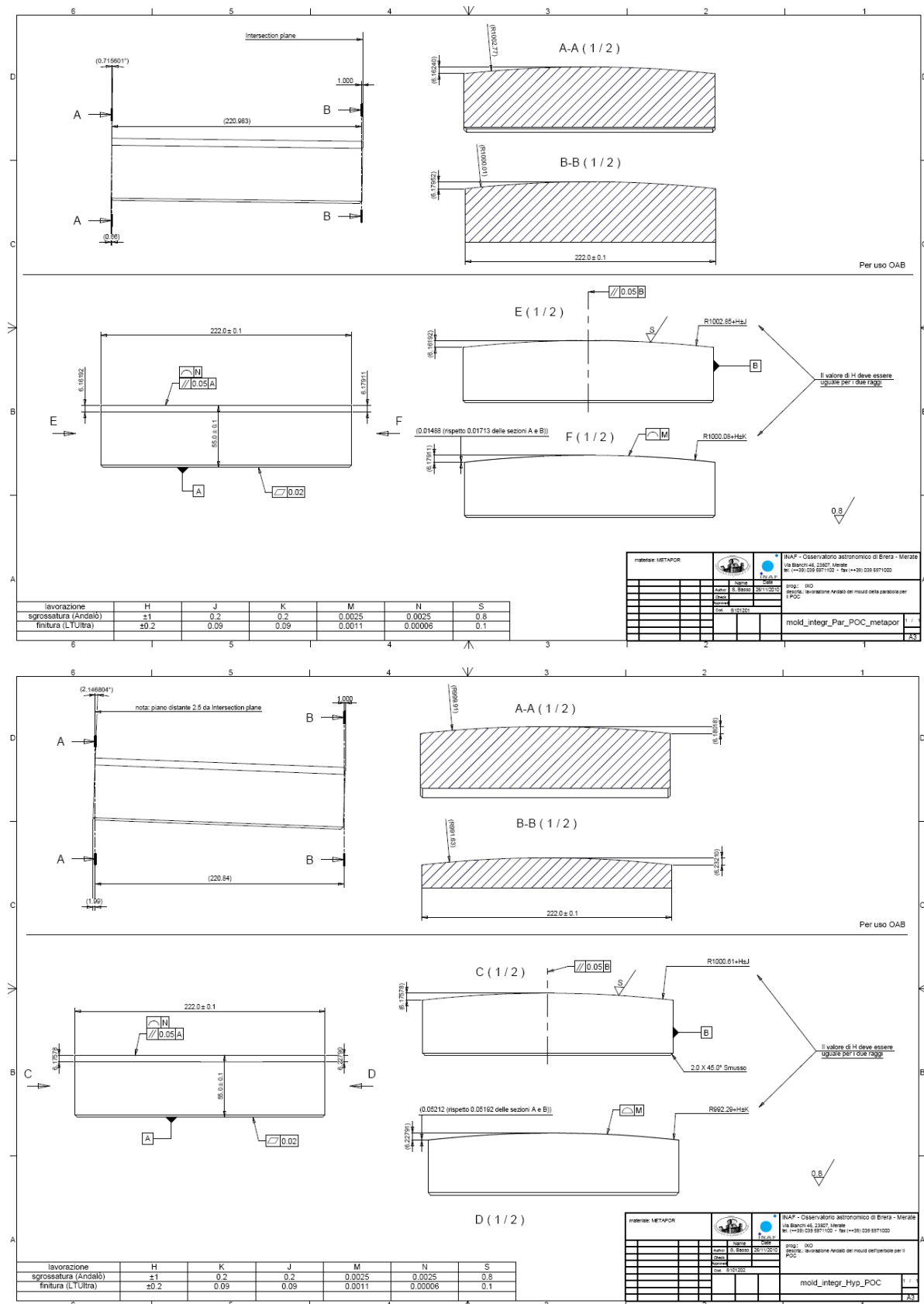


Fig. 5.14: Mechanical drawing of the front (par.) and rear (hyp.) integration moulds to be utilized for prototypes realization. They are in the production phase at the moment of writing.

5.2.3.3 Summary of the materials and tools used during the experiments

In addition to the appositely designed parts, many others market available tools have been procured for preliminary or destructive tests. A complete list of materials and tools utilized during the experiments performed in the timeframe of the PhD research is provided in the following Table 5.7. Once all the necessary materials and tools were available, the slumping tests could finally start. The research was always conducted taking in mind its final scope: to achieve a reliable technology to be considered for IXO optical payload manufacturing.

Table 5.7: List of the main tools and materials utilized in the experiments performed in the time frame of the PhD research.

Muffles:

- Old circular muffle: diam. 330 mm, used for preliminary tests on small components
- Square plane muffle: dimension 440 mm x 440 mm, the most used
- Square cylindrical muffle: dimension 360 mm x 360 mm, available only the last month of activities

Moulds:

- Several flat moulds made in Fused Silica, circular with diameter of 100 mm or 150 mm and thickness of 20 mm
- Two Cylindrical Fused Silica moulds, square with dimension of 250 mm x 250 mm x 50 mm (CT) and ROC of 1 m (named MCX1 & MCX2)
- One Cylindrical Zerodur K20 mould, square with dimension of 210 mm x 210 mm x 50 mm (CT) and ROC of 1 m (named MK20_1)
- One Cylindrical Zerodur K20 mould, square with dimension of 250 mm x 250 mm x 50 mm (CT) and ROC of 1 m (named MK20_10)*
- One Cylindrical Silicon mould, square with dimension of 220 mm x 220 mm x 50 mm (CT) and ROC of 1 m (named MSI_01)**

Glasses:

D263 glasses, supplied by the vendor in three moments, they have been numbered consecutively:

- from T0 to T30 and from ECO0 to ECO50 the first delivered batch: dimension 200 mm x 200 mm, thickness 0.4 mm
- from 100 to 150 the second delivered batch: dimension 200 mm x 200 mm, thickness 0.4 mm
- from 200 to 250 the third delivered batch: dimension 200 mm x 200 mm, thickness 0.4 mm
- from 300 to 315 the fourth delivered batch: dimension 360 mm x 440 mm, thickness 0.4 mm

Steel sheet:

- ESPI metal, aisi 304 steel sheet of thickness 25 micron
- ESPI metal, aisi 304 steel sheet of thickness 50 micron

*MK20_10 was delivered at the end of August 2011 and was characterized the first days of September. No slumping tests performed on this muold are reported in this test.

**MSI_01 will be delivered by the end of October 2011. It was not available at the time of writing so no slumping tests performed on it are reported in this test. It is in the list for completeness reason. Notice that its dimension is smaller than 250 mm side: this is related to the procurement of blank material. Silicon is produced for the wafer industry with maximum diameter of 310 mm.

6 Results on the application of the slumping technology to the IXO case

This chapter reports on the main results obtained during the PhD research program in the field of the *hot slumping technology*. The work done allowed advancement in the results obtained with the technology and permitted to individuate the further improvements necessary to fully exploit its potentiality in the accomplishment of the IXO X-ray optic requirements. The chapter follows the scheme presented in Table 6.1 that summarizes the activities in which the author was actively involved. Substantially, it is divided in three sections, which follow the three major steps of development.

Table 6.1: Summary of the activities related to the assessment of the slumping technology in which the author was actively involved; they are divided in three main sections following the progresses in the different aspects of the technique (rather than their temporal execution). These three main sections are followed in the chapter to present the main results of the research.

Review of INAF-OAB slumping procedure and know-how for its application to the IXO case

- Modification in the process environment: from vacuum to controlled Ar atmosphere due to S contamination
- Modification in the cleaning procedures: elimination of the peel-off paint First Contact that causes contamination
- Selection of Cr+Pt as antisticking layer

Cylindrical slumping compliant with the IXO optical design

- Characterization of procured moulds and preparatory activities for their application in the slumping process
- Characterization of procured glass foils and analyses on their cutting process and strength characteristics
- Selection of the p-T cycle of slumping
- Characterization of the slumped plates in terms of shape
- Characterization of the slumped plates in terms of roughness

Understanding of the still open issues and proposed improvements for follow up activities

- Investigation on the origin of deformations still present in the slumped plates
 - Proposed solutions to be implemented in the near future
-

First of all, a review of INAF-OAB know-how in the field of hot slumping technology was performed, with the aim of adapting the technique to the case of IXO. Necessary modifications and upgrades were made to the process set up. Then, the tests on cylindrical slumping started. During the first phase of the project, cylindrical Fused Silica moulds and glass D263 were chosen with the aim of selecting, between the direct and the indirect process, which approach presented the highest

potentiality to fit the IXO demanding requirements. This could have been achieved through a number of characterizations and measurements of both the glass foils and the moulds (in terms of shape and roughness) and of the process parameters (the thermal cycle temperatures and gradients, and the pressure value and time of application in primis). The indirect slumping tests were performed by the German colleagues at MPE and are not reported here (for more details see [131]). The second phase was mainly intended to the production of slumped segments to be integrated in demonstrative prototypes. However, optimization works continued and, on the base of first phase results, new materials (Zerodur K20 and Silicon) were considered other than the Fused Silica for the production of mould while the glass did not change. It is here anticipated that the production of the slumped plates to be integrated into prototypes is not finished yet; however the research performed allowed to freeze the procedure to follow for their manufacturing (see Annex D). The division of results in three main sections is adopted to present the several aspects in a useful and tidy way. They do not have to be intended as consecutive in time. In fact a mere list of performed tests in chronological order would have resulted meaningful and with no clear connection. That is because several aspects of the process were analyzed in parallel and many of the experiments were not intended only to one specific aspect but were considered for several scopes. For this reason, few of the presented results might seem to come before the following ones due to the fact that most of the topics are correlated each other. Cross references are supply throughout the text to help the reader interpreting the several correlations between the parameters of the process under development. Also, it might happen that only the process parameters and details relevant to the specific aspects under analyses are presented in each section, omitting other information. For a complete list of experiments and their main goals refer to Annex C.

6.1 Modification of past INAF-OAB slumping procedure

Before starting its involvement in the slumping of X-ray optics, INAF-OAB possessed a solid know-how of the technology coming from past research experiences aimed at the demonstration of thin Adaptive Optics production. The original process procedure included the steps reported in Fig. 6.1. It required some variations before being applied to the X-ray mirrors case. In particular, the type of glass had to be changed to a thinner one, and so the results in terms of mould shape and roughness replication had to be assessed again for the new material. Two main elements had been modified in the slumping procedure with respect to the previous employed for Adaptive Optics shaping: the cleaning step and the environmental condition set during the process. They are discussed in the following paragraphs § 6.1.1 and § 6.1.2.

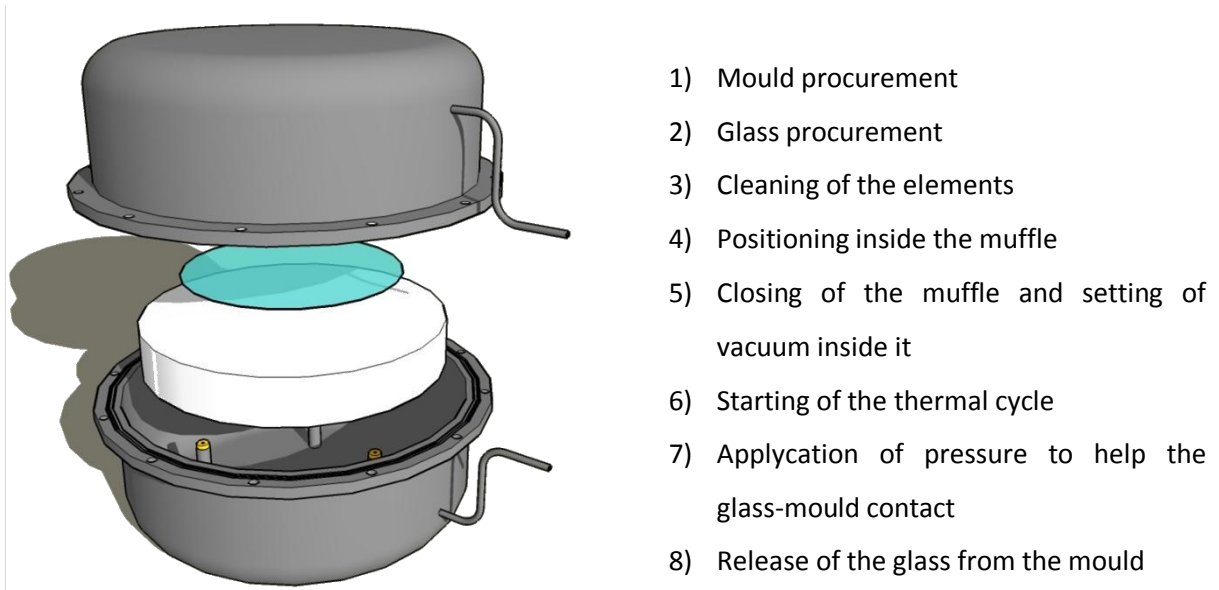


Fig. 6.1: Scheme of the old slumping process set up utilized by INAF-OAB for the assessment study of Adaptive Optics realization. It has been entirely revised at the beginning of this study to assess its application to the case of X-ray mirrors production. In particular, step 3 (cleaning procedure) and 5 (process environmental condition) needed to be modified to be compliant with X-ray mirrors requirements.

6.1.1 Modification in the process environment conditions: from vacuum to Ar controlled atmosphere

The old slumping procedures followed by INAF-OAB foresaw the realization of the process in vacuum environment. Vacuum value was not high, in the range of 10^{-2} bar, obtained by the mechanical action of a vacuum pump. Anyway, the removal of a large fraction of air was enough to guarantee a reduced convection, obtaining in this way two important consequences:

- The percentage of heat exchange by convection was negligible. Practically all the heat was exchanged by radiation, allowing a more uniform and predictable thermal condition on and around the glass and the mould. The entire process was realized inside a muffle, a stainless steel container. To obtain its hermetical closure, a graphite rope was utilized as sealant, acting as an O-ring between the two parts of the muffle; traditional O-ring materials could not be considered because of the relatively high (up to around 620-640°C) maximum temperatures of the slumping thermal cycle.

- The protection against dust particles was complete. The presence of dust particles between the mould and the glass surfaces, no matter as small as they are, is detrimental for the process since it prevents their correct contact. The use of vacuum guaranteed no circulation of dust particles eventually still present in the muffle.

During preliminary tests on small cylindrical moulds, it was discovered a sort of white powder contamination on the optical surfaces of the slumped glass and the mould (see Fig. 6.2). The test was realized twice, giving the same results, on small Fused Silica mould (a plano-convex lens of dimension 50 mm x 50 mm, Central Thickness of 10 mm and Radius Of Curvature of 257.5mm) and a foil of D263 glass (45 mm x 45 mm, thickness 0.4 mm, hand cut). During those particular tests, an antisticking layer was applied on the glass foil giving the chance to visually realize the contamination (see § 6.1.3 for further details on antisticking layer). A deeper examination of the issue was conducted by SEM analyses, performed at Politecnico di Milano, allowing discovering that the contaminant was Sulfur. After an investigation on the possible origins, it came up to be introduced by the graphite rope used to obtain the vacuum tight: Sulfur is a typical contaminant in the production of graphite, and indeed the datasheet of the material reports a value of about 500 ppm for the Sulfur content. It might be contained in small quantity also in the steel of the muffle; however this origin of the contamination is unlikely since each muffle undergoes a thermal cycle at high temperature (up to 850°C) before its first use in slumping processes to release any eventual contaminants from material and manufacturing steps. Furthermore, the new muffle realized in the same material did not show this problem. Sulfur might be present on the glass surfaces because it is an element typically used during one step of the glass production. However, also this is not the case since the peak in Sulfur content (see Fig. 6.3) is obtained with respect to a point on the same glass sample with no contamination (if the contamination comes from the glass, each point of the glass should be equally affected). The graphite sealing ring has been eliminated from the process; without it, it is not possible to obtain an acceptable vacuum tight. For this reason, we started to realize the slumping process in a controlled atmosphere of inert gas: Argon was employed to eliminate the oxygen and reduce any kind of oxidation occurrence. The muffle is still used for the benefits in terms of dust control and because it allows the setting of the controlled atmosphere only around the process area and not in the entire oven. Recently, one new graphite material has been individuated to solve the scope of ensuring the sealing at high temperature (Papyex 998 by Mersen); the first preliminary tests to check for eventual contamination gave good results and further analyses are in progress to definitively verify that this material is compliant with the non-contamination requirement and can be employed as sealant for the muffle closing.



Fig. 6.2: Small cylindrical slumping tests (PS-IXO-5 and PS-IXO-8) realized on 50 mm x 50 mm Fused Silica mould. A layer of Pt was applied on Schott glass D263 as release agent. Its presence permitted to visually evidence the presence of Sulfur contamination introduced by the graphite rope used as sealing ring for vacuum tight at temperatures up to 600°C.

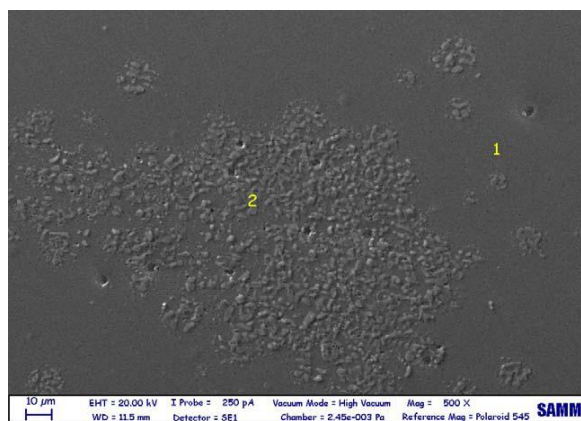


Fig. 6.3: Sulfur contaminated zone at high magnification. Positions 1 and 2 are the points of execution of EDS (Energy Dispersion Spectroscopy) elements analyses performed at Politecnico di Milano, chemical and materials department "Giulio Natta".

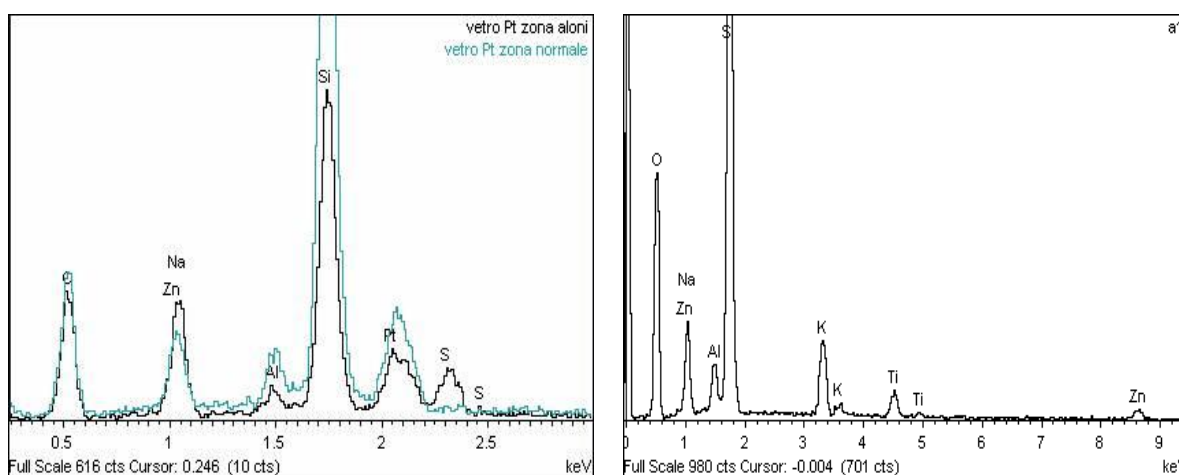


Fig. 6.4 (Left Side): Comparison of the relevant peaks of the EDS analyses performed by Politecnico di Milano on the not contaminated zone (1) and on the contaminated zone (2) of the sample shown in Fig. 6.3. Sulfur peak is higher in zone two, indicating that sulfur contamination is present. **(Right Side):** The same analyses performed on a glass sample slumped in presence of the new graphite type (PS-IXO-116). Sulfur peak (located at 2300 keV) is not present indicating

the absence of any contamination (the plot is exactly the same as that obtained on a new untreated glass).

6.1.2 Modifications in cleaning procedures: elimination of First Contact

The old slumping procedures followed by INAF-OAB foresaw the utilization of peel-off paint, called First Contact, during the glass and mould cleaning steps. Cleanliness of the two elements is a critical issue since dust presence between them prevents their optimal contact and originates mid-frequencies errors that degrade the performances of the slumped mirror plate. The First Contact was applied with an ad-hoc brush, as the very last step in the cleaning procedures, and was allowed 12 hours to completely polymerize. It was then peel off from the surface just before positioning the glass over the mould and closing the muffle. In that right instant the surfaces are “ideally clean” since First Contact entraps and removes any grain of dust from the surface. The peeling action creates electrostatic charges on the surfaces that attract dust from the surrounding environment; to overcome this problem, an antistatic system was appositely installed in the laboratory. Unfortunately, one other complication that prevent the application of the First Contact was discovered. While for other optical application it is of effective use, in the field of X-ray optics it cannot be applied because it leaves contaminants on the surfaces. The first doubt on its efficiency derived from having noticed a change in the friction of a Fused Silica mould surface after the removal of the First Contact with respect to the friction experienced on a part of the surface not treated with First Contact. A deeper investigation of the phenomenon was carried out. SEM analyses realized at Politecnico di Milano and AFM images realized in house evidenced a sort of contamination coming from the First Contact. For this reason the product is not used anymore in the cleaning steps.

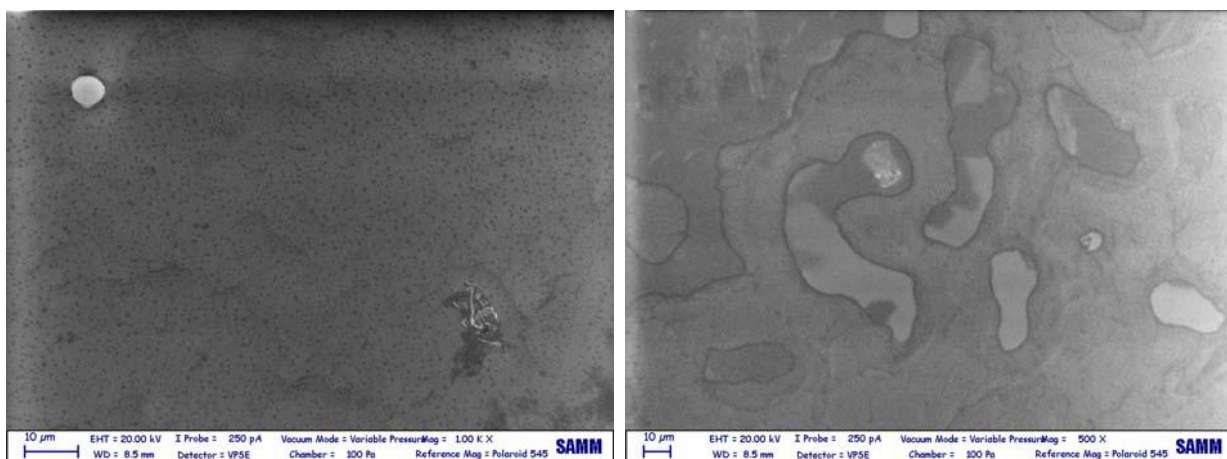


Fig. 6.5: SEM images of the surface of glass samples after First Contact peel-off. The First Contact contamination is clearly visible. (Left Side): Paint peel-off after more than 24 hours from application. Pits are visible on the sample. (Right Side): Paint peel-off after 15 minutes from application. Local residua and dark halos are visible and probably due to a non-uniform removal of the product.

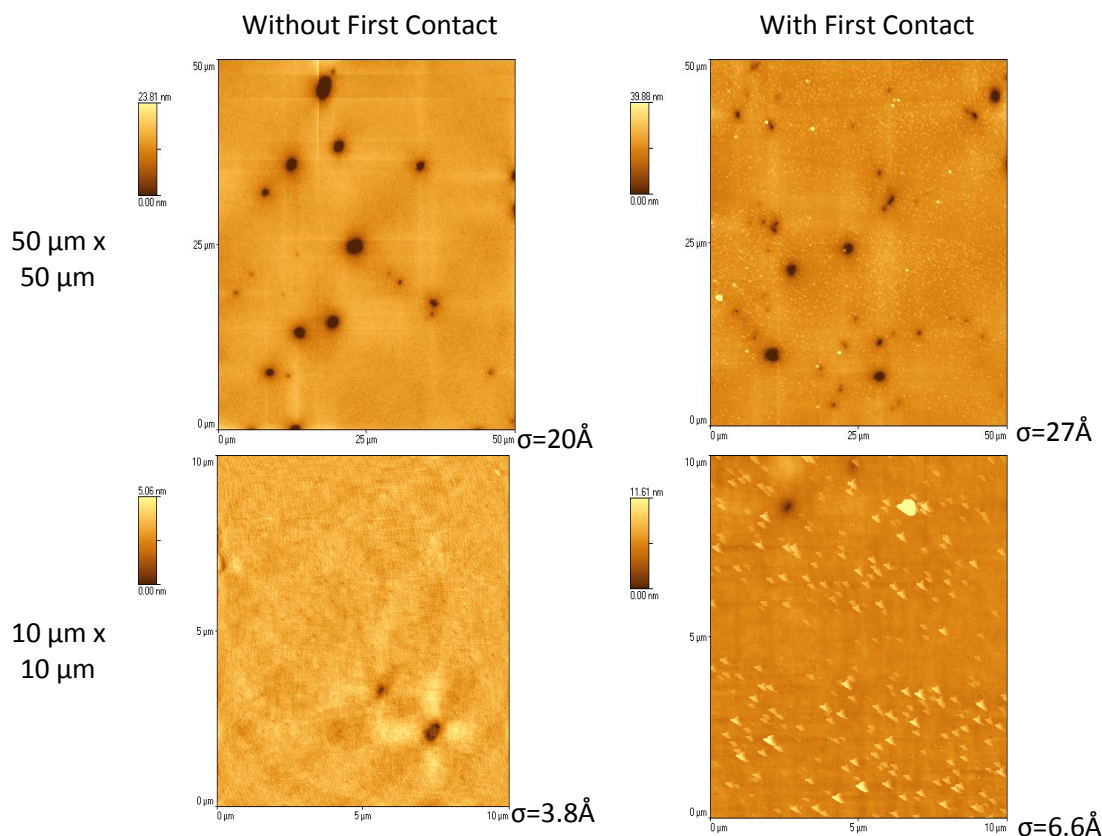


Fig. 6.6: AFM images showing the surface of a slumped glass (PS-IXO-81), half cleaned with First Contact and the other half cleaned only with bi-distilled water and Amber clean. By comparing the two columns, the contamination coming from First Contact peel-off paint is clearly visible as bright pits, present on the right images but not on the left ones. (The dark areas are holes in the glass coming from the slumping on a damaged mould, in any case used for this test since the goal of the experiment was to check for First Contact contamination).

6.1.3 Selection of a reliable antisticking layer

Depending on the mould and glass material selected and on the process p-T cycle parameters, the problem of glass adhesion to the mould surface might arise due to chemical reactions. Qualitative in house experiences allowed to individuate which couple of materials could be used without antisticking (or release) layer and which one, instead, necessitate it. A summary is supplied in Table 6.2. The release layer came up to be fundamental in the majority of cases, except the case of Zerodur K20 mould for temperature up to 600-610°C. Anyway, problems of sticking might arise also on Zerodur K20 mould for particular setting of process parameters. It was therefore important to get experience and study a solution to the adhesion problem.

In dependence on the CTE mismatch between the two materials, the breaking behavior consequent to sticking is different. The analyzed cases comprise all the possibilities:

- Glass CTE lower than mould CTE

This is for example the case of Alumina mould with Borofloat 33¹⁶ glass whose CTEs are respectively $8.2 \times 10^{-6}/K$ and $3.3 \times 10^{-6}/K$. At high temperature the glass sticks on the mould and during the cooling down phase it suffers from compression forces caused by the differential shrinkage related to the CTEs difference. These compressive forces might cause the “implosion” of the glass foil, with ejection of chips and small piece away from the mould.

- Glass CTE almost equal to mould CTE

This is for example the case of Silicon Carbide mould with Borofloat 33 glass whose CTEs are respectively $4.0 \times 10^{-6}/K$ (for the particular SiC type employed in the experiment) and $3.3 \times 10^{-6}/K$. At high temperature the glass sticks on the mould and during the cooling down phase it shrinks almost following the shrinkage of the mould because of the close proximity of the CTE values. Even if stuck on the mould, in this case the glass piece does not break.

- Glass CTE higher than mould CTE

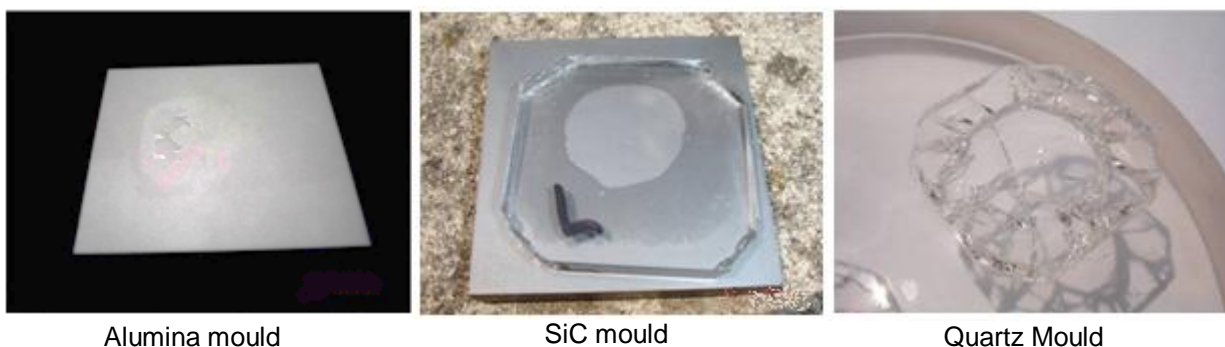
This is for example the case of Quartz mould with Borofloat 33 glass whose CTEs are respectively $0.5 \times 10^{-6}/K$ and $3.3 \times 10^{-6}/K$. At high temperature the glass sticks on the surface of the mould and during the cooling down phase it suffers from tensile forces caused by the different shrinkage connected to the CTE difference. These tensile forces cause the breaking of the glass.

Table 6.2: Summary on the results of empirical tests carried out to check the sticking behavior of different couples of glass and mould materials.

Mould Material	Glass Type	Adhesion (Sticking)	Explanation
HP Alumina	Borofloat 33	Yes	Observed experimentally
	D 263	Yes	
HP SiC	Borofloat 33	Yes	Free Si atoms are present on the Silicon Carbide surface: at high temperature in presence of O ₂ they form SiO ₂ , i.e. glass.
	D 263	Yes	
Technical Quartz/FS	Borofloat 33	Yes	The main component of both the glass and the mould is SiO ₂ that at high T tends to adheres to itself.
	D 263	Yes	
Zerodur K20	Borofloat 33	No (up to 640°C)* (up to 660°C if no p is applied)	Above this temperature the sticking happens also on this material
	D 263	No (up to 610°C)*	
Silicon	Borofloat 33	Yes	The same explanation as the case of SiC applies.
	D 263	Yes	

* This has to be considered as an indicative value obtained from specific tests: the value might change if different slumping cycle parameters (meaning the applied pressure and time of application and the soaking time) are adopted.

¹⁶ These tests were realized at the very beginning of the activities, when D263 was not yet available.



Alumina mould

SiC mould

Quartz Mould

Fig. 6.7: Example of results of mould-glass sticking tests performed with mould made in Alumina, Quartz or Silicon Carbide. The shown tests were performed with glass Borofloat 33. No p was applied and the maximum reached temperature was 600°C . This is the empirical evidence of the need of an antisticking layer to prevent glass adhesion on the mould surface.

The sticking problem arises from the chemical behavior of the two materials that are influenced by the parameters set in the process, and in particular: the maximum T , the applied pressure and the duration of its application, the time spent at high temperatures. What makes the investigation challenging is the fact that these parameters cannot be considered separately since the final results is a no-linear combination of the single effects.



Fig. 6.8: Comparison of the sticking behavior in two cases where the same thermal cycle is performed with or without the application of pressure. This test in particular was performed with D263 glass pieces (dim. 70 mm x 70 mm, thickness 0.4 mm) on Fused Silica mould (diameter 100 mm, thickness 20 mm). Figure on the left refers to the case of no pressure application. Figure on the right refers to the case of 150 g/cm^2 pressure. The maximum T reached during the 18 hours thermal cycle was of 575°C . It is clear how these two parameters of the process (T and p) have to be considered together (PS-IXO-36).

The evaluation of pressure effect on the sticking behavior is particularly complicated and could only be checked with empirical tests. Even more complicated is the situation at the glass edges, where the metal membrane utilized to apply pressure causes points of force concentration that sometimes bring to local sticking with consequent breaking of the glass foil. The problem was initially solved by applying Boron Nitride, in the form of thin powder, at the glass foil edges. However, this time-

consuming process introduced dust contamination and prevented the good contact of glass edges to the mould. A more reliable solution is to use a glass frame, with the same thickness of the glass to be slumped, positioned 1.5-2 mm close to the glass plate edges. Closer gaps are not safe since the glass foils and the glass frame could come in contact due to the elongation caused by the increasing in temperature: consider for example that a D263 glass of 200 mm will be 0.8 mm larger at 600°C. In this way the pressing membrane does not feel the step between the glass and the mould and better conform to the mould shape without introducing points of pressure concentration.

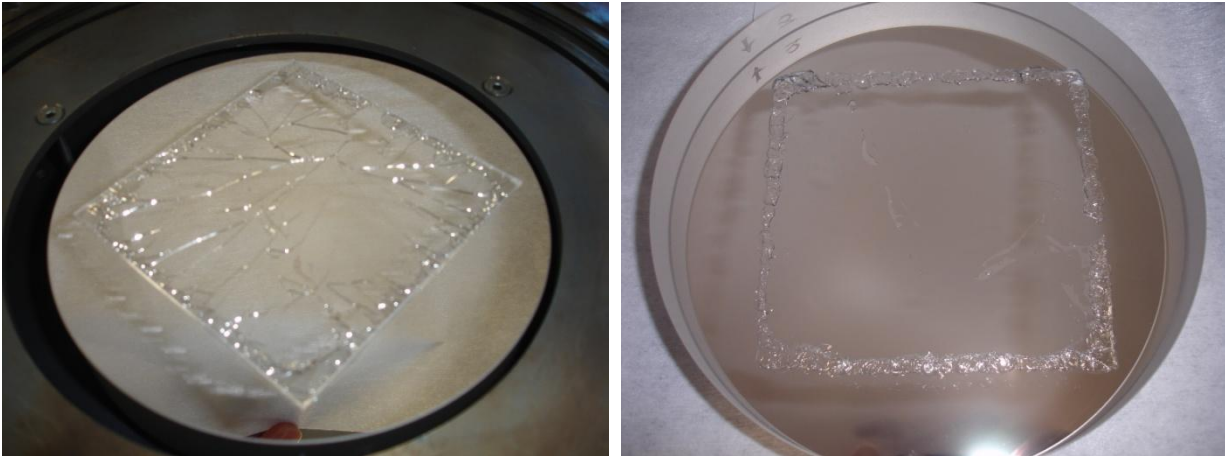


Fig. 6.9: *Sticking issues mainly related to pressure concentration on the glass edges: the pressing membrane feels the 0.4 mm step between the glass and the mould and, because of its rigidity, creates points in correspondence of glass edges where the pressing force is higher. The images clearly show it. (Left Side): The broken glass at the muffle aperture; (Right Side): A shot taken from the back side of the transparent Fused Silica mould that clearly shows how the sticking was confined on the edges areas of the glass. This test was performed with D263 glass on Fused Silica mould with Pt antisticking layer: the maximum T was 600°C and the pressure 50 g/cm², applied till the end of the process (PS-IXO-49).*

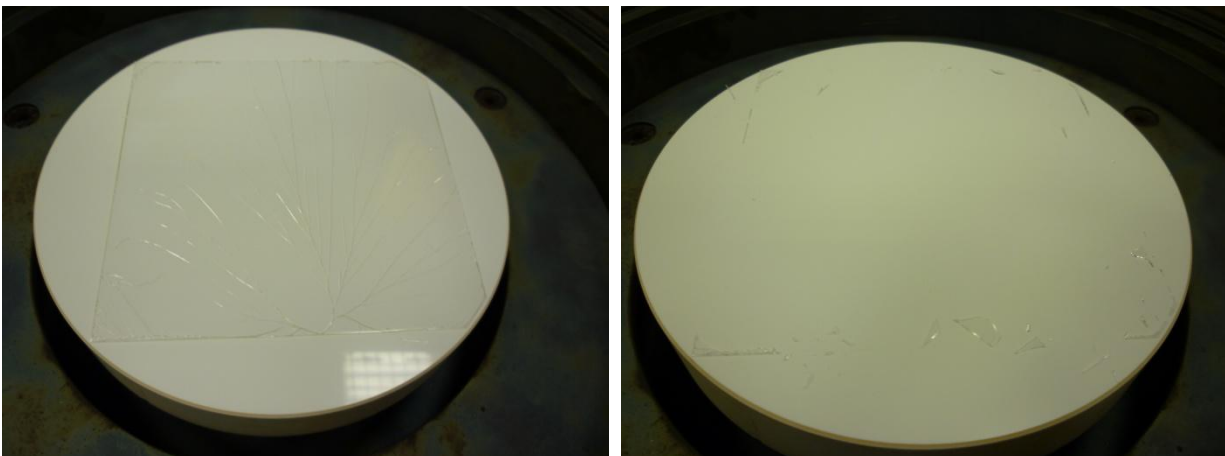


Fig. 6.10: *The problem of edges sticking due to concentration of forces when applying pressure through the steel sheet was observed also on Zerodur K20. The damage on the mould was certainly very small (Right Side), however the effect caused the breaking of the glass starting from the edges (Left Side). This particular experiment was realized with Zerodur K20 mould with diameter 138 mm and D263 glass of almost 100 mm x 100 mm. the maximum T of the cycle was 570°C and the pressure 80 g/cm² applied till the end of the process. These parameters were considered safe: the problem of sticking rose due to the very poor surface finishing of the mould (PS-IXO-73).*

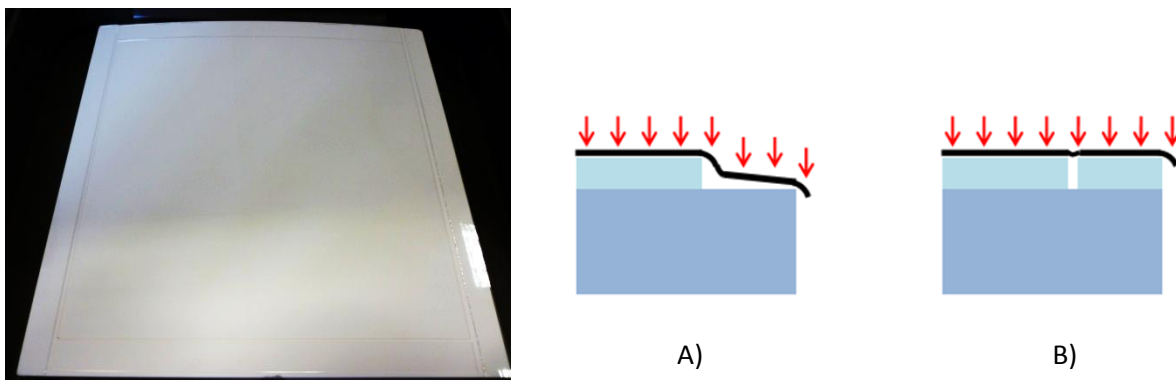


Fig. 6.11: (Left Side): Example of application of the glass frame to overcome the problem of points of force concentration on the edges of glass when applying pressure through the steel sheet. The gap between the frame and the glass is of about 1.5-2 mm (PS-IXO-86). (Right Side): A) Schematic of what happens near the edges of the glass when pressure is applied. The pressing membrane falls a gap and it deforms changing the Radius Of Curvature of its shape so that forces might result concentrated in points near glass edges. B) Schematic of the deformation of the metal sheet when a piece of glass with the same thickness is positioned near the edges of the glass to be slumped, forming a sort of frame. In this way, the forces on the slumped glass are more uniform.

To overcome the sticking problem, different release layers were considered. The first idea was to use Boron Nitride, a material well known for its anti-adhesion properties. It is indeed the material used by the American groups that developed a proprietary process for its application on the mould surface¹⁷. However, its dusty consistency makes the process “dusty” and might introduce mid-frequencies errors in the slumped segments. Elements able to withstand high temperatures have been qualitatively investigated, and finally the Pt was selected for further investigation because of its promising results. When talking about the antisticking layer, it has to be considered that, in principle, it can be applied as on the mould surface as on the glass one. The advantage of applying it on the glass surface is to already have a reflecting coating layer on the slumped mirror segment, with no need of further coating steps. For this consideration, but also because of practical time and cost reasons, the investigation started in this direction. Ti, W, Pt, Ir and Diamond Like Coating (DLC) were applied (by evaporation or by sputtering techniques) on glass samples and slumping were performed. Fig. 6.12 shows an example: obtained results demonstrate that, in the considered range of temperature and pressure (T range 570-600°C, p range 50-150g/cm²) the Pt acts as a good release agent in case of D263 glass and Fused Silica, Silicon Carbide, and Silicon mould. It does not work for Zerodur K20 in the case temperature higher than 610°C are required, since Pt migrates on the surface of the mould, contaminating it. Also the Ir acts quite well as release agent, showing a similar

¹⁷ It is worth reminding that the American groups follow a process with no pressure application, and so the BN is sufficient in small quantity to act as release layer. With the pressure application, the BN might not be effective anymore in preventing the adhesion.

behavior than Pt, but the glass seems more stressed at the end; Tungsten evaporates from the glass and in part migrates to the Zerodur mould; it was not tested with other moulds. Exactly the same happened also in the case of DLC. Concerning Ti, the visible result was pretty good from the point of view of the glass; however it creates a pink contaminated area on the Zerodur K20 moulds.

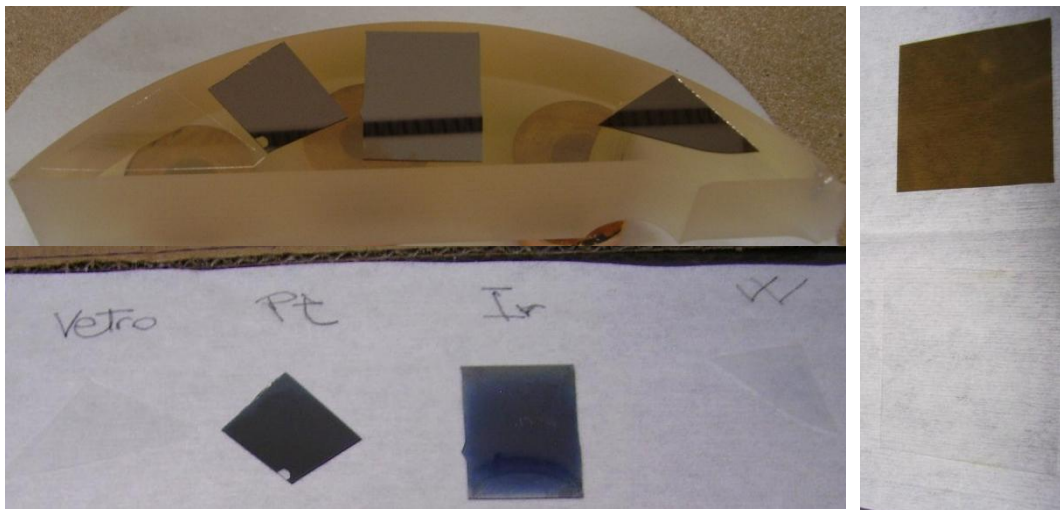


Fig. 6.12: Example of qualitative tests to select the material for the antisticking layer: top view is before the thermal cycle; bottom view is after the thermal cycle application. The glass is in the pictures to compare its color with that of the slumped sample that was originally coated with Tungsten, which evaporated at high temperature and migrates in part to the mould. The same happened in the case of DLC that originally conferred to the glass gold-like-color but during the thermal cycle evaporates (Right Panel). This particular test was realized on Zerodur mould with D263 glass. Other mould materials have been tested in the same way, in particular Fused Silica.

At the end of the qualitative testing, Pt was selected for further quantitative experiments. Most of these further tests were realized considering a mould in Fused Silica and the D263 glass, since those materials had been selected for the cylindrical slumping experiences. Few more tests were later performed with Silicon mould and D263 glass, showing the same behaviour of the Pt layer also on Silicon substrate. The subsequent step foresaw the final decision on where to deposit the release layer: on the mould surface or directly on the optical surface of the glass foil being shaped. Also if the second option would have been preferable so to already have on the glass, at the end of the slumping process, a stress-free reflective layer, it was demonstrated not to be applicable. During the thermal cycle, the Pt layer on the glass undergoes a visible degradation, measured and reported in Fig. 6.13 in terms of PSD, which set it out of the optical requirements range. The application of the antisticking layer on the mould came out to be the only appropriate solution.

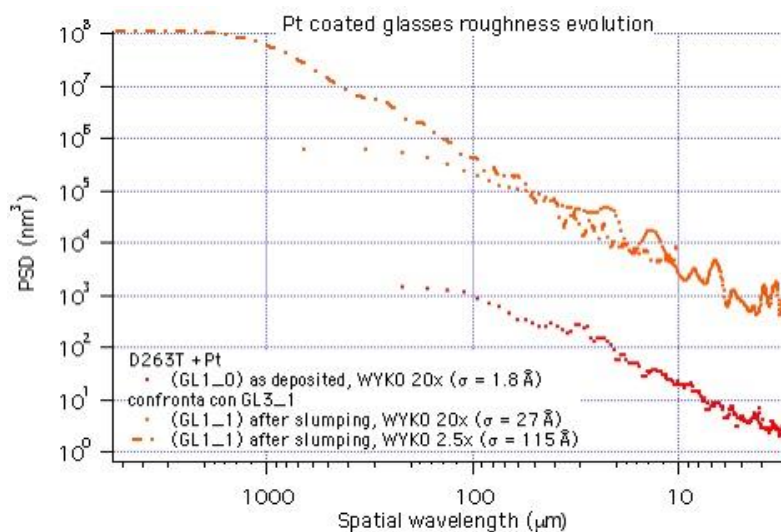


Fig. 6.13: Degradation of the Pt layer roughness as measured by WYKO and expressed in terms of PSD.

The Pt layer was deposited by evaporation technique by Media Lario Technologies (industrial partner of INAF-OAB). In principle, the sputtering technique would have been preferable because of the generally higher adhesion of the deposited layer to the substrate. However, this solution was not applicable because of time constraint and deposition machine capability and availability. To enhance the relatively low adhesion of evaporated Pt layer on Fused Silica substrate (see Fig. 6.14), several solutions have been considered and tests have been performed to check their suitability. In particular, the application of a thin Cr interlayer (normally used to this aim for RT applications) and of a suitable thermal cycle (called thermal cycle of annealing) have been investigated and they came up to be valid solutions to solve the issue related to the coating adhesion. Currently, a Cr interlayer is applied in the same deposition run of the Pt layer: 5 nm of Cr are evaporated before the 50 nm layer of Pt. The thickness of 50 nm was selected as the best compromise given that thicker Pt layer would crack, while thinner layer would contain small holes, i.e. not coated areas.

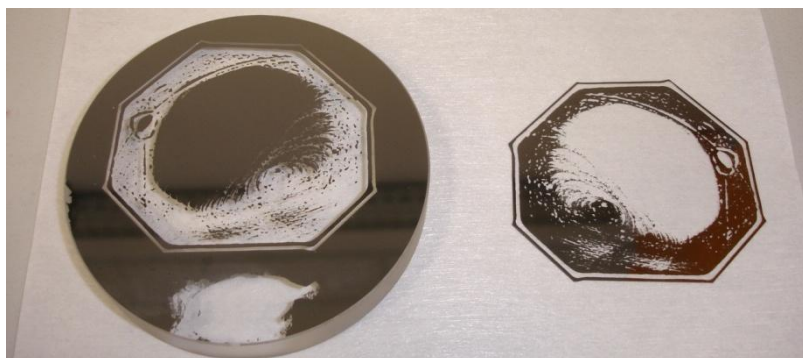


Fig. 6.14: This test evidenced for the first time the necessity of improving the evaporated Pt release layer adhesion to the substrate; it actually worked as antisticking, but part of it migrated to the glass surface. In this case the annealing thermal cycle was performed but the Cr layer was not yet present (PS-IXO-31).

The annealing thermal cycle is depicted in Fig. 6.15: it is realized inside the muffle in a controlled Ar atmosphere to prevent oxygen presence and the maximum reached temperature is close to the maximum temperature reached during the slumping of glass plates, 580°C.

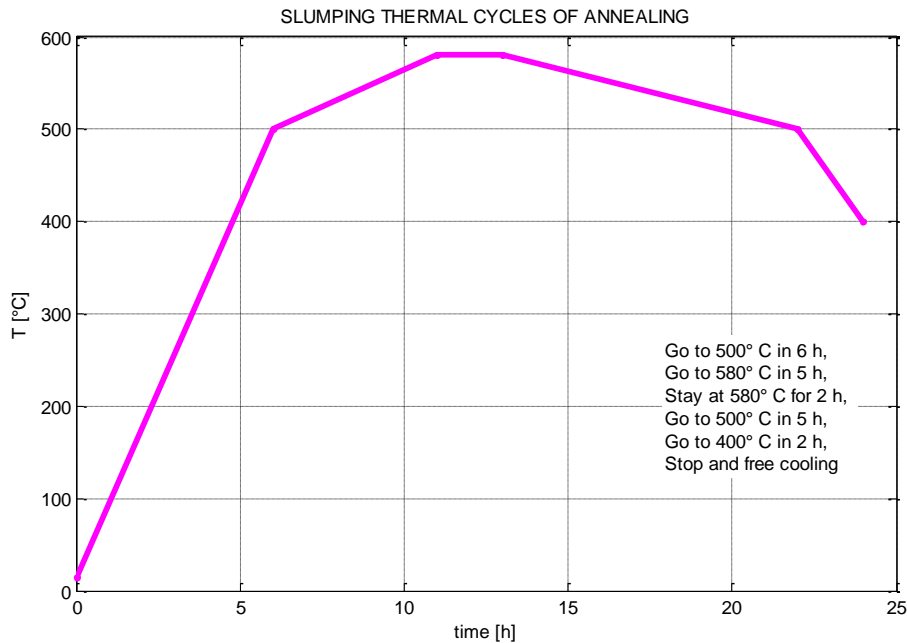


Fig. 6.15: Typical thermal cycle of annealing employed to enhance the Cr+Pt coating adhesion to the mould surface.

Despite the good behavior at “macroscopic” level (it indubitably prevent glass to stick on the mould), the “microscopic” performances of the Pt layer are not so good; when subject to repeated thermal cycles, the Pt coating surface suffers from degradation. This degradation might be divided in two different phenomena:

1. The roughness of Pt layer increases after each thermal cycle and in particular during the first thermal cycle of annealing. This phenomenon is known as Hillock effect: Pt agglomerates appear on the layer due to Pt atoms migration at high temperature [127]. In this case, the degradation might transfer on the glass slumped plate in the form of microscopic holes on its surfaces (depending on T and p process parameters, see § 6.2.5). They are due to the imprinting of the roughness of the mould into the glass and are directly connected to the value of applied pressure: the higher the pressure, the higher the degradation (keeping constant all the other parameters) since higher is the percentage of mould roughness replicated in the glass. Despite the roughness degradation, Pt layer

was used as release layer on the Fused Silica moulds employed to test the performances of the slumping for the manufacturing of precise cylindrical surfaces. Process parameters could be set in such a way to preserve the original microroughness of the glass, avoiding the mould surface roughness replication during the process. This is indeed a very important result that allows re-considering Zerodur K20 as candidate materials for the manufacturing of slumping mould. It is here remind that it was not selected at the beginning of the study because of its relatively low surface polishability. Using a mould with surface roughness of 70-80 Å rms in the AFM range, the roughness is not replicated in the glass surface with pressure values of 50-80 g/cm² or lower. The degradation starts at higher pressure values or at higher mould surface rms. In fact, slumping onto a mould with lower surface finishing, holes start to appear in the glass surface also at a pressure of 80 g/cm². This is one of the main results coming from this study: by properly setting the value of pressure applied during the slumping process, it is possible to maintain the original microroughness of the glass also with a not super-polished mould. This allows for mould procurement time and cost to be reduced. One second effect might happen on the Pt coating layer, after the application of the annealing thermal cycle. That has not to be confused with the Hillock accretion. It appears as a huge number of uniformly distributed pits on the mould surface and is related to a not suitable cleaning procedure of the part before the deposition of the layer. This effect has been encountered during the very first tests and it was possible to eliminate it by applying an additional cleaning step, realized by ultrasonic cleaning, before the coating deposition on the mould.

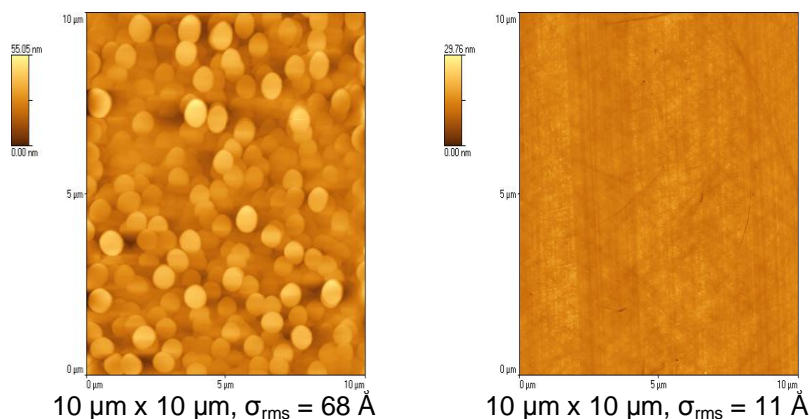
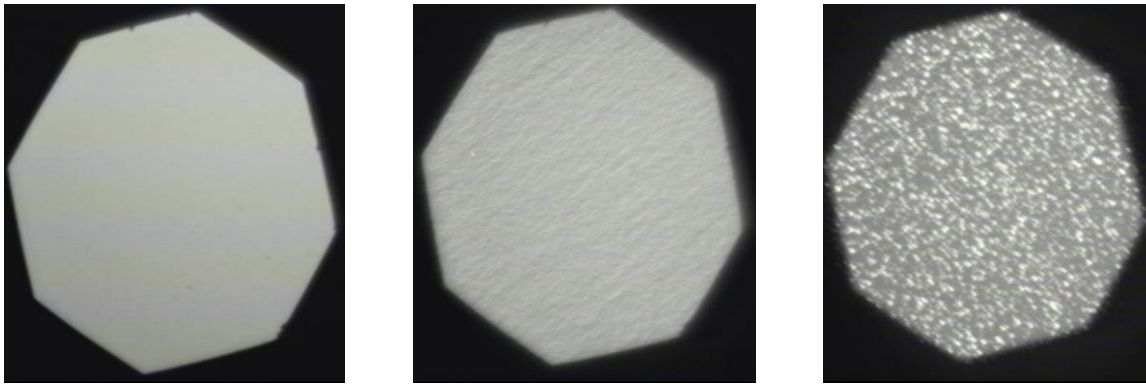


Fig. 6.16: (Left Side): AFM image taken on MCX2 mould after the annealing thermal cycle (PS-IXO-53). The visible effect is due to the Hillock accretions of Pt agglomerates. (Right Side): AFM image of the same coating as it appears before the annealing thermal cycle.



MCX2 before annealing

MCX2 after annealing

CVI2 after annealing

Fig. 6.17: (Centre): The Hillock effects as seen with the Nomarki microscope (20X magnifications) compared to the effect introduced by the not-suitable cleaning procedure before coating (Right Side). The two effects are both characterized by the presence of pits on the coating surface; however their scale is completely different. (Left Side): For comparison, the image on the left shows the Cr+Pt coating after the deposition on the MCX2 mould but before the application of the annealing thermal cycle.

2. After several thermal cycles, Pt starts to migrate from the mould to the glass, contaminating its surface. In this case, the degradation transfers to the glass as a presence of pick structures on its surface, like contaminants.

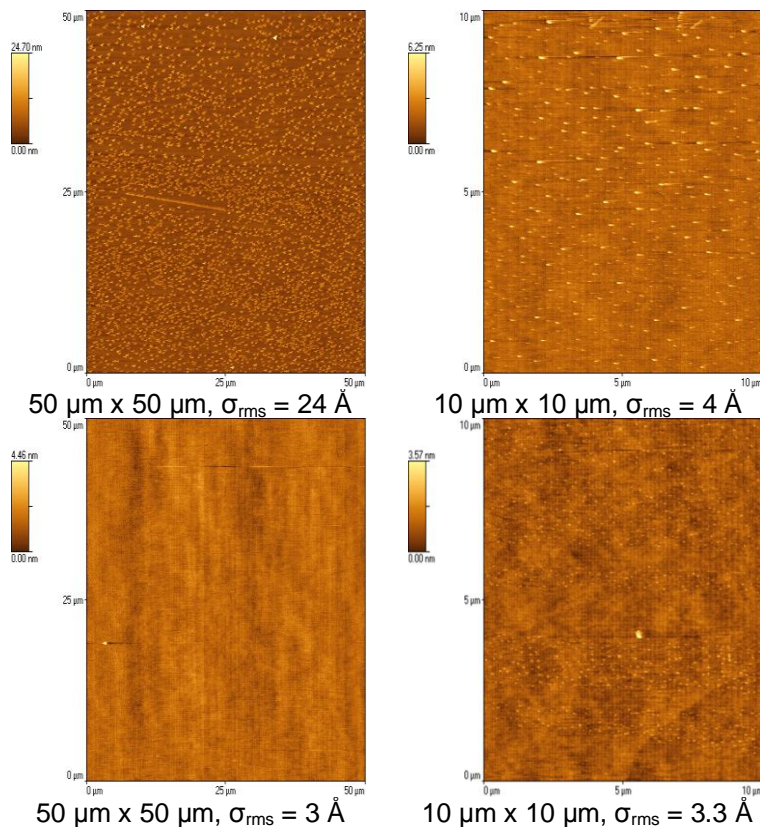


Fig. 6.18: AFM images that shows the problem of Pt atoms migration to the slumped glass after several thermal cycles. Images refer to glass obtained with tests PS-IXO-72 (the first three), and PS-IXO-74 (the last one). They were the 8th and 9th slumping performed on MCX2 and this effect started to appear at that time.

The Cr + Pt antisticking layer was tested also on Silicon to check its behavior on that material. The used substrates were Silicon wafer from the electronic market: they have diameter of 100 mm and thickness of 0.7 mm. The obtained results showed that the Cr + Pt layer behaves the same way as it does on Fused Silica substrate: it actually works as antisticking, however it suffer from the Hillock formation that degrades its surface roughness. Only 3 consecutive slumping tests have been performed on the same mould and the Pt migration on Pt has not been observed yet.

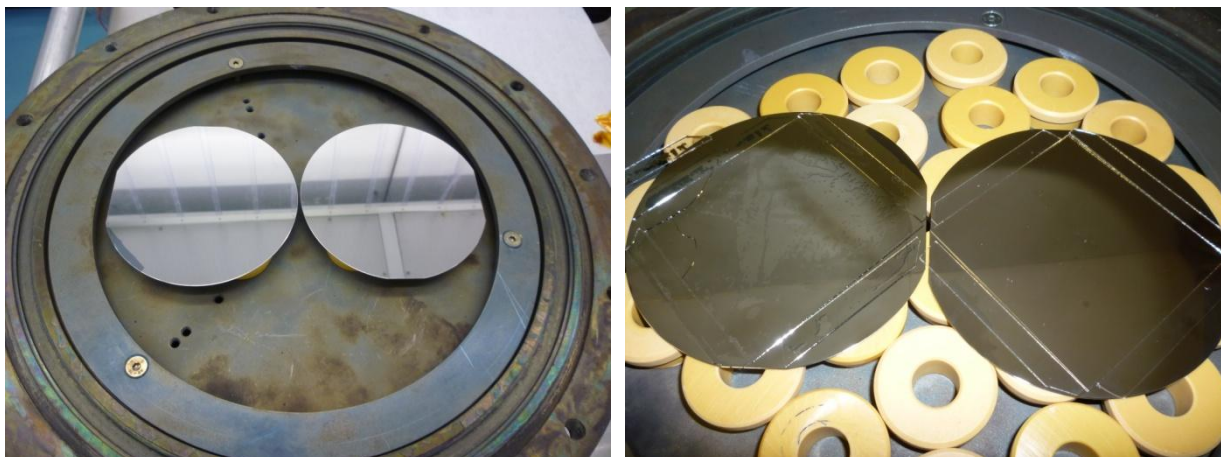


Fig. 6.19: Example of slumping experiences realized on Silicon mould with Cr + Pt release layer. (Left Side): Annealing thermal cycle (PS-IXO-85) on the antisticking layer on Silicon wafers used as mould: sample on the left is coated only with Pt; sample on the right is coated with Pt plus an interlayer of Cr. (Right Side): First slumping experience on Silicon mould with annealed antisticking layers (PS-IXO-88). Sample with only Pt suffer from Pt migration on the glass.

Pt has been demonstrated to be a good release layer in the case of Fused Silica or Silicon mould and glass D263. However, the experienced degradation might require the re-coating of the mould after few thermal slumping. To further optimize the production chain and avoid this necessity, research are underway to individuate new release agents other than Pt; Silicon Nitride is actually under investigation for a possible use on Silicon mould as it is reported in literature to be a good release agent in glass molding processes [128]. Silicon mould is considered instead of Fused Silica because of its higher thermal conductivity. At the moment of writing, a sample was realized with this coating and the annealing thermal cycle was performed. It consists of a thick Silicon wafer with diameter 100 mm and thickness of 7 mm, coated with 100 nm of sputtered Silicon Nitride. However, a problem of cleaning was experienced before the coating deposition and the thermal cycle of annealing highlighted all the effects: also to the naked eye the coating shows halos. Despite this, the mould has been used for a first slumping cycle (PS-IXO-117) to check the suitability of the Silicon Nitride coating as antisticking layer. The test gave a positive result and a second mould with the same coating is at the moment under production to eliminate the cleaning problem and evaluate if the Silicon Nitride coating suffer from the same effect of atom migration to the glass surface after several cycles.

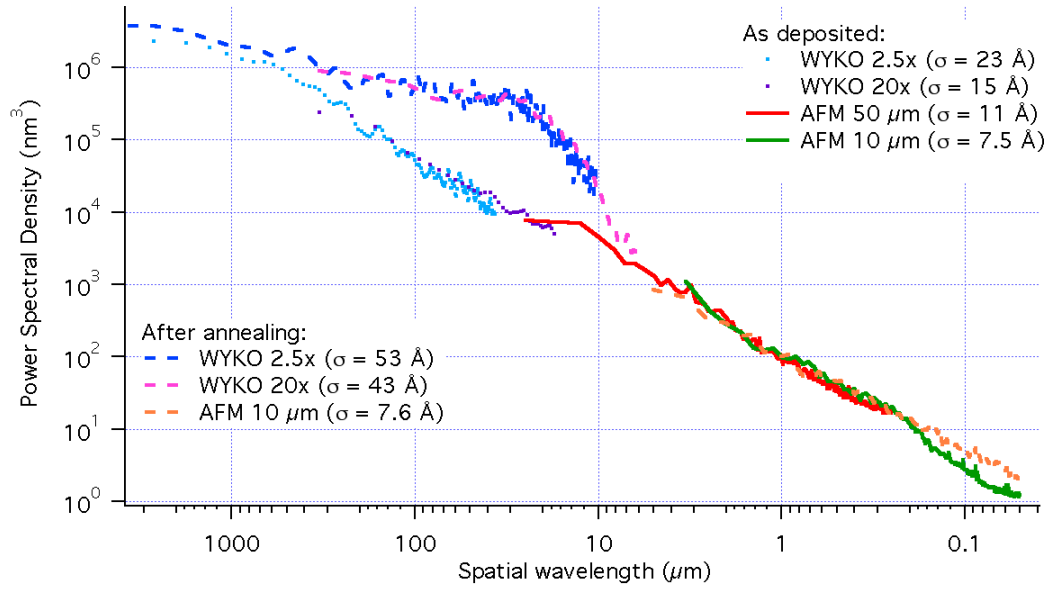


Fig. 6.20: Roughness degradation of the Silicon Nitride coating shown as PSD plot.

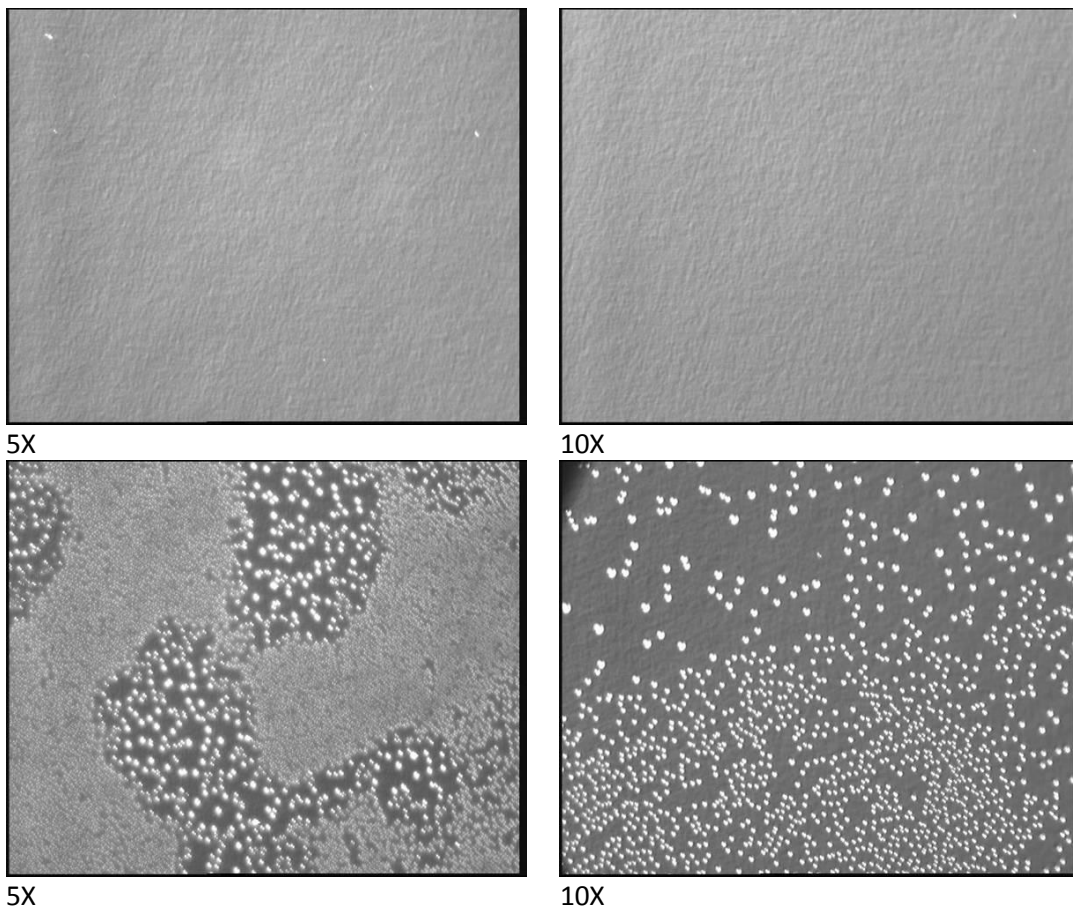


Fig. 6.21: Nomarski images at 5X and 10X magnifications taken on the Silicon mould with a coating of Silicon Nitride. (Top Row): the coating as it appears after the deposition. (Bottom Row): the coating as it appears after the annealing thermal cycle (PS-IXO-114). Problems of cleaning were experienced before the deposition of the coating and the annealing thermal cycle highlight the effect, not to be confused with the Hillock one.

6.2 Cylindrical slumping on procured moulds

The main scope of the project is to demonstrate the suitability and potentiality of the technology for the realization of slumped and integrated X-ray mirror segments able to deliver the required performances of 5 arcsec HEW, with a goal of 15 arcsec accepted for the first prototypes. It has been therefore crucial to work since the beginning on representative shapes and dimensions. As described in chapter 5, cylindrical convex moulds with dimension of 250 mm x 250 mm and Radius of Curvature of 1 m have been procured to work with glass plates of dimension 200 mm x 200 mm.

6.2.1 Cylindrical slumping moulds characterization

All the activities on cylindrical slumping have been realized using two moulds made in Fused Silica (first phase of the project) and one mould realized in Zerodur K20 (second phase of the project). A second mould in Zerodur K20 has been realized but has not been used so far for slumping. Silicon material was also considered for mould production; however the Silicon mould was not available for slumping experiments at the time of presented research. This section reports on the characterization and preparatory activities performed on the moulds before they could be employed in the slumping experiments. The two moulds used during the first set of cylindrical slumping test are named MCX1 and MCX2. They have the same characteristics, the second being initially realized as the backup of the first one as risk mitigation action in case of contingency. Both have been manufactured in Fused Silica by the firm Hellma Optik Jena, specialized in the production of cylindrical optical components. After their delivery, they have been coated with an antisticking layer of 50 nm evaporated Pt plus an interlayer of 5 nm Cr so to avoid problems of glass adhesion during the slumping, and the annealing thermal cycle was performed. Two complete measurement campaigns were performed on MCX1 and MCX2 moulds: at delivery and after the application of the release layer. The characterizations were entirely performed at INAF-OAB laboratories and comprised longitudinal and azimuthal profile scans performed with LTP (in its nominal configuration or mounting the CHRcodile optical sensor), roughness measurements performed with WYKO and AFM, and Nomarski qualitative images. The requirements have not been completely obtained from the producer, as evidenced by the main results summarized in Table 6.3. However, even if they were not in the specific, due to the time constrain posed by the aggressive schedule of the project, the two moulds had to be used for cylindrical slumping experiments. At some point of its life, mould MCX2 was reconditioned to eliminate, after several repeated thermal cycles, the degraded Pt layer; it was re-polished and coated again with a release layer of Cr+Pt. For this reason its name was changed in MCX2_B. One mould in Zerodur K20 has been in house realized for the first set of cylindrical slumping experiments to be carried out during phase two of the project. MK20-01, as it is named, has been largely used even if its

characteristics in terms of shape and roughness were not optimal. The decision of using a not optimal mould was forced by schedule constraints and by the necessity to check the behavior of this material while waiting for the new mould MK20-10 in Zerodur K20 to be produced by Hellma. The last one has been delivered in late summer 2011. A first characterization campaign has been already realized on it. It is here remind that moulds in Zerodur K20 do not need any antisticking layer and so no preparatory activities are necessary before their use in the slumping experiments. The results of all the characterizations performed on the available moulds are summarized in Table 6.3 and reported in the following pictures.

Table 6.3: Summary of the characteristics of the moulds used during the presented research activities.

Mould	Requirement	MCX1	MCX2	MCX2_B**	MK20-10	MK20-01 [†]
Radius of Curvature	1000 ± 5 mm	1001.55 mm	996.88 mm	999.15 mm	999.4 mm	999.6
Profile accuracy	< λ/8 (on 80mm windows)	> λ/8	> λ/8	> λ/8	≤ λ/8	» λ/8
Profile P-V	0.5 μm	3 μm	2.2 μm	4.1 μm	0.44 μm	30 μm
Surface roughness	< 5 Å @ AFM spatial frequ. (goal 2.6 Å)	9 - 12 Å @ AFM spatial freq.	6 - 12 Å @ AFM spatial freq.	9 - 10 Å @ AFM spatial freq.	90 - 180 Å @ AFM spatial freq. (TBC)	58 - 136 Å @ AFM spatial freq.
HEW (inferred from the profile metrology)	5"	11.7"	8.6"	31"	2.6 – 3.4"	> 200"
XRS* contribution to HEW delivery	~ 0	2"	3"	3.2"	N.A.	N.A.
XRS* contribution to HEW after antisticking application	~ 0	> 4.5"	> 4.5"	> 4.5"	N.A.	N.A.

* X-Ray Scattering contribution to the HEW at 1 keV (2 refl. 0.72 deg inc. angle).

**At some time in its life, mould MCX2 has been reconditioned, meaning it was re-polished and coated again with the Cr+Pt antisticking layer: for this reason it is referred as MCX2_B

[†]MK20-01 was realized in house to start working on Zerodur K20 material while waiting for the mould MK20_10 to be realized by Hellma; its characteristics are not optimal in terms of shape and roughness.

- SHAPE CHARACTERIZATION OF MOULDS MCX1, MCX2 & MCX2_B, MK20-10, and MK20-01

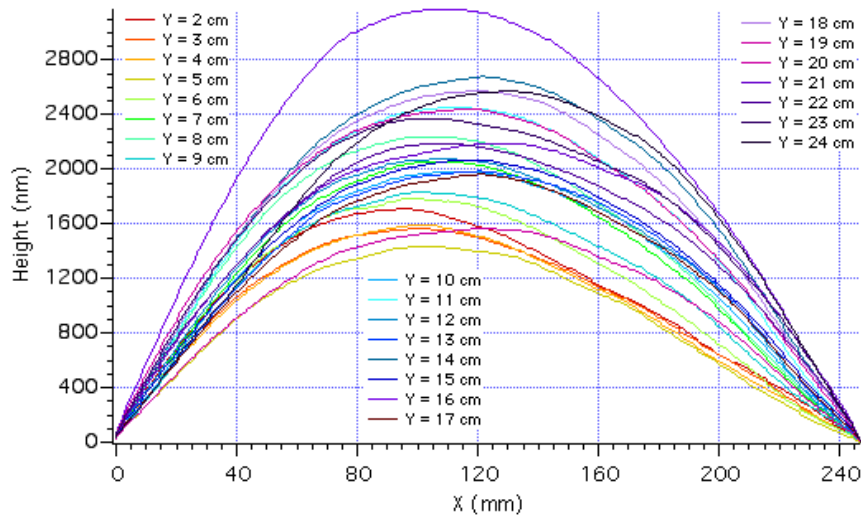


Fig. 6.22: Example of MCX1 mould longitudinal profile measurements taken with LTP: 24 profiles are shown at different distances from the mould lateral edge.

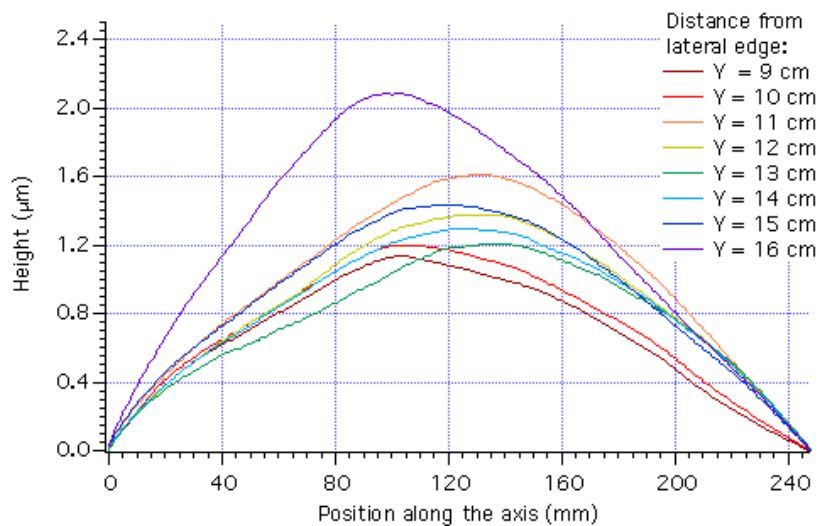
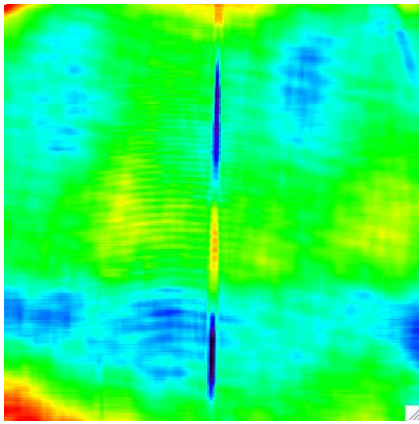


Fig. 6.23: Example of MCX2 mould longitudinal profile measurements taken with LTP: 9 profiles are shown at different distances from the lateral edge. An improvement in the mould manufacturing has been observed (sag values slightly lower).



P-V = 64 nm (fringing removed)

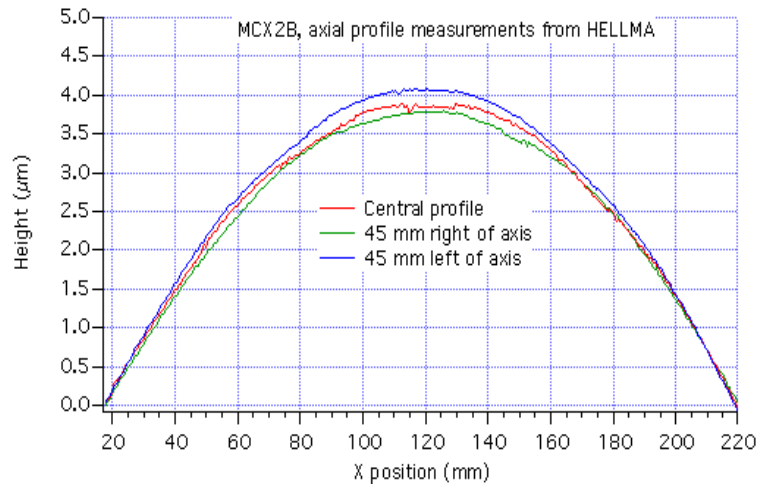
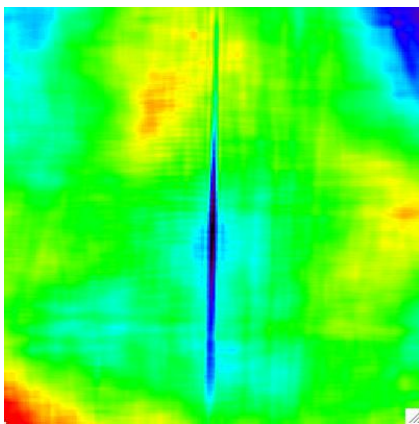


Fig. 6.24: (Right Side): MCX2_B interferometric profiles as provided by Hellma manufacturer. In house characterization with LTP confirmed these data. (Left Side): 2D interferometric maps of mould MCX2_B as measured by Hellma on areas of 54 mm x 54 mm: the requirements of $\lambda/8 = 80$ nm is reached.



P-V = 73 nm (fringing removed)

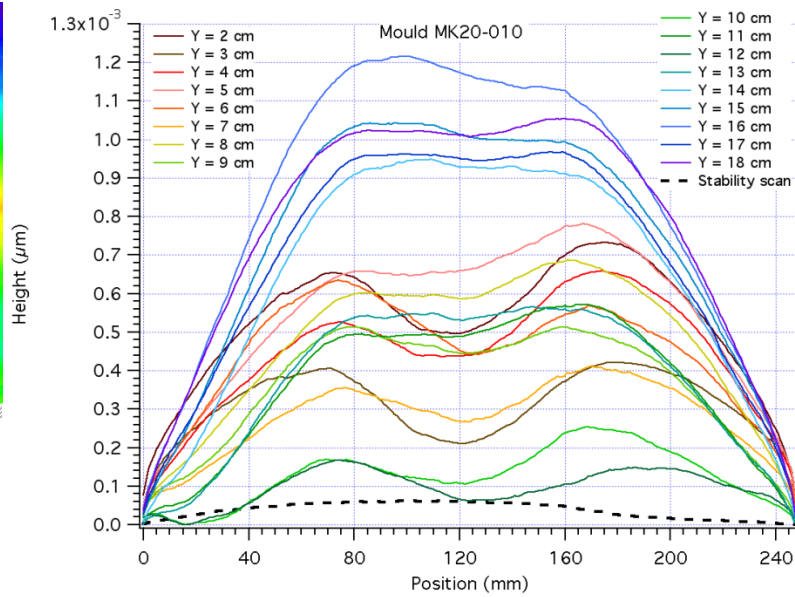


Fig. 6.25: (Right Side): MK20-10 longitudinal profiles realized with LTP at different longitudinal position, at the indicated distance from the lateral side of the mould. (Left Side): 2D interferometric maps of mould MK20-10 as measured by Hellma on areas of 54 mm x 54 mm: the requirements of $\lambda/8 = 80$ nm is reached.

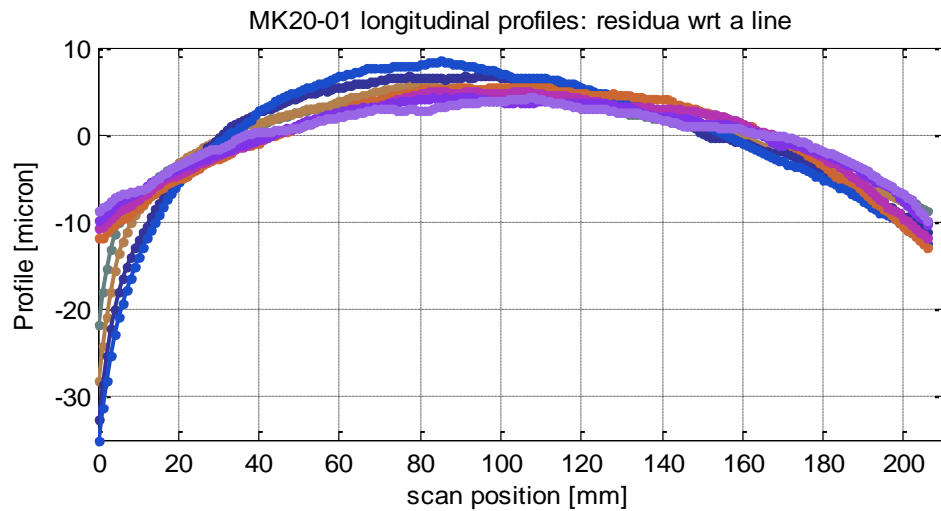


Fig. 6.26: MK20-01 profiles as acquired with CHRcodile optical sensor on LTP carriage. The sag values of these profiles are very high. However the mould was used, while waiting for the “good” one to be produced, to test the behavior of Zerodur K20 material for mould in case of D263 glass.

- ROUGHNESS CHARACTERIZATION OF MOULDS MCX1, MCX2 & MCX2_B, MK20-10 and MK20-01

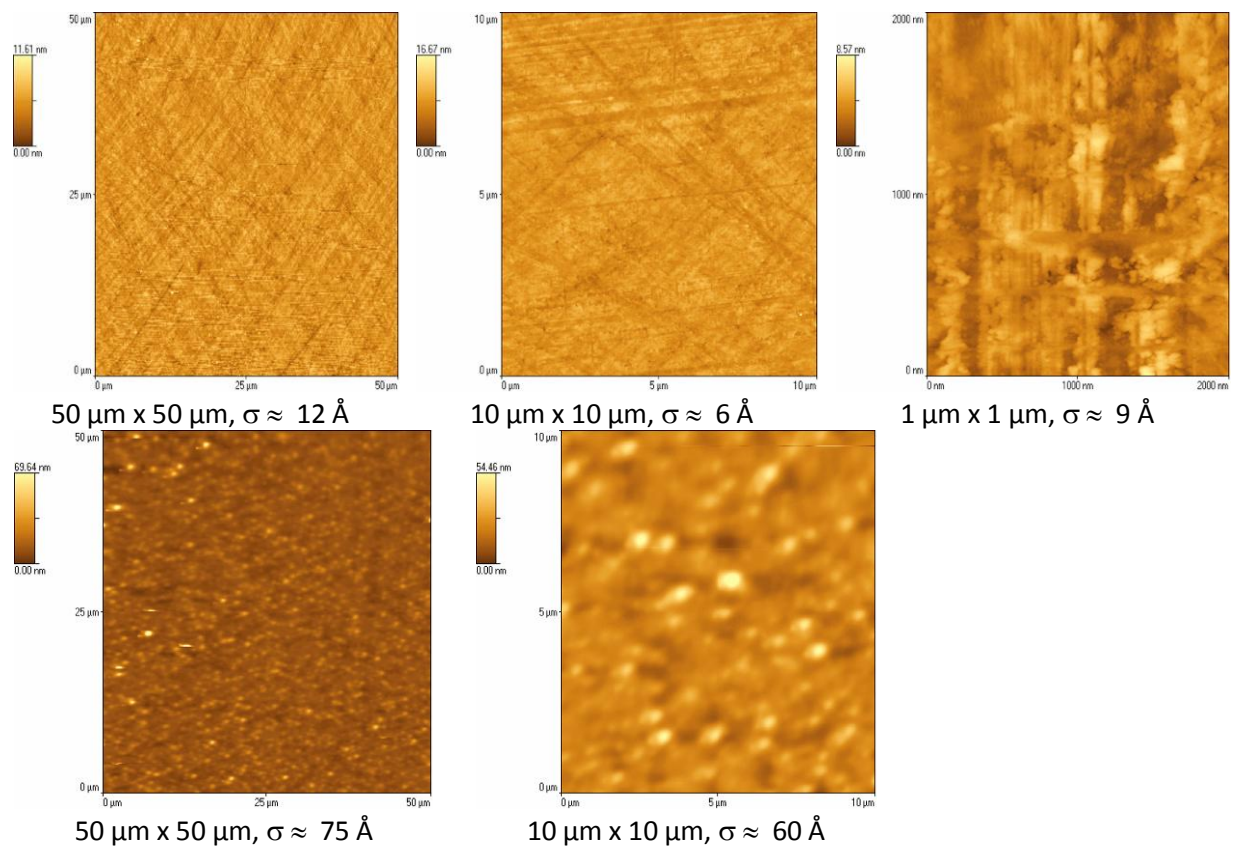


Fig. 6.27: AFM measurements of MCX1 mould as delivered by Hellma Optik (First Row) and after the annealing thermal cycle PS-IXO-37 (Second Row). The axis scale in the upper right images is doubled. The actual size is 1 micron: the optical axis of the mould is oriented like the x-axis in the images.

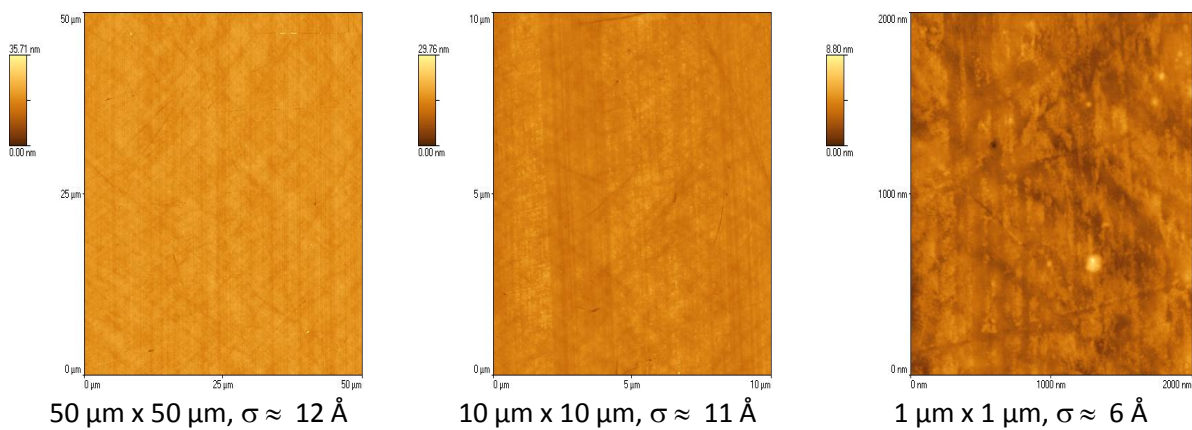


Fig. 6.28: AFM measurements of MCX2 mould as delivered by Hellma Optik: (Left Side) 50 μm x 50 μm scan range; (Center) 10 μm x 10 μm scan range (Right Side) 1 μm x 1 μm scan range. The axis scale in the right images is doubled. The actual size is 1 micron. The optical axis of the mould is oriented like the x-axis in the images.

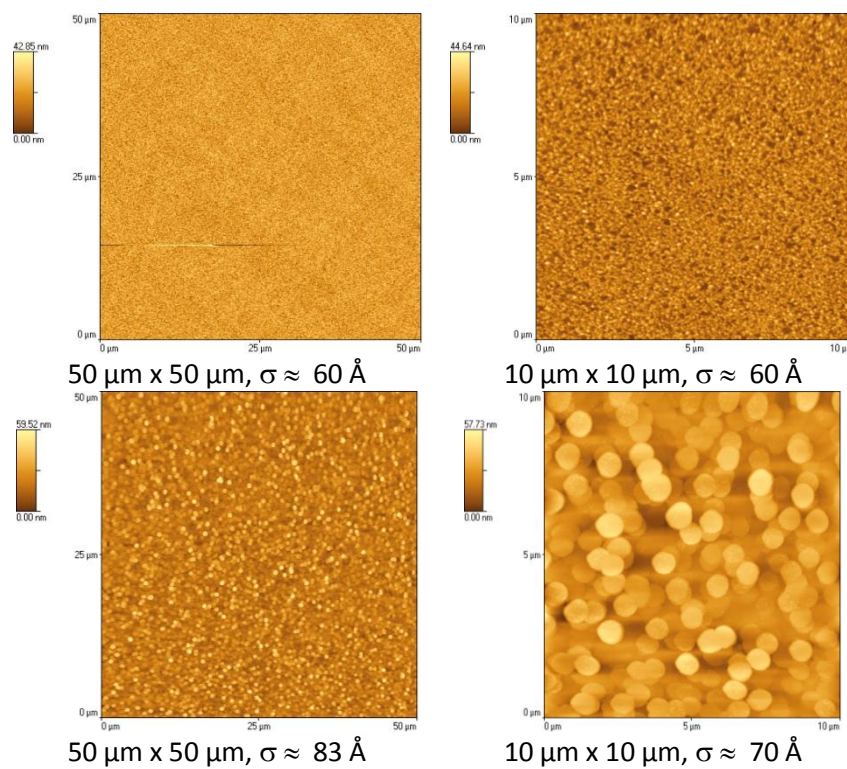


Fig. 6.29: AFM measurements of MCX2 mould after coating application and annealing PS-IXO-53 (First Row), and after several thermal cycles (Second Row).

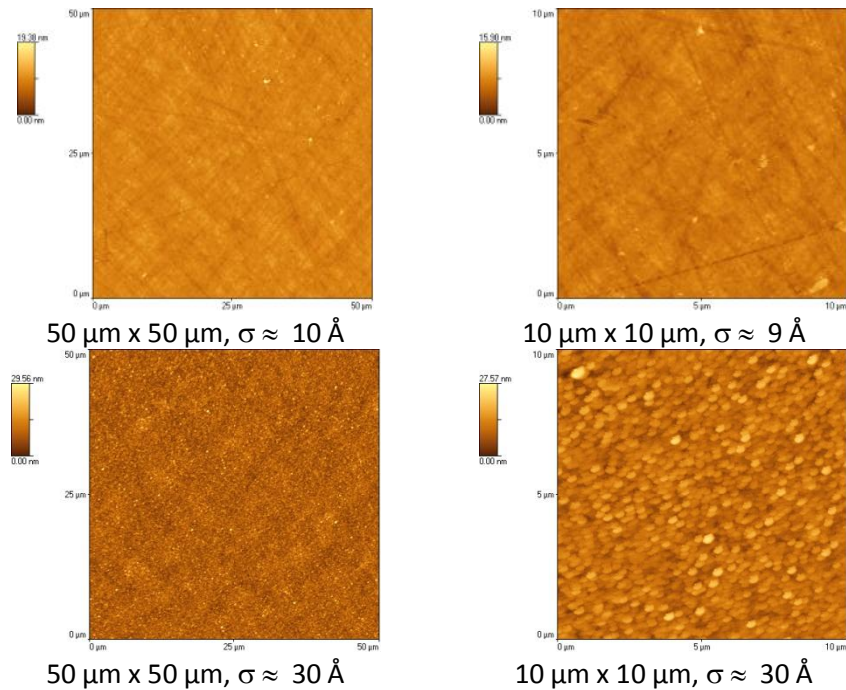


Fig. 6.30: AFM characterization of MCF2_B mould at its delivery by Hellma (First Row) and after the annealing of the Cr+Pt antisticking layer PS-IXO-126 (Second Row).

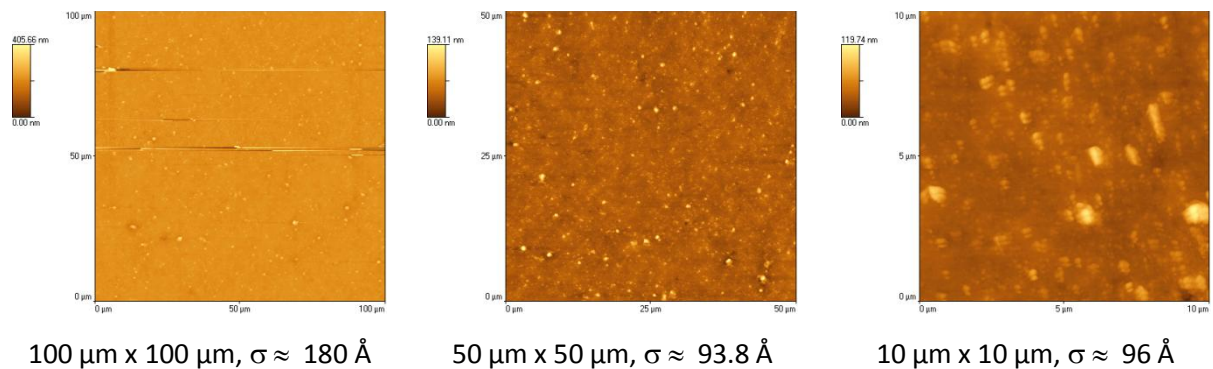


Fig. 6.31: AFM preliminary characterization on mould MK20-10 as delivered by Hellma Optik. The values are very high and contrast with the data given by the producer. They are probably affected by cleaning issue and AFM calibration problems that are presently under evaluation (TBC).

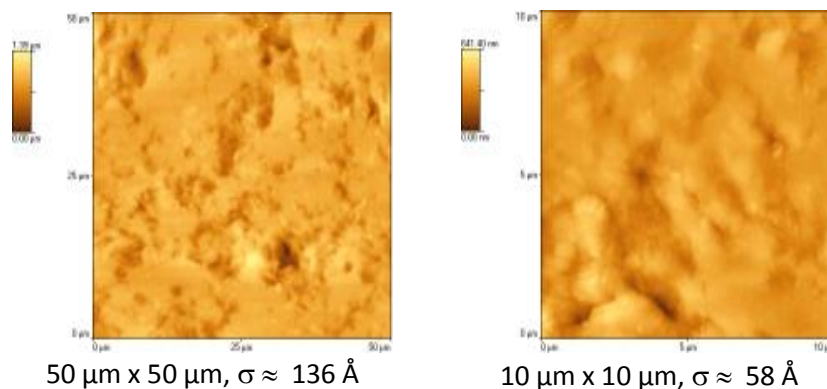


Fig. 6.32: AFM characterization of mould MK20-01. It was realized in house to start working while waiting for the delivery of the ordered one; so it is not polished and the roughness is very high.

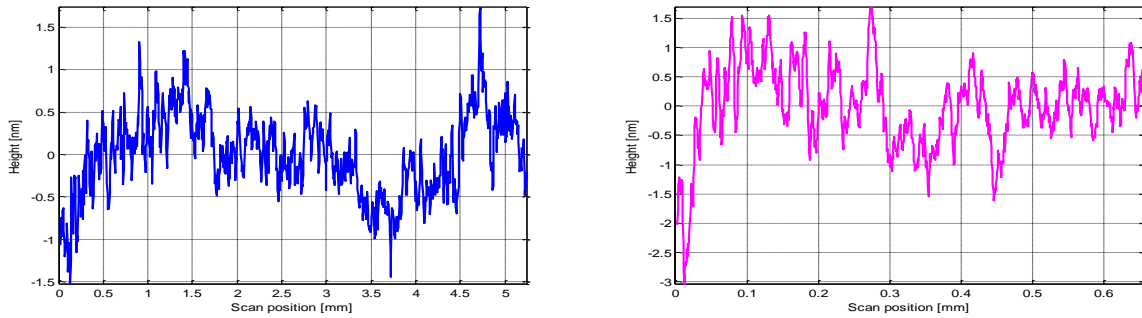


Fig. 6.33: Example of rough WYKO profiles acquired on mould MCX1, as delivered by the vendor (MCX2 profiles are very similar). (Left Side): 2.5X magnification: PV = 3.2 nm, rms = 0.4 nm. (Right Side): 20X magnification PV = 4.7 nm, rms = 0.7 nm.

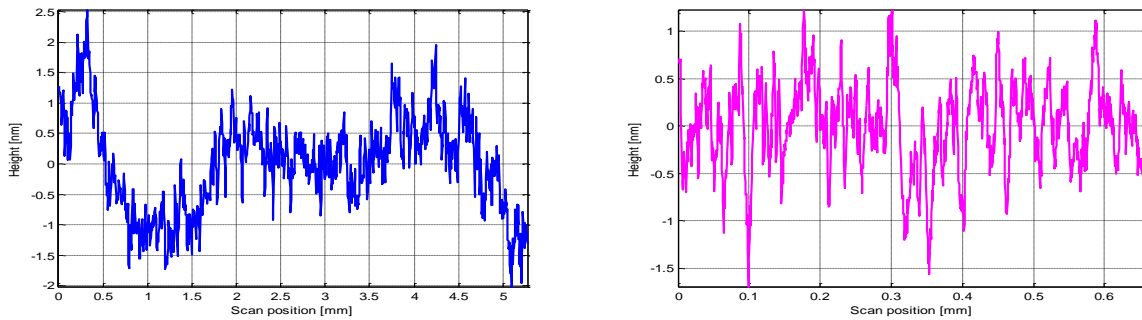


Fig. 6.34: Example of rough WYKO profiles acquired on mould MCX2_B. (Left Side): 2.5X magnification: PV= 4.5 nm, rms=0.7 nm. (Right Side): 20X magnification: PV=2.9 nm, rms=0.4 nm.

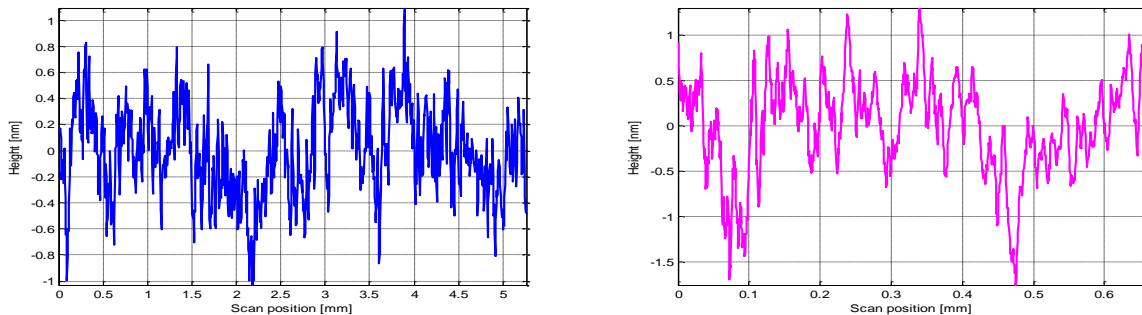


Fig. 6.35: Example of rough WYKO profiles acquired on mould MCX2_B, after the annealing thermal cycle. (Left Side): 2.5X magnification: PV = 2.2 nm, rms = 0.4 nm. (Right Side): 20X magnification: PV = 3.1 nm, rms = 0.5 nm. Note how the Coating degradation, due to Hillock effect, interests AFM frequencies but does not have strong effects on WYKO frequencies.

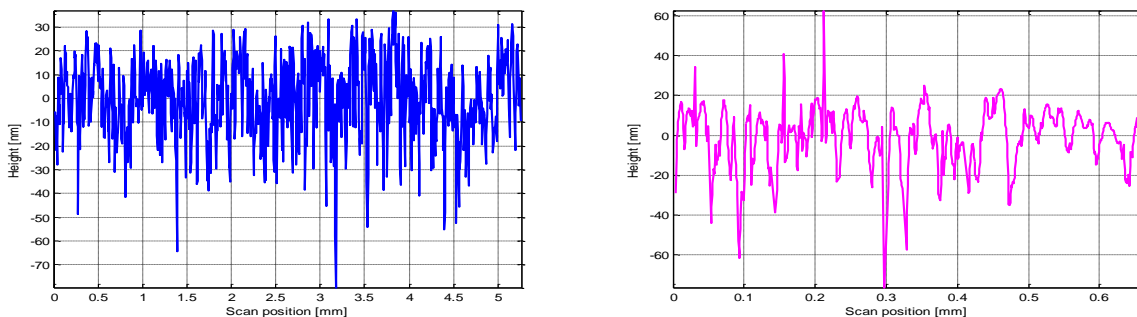


Fig. 6.36: Example of rough WYKO profiles acquired on mould MK20-01, realized in house. The characterization was not easy since the WYKO CCD lost points with low reflectivity because of the poor surface finishing of the sample. (Left Side): 2.5X magnification: PV = 116 nm, rms = 16.3 nm. (Right Side): 20X magnification: PV = 139nm, rms = 13.7 nm.

All the roughness data are hereafter summarized for each mould, in terms of PSD plot. The PSD of mould MK20-10 is still in elaboration phase.

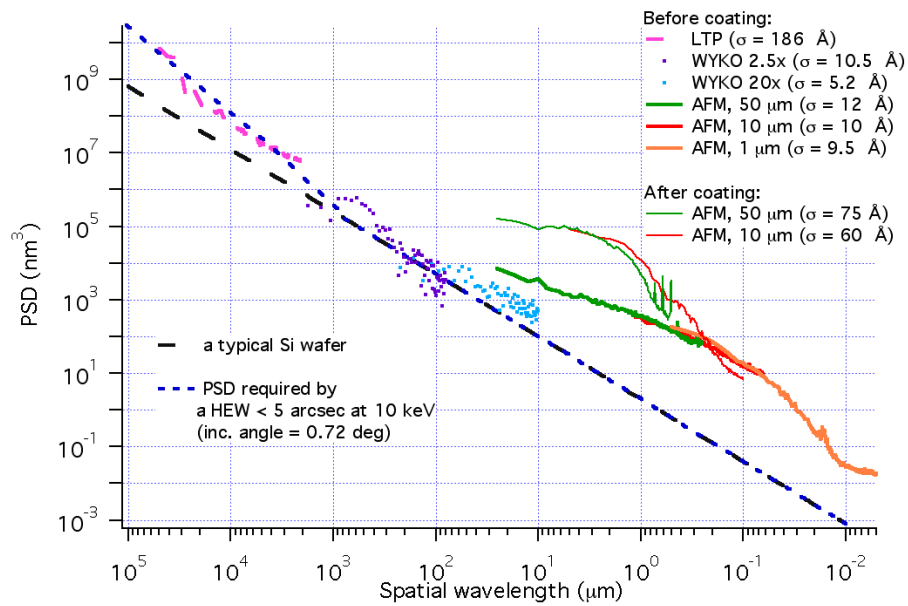


Fig. 6.37: Comparison of PSDs evaluated for MCX1 mould before and after coating application and annealing, as derived from available metrological instruments at INAF-OAB.

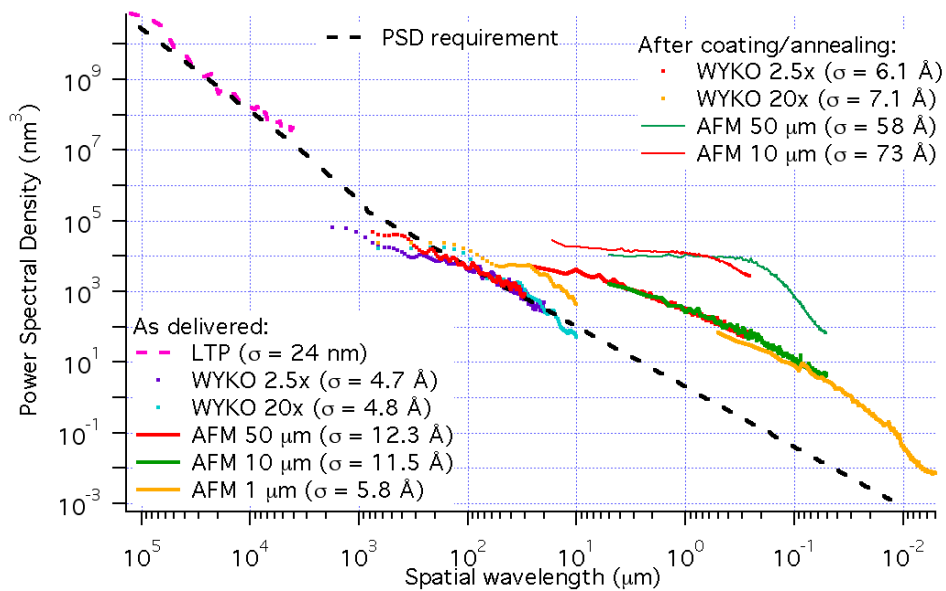


Fig. 6.38: PSDs evaluated for MCX2 mould after annealing as derived from available metrological instruments at INAF-OAB.

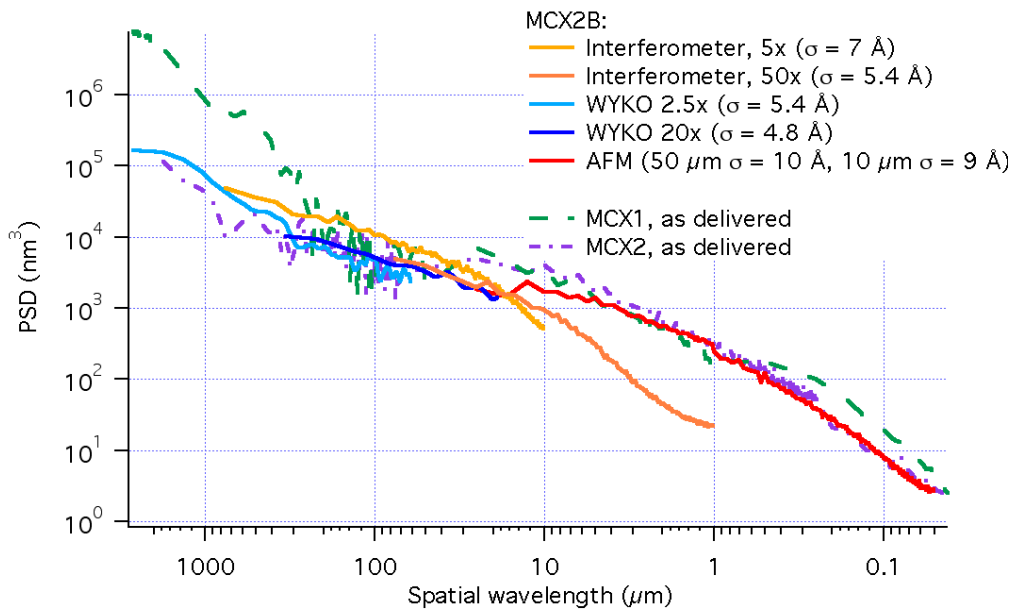


Fig. 6.39: PSD of surface roughness of mould MCX2_B, compared with that of mould MCX1 and MCX2.

For completeness, it is mentioned that a new mould in Silicon is currently under polishing at Hellma Optik and its delivery is expected for the end of September 2011. It will be used for slumping tests to check the behavior of a material with higher thermal conductivity that should help in lower thermal gradients and speed up the process.



Fig. 6.40: Images of the moulds in different material used during the research activities: Fused Silica mould, Zerodur K20 mould, and Silicon mould.

6.2.2 Schott glass D263 characterization

The glass used for the present research activities is Schott glass D263. Until one year and an half ago, it was called glass D263T; now it is normally referred to as D263ECO. The change in the last letters of nomenclature reflects a change occurred in the production chain; some substances¹⁸ are not used any more during this glass production because of the latest ecological regulation and are substituted by elements not dangerous for the environment. This change did not have any impact on the chemical composition and hence on the glass properties according to the vendor; indeed the two available product data sheets are exactly the same, apart for a really small difference in the c_p value ($c_p(20\text{ °C to }100\text{ °C})$ in $J/(g \cdot K) = 0.82$ and 0.75 for T and ECO type respectively). In 2010, Schott completely stopped the production of D263 glass of type T; few foils could be found for the last time on the market at some dealers' stocks, however the passage to the ECO type was unavoidable. During the passage period (let's say the first and second year of the study) several tests have been performed both with T and ECO glass types and no differences were noticed on the behavior of these glasses and on their response to the slumping process. For this reason, throughout the whole text, apart for this paragraph, the glass is referred to as Schott D263 without specifying the exact type. Glass D263 is a clear borosilicate glass produced in flat foils of maximum dimension of 440 mm x 360 mm, with thickness ranging from 0.03 mm to 1.1 mm. For the purposes of this study, glass sheets of dimension 200 mm x 200 mm and thickness of 0.4 mm were used. The foils have been cut at the required dimension using the laser cutting technology and preliminary tests have been performed on other cutting techniques (see later, paragraph 6.2.2.1). On representative sets of glass samples, characterizations have been performed to have the initial situation to be compared with the results of the slumping processes. Besides, this initial measurement campaign was also intended as quality assurance check and was quite useful to acquire familiarity with the material. The following pictures from Fig. 6.41 to 6.46 summarize the results, going from surface finishing to thickness variation and intrinsic shape characterization. Measured thickness variation in 200 mm x 200 mm glass foils ranges from $\pm 1\text{-}7\ \mu\text{m}$ for T type glass and $\pm 3\text{-}10\ \mu\text{m}$ for ECO type glass, in accordance with the value of $20\ \mu\text{m}$ thickness variation on a 400 micron thick glass given by the manufacturer Schott. The difference is due to the production batch, rather than to the different type of glass. The glass is produced by the down-draw method: it consists in an overflow process in which the glass is vertically drawn under the influence of gravity. During consecutive runs, the tool used for fluid glass overflow seems to suffer from degradation and this translates in larger thickness variations [128p]; however it is not easy to act on this parameter because of vendor proprietary right.

¹⁸ Lead and arsenic have been eliminated from the production chain for health and environmental reasons.

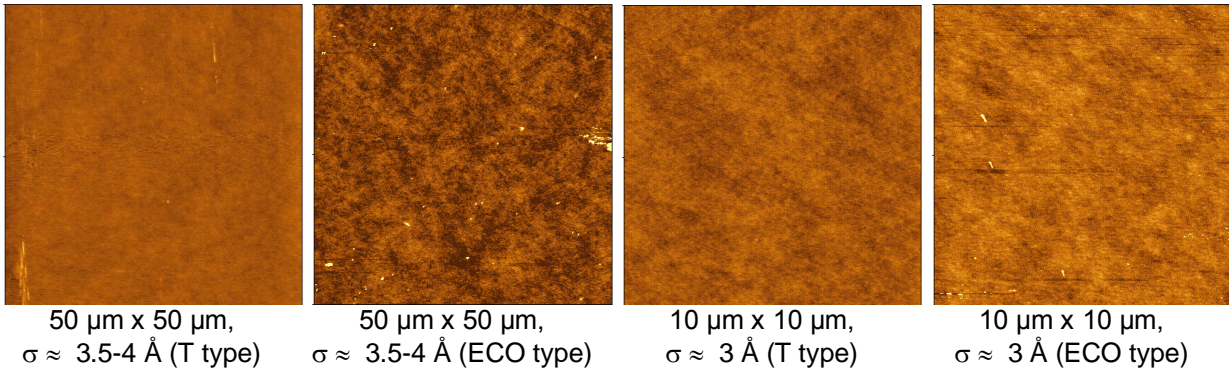


Fig. 6.41: AFM images of D263 glass as delivered by Schott: no differences were evidenced between the T and ECO type for what concern its AFM range micro-roughness.

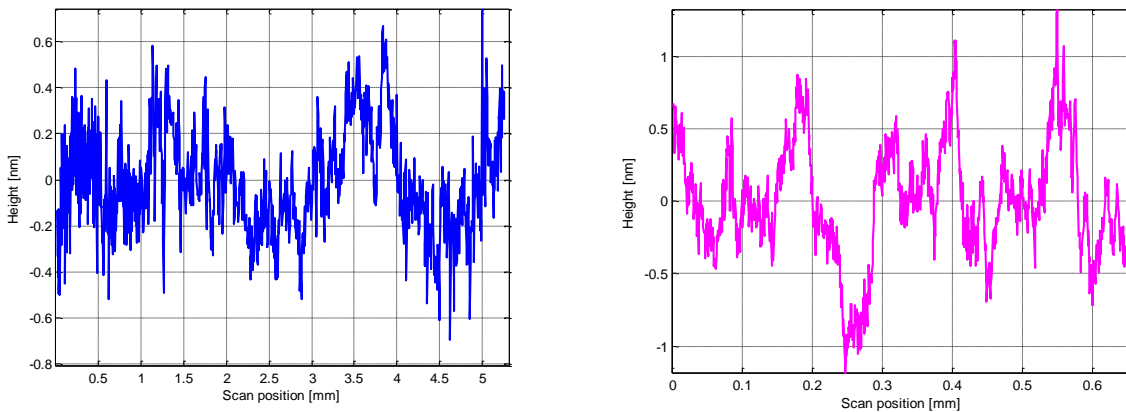


Fig. 6.42: Example of WYKO profile acquired with on D263 glass as delivered. (Left Side): 2.5X magnification PV = 1.5 nm, rms = 0.3 nm. (Right Side): 2.5X magnification PV = 2.5 nm, rms = 0.4 nm.

Since during the production there is never physical contact with the glass, the resulting product has extraordinary good flatness and uniformity with respect to other thin glass foils available on the market, particularly in the drawing direction. Thickness variations in the glass typically occur perpendicularly to the drawing direction. This process of glass manufacturing gives foils that are more homogeneous in the central area than at the edges; so, by choosing central pieces during the cutting process, the thickness variations can be as low as few μm . It has been verified that, when positioning the glass on the mould for the slumping, the drawing direction of the glass should be aligned with the mould's axis of symmetry since the performance of the optic is dominated by the slope errors along the optical axis, while slope errors in the azimuthal direction of the mirror are of the second order, suppressed by the ratio of the mirror radius and the telescope focal length.

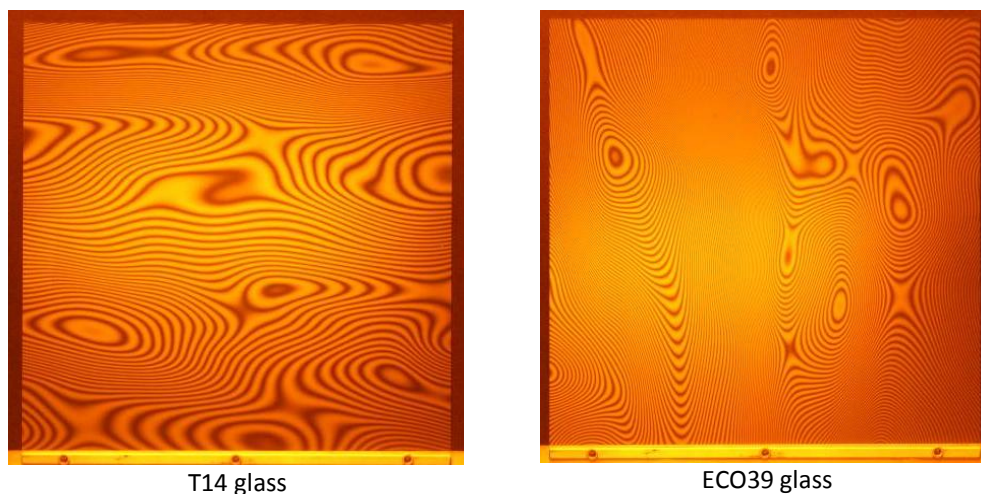


Fig. 6.43: Sodium light images of thickness variation on a foil of T and ECO glass taken under the sodium light (image courtesy: MPE colleagues). They appear pretty different: both fringes patterns present a preferential direction connected to the production process drawing direction, plus jeopardized zones; however the pattern is thicker in case of ECO glass type. This is related to the production run rather than to the type of glass itself.

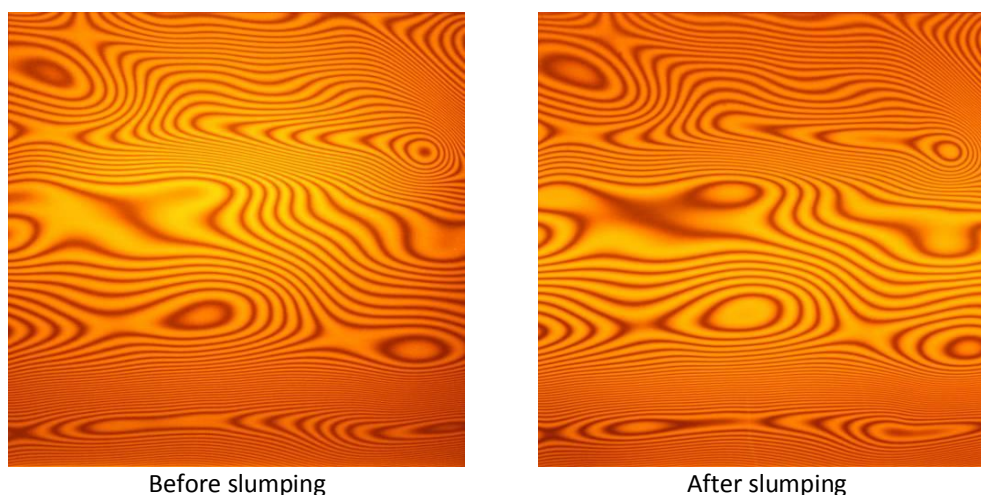


Fig. 6.44: Fringes of thickness variation under sodium light have been acquired on the same glass foil before and after the slumping process. No important differences in terms of thickness variations are observed after the cycle, also if some of them are flattened.

The intrinsic shape of the starting 200 mm x 200 mm glass foil is not flat: it presents sagittas on the two orthogonal directions parallel to the glass edges. The sagitta ranges on average from 150 to 250 in one direction and from 40 to 80 (with opposite sign) in the other direction. The computation of the intrinsic glass shape was realized by combining two measurements of the same scan line in order to subtract the deformation introduced in the sample by gravity. Four possibilities exist of positioning the glass foil on the mould for slumping. They have all been considered. It came up that this

parameter is of the second order with respect to the previous described thickness variation. When positioning the glass on the mould for the slumping, its drawing direction should be put parallel to the optical axis of the mould to optimize the results.

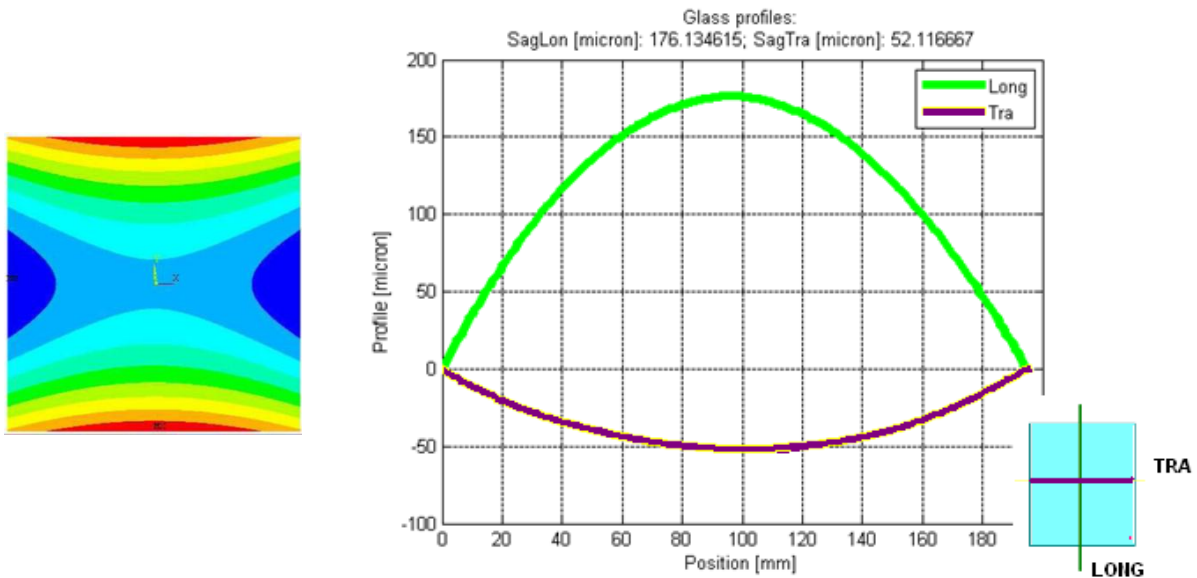


Fig. 6.45: The original intrinsic shape of the glass as delivered by the vendor is not flat but present saggittas up to 250 μm in one direction and lower in the other direction. The profiles on the glass foils sustained on three supporting points at 120° are measured with CHRcodile optical sensor mounted on the LTP translational stage and are elaborated to subtract the deformation coming from gravity effects.

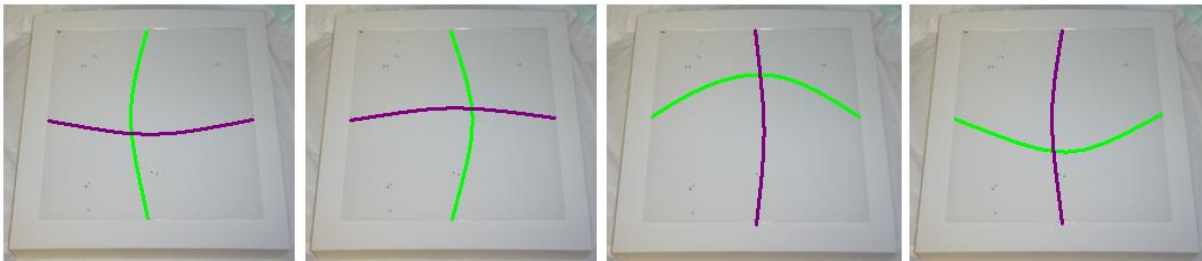


Fig. 6.46: The four different possibilities to orient the glass on the mould considering its original intrinsic shape. It has been demonstrated that no differences are visible in the slumped plates related to this parameter, that introduce an eventual effect of the second order with respect to the more important one represented by the main direction of thickness variation.

6.2.2.1 Consideration on glass cutting

The thin glass D263 is produced and sold by Schott in sheets having dimension of 360 mm x 440 mm, and thickness ranging from 0.03 mm to 1.1 mm. For the particular application, 0.4 mm thick glass foils, with average dimension close to 200 mm x 200 mm, are considered, as derived from optical design and manufacturing compromises. It is, therefore, necessary to employ a reliably cutting process to obtain the required dimensions from the original glass foils: it cannot introduce cracks or defects on the cut edges that might be detrimental for the glass strength (see § 6.2.2.2). To this

primary demand, one second potential requirement is placed side by side: the need of cutting the glass edges after the forming process. The reason why this might be required is twofold: from one side, it might help in eliminating edges deformations coming from the shaping process (see later § 6.2.4); from the other, it might be useful due to the XOU module design. In fact, even in absence of edges deformations on the slumped glass, there might be the need of cutting after the thermal process because all the plates stacked in the XOU present a different width. Although if the difference between two consecutive plates is of the order of few hundreds of microns, between the first and the last plate of the XOU stack there is a difference in the order of 20 mm. It is true that the glass can be cut at the exact required dimension before being shaped, however the option of a successive cut can also account for small displacement between the mould and the glass foil during the slumping (meaning that the glass might move for whatever reason and slump roto-translated with respect to the mould optical axis)¹⁹. Anyway, whenever the moment of cutting is (if before or after the hot slumping process), a reliable cutting procedure has to be implemented. Three main cutting technologies have been assessed:

- Traditional cutting (with diamond or ad-hoc developed tools);
- Laser cutting;
- Hot wire cutting.

The first qualitative comparison, see Fig. 6.47, displays how the traditional cutting leaves less clean and sharp edges with respect to the laser and hot wire techniques, which instead show smooth surfaces. Both the laser and the hot wire technology were further investigated.

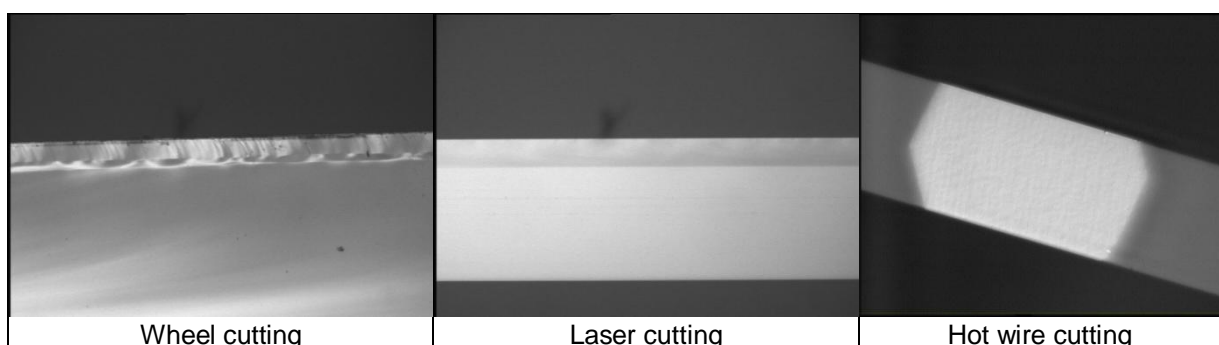


Fig. 6.47: Comparison of Nomarski microscope images of the cut edges obtained with different cutting technology.

¹⁹ The application of markers on the mould that leave an imprinting on the slumped glass plate is a solution under evaluation at the moment of writing.

The laser technology requires the employment of expensive machines, whose purchase could not be afforded: it was followed through MDI Schott from which INAF-OAB purchases the glass already cut. The company employs a red light CO₂ laser: the laser beam heats the surface of the glass scanning the line where the cut is desired; it is immediately followed by a jet of freezing air and liquid that creates the thermal shock at the origin of glass scribing. Along the scribing line the glass is then “broken”, i.e. separated, finalizing the cutting process. The hot wire technology is instead not available on the market for so thin glasses. It is based on the same principle of the laser cutting technology: to create a temperature difference between the two opposite sides of the glass so to induce internal tension on the glass thickness. Tensile stresses are generated on the heated surface and compressive stresses are generated on the cold side: this combination causes a precise controlled breaking of the glass. A conductor wire crossed by electric current is used for heat generation. The cutting is obtained by scanning the hot wire on the glass surface. Two possibilities exist in principle: having or not contact between the hot wire and the glass surface. A fine-tuning of process parameters allows exploiting the entire potentiality of the technique. A dedicated machine has been assembled in the institute for preliminary tests on this option, with a conductor wire made by Tungsten. The preferred approach is the one with the hot wire not coming in contact with the glass surface: in this way local melting of glass close to the cutting line is prevented. Even if the cut edge is visually smooth, quantitative measurements demonstrated that the current hot wire cutting degrades glass edges causing a notable reduction in the glass strength. This is probably related to the assembled system and adopted procedures (mainly contamination issue) rather than to the process itself (see § 6.2.2.2 for details). Further tests are foreseen in the near future to better assess this issue. Meanwhile, the laser technology is considered the base-line for each cutting necessity.

One eventuality that has to be kept under control in case of cutting after the slumping process is the possible shape change glass might experience due to the modification of the internal distribution of potential stresses and/or due to the local heating imposed by the laser. The first point is discussed in § 6.3.2. Regarding the second one, preliminary empirical results suggest this should not be a problem: average shape changes of 1 micron or less were measured, as on scans lines in the central part of a stress free glass as on lines close to the cutting edge; considering that 0.5 µm is the accuracy of the system employed for the measurements, the value has to be taken as an upper limit. During the laser scribing, 98% of the laser energy is absorbed by the first 80 microns of the glass thickness; the maximum substrate temperature recorded is less than 200°C, much lower than the glass Transformation T_g. Hence, no further stresses and permanent deformations are introduced in the glass by the cutting process itself [129p]. Similar tests are planned for the near future with more accurate measuring set up in order to confirm the result.

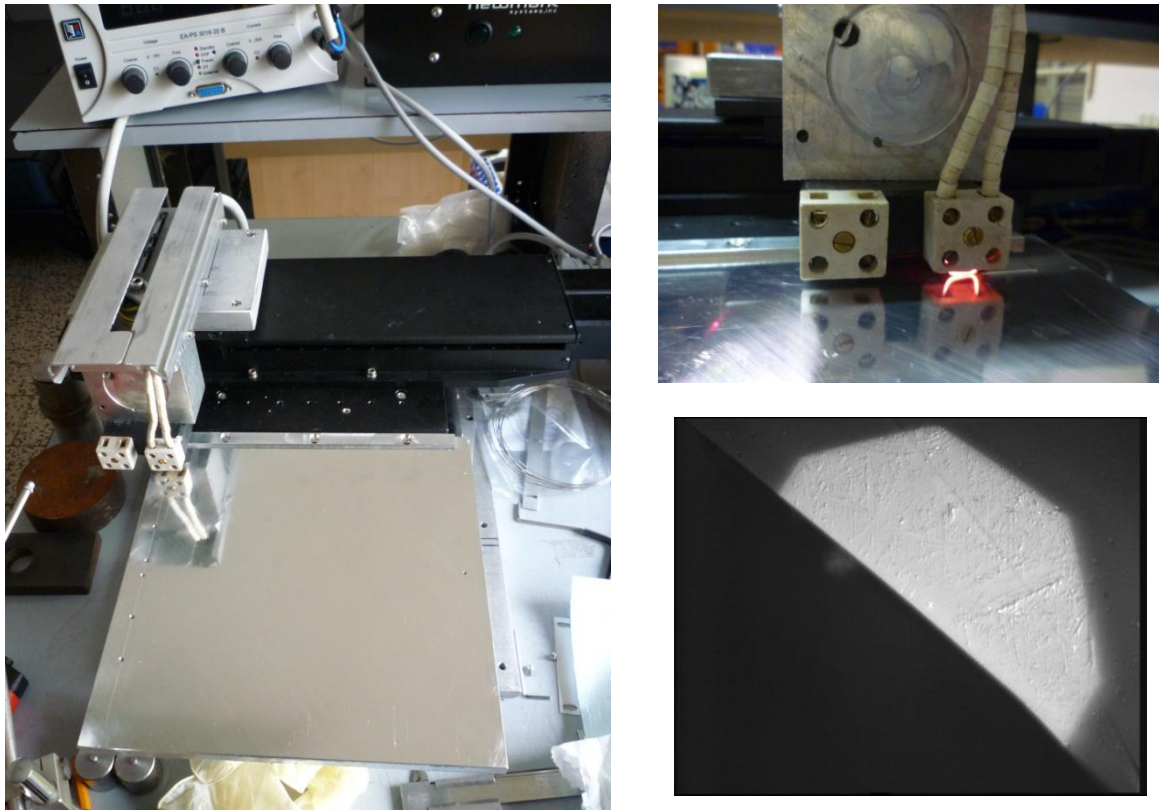


Fig. 6.48: (Left Side): Picture of the hot wire system assembled to assess this method for glass cutting. (Right Side): Electrical current pass through the Tungsten wire, locally heating the glass below during the scan. (Lower Right): 20X Nomarski microscope image on the top view of the cut edge: while the side of the cut is very sharp, the top view reveal contamination issues that causes glass strength reduction.

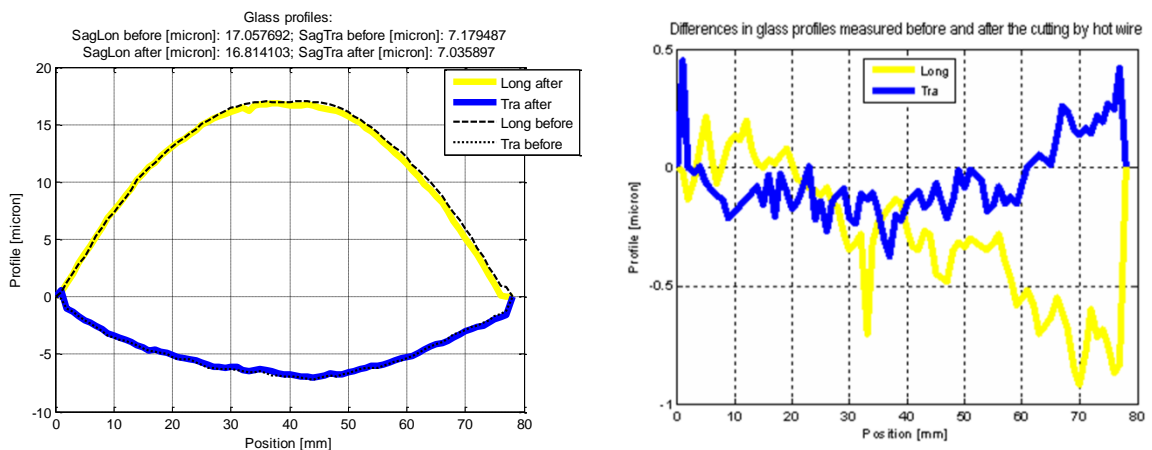


Fig. 6.49: Example of glass profiles comparison before and after the laser cutting: one glass foil, as delivered by the vendor, was characterized in terms of profile shape and then was cut by means of the laser technology. The same profile has been acquired before and after the cutting process. No important differences were clearly visible in the measurements, demonstrating that the cutting itself does not introduce detrimental stresses in the glass.

6.2.2.2 Verification of the glass mechanical parameters

Being a fundamental parameter for the structural design of the entire telescope, the mechanical strength of the used glass foils has been evaluated with ad-hoc test campaign performed by INAF-OAB with the collaboration of SpeVetro. Due to the very thin thickness of the glass, no specific standards exist to conduct the tests. To check the goodness of the experiment set up (coming as from adjustment of existing standards and procedures as from the experience of SpeVetro operators) the glass has been tested at first as it is delivered by the vendor, since in this case the procurement of the samples for the analysis was easier and faster. In principle, the mechanical strength should be evaluated on glass segments that undergone a slumping thermal cycle. However, the statistical fundament of the analysis requires a quite large number of samples, at least 30-50 samples, difficult to be provided in limited time. Besides, the slumping thermal cycle was not yet optimized when these tests started; thus, the evaluation of the mechanical characteristics started from the glass as it is delivered by the vendor. The tests for mechanical strength of the surface were performed through coaxial double-ring tests on flat specimens. The data were elaborated through the statistical analysis of Weibull and fracture analyses. The results showed a good agreement between fracture analysis and FEM simulations, confirming the goodness and reliability of testing procedure for so thin glasses. In particular, the co-axial double-ring test was performed on fifty 100 mm x 100 mm x 0.4 mm glass samples. Each sample was positioned on the testing machine with the surface to be test looking downward, supported by a 70 mm diameter ring. Between the ring support and the glass, a small protective part of cardboard was inserted to prevent surface damage due to the support itself or to small scraps coming from glass breakage. On the top surface of the glass, an electrostatic plastic film was applied to hold together the glass fragments after the sample breakage, allowing for the individuation of the fracture origin location: the procedure worked for the majority of the specimens although if not for all of them. During the test a load was applied on the glass until its breakage through a second ring with diameter of 40 mm. For each sample, the displacement and the load were recorded: the average displacement at fracture was 3.75-4 mm, with an average load of 400-600 N. Also, the origin of the fracture was individuated (see Fig. 6.52). The results of the analyses performed on the collected data show a terrific surface strength of the glass D263. So high values are correlated to the small thickness and to the manufacturing process of the glass foils: they can be explained with the lack of surface defects coming from the manufacturing steps and can be maintained with careful handling and surface protection of the glass foils. Table 6.5 reports the results obtained in terms of Weibull parameters and mechanical strength. The obtained Weibull parameters are an estimation of the glass properties, independently from its geometry, and are useful for preliminary FEA simulation of the entire telescope. The next step correlated to this topic foresees the realization of the same

kind of test on samples that underwent the slumping thermal cycle, to check the eventual changes in glass strength introduced by the process itself. When delivered by the vendor, the glass foils present a superficial layer of few tens of microns characterized by compressive stress, which enhance its overall strength. When subject to the thermal cycle for slumping, this layer is removed from the glass. It is therefore very important to check for the glass strength characteristics after the thermal forming process, since these are the right parameters to be used for the final mechanical design of the Mirror Assembly. Now that the parameters of the slumping process are almost frozen after the optimization work performed, the production of those samples started and their tests are planned for the end of the year. In principle, two sets of specimens need to be produced: one to check for the strength value of the optical surface of the slumped glass plate, and one to test the same parameter on the back surface. This necessity comes from the fact that the two surfaces present different texture since during the forming process they come in contact with diverse materials: the optical side comes in contact with the polished mould surface, the back one comes in contact with the pressing metal membrane. The back surface finishing is particularly dependent on the value of parameters set during the slumping process: not only the pressure but also T_{\max} and soaking time.

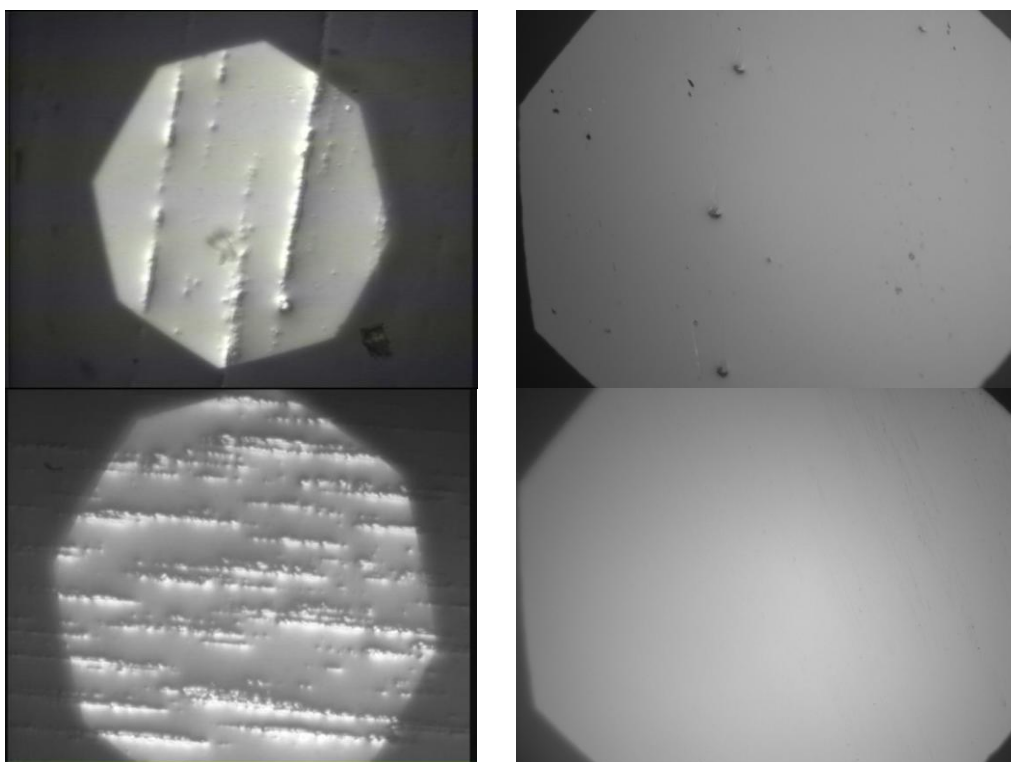


Fig. 6.50: Nomarski images (20X) of the back surface of the slumped glass that, for applied pressure higher than 80 g/cm^2 (Top Left), is affected by the imprinting of the pressing membrane. (Top Right): the lower the applied pressure, the lower this effect; in the picture an example of glass slumped with pressure 50 g/cm^2 (PS-IXO-119). (Bottom Left): With an applied pressure of 150 g/cm^2 and a maximum T of 595°C maintained for 4 h (PS-IXO-33). (Bottom Right): with no applied pressure and a maximum T of 610°C (PS-IXO-46).

A total of one hundred samples need to be produced: fifty to test the optical surface and fifty to test the back surface. The research work described in this text allowed to fix the procedure for their production that is currently underway. In case the strength of slumped glasses results to low after the forming process, chemical tempering could be considered to reconstitute the original properties after an assessment on its effects on the glass plate shape.

The mechanical strength was also evaluated at the edges of the glass: rectangular glass specimens of dimension 130 mm x 20 mm x 0.4 mm were subject to tensile test. The displacement and the applied load at failure were recorded, together with the fracture origin location. To allow for the correct positioning of such thin samples on the testing machine, 50 mm long aluminum parts were glued on their ends, leaving a central free zone of 30 mm x 20 mm x 0.4 mm for the test. The recorded data were analyzed through Weibull statistics and fracture analysis. The test was performed on fifty samples cut with the laser technology and on fifty samples realized through the hot-wire cutting, with the aim of comparing the two cutting techniques. The results show that the edges strength for the laser cut samples is close to the superficial one: an average value of 213 ± 60 MPa was recorded for the fractures that origin from the edges, 225 ± 82 MPa was recorded for the fractures that origin from the surface. For the laser cutting, no substantial differences are evidenced between the edges and the surface of the glass samples. The situation is different in the case of hot wire cutting: the majority of failures originated from the samples edges, with a relative low value with respect to the one evaluated for the glass surface (almost a factor of two lower): an average of 115 ± 42 MPa, compared to around 250 MPa for surface. This result is more related to the environmental condition during the hot-wire cut realization, rather than to the cutting process itself. In fact, while the laser cutting was realized with a dedicated machine in a clean room environment, the hot-wire cutting was realized with a prototype machine in a not controlled environment. Careful check through Nomarski microscope near glass edges showed the presence of small glass splinters and chips that degraded its surface finishing, hence its strength. For this reason, the current results on hot wire cutting should be considered spurious and affected by the presence of superficial defects near glass edges coming from not optimal foils handling. Further hot-wire technology tests and upgrades on the cutting machine are planned for the next steps of the present study: meanwhile the laser cutting technology is employed.

Table 6.4: Mechanical strength of the surface and the edges of the tested glass.

	Surface NL*-FEM	Surface	Edge Laser	Edge Hot-Wire
	σ [MPa]	σ [MPa]	σ [MPa]	σ [MPa]
Average (std dev.)	251.5 (36.9)	239.6 (42.1)	213 (60)	115 (42)

*NL stands for Non Linear

Table 6.5: Summary of the Weibull parameters estimated for the surface and edge strength of analyzed glass.

Cutting process (estimator adopted) [130]	Weibull modulus β	Weibull characteristic strength σ_0 [MPa]	Weibull material scale parameter σ_0 [MPa mm ^{2/β}]
SURFACE (EN 12603:2002)	7.76	--	610.7
SURFACE (ASTM C1239-06A)	6.47	--	732.2
EDGE Laser cutting (ASTM C1239-06A)	3.39	264.0	674.1
EDGE Hot-wire cutting (ASTM C1239-06A)	2.99	140.2	405.6

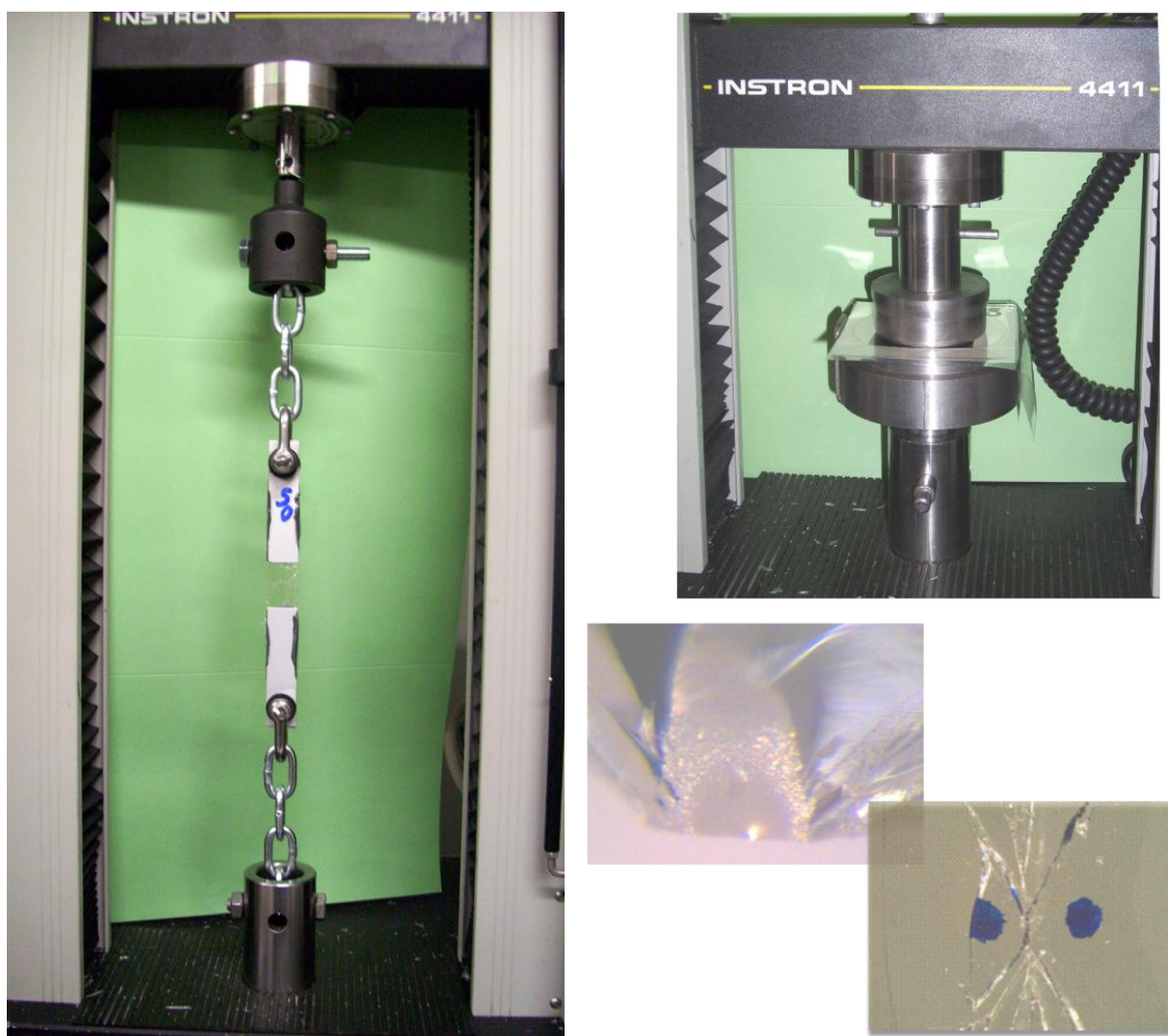


Fig. 6.51: Testing machines employed for the evaluation of glass surface end edges strength. (Left Side): Tensile tests for edges strength testing. (Right Side Top): Coaxial-double ring test for surface mechanical strength testing. (Right Side Bottom): Example of images acquired on the fracture origin's location, employed for the fracture analyses.

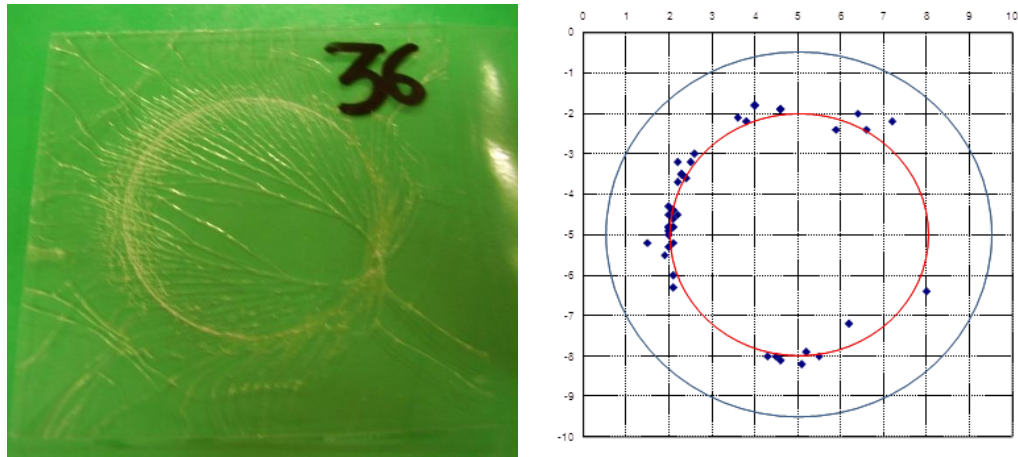


Fig. 6.52: (Left Side): One of the fifty 100 mm x 100 mm x 0.4 mm glass specimens after the double ring test: the presence of electrostatic plastic film kept together the glass pieces after failure, giving the possibility to individuate the fracture origin location for almost all the samples. (Right Side): Fracture origin location on the tested glass samples: the glass mainly broke from surface (and not from edges) near the loading ring, where the stresses are higher.

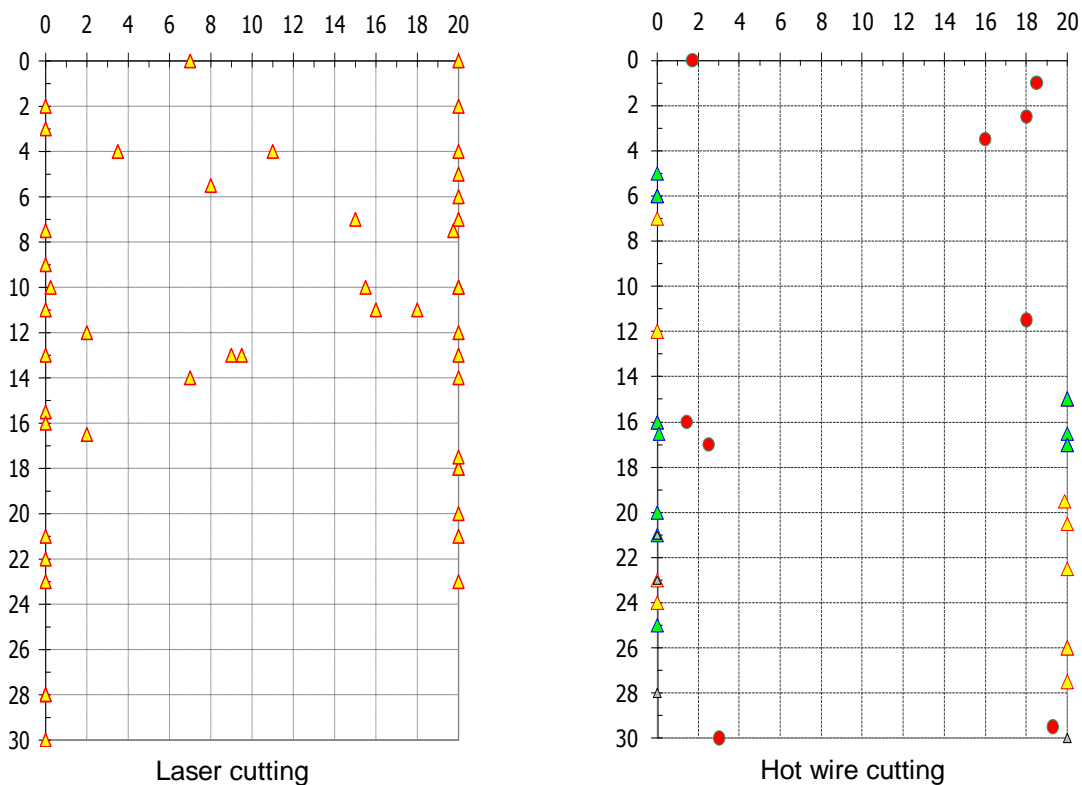


Fig. 6.53: Fracture origin location on the specimens employed to test the edges strength in the case of laser cutting (Left Side) or hot wire cutting (Right Side). In the case of hot wire cutting, a distinction has been made between failure starting from the cutting side or the back one (yellow and blue markers respectively).

6.2.3 Slumping thermal cycle optimization

Many tests have been performed to individuate the optimum thermal cycle to apply, as in the case of Fused Silica as in the case of Zerodur K20 mould. The majority of these experiments has been performed in the big oven, selected for the realization of representative plates because of its thermal behavior. Part of the tests has been realized on cylindrical moulds while others were realized on smaller flat samples. Table 6.6 lists the ranges of all the main parameters explored and considered and gives the status of the art in the selection of the optimal parameters to be set for the process.

Table 6.6: Lists of all the slumping process parameters considered and analyzed during the study.

Considered Parameter	Range of explored value	Comments
T_{\max}	570°C – 610°C	Too high temperatures are problematic for sticking behavior and glass surface degradation. Too low values don't allow a permanent shape change in the glass. Optimal T found to be around 575-580°C (for glass D263).
p	10 – 150 g/cm ²	Too high pressure might introduce deformations in the glass plates. No pressure or too low pressure does not allow to correct mid-frequencies in the glass. Optimal range found to be between 20 and 50 g/cm ² , the exact value depending on the cycle duration (the longer the cycle, the lower the acceptable p).
Time of p application	4 – 10 h	The present optimized value is of 6 h, a trade-off between results and speed of process realization (important for the industrialization of the entire IXO production chain).
Soaking time	2 – 10 h	An optimized value has been found in 6 h soaking time, as better compromise between results and duration of the process. The duration of the entire process is an important parameter when considering the industrialization of IXO telescope production chain and should be taken into account since the beginning.
Heating up rate	12.5 – 60 °C/h	No critical since the soaking phase allows reaching T uniformity inside the muffle. This has been found to be a second order parameter with respect to cooling down rate.
Cooling down rate	2.5 – 60°C/h	The lower the better, to eliminate thermal gradients inside the muffle. Currently a value of 2.5°C/h is set.
Positioning of the glass on the mould	Thickn. variation orientation wrt* mould axis	To optimize results, the glass direction of lower thickness variation, corresponding to the glass drawing direction, must be positioned parallel to mould axis.
	Glass original shape orientation wrt mould axis	No important differences have been evidenced: this has been found to be a second order parameter with respect to thickness variation.
Positioning of the mould inside the muffle	Height with respect to the pressing membrane plane	The mould should be positioned in such a way to have the glass being slumped on it at the same height of the pressing membrane plane. This is essential to give uniform pressure on the whole glass plate, avoiding points of pressure concentration on its edges.

*wrt = with respect to

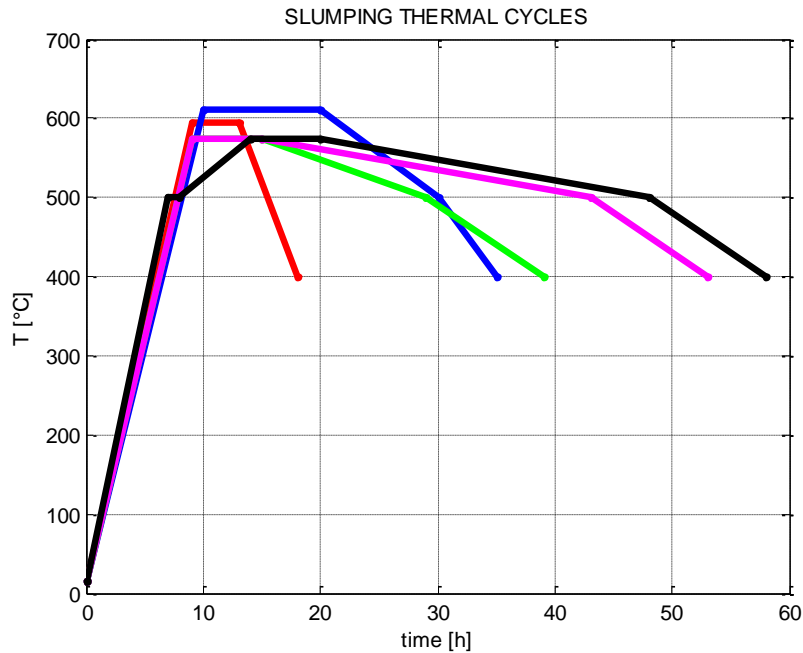


Fig. 6.54: The plot shows the history of the slumping thermal cycle. Different T_{max} , soaking time, and cooling down rate have been empirically tested. The current adopted cycle is represented by the black curve, characterized by the lower cooling down rate with respect to the others. This cycle applies as for the Fused Silica, as for the Zerodur K20 mould. At 400°C the oven is switch off and it is allowed to freely cool down up to Room Temperature since below 400°C the glass does not change permanently its shape anymore. Pressure is applied in the middle of soaking phase and maintained till the end of the process, i.e. RT.

6.2.4 Slumping results in terms of plates shape

The shape of the slumped glass plates has been widely evaluated by means of the optical CHRcodile sensor mounted on the linear stage of the LTP machine. By scanning line profiles of the glass, height data were acquired and their elaboration allowed to obtain the intrinsic shape of the glass (i.e. with gravity effects removed) and consecutively an estimation of their performances in terms of figure HEW through ray tracing methods. The results are hereafter reported.

6.2.4.1 Glass intrinsic shape evaluation

After their slumping, all glass plates were characterized in 1D longitudinal profiles acquired at several distances from the central profile. Before this quantitative characterization, a qualitative check was possible at the muffle opening by looking at the interference fringes between the mould and the glass. The collected data are reported in the following pictures. The plots are divided for glasses slumped on mould MCX1, MCX2, and MCX2_B. On mould MCX2_B, larger glass foils (240 mm side instead of 200 mm) have been slumped to test the cutting of edges area (see § 6.3.2 for explanation).

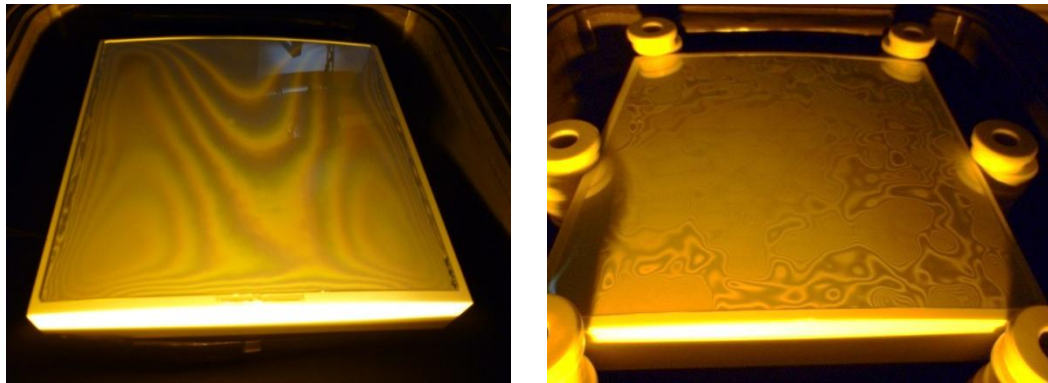


Fig. 6.55: Interference fringes visible between the glass and the mould at the opening of the muffle once the process is terminated. A first qualitative indication on the goodness of the process can already be drawn by looking at them. (Left Side): The presence of dense fringes near glass edges suggest that the deformation is mainly concentrated in those perimeter areas (PS-IXO-112). (Right Side): The fringes patterns suggest that the glass is highly affected by mid-frequencies: this sample was obtained by slumping it with no pressure (PS-IXO-102). It is clear the necessity to apply pressure to eliminate this problem.



Fig. 6.56: The presence of mid-frequencies in the slumped glass plates can also be seen through their reflection, for example of the laboratory lamps. Glass on the left was slumped with 50 g/cm^2 pressure (PS-IXO-104) while glass on the right was obtained with no pressure application (PS-IXO-102); the presence of mid-frequencies deformations is clearly visible in it.

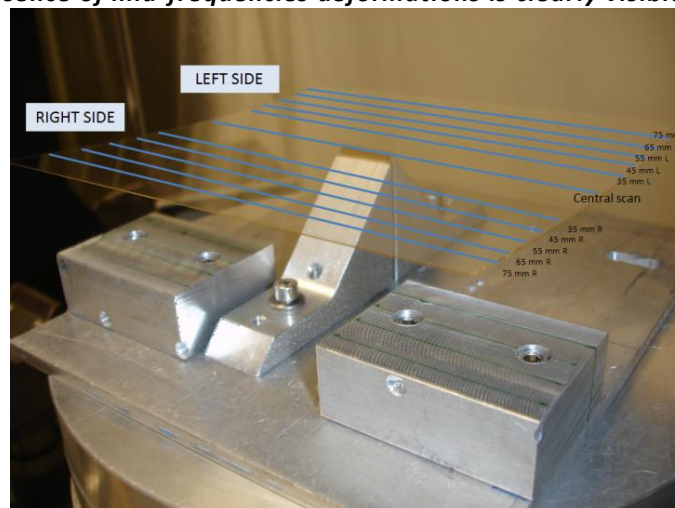


Fig. 6.57: Scheme of all the measurements shown in the following pictures: longitudinal profiles of the glass have been acquired, with the glass lying on a central supporting point (as depicted in the picture) or sustained on three supports at 120° . The curves in the following plots represent the residua wrt a linear fit. PV values indicate deformations introduced by the forming process not yet fully optimized. The data are plot as if looking at the glass with the concavity downward.

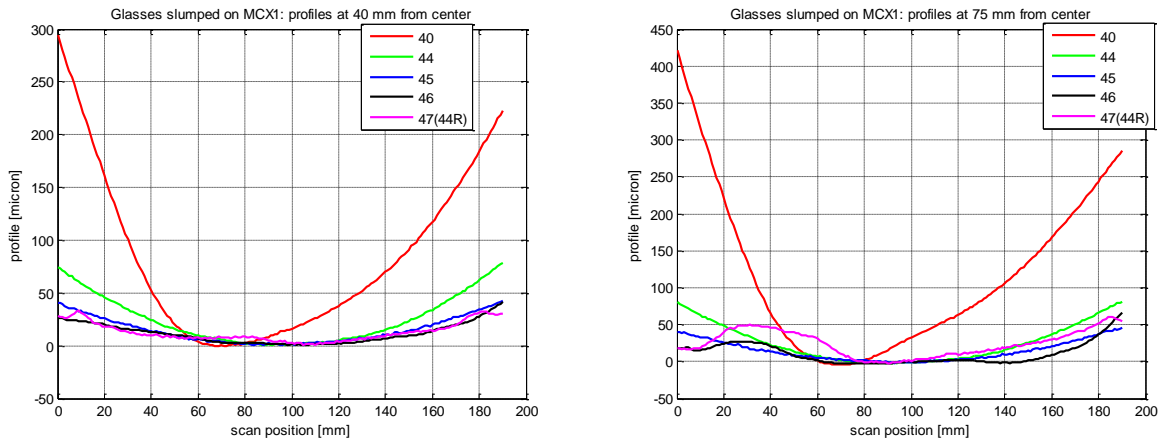


Fig. 6.58: Comparison of profiles acquired on glasses slumped on MCX1 mould (only experiment PS-IXO-39 and 41 are missing – see annex C for a complete list). Profiles on the left refer to scans acquired at 40 mm from the center of the glass; profiles on the right are acquired at 75 mm from the center of the glass. These profiles should be an almost straight line if the cylindrical shape of the mould is effectively replicated during the thermal shaping process. A positive trend is visible in the results; however low-frequency deformations are still present with sagittas of tens of μm , responsible for average HEW values in the order of 300-600 arcsec.

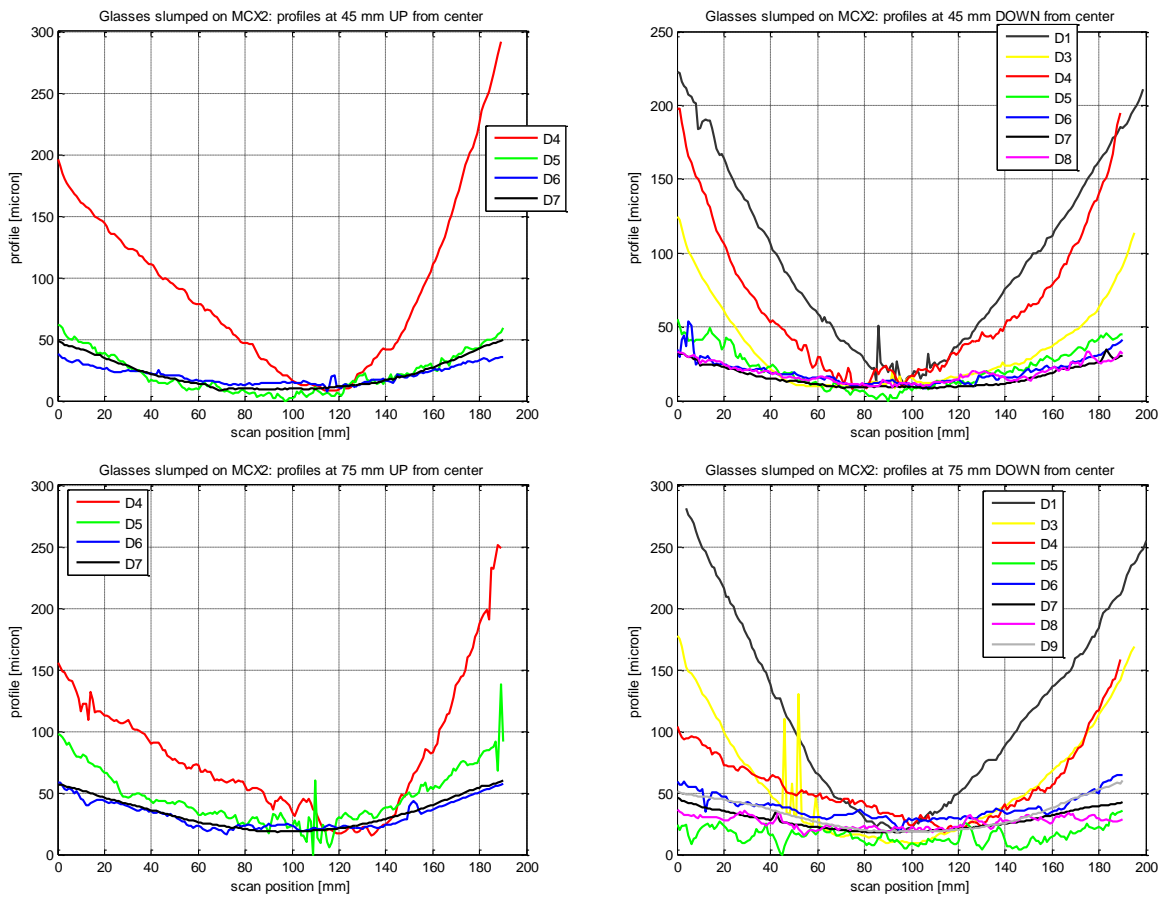


Fig. 6.59: Comparisons between intrinsic profiles acquired on the glass foils slumped on mould MCX2: they have been taken at several azimuthal positions with respect to the central longitudinal profile. Note that the high frequency visible in the picture was due to instrumental noise and was eliminated in later characterizations. Also those slumped plates present low-frequency deformations, with PV lower than $40 \mu\text{m}$ (in the best cases). The obtained HEW span from 150 to 650.

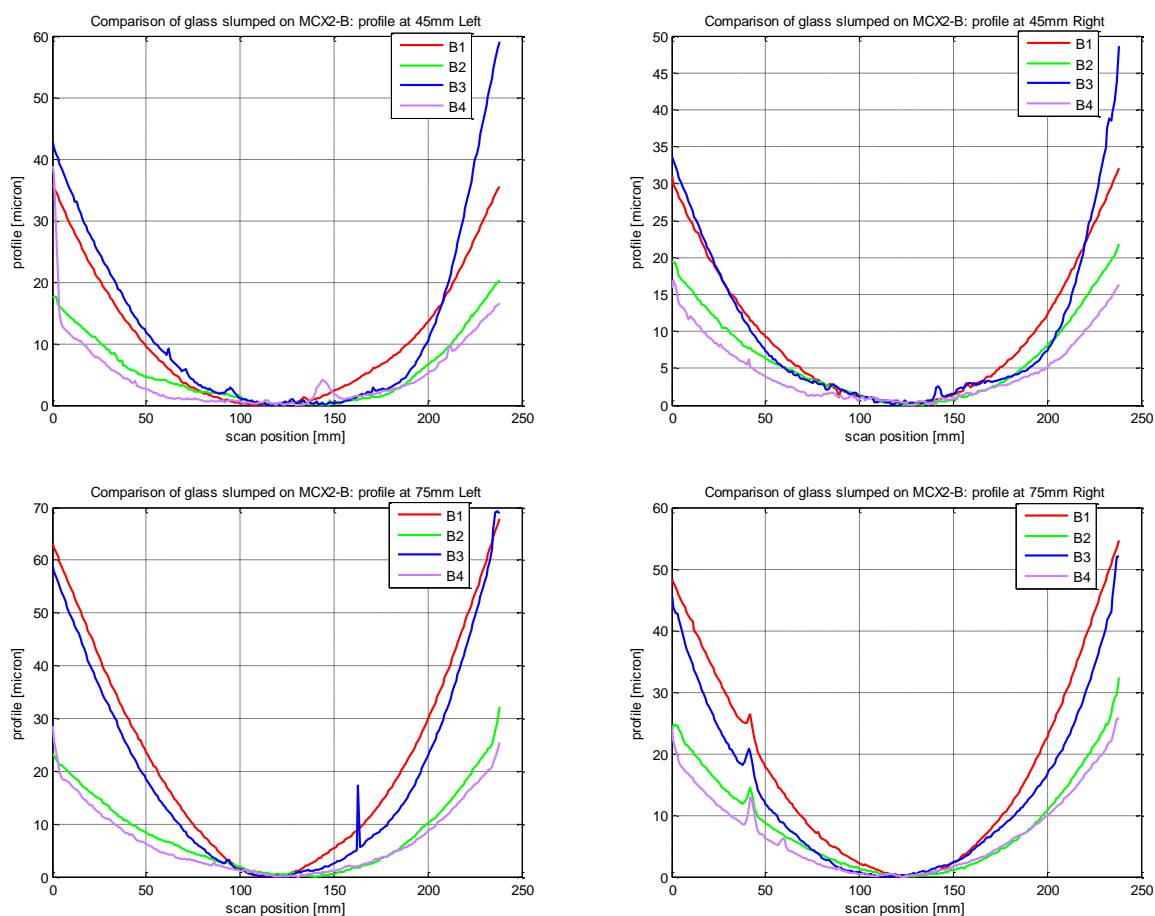


Fig. 6.60: Comparisons between intrinsic profiles acquired on the glass foils slumped on mould MCX2_B (PS-IXO-128, 129, 130, 131): they have been taken at several azimuthal positions with respect to the central longitudinal profile. Note on the right plot the presence, at about 40 mm, of a peak on all the foils: it is due to a damaged area on the slumping mould. The shown profiles have an HEW in the range of 140 – 350 arcsec.

In the case of MCX2_B, with respect to MCX1 and MCX2 slumping, the positive trend toward reduced sagittas could be obtained with lower pressure value of 20 g/cm^2 , whose application was possible thanks to an upgrade in the system to give pressure. Essentially, the pressure sealing was enhanced in comparison to previous experiences and this translated also in a more uniform thermal condition on the glass being formed: in fact it was guaranteed a lower flow of air entering the muffle to keep the constant pressure. Even lower pressure values (e.g. 5 or 10 g/cm^2) appeared from preliminary tests not to be reliable in eliminating mid-frequencies presents in the slumped glasses.

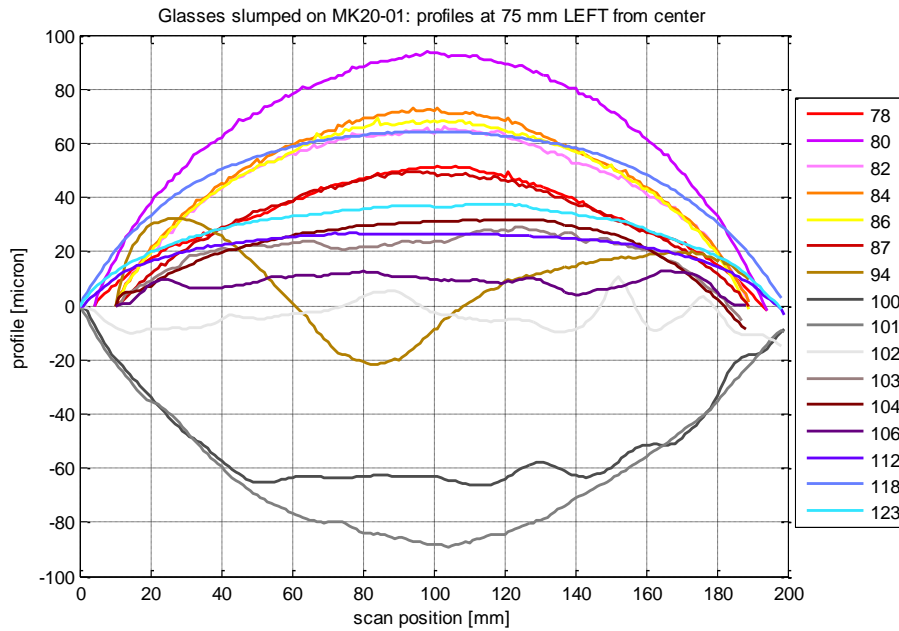


Fig. 6.61: Example of comparison between representative profiles of slumped plates obtained with mould MK20-01. Tests PS-IXO-100 and PS-IXO-102 were realized in the small oven whose thermal conditions are not optimal and in fact the obtained glasses have a deformation opposite with respect to the other glasses slumped on MK20-01. The positive trend in improvements is obtained with fine tuning of process parameters. HEW values as low as 50 arcsec have been obtained in the best cases, that reduce to 15 arcsec if the deformed edges areas are not considered (see § 6.3.2).

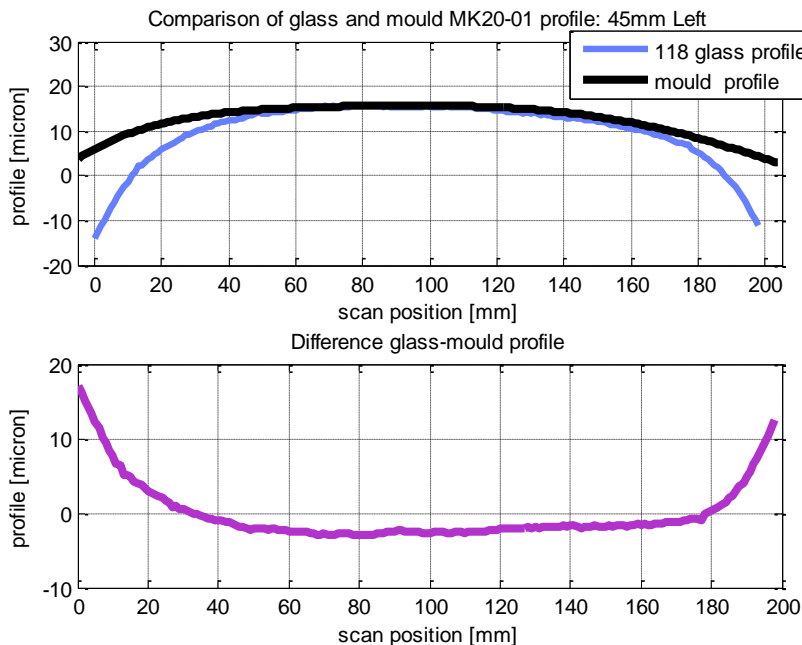


Fig. 6.62: Example of difference between the mould and the slumped glass profiles. The experiences realized on MK20-01 mould show a deformation in the slumped glass that is mainly concentrated on the edge areas, while in the central part the shape of the not-optimal mould is replicated within few microns.

All the acquired data regarding shape results allowed drawing the following conclusions on the slumping that represent the current state of the art in the knowledge of the hot slumping technology with pressure:

- D263 glass foils slumped on Fused Silica mould presents low-frequency sag deformation. D263 glass foil slumped on Zerodur K20 mould present low-frequency errors of reduced values, with respect to Fused Silica when the same thermal cycle is considered. The still present deformations are mainly concentrated on the edges areas of the glass.
- The experiments realized allowed fixing some parameters in the process, reaching a positive trend of improvements in the results. They are:
 - Mould height and positioning inside the muffle with respect to the pressing membrane plane;
 - Experiment set up to allow a better pressure sealing (introduction to additional volume in the pressing line to damp losses);
 - Tools to be employed during the slumping preparation phase (for example, the use of a rigid aluminum frame to keep the metal pressing membrane in position during the muffle closing and to allow its handling without introducing wrinkles);
 - Positioning of the glass on the mould with the direction of drawing parallel to the optical axis of the mould.
- The application of pressure is of fundamental importance to eliminate mid-frequency, detrimental in terms of HEW performances. The pressure value and cycle duration are deeply interconnected and need further investigation to individuate their optimal setting. It has been observed, in fact, that the same result can be obtained with a faster thermal cycle if pressure is applied. However, higher p values translate in more stresses inside the glass plate and deeper imprinting on its back surface that lower its strength overall. The possibility to have a faster process is however extremely important when considering the industrialization of the production chain for the totality of 15-20 thousand of plates necessary for IXO; so a tradeoff between the two parameters is fundamental. At this regard, it must also be considered that, although if the maximum temperature of the cycle is more important from roughness results point of view, a higher temperature might allow to speed up the process.

6.2.4.2 Glass shape after integration

Three of the plates slumped on Fused Silica moulds have been integrated into stiffening back plates to test the reliability of the integration procedures. They have dimension of 192 mm x 192 mm, with a thickness of 0.4 mm. They have been integrated on back plates made by glass, with dimension of 210 mm x 210 mm, thickness of 19 mm, and cylindrical shape of 1 m Radius of Curvature. Five ribs have been used; note that the current optical design foresees the use of 6 ribs instead of 5, which was the considered number at the time of integration. For these first integration experiments the appositely designed IMA machine was not available since still in definition phase: they were realized manually making used of ad-hoc design jig. Also ad-hoc procured integration moulds were not available and the tests were conducted using the slumping mould as integration mould. The adopted procedure is depicted in Fig. 6.63. Plates slumped on Zerodur K20 mould have not been so far integrated.

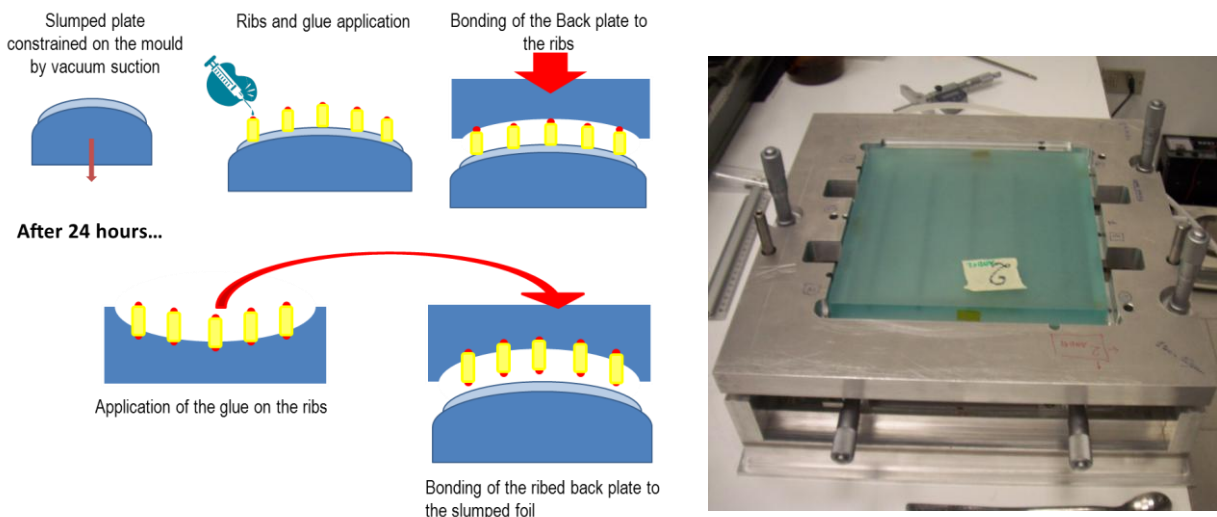


Fig. 6.63: Scheme of integration (Left Side) and used jig (Right Side).

To test the proposed integration approach, also three plates obtained with the indirect slumping, supplied by the MPE colleagues, have been integrated. They have the same characteristics of the ones realized with the direct approach: dimensions of 192 mm x 192 mm x 0.4 mm and RoC of 1 m. Compared to the glass plates slumped with the direct approach, the plates obtained through the indirect technique are more affected by mid-frequencies since no pressure is applied during the forming process. This is one of the main reasons why the direct approach was chosen for phase two of the project [130c].

The following plots in Fig. 6.65 – 6.71 report on the integration results obtained, as measured with the CHR on LTP (1D profiles) as with the CUP (3D map of the entire glass). Note that the 3D maps could be acquired only on integrated plates; the complete map characterization before integration

was in fact not reliable because of metrology systems limitation. The CUP was available only after the glasses integration; before that only CHR on LTP stage was available. Besides, difficulties in sustain so thin and floppy sample avoiding the introduction of gravity deformation effects had to be taken into consideration and were eliminated from the data with ad-hoc procedure.

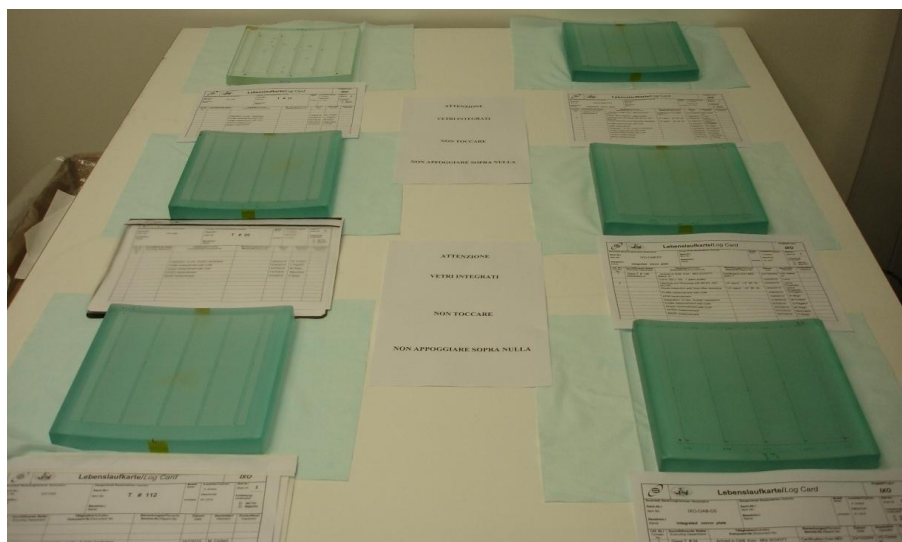


Fig. 6.64: All the glasses integrated during phase one of the project to test the integration principle are together shown in the picture. Each one of them is accompanied by its own log book in which every step of their production and characterization is recorded.

Table 6.7: Characteristics of the slumped plates so far integrated

Number of integrated plates	6 3 obtained with direct slumping 3 obtained with indirect slumping*
Plate dimension	192 mm x 192 mm
Plate thickness	0.4 mm
Number of ribs	5
Ribs material	BK7 glass
Ribs dimensions	190 mm x 2.5 mm x 2 mm
Ribs shape	Cuboidal
Spacing between ribs	41 mm (from ribs axis)
Glass cantilever length	18 mm (from outermost ribs axis)
Glue	Masterbond EP30-02
Glue thickness	25 μ m
Back plate material	Glass
Back plate dimensions	210 mm x 210 mm x 19 mm
Back plate shape	Cylindrical, ROC = 1m

* The samples obtained through the indirect slumping were realized by MPE colleagues during phase one of the project.

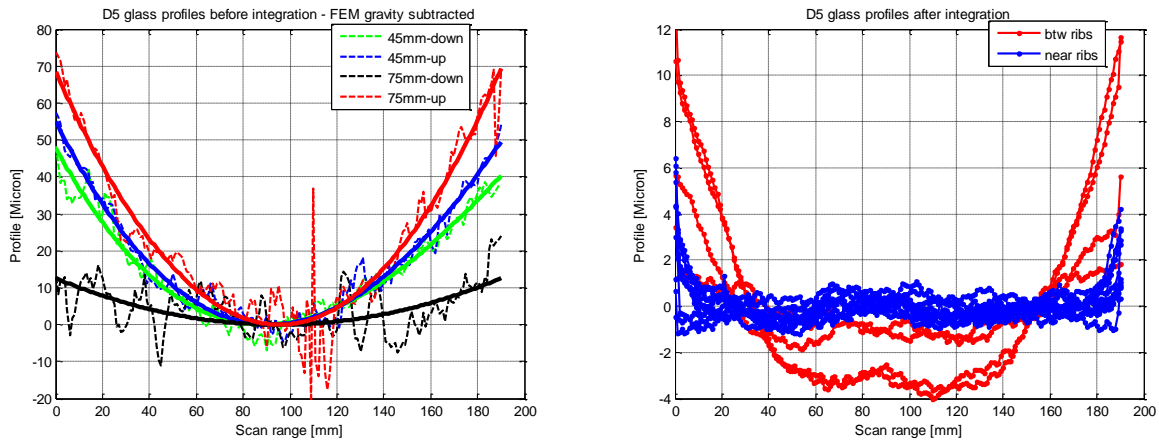


Fig. 6.65: Comparison between the longitudinal profiles acquired with CHRcodile sensor on LTP linear stage of glass D5 (PS-IXO-66) before (Left Side) and after (Right Side) its integration on the stiffening back plate. Note the effective capability of the proposed integration approach to correct for low-frequency shape errors. Solid lines in the plots before integration represent polynomial fit of the acquired data affected by instrumental noise.

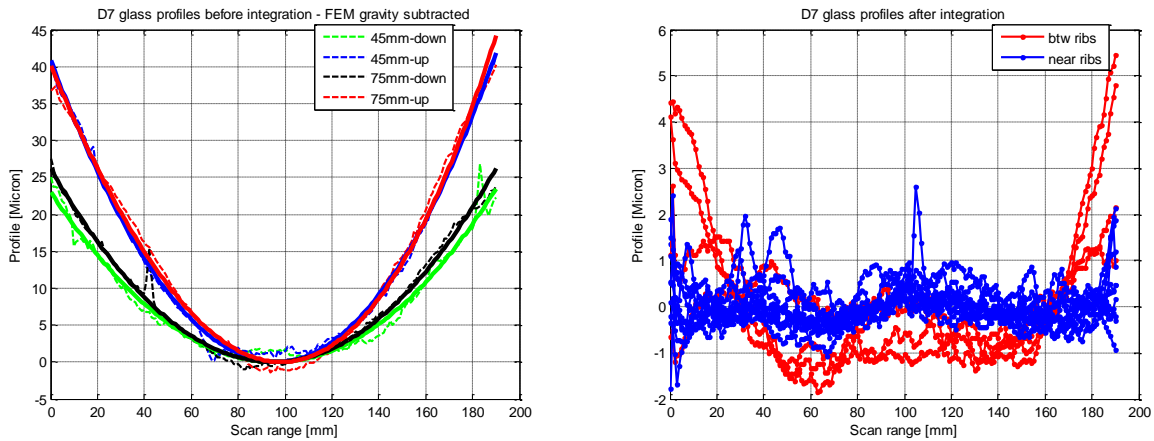


Fig. 6.66: Comparison between the longitudinal profiles acquired with CHRcodile sensor on LTP linear stage of glass D7 (PS-IXO-68) before (Left Side) and after (Right Side) its integration on the stiffening back plate.

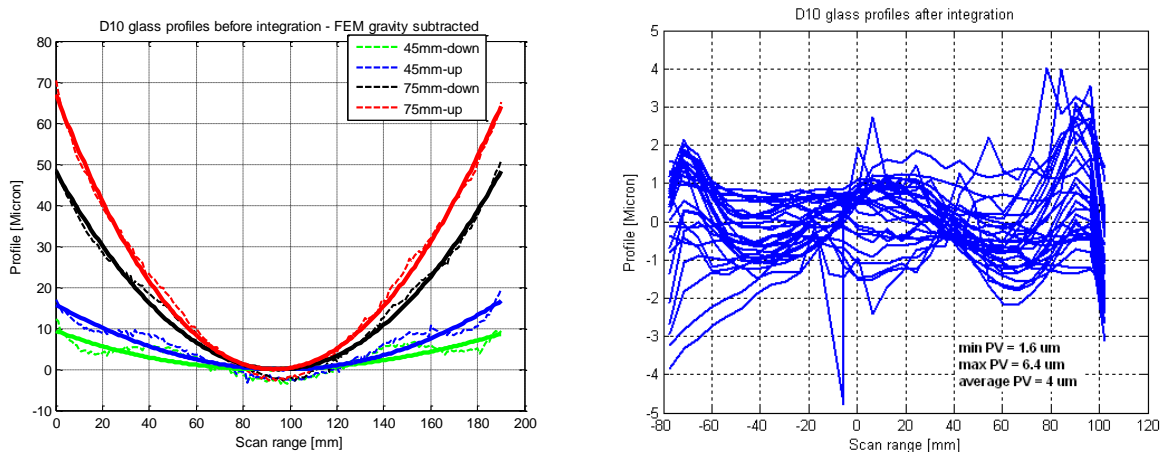


Fig. 6.67: Comparison between the longitudinal profiles acquired with CHRcodile sensor on LTP linear stage of glass D10 (PS-IXO-78) before (Left Side) and after (Right Side) its integration on the stiffening back plate. The profiles after integration are, in this case, acquired with CUP.

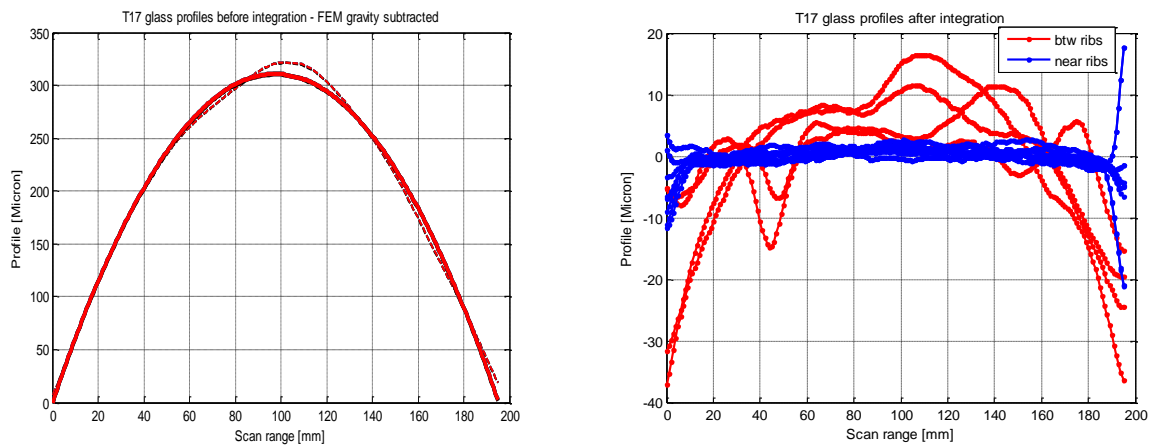


Fig. 6.68: Comparison between the longitudinal profiles acquired with CHRcodile sensor on LTP linear stage of glass T17 (indirectly slumped plate by MPE) before (Left Side) and after (Right Side) its integration on the stiffening back plate. This was actually the first integrated glass and only one reliable scan is available before its integration since the measuring procedure was still in definition phase.

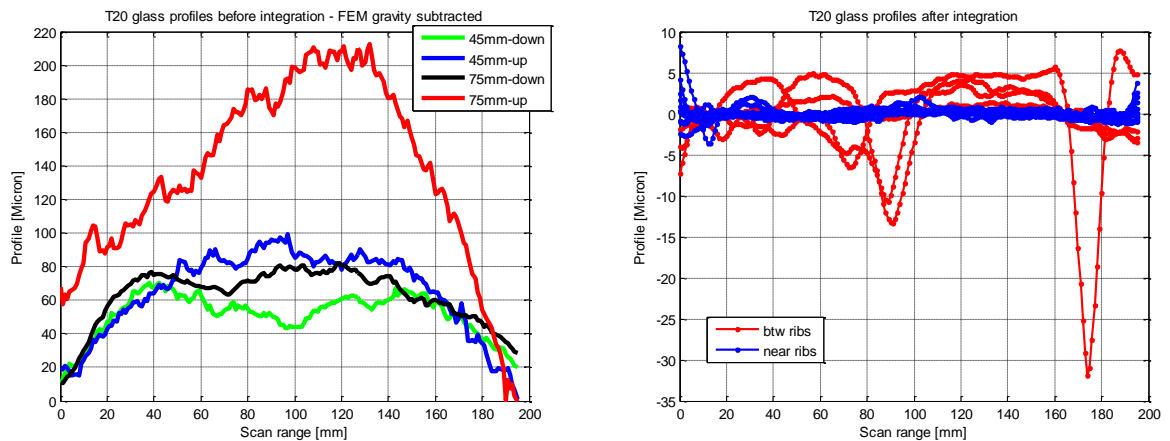


Fig. 6.69: Comparison between the longitudinal profiles acquired with CHRcodile sensor on LTP linear stage of glass T20 (indirectly slumped plate by MPE before (Left Side) and after (Right Side) its integration on the stiffening back plate. Note how the proposed integration procedure is less effective in correcting mid-frequency errors that are visible also in the scans after integration.

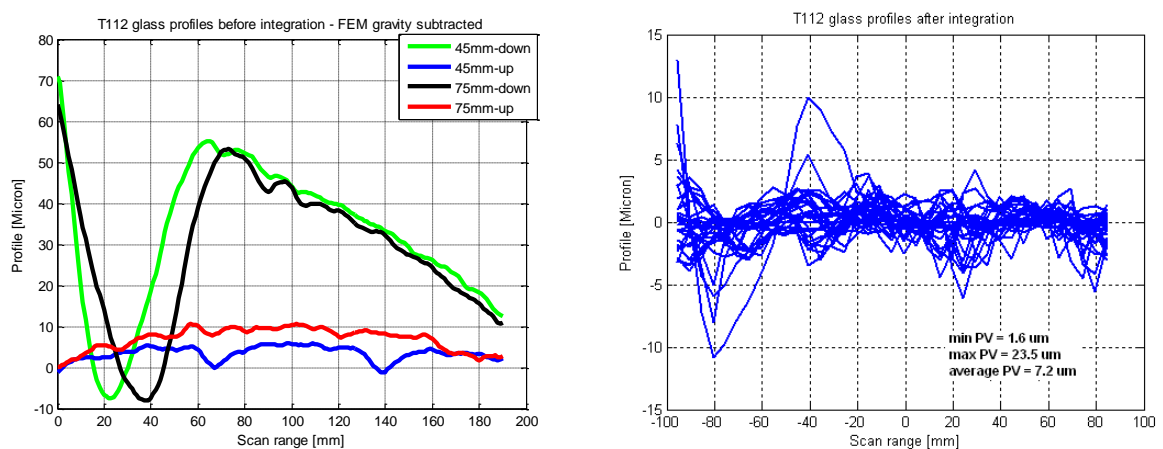
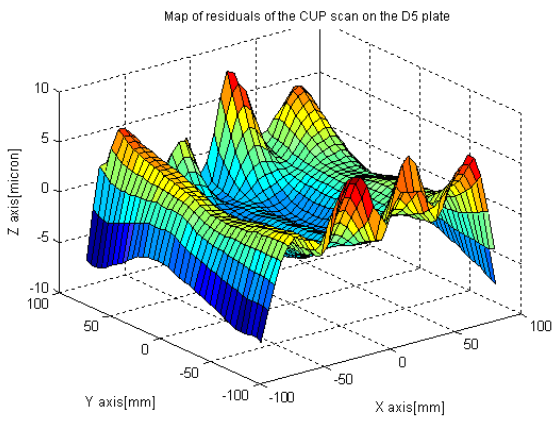
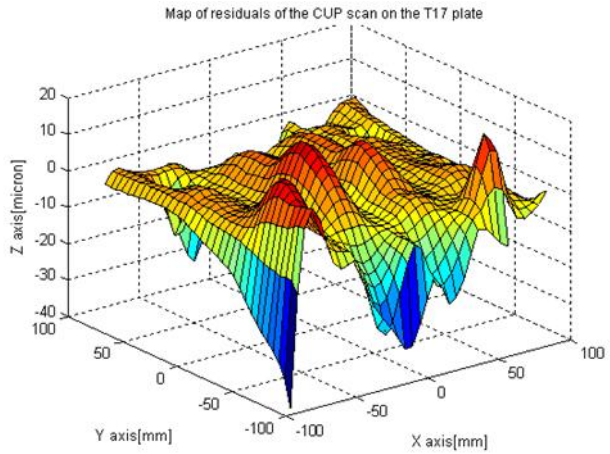


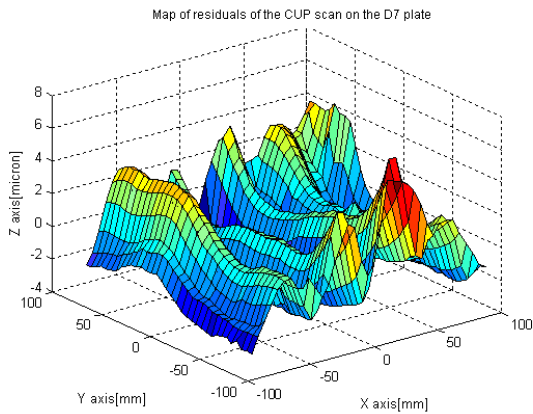
Fig. 6.70: Comparison between the longitudinal profiles acquired with CHRcodile sensor on LTP linear stage of glass T112 (indirectly slumped plate by MPE) before (Left Side) and after (Right Side) its integration on the stiffening back plate.



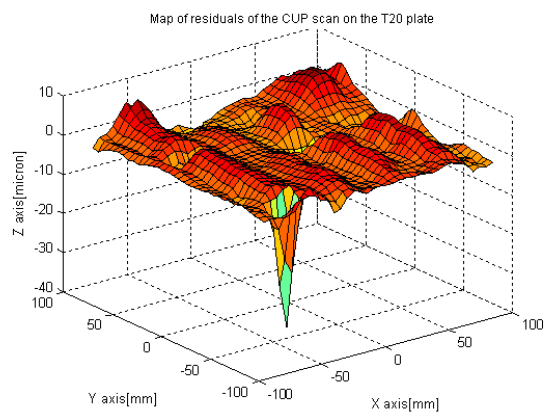
D5 glass, HEW = 25.8



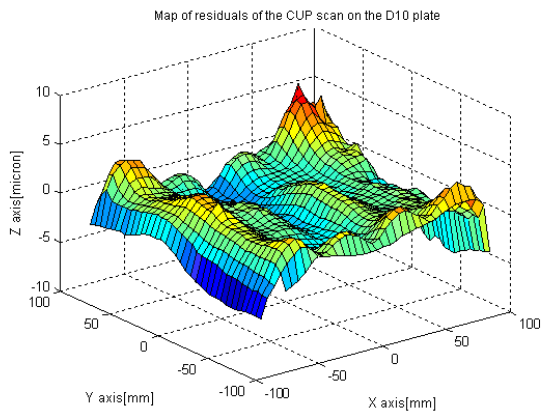
T17 glass, HEW = 94.6



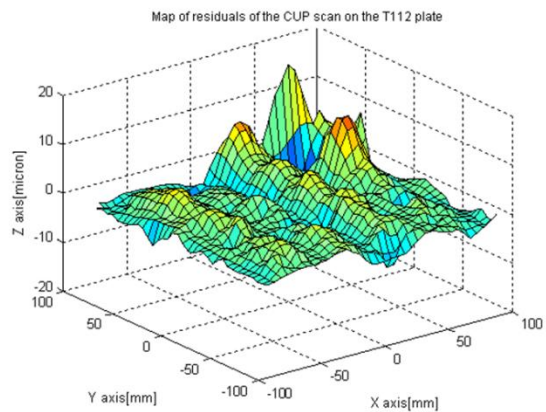
D7 glass, HEW = 22.1



T20 glass, HEW = 51.1



D10 glass, HEW = 29.5



T112 glass, HEW = 95.5

Fig. 6.71: Surface maps of the integrated glass plates obtained with the CUP. The best fit cylinder has been subtracted from raw data. The optical axis is aligned like the y axis in the plots; therefore the HEW is not affected by the transversal undulations. Note the presence of the 5 ribs: the integration correction effect is larger close to the ribs while between them spring back effects can be observed.

Table 6.8 summarizes the results obtained regarding the integration.

Table 6.8: Summary of the slumped and integrated plates characteristics.

Glass sample	Slumping T_{max}	Slumping p	PV shape error before integr. (1D scan value)	PV shape error after integr. (map)	HEW due to roughness*	HEW figure before integr. -CHR data-	HEW figure after integr. -CHR data-	Global HEW after integr. -CUP data-	% PV correction	% HEW correction**
D5	575°C	150 g/cm ²	12-69 μ m	17.1 μ m	2 arcsec	520 arcsec (109-595)	17-85	25.8 arcsec	~ 75 %	~ 95 %
D7	575°C	80 g/cm ²	23-44 μ m	12.7 μ m	2 arcsec	498 arcsec (201-363)	15-20	22.1 arcsec	~ 71 %	~ 95 %
D10	575°C	50 g/cm ²	9-67 μ m	12.3 μ m	10 arcsec	590 arcsec (77-567)	7-55	29.5 arcsec	~ 81 %	~ 95 %
T117	575°C	N.A. indirect slumping	~ 300 μ m	68.3 μ m	3 arcsec	2460 arcsec (2460)	141-567	94.6 arcsec	~ 77 %	~ 96 %
T20	575°C	N.A. indirect slumping	32-219 μ m	44.3 μ m	< 1 arcsec	572 arcsec (255-1400)	29-135	51.1 arcsec	~ 80 %	~ 91 %
T112	575°C	N.A. indirect slumping	4-83 μ m	31.4 μ m	< 1 arcsec	175 arcsec (25-401)	9-247	95.5 arcsec	~ 62 %	~ 45 %

*as measured with BEDE-D1 Diffractometer at (1keV) [0.1-660 μ m]

**These percentages confirm FEM simulation results for mirror shells with ROC of 1 m. In the case of indirectly slumped plates the values are less uniform because of the presence of mid-frequencies errors for which the correction is less effective. When considering 95% of correction, HEW in the order of 15 arcsec or less (and so very close to the goal of the project) can be expected for the last slumped plates: this expectation will be empirically checked during the manufacturing of prototypes.








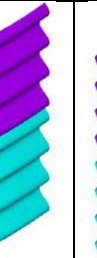
All these data allow to draw the following conclusions on the integration process:

- The proposed integration process is able to correct for low frequencies (shape) errors present in the glass plates at the end of the hot slumping phase.
- The results of FEM simulations on integration are confirmed, giving reason of the goodness of the simulation itself.

Once that the integration concept has been demonstrated for low-frequency errors, parametric FEM analyses were conducted to evaluate the behavior in presence of larger spatial scale errors in the slumped plate. The final aim was to evaluate the initial error that can be accepted in the slumped segments in order to have, at the end of the integration process, a final residual error, and a consequent optical degradation, compatible with the IXO requirements. Just sinusoidal shape errors (see Table 6.9) along meridians (generating lines of the cylinder) were considered since they are more important from a point of view of image resolution on the focal plane detectors. No errors in azimuthal directions are taken into account. The percentage of correction which is retained after the spring back depends on the Radius Of Curvature in azimuthal plane, being higher for larger radius. The radius of curvature considered in the analyses is 1 m. The computation is performed taking into account cylindrical moulds for the slumping and integration moulds with the theoretical Wolter I desired shape (parabola or hyperbola). The results, summarized in Table 6.10, point out that:

- In the configuration analyzed (5 infinitely stiff ribs to reproduce the case of glass plates integrated on back plate during phase one of the project) the integration procedure achieves a reduction of the P-V of shape errors along generating line of the order 80-70% for large spatial scale errors (λ in the range 133-400 mm). Note that this is in agreement with the empirical data, showing the goodness of FEM analyses results. Corrections of errors having higher spatial frequency are less effective. The correction (in terms of P-V) being just 40-15% for errors having spatial wavelength in the range 66.7-50 mm.
- In the range of the amplitudes considered for the analyses (2-100 μm P-V original error), results confirm a quasi-linear behavior, i.e. the percentage of P-V correction is always the same regardless the initial error P-V.

Table 6.9: Shape errors considered during the FEM analyses.

	Case 1	Case 2	Case 3	Case 4	Case 5	Case 6	Case 7	Case 8
								
A [μm]	10	10	10	10	10	10	10	10
λ [mm]	400	200	133.3	100	80	66.6	57.143	50
PAR phase	0°-0°	0°-0°	0°-0°	0°-0°	0°-0°	0°-0°	0°-0°	0°-0°
HYP phase	0°-90°	0°-90°	0°-90°	0°-90°	0°-90°	0°-90°	0°-90°	0°-90°

- A = Amplitude of the considered initial sinusoidal error. This is half of error P-V except than in the case of wavelength 400 for which it is equal to the P-V value.

- λ = Wavelength of the considered initial sinusoidal error

- PAR & HYP phase = Phase considered for the sinusoidal errors in the parabola and hyperbola segments: parabola segments (at the bottom in the figures) is always considered at 0°; hyperbola segments (at the top in the figures) is considered both in the case of no phase shift between error on front and rear foil (0°) and in the case the error shift between front and rear foil is equal to $\lambda/4$ (90°) for all the errors terms shown.

Fig. 6.72 and 6.73 show examples of the spring back effect: the isocontours of the radial component of the residual shape errors after the removal of the integration mould are reported for two different initial error cases. Such errors have been computed assuming the ribs infinitely stiff versus displacements and rotations; the effect of the five ribs is clearly visible (as it actually is on empirical maps obtained with CUP as previously shown in Fig. 6.70).

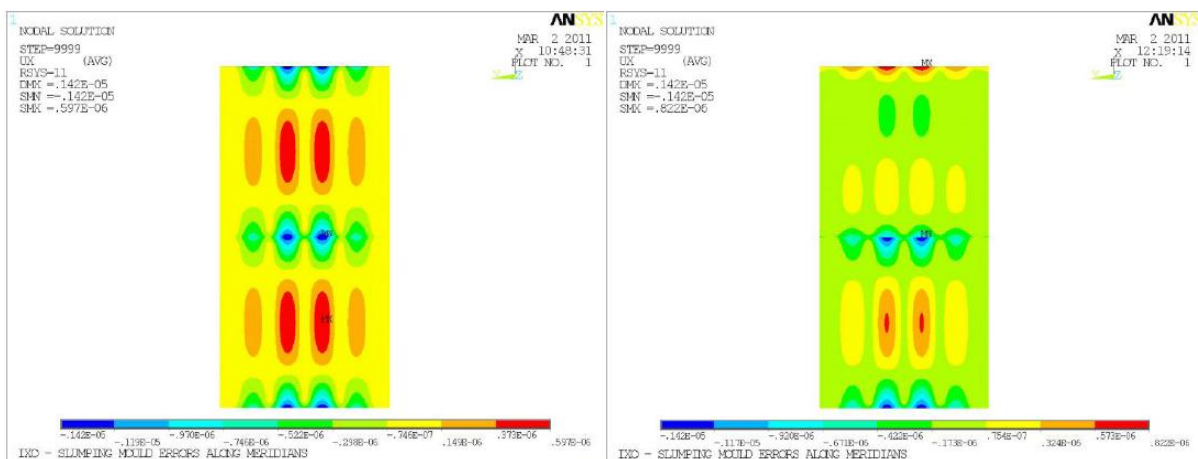


Fig. 6.72: Example of spring back effect at the integration end computed in the case of an initial sinusoidal error of amplitude 10 μm and wave length 400 mm. The isocontour of the radial components of the residual shape errors after integration are reported. (Left Side): parabola and hyperbola present “in phase errors”. The residual P-V error is 2.02 μm , accounting for P-V correction of 79.8%. (Right Side): hyperbola error present a phase shift of 90° with respect to parabola one. The residual P-V error is 2.24 μm , accounting for P-V correction of 77.6% (isocontours are quoted in m and positive displacements are outward).

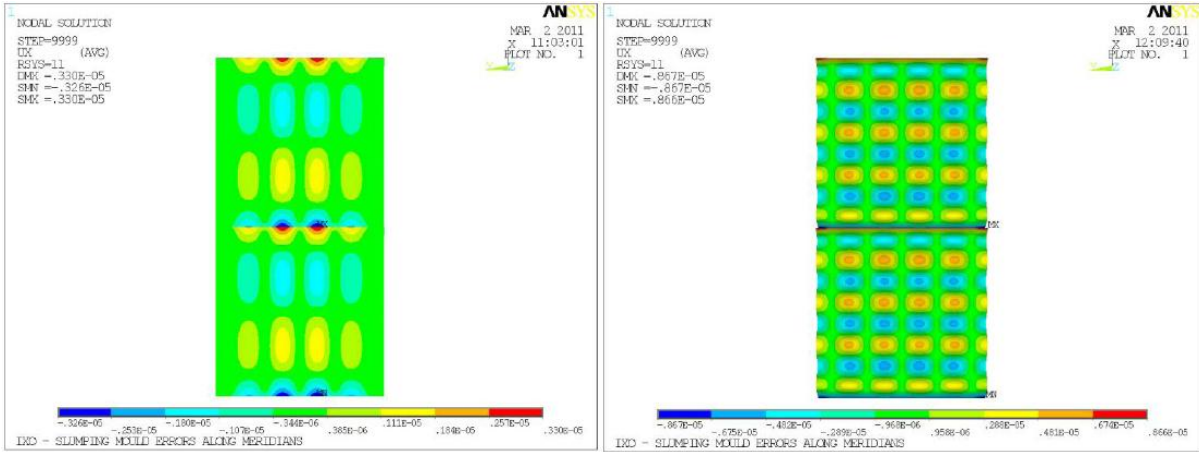


Fig. 6.73: Example of spring back effect at the integration end computed in the case of an initial sinusoidal error of amplitude 10 µm (that is P-V of 20 µm) and wave length 200 mm (Left Side) and 50 mm (Right Side). The isocontour of the radial components of the residual shape errors after integration are reported. In both cases, parabola and hyperbola present “in phase errors”. (Left Side): The residual P-V error is 6.56 µm, accounting for P-V correction of 67.2%. (Right Side): The residual P-V error is 17.33 µm, accounting for P-V correction of 13.3%.

Table 6.10: Comparing the results obtained for different initial errors amplitudes it is possible to state the linearity behavior of the correction. To meet IXO goal of 5 arcsec HEW, low-frequency errors of around 5 µm in amplitude can be accepted.

Case	λ [mm]	PV-before Int.	PAR phase	HYP phase	PV-after Int.	% correction	HEW* [arcsec] In phase	HEW [arcsec] 90° phase
01	400	2.5	0°	0°	2.02	79.8	1.81	0.87
02	200	5	0°	0°	6.56	67.2	0.24	6.19
03	133	5	0°	0°	5.46	72.7	21.1	14.79
04	100	5	0°	0°	7.67	61.6	1.26	25.0
05	80	5	0°	0°	8.09	59.5	59.0	43.9
06	66.7	5	0°	0°	11.16	44.2	5.59	56.4
07	57.14	5	0°	0°	12.16	39.2	108	84.2
08	50	5	0°	0°	17.33	13.3	25.3	106.9
01a	400	10	0°	0°-90°	2.02-2.24	79.8	-	-
02a	200	20	0°	0°-90°	6.56-6.56	67.2	-	-
03a	133	20	0°	0°-90°	5.46-6.51	72.7	-	-
04a	100	20	0°	0°-90°	7.67-7.67	61.6	-	-
05a	80	20	0°	0°-90°	8.09-8.09	59.5	-	-
06a	66.7	20	0°	0°-90°	11.16-11.16	44.2	-	-
07a	57.14	20	0°	0°-90°	12.16-12.23	39.2	-	-
08a	50	20	0°	0°-90°	17.33-17.33	13.3	-	-
01b	400	50	0°	0°	10.0	80.0	-	-
02b	200	100	0°	0°	32.8	67.2	-	-
03b	133	100	0°	0°	26.9	73.1	-	-
04b	100	100	0°	0°	38.3	61.7	-	-
05b	80	100	0°	0°	40.7	59.3	-	-
06b	66.7	100	0°	0°	55.8	44.2	-	-
07b	57.14	100	0°	0°	61.4	38.6	-	-
08b	50	100	0°	0°	86.7	13.3	-	-

* value expected after the correction realized with the integration

Table 6.10 first two rows can be intended as the maximum acceptable P-V errors in the glass segments after the slumping process in order to have acceptable HEW after integration. It has to be considered, however, that they represent the worst case: in fact they are obtained on the entire glass map while the correction degree can be higher if considering single profiles, especially those closed to the ribs. The value in the table will be experimentally verified with already planned tests foreseen for the end of the year.

6.2.5 Slumping results in terms of roughness

The results in terms of micro-roughness of the slumped glass plates are positive and demonstrate that the good original surface finishing of the glass can be maintained through suitable setting of process parameters. To identify the process capability to replicate or not the micro-roughness of the mould was an important scope posed at the beginning of the study. Remind that the initial selection of Fused Silica as material for the mould was also dictated from the need of having its surface super-polished, since the roughness replication capability of the process was not known at the beginning of the project. The numerous tests performed allowed concluding that the forming process has the potentiality of preserving the glass original micro-roughness without introducing unacceptable degradation. Particular attention was posed on the impact of the pressure application: by varying the pressure of the process, keeping constant all the other slumping parameters, it has been possible to evaluate the effect of pressure on the surface quality of the final plates. At this regard, AFM measurements have been performed on the moulds and the glass segments, both before and after the slumping processes: from their comparison, it was possible to understand the effect of the process on the roughness of the glass. Results suggest that the pressure has effect on the roughness of the glass foil, depending on the surface condition of the mould and on the presence of dust between the mould and the glass surfaces during the forming process. In particular:

- The application of pressure is essential to avoid mid-frequencies in the slumped plates;
- The applied pressure should be at least 20 g/cm^2 in order to press the whole glass up to its edges;
- The applied pressure should not exceed the value of 150 g/cm^2 since with higher pressure the metal membrane deformation does not change but its internal stresses are bigger and might create problematic points of forces concentration with the possibility to increase sticking behavior;
- Pressure should not be applied at temperature higher than 590°C because sticking problems will arise;

- Present results indicate that the microroughness of the original glass foil is maintained also up to 595°C if pressure is not applied. However in this case the absence of pressure does not allow to avoid undesired mid-frequencies in the glass plate;
- With temperature higher than 595°C the surface texture of the glass start to replicate that of the moulds, hence it should be super-polished;
- If pressure is applied, the microroughness of the original glass foil can suffer from degradation, depending on the value of the applied pressure itself and on mould surface conditions, as reported in Table 6.11. The presence of dust contamination is also an important parameter;
- With mould of low surface finishing (roughness in the AFM range > 50 nm), the original surface of the glass can be maintained only with relatively low slumping temperature and soaking time ($T \leq 575^\circ\text{C}$ and soaking $t \leq 6\text{h}$), however in this case the obtained shape might contain deformations.

Table 6.11: Summary of the results in terms of roughness obtained with AFM characterization on glass foils slumped with different conditions, summarized in the first row. The degradation of glass micro-roughness is shown in dependence of pressure, low mould surface finishing and Pt degradation.

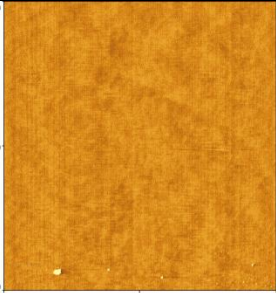

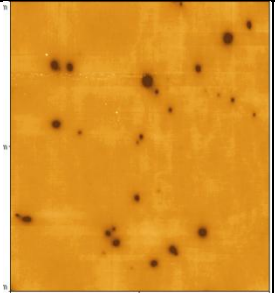

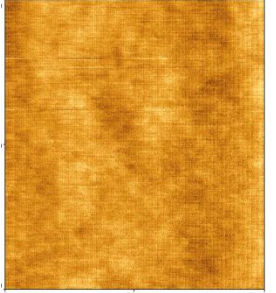
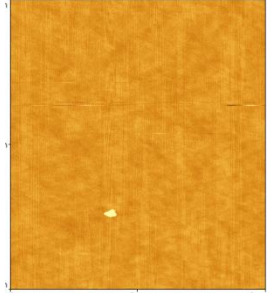
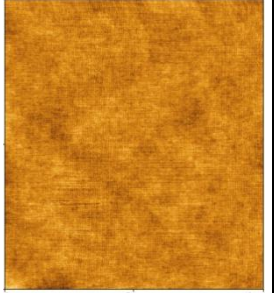

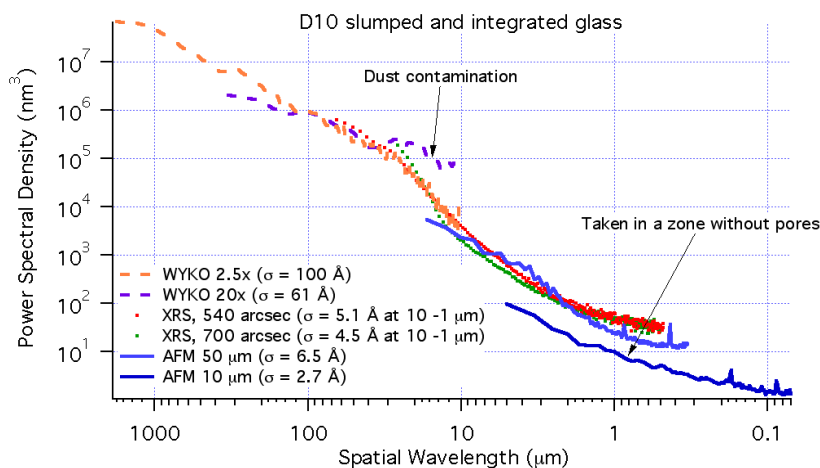
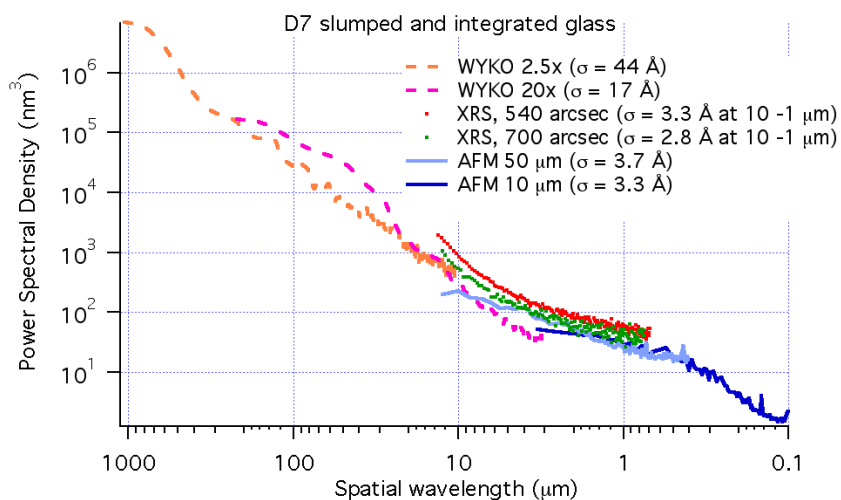
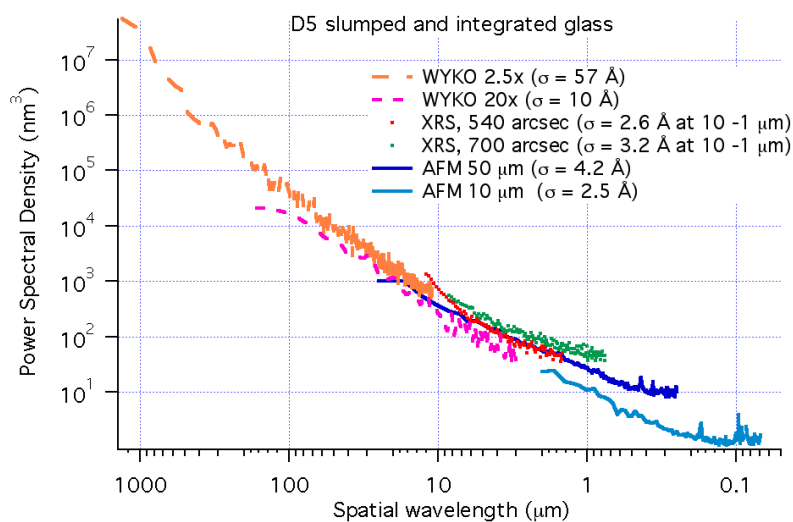
	Glass slumped on 70-80 Å rms mould with pressure < 80 g/cm²	Glass slumped on 70-80 Å rms mould with pressure > 80 g/cm²	Glass slumped with p 50 g/cm² on mould with lower surface finishing	Case of degraded Pt release layer on FS mould: Pt migration to the glass
	Practically, the original glass surface finishing is maintained	Degradation starting	Glass surface texture start to replicate mould roughness	Case after more than 8 thermal cycle
50 µm x 50 µm	 $\sigma \approx 3.1 \text{ \AA}$	 $\sigma \approx 5.65 \text{ \AA}$	 $\sigma \approx 9.5 \text{ \AA}$	 $\sigma \approx 16.6 \text{ \AA}$
10 µm x 10 µm	 $\sigma \approx 3.6 \text{ \AA}$	 $\sigma \approx 5.35 \text{ \AA}$	 $\sigma \approx 2.6 \text{ \AA}$	 $\sigma \approx 17.6 \text{ \AA}$

Table 6.12: Results in terms of PSD evaluated through AFM and WYKO characterization of the slumped and integrated glasses. All the measurement (AFM, WYKO and BEDE Diffractometer data) are in good agreement. The relatively high values obtained in the WYKO 2.5X range of frequencies are presently under analyses to check the eventual influence of the measuring instrument (TBC).



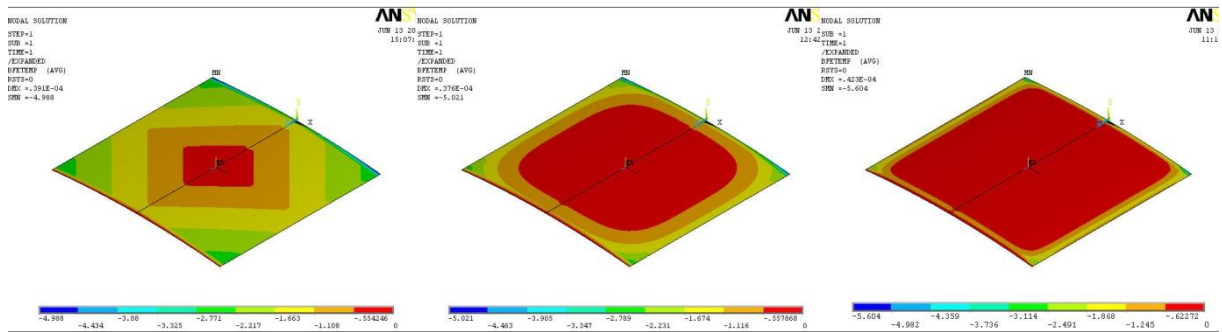
6.3 Analyses and understanding of still open questions

The numerous tests performed in the last two and an half year during the PhD period, allowed improving the INAF-OAB competences in the field of slumping technology. The entire process undergone a complete assessment and important parameters modifications have been introduced to account for the demanding requirements of X-ray optical segments. Positive trends toward the right direction have been observed and are still on going. Few important points are still opened, for which the gained experience suggests possible causes and solutions; some of them are already on the course to be realized, others are foreseen for the next months (until the end, in spring 2012, of the ESA contract under which this research was conducted). As previously shown, the results in terms of shape, obtained on the glasses slumped on Fused Silica MCX1 and MCX2 moulds and on MK20-01 Zerodur K20 mould, do not meet the requirements, even if they show a positive trend in the right direction of improvement. This is the main open issue; the longitudinal profiles are not almost straight line replicating mould profiles as they should be but present a first-harmonic-like sag error in the range of 20-50 micron. This deformation can be partially corrected during the integration of the slumped plates into the XOUs stack; however, it is necessary to reduce it to demonstrate a TRL of 5 for the slumping technology of IXO X-ray mirror segments. It is first of all important to understand where the deformation comes from. Two main possible causes have been individuated and analyzed: thermal effects or pressure effects. They are described hereafter.

6.3.1 Thermal origin of the edge shape deformations

Thermal FEM analyses suggested that the shape deformations still present in the slumped glasses might originate due to stresses that arise inside the foils because of thermal gradients between their center and edges during the cooling down phase. To limit the radial thermal gradient, the big oven was selected for the cylindrical slumping experiments. However, the obtained gradients of around 5°C (notice that this value is only 1% of process maximum T) are sufficient to cause low frequencies deformations of tens of μm , comparable with those observed in the slumped plates. Working on the thermal cycle parameters it was possible to lower the values of deformations, which however are still in the order of 20-50 μm sagittas. Simulations have been carried out under the hypothesis that the thermal gradients present in the glass foil during the process causes an internal stress distribution that is frozen in the plate itself. While it is known that during the cooling down the central part is hotter than edge areas, the real T distribution is not known because of the difficult in placing the thermocouples in fixed positions on the mould. The situation should be better with the new moulds (MK20-10 and MSI-1) that have been produced with ad-hoc holes to house the thermocouples.

Hence, lacking of direct measurements, three different cases have been considered for the distribution of temperature, as shown in Fig. 6.74.



1) Linear distribution in radial direction | 2) Exponential, parallel to the edges | 3) Higher degree exponential
Fig. 6.74: Temperature gradients in the 200 mm x 200 mm x 0.4 mm glass foil considered for the simulation as representative of the cooling down phase of the slumping process (red = hot, green = cold). The Z axis is parallel to the optical axis; X is the perpendicular direction along the glass plane; and Y represents the vertical deformations.

The considered temperature distributions are responsible for the formation of stresses inside the glasses which in turn cause longitudinal profiles to present low-frequency trend. By comparing the results of some slumped plates with the simulation results, it was possible to discriminate between the three conditions taken into account. Fig. 6.75 reports two examples to be compared with simulated data of case three reported in Fig. 6.76. Further tests are presently ongoing to check for this behavior and get more statistics; if the results are confirmed, the thermal simulation is validated and can be employed for process parameters optimization.

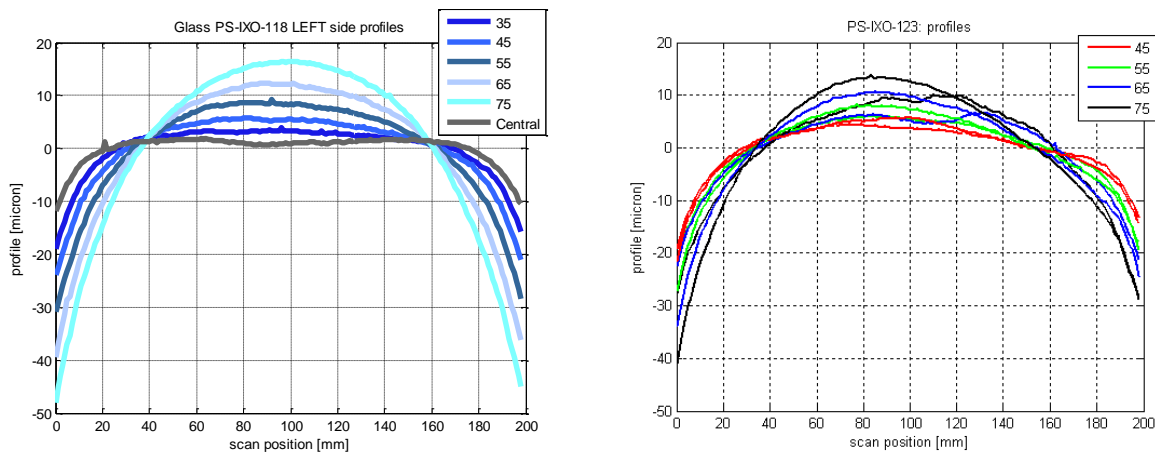


Fig. 6.75: Example of profiles obtained on glass foils slumped on MK20-01. The shape deformation that they show is in large part due to thermal issue, as clear when comparing the empirical data with the simulations results. (Left Side): PS-IXO-118: the measured profiles match the simulation. (Right Side): PS-IXO-123: other contributions to the deformation exists in fact the data follow the trend of the simulation but present few differences, which in this case resemble the profile trend of the not optimal employed mould.

However, at the moment the simulation results are applicable only to the case of Zerodur K20 mould. In the case of Fused Silica in fact the results observed on realized sample show different trend with

respect to the simulated one. The reason why lies in the presence of the reflective Pt layer whose behavior is not easy to simulate and it is not present in the simulation yet. Besides, also the presence of the metal pressing membrane at the moment simulated in a simplified way and need to be upgraded. Activities to improve the knowledge of this aspect of the technique are already planned and foresee as simulation as empirical work.

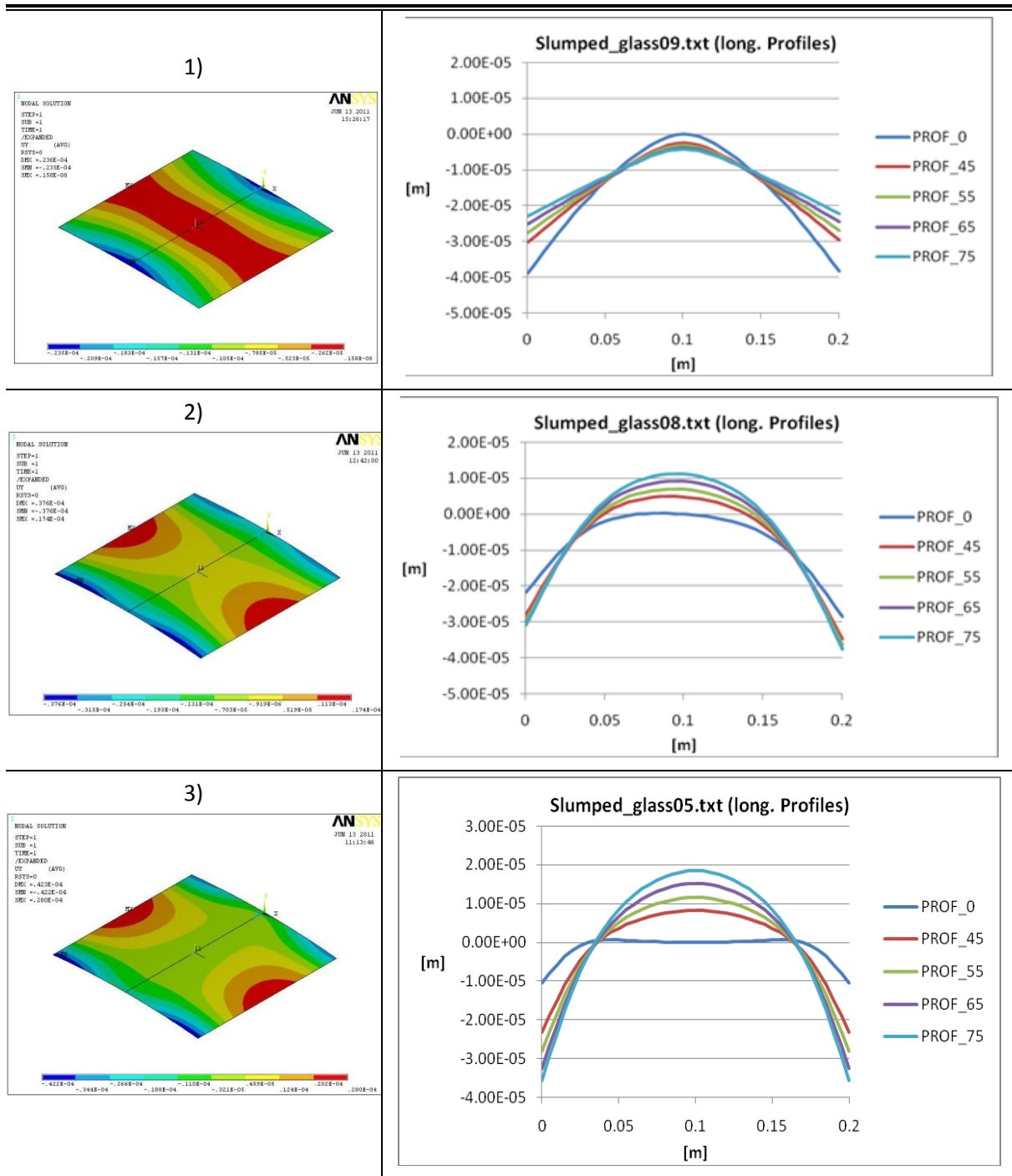


Fig. 6.76: (First Row): Vertical displacement originated in the slumped glass foil due to the stress distribution induced by T gradients. (Second Row): Mono-dimensional longitudinal profiles taken at several distances from the central one.

6.3.2 Simulation of glass edges cutting

Given the presence of shape deformations in the slumped glass, and considering that at least in the case of Zerodur K20 mould they seems to be concentrated on the glass edges, the investigation on the effects of a possible cutting was started. Fig. 6.76 reports the results of the cutting of 30 mm per side passing from 240 mm x 240 mm glass to a smaller plate of 180 mm x 180 mm. The final intrinsic shape of the slumped plate changed due to the release of stresses consequent to the removal of one part of the glass so that the internal stresses undergo a re-distribution inside the glass. Also this analysis needs to be verified with empirical tests to check the goodness of the simulations. Activities have already started in this direction and the preliminary results confirmed in part the simulation results as reported in Fig. 6.78. The reason why they are not completely identical might lie in the fact that other effects act concurrently to the presence of deformation that are dictated not only by the thermal conditions, which however remains the main cause.

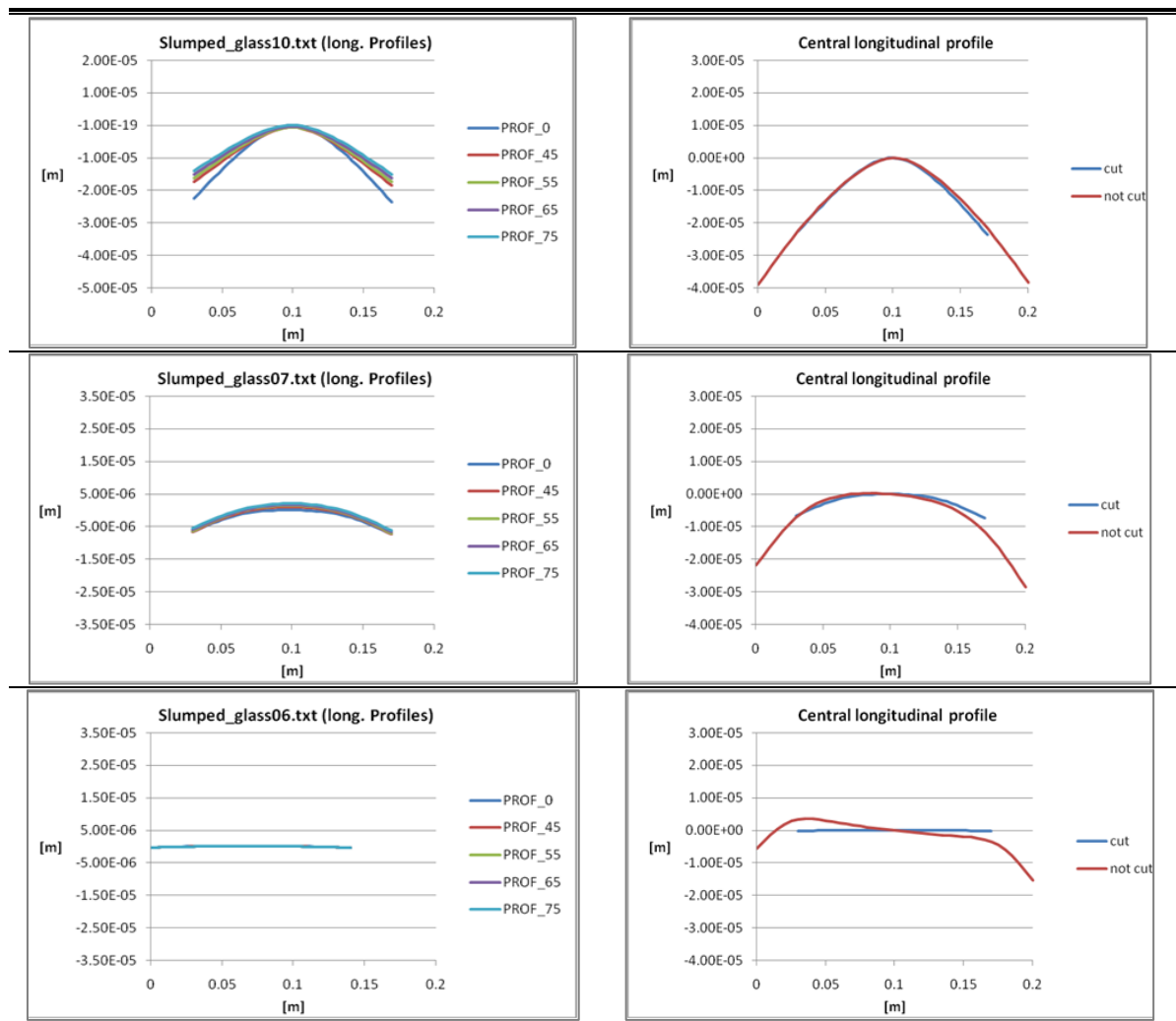


Fig. 6.77: Profiles as they will look like if the simulation on edges cut is confirmed. The comparison is more appreciable on the right column.

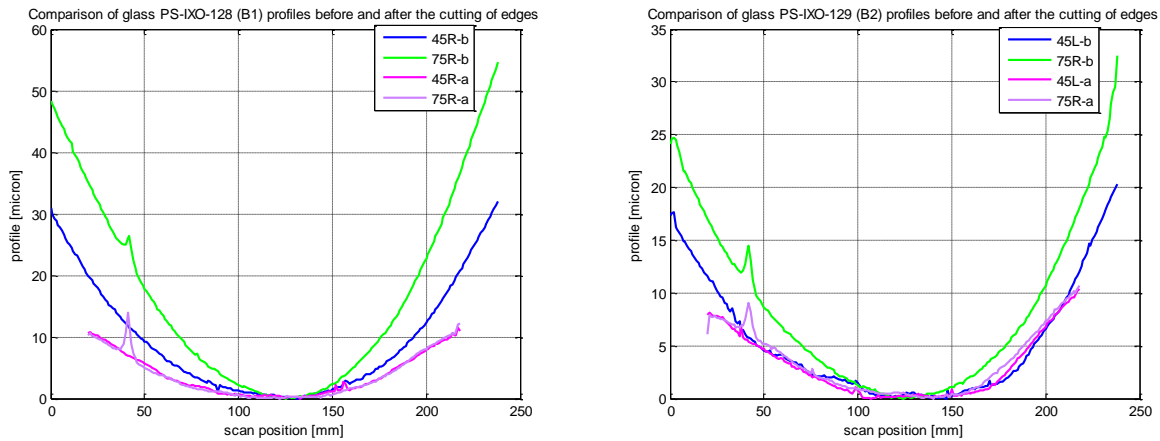


Fig. 6.78: Preliminary results obtained on the glass edges cut. The trend seems to follow the simulation results however further analyses are ongoing to confirm the result. In this case the HEW values pass from around 200-300 arcsec to 45-50 arcsec, which have the potentiality to give a final HEW close to the goal considering the percentage of correction obtainable with integration.

It is worth noting that these results do not contradict what previously shown in § 6.2.2.1; they refer to two different aspects of the cutting, and in this particular case of the laser cutting. The laser cutting technology does not introduce itself permanent deformations in the plate; however by eliminating a portion of the glass it generates a different equilibrium distribution of eventual internal stresses already present in the glass and this causes the shape to change. Finally, it has to be mentioned that also the presence of pressing steel membrane causes temperature gradients in the glass plate: this element is not present in the simulations at the moment and will be added in the near future. Fig. 6.79 shows the qualitative effect from a thermal point of view of the presence of the metal membrane used to apply pressure.

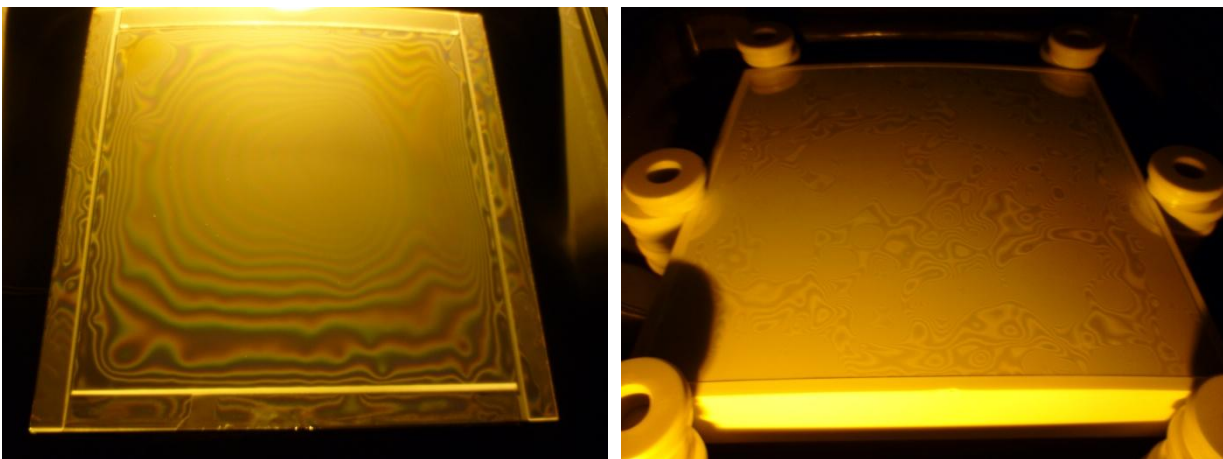


Fig. 6.79: Qualitative effects generated by the presence of metal membrane with no pressure application. (Left Side) PS-IXO-106: The case in which the steel sheet was present. (Right Side): PS-IXO-102: slumping with no pressure (and no steel sheet) in the big oven.

An accurate modeling of the glass thermal condition is difficult to obtain because of the asymmetry of the process configuration that foresees the glass closed in between the mould and a thin steel sheet.

6.3.3 Investigation on the effects of the pressing membrane

Although if the deformation mainly originates from thermal condition, the presence of the pressing membrane might have same impact, too: not only because it itself influences the thermal conditions of the glass foil but also through the application of pressure. Its effects on the final result of the slumping process have been analyzed and the main results are reported hereafter. The effects on the glass sticking behavior of point of force concentration in correspondence of glass edges have already been introduced in section § 6.1.3. The attention should be posed now on the fact that the pressing membrane is constrained on a plane but has to conform its shape to the cylindrical one of the mould when pressure is applied. Because of its intrinsic rigidity, it tends to form wrinkle that causes non-uniformity in the applied pressure. The application of pressure is realized by means of a thin T 304 Stainless steel sheet, acting as a membrane that divides the internal muffle volume in two parts. Its dimensions are 440 mm x 440 mm and the thickness is very low, 25 micron. This thickness is the lowest thickness available on the market for foils of that dimension. Thinner foils are not produced only for commercial reason, since there is no request on the market. Due to the relatively small quantity of steel sheet necessary for the development phase, it was not possible to obtain thinner foils and so the 25 micron thick was used. The main characteristics of this steel sheet are reported in Table 6.13.

Table 6.13: Main characteristics of the metal sheets used as pressing membrane.

Manufacturer	ESPI Metals
Material	High purity stainless steel AISI 304
Max. Dimension	Height of 600 mm
Min. available thickness	25 μm
CTE	$18.7 \times 10^{-6} / ^\circ\text{C}$

INAF-OAB had previous experience with 12.5 micron thick sheets. They easier conform to the shape of the mould because of the lower rigidity, however they sometimes presents problems of sealing since air pass through their very thin structure. The optimal range lays somewhere in between 15 and 20 μm . Two kinds of tests were performed to investigate the behavior of steel sheets and possible impacts on the final shape of the glass segment. The first set of tests was performed at Room Temperature to start getting preliminary information about steel sheet effects. The second set of tests was performed at high temperature. Tests performed at Room Temperature presented an intrinsic limitation due to the fact that during the process the pressure is applied at high temperature (around 570-590°C) when the materials characteristics are different from those at Room Temperature. For this reason the behavior of the metal sheet might be different. Nevertheless, they

gave some indications on how to improve the direct slumping set up. Those indications were implemented in the tests performed at high temperature (up to 610°C), which in practice comprise all the slumping experiments performed during the study.

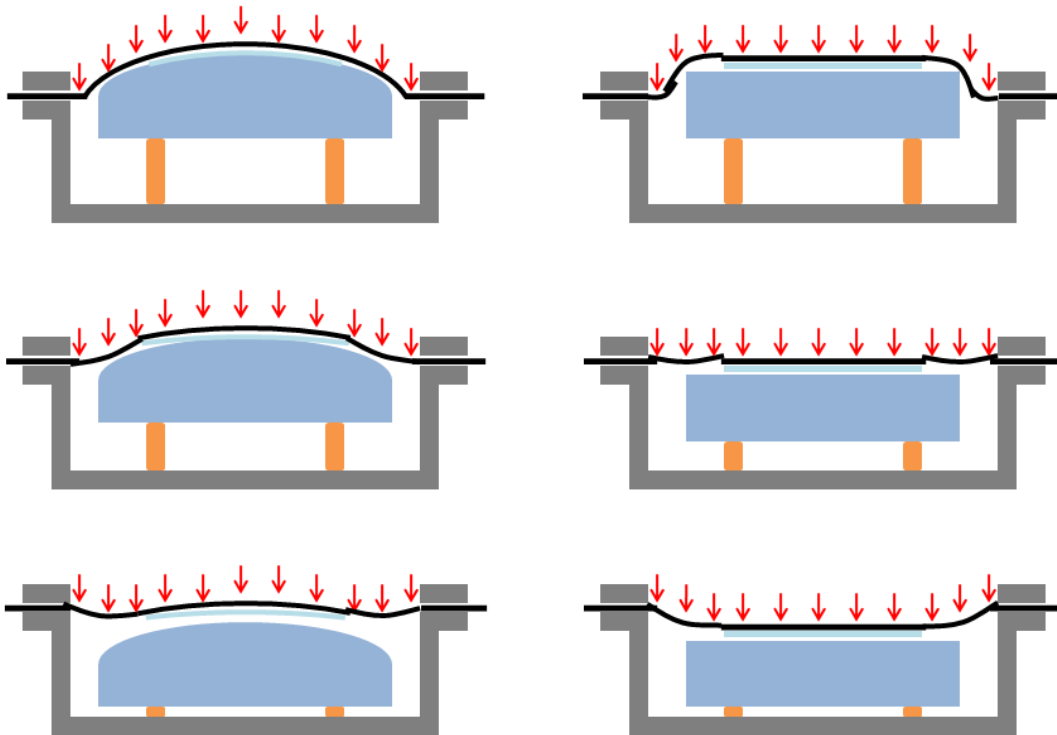


Fig. 6.80: Cold Tests set up. (Left Side): Configuration of the tests performed on the convex mould. (Right Side): Configuration of the tests performed on a plane mould. Depending on the height of the mould with respect to the plane of the pressing membrane, the obtained deformation of the metal sheet is different and might have different effects on the slumped glass foil.

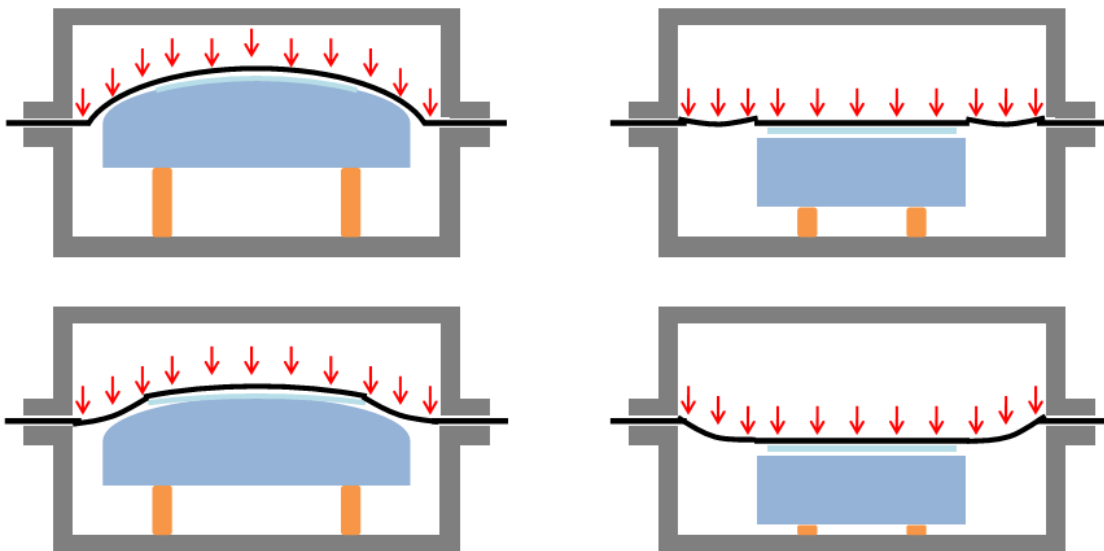
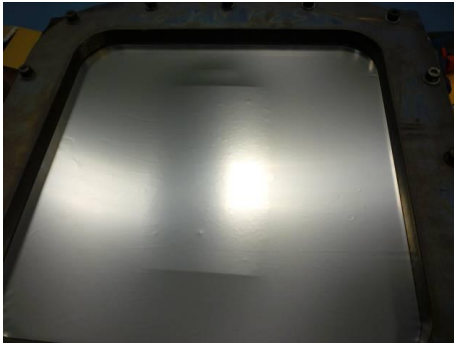


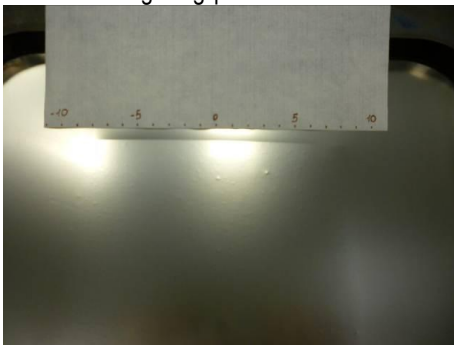
Fig. 6.81: Hot Tests set up. (Left Side): Configuration of the tests performed on the convex mould. (Right Side): Configuration of the tests performed on a plane mould. Depending on the height of the mould with respect to the plane of the metal sheet, the obtained deformation of the pressing membrane is different and might have different effects on the slumped glass foil.



If the mould height is below the pressing membrane plane, this does not press the entire glass foil when giving pressure.



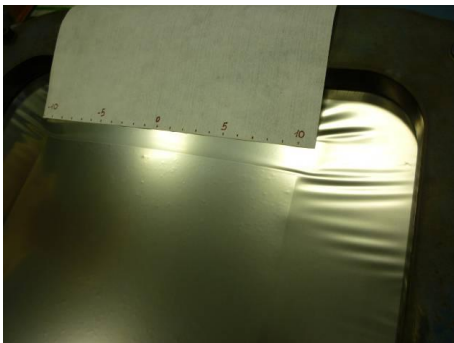
Also with higher values of pressure, the metal sheet cannot reach the edge of the glass parallel to the cylinder axis.



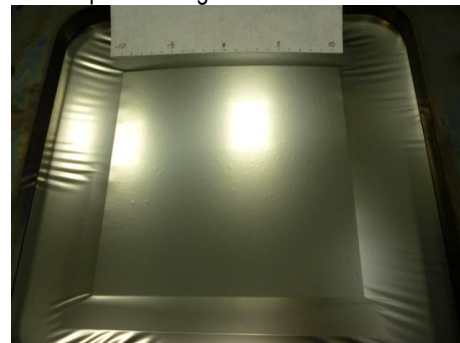
The situation becomes better when the mould is put in a higher position.



This position should be at least 8 mm above the metal membrane plane to have the entire glass pressed against the mould.



Higher pressure value guarantees no or less wrinkle on the glass angles.



With the present plane-muffle set up, the steel sheet cannot reach the edges of the mould in longitudinal direction but can press the entire 200 mm x 200 mm glass area.

Fig. 6.82: Images of cold tests performed with the cylindrical mould: effects of different mould height with respect to pressing membrane plane and of different pressure value are reported.

Despite their intrinsic limitation, the performed cold tests have been useful to better understand the behavior of metal membrane during the application of pressure and to draw some conclusions to be applied during the hot slumping of cylindrical mirror plates:

- The cylindrical mould central point needs to be at least 8 mm higher with respect to the metal sheet plane, to allow the pressing up to the glass edges;
- The cylindrical mould needs to be perfectly horizontal with respect to the steel sheet plane, to avoid points of forces concentration with different values on two opposite glass sides;
- The applied pressure needs to be in the range 20 - 50 g/cm², to eliminate the majority of wrinkles on the steel sheet in correspondence of the glass foil;
- Pressure higher than 50 g/cm² guarantee even less or no wrinkles on the metal sheet, (however known to introduce issue on the final roughness of the glass surface).

The hot tests were performed implementing the cold tests results. It is worth noting that the hot tests are represented by almost all the slumping experiences realized: some of them were specifically performed to evaluate the effects of pressure, some others were made with the main aim of evaluating the effects of other parameters (i.e. temperature, thermal gradients, heating up and cooling down rate, Ar flow). Anyway, all the hot tests, also those whose main aim was not to evaluate the pressure effects, gave useful information with regards to this topic:

- The application of pressure is necessary during the process of direct slumping to help the glass coming in full contact with the mould and eliminate mid-frequencies;
- The application of pressure has an important effect on the edges of the glass. In particular, due to the step present between the mould and the glass surface, the edges of the glass become points of concentration of forces that increase the sticking probability;
- The application of pressure might contribute to local deformations on slumped glass, especially on those concentrated near the edges of the glasses, because of wrinkle that form in the metal sheet constrained on a plane when it is forced to assume a cylindrical shape;
- As already discussed (see § 6.2.5), the value of the applied pressure has consequences on the final micro-roughness of the slumped glass plates;
- The application of pressure through a metal pressing membrane leaves an imprinting on the back surface of the glass and local deformations in correspondence of points with imperfections in the steel sheet. Those deformations are on the back of the glass and do not have any impact on the optical surfaces and performances, although if they might have impacts on the strength of the glass and must be taken into account.

To better understand and eventually eliminate the potential effect on glass edges deformation coming from wrinkles in the metal sheet, a cylindrical muffle was designed and realized. It was

delivered in late spring 2011. Because of the difficult in realizing two coupled cylindrical surfaces, the pressure sealing it could guarantee was very poor. Efforts, based on past experience, have been spent to individuate a way to guarantee it. It was finally identified the optimum set up for the use of the cylindrical muffle that should allow a more reliable application of uniform pressure, since the pressing membrane is bind on a cylindrical surface instead than on a plane, and will be used for tests planned for the end of October.

6.3.4 Summary of open questions and proposed solutions for follow up studies

The present state of the art in the *hot slumping technology with pressure assistance* has been discussed in the previous paragraphs of this chapter, considering several aspects of the process. The still open questions have been individuated and described, together with the planned activities proposed to solve them. Table 6.14 summarized these topics.

Table 6.14: Summary of the still open questions and of the solutions proposed on the base of the gained experience.

Open point	Individuated causes	Proposed solution
Shape deformations on slumped glasses	Thermal effects	<ul style="list-style-type: none"> - Reduce gradients inside mould (a possibility might be to shape the mould profile as computable by FEM analyses). - Since the deformations are mainly concentrated on the glass plates edges, cut them away. The tests on the cutting have already started and other are planned to check the results.
Local shape deformations	Wrinkles and defects on pressing membrane	<p>Modification or elimination of the pressing membrane: Al sheets might be used instead of steel.</p> <p>A solution has been found and already tested to slump the glass using the glass foil itself as membrane to separate the muffle cavity in two chambers allowing for pressure gradient application.</p>
Potential reduction of the slumped glass strength	Application of the thermal cycle itself	A procedure has been individuated for the realization of the samples necessary to test this parameter through destructive double-ring tests. A possible solution to be investigated is the application of chemical tempering on slumped plates.

7 Conclusions and final remarks

This text reported on the research activities carried out by the author at the INAF-OAB laboratories over a period of 3 years. The main topic was the application of the *hot slumping technology with pressure* for the realization of segmented Grazing Incidence optics, with particular reference to the IXO mission case. The slumping technology is a thermal process that foresees the manufacturing of thin glass mirrors by shaping them over a mould at high temperature: when heated up in an oven at the suitable slumping temperature, the glass foil reaches a viscosity low enough to allow the replication of the mould shape while still permitting to maintain the original glass surface finishing. As compared to traditional technologies for making mirrors, thermal slumping is preferable because it is a high-volume, low cost, and one step fabrication process, with reduced associated risks: this makes the application of the slumping technique very attractive for the realization of next generation X-ray telescopes, that require a huge number of equal optical segments (>15000 pieces) to be produced in a relatively short time (around 4 years to be compliant with mission schedules). In this contest, a research was conducted to assess the technology and fully explore its potentiality in the case of X-ray mirror production. The IXO - International X-ray Observatory mission, nowadays under study by several Space Agencies (ESA, NASA, JAXA), has been taken as reference: the entire research was carried out in the frame of a project, financed by ESA, for the study of a *back-up technology for IXO optics* (contract number 22545). The project is planned to finish in spring 2012 with the production of a prototype representative of the IXO optical units.

The manufacturing of X-ray telescopes poses stimulating challenges because of the stringent requirements in terms of shape accuracy and surface roughness: typically, the shape of the mirrors should be controlled at sub-micron level while their micro-roughness must be maintained at level of Å. In addition to these requirements, for the next generation telescopes that foresee an effective area at least 10 times larger with respect to the current ones, also the mass of the optical payload might become problematic. Manufacturing techniques employed in the past for the realization of X-ray optics (such as direct polishing, replication by electroformed Nickel or epoxy, and aluminum thin foil shaping) will result in too heavy and large systems to be lift in space by the available or near future launchers. In this light the work done assumes fundamental importance since it might be the key to open the way to future X-ray missions for which the optical payload manufacturing could represent a show-stopper if required TRL are not verified. In addition, it has to be considered that the same technique can be used for the production of other elements, such as for example adaptive

optics or lightweight mirrors: also for those cases the main results of this study can be applicable with no major changes.

The entire work has been conducted with the collaboration of valuable and motivated persons, each one devoted to a particular topic of the project. The author's main responsibility was the assessment of the process of slumping: this includes the analyses of every step of the procedure, the careful selection of materials, and the choice of cycle parameters.

The author was actively involved in the realization of more than one hundred slumping experiments and in the analyses of the results through shape and surface morphology characterizations. In particular, she conducted autonomously the experiments in the oven laboratory and selected the more reliable materials and set up to be employed. Besides, she participated in the characterization campaigns of the moulds, glass foils, and slumped plates. Through the analyses of measurement data she could compare the empirical experiences with FEM simulations and derive an improved understanding of the process. Even if the final aim of the study was not completely met at the present stage, the work till here performed allowed to obtain important enhancements in the process set up and parameters definition, showing a positive trend in the results. In particular:

- The assessment of the slumping technology allowed to define the procedure to be followed for the slumping of Grazing Incidence optics (see Annex D);
- New tools have been realized to produce slumped plates representative of the IXO X-ray telescope design (see § 5.2.2);
- Improvements have been added to the laboratories, specifically related to cleaning control during process preparation (see § 5.2.1);
- The materials for the moulds have been selected and the requirements on their geometrical shape and surface finishing have been derived to be representative of the IXO design and discussed with the manufacturer (see § 5.2.3);
- The glass has been selected and procured from the vendor (see § 5.2.3);
- A complete test campaign was conducted on the mould and on the glasses procured, to check their compliance with the requirements (see § 6.2.1 and 6.2.2);
- Several experiments allowed to individuate a reliable antisticking layer, and a procedure for its deposition, to be applied on the Fused Silica moulds to prevent glass adhesion during the process (see § 6.1.3);
- The main parameters of the process have been considered and their impact on the final results has been analyzed. The thermal gradients inside the glass during the cooling down phase have been individuated to be the most important parameter driving the results in

- terms of shape. The pressure, together with the soaking temperature and time has been individuated as the main parameters from a point of view of roughness results (see § 6.2.3);
- It has been demonstrated the possibility to maintain the original surface texture of the glass by the suitable tuning of process parameters (see § 6.2.5);
 - The results obtained in terms of slumped glass shape showed a positive trend of improvement, even if low-frequencies deformation are still present in the plates after the hot slumping phase (see § 6.2.4);
 - Cutting processes have been considered to select the best one which leaves sharp cut edges and does not introduce stresses in the glass; the laser cutting has been individuated to be the most reliable from this point of view (see § 6.2.2.1 and 6.2.2.2);
 - The mechanical strength parameter of the glass as delivered by the vendor has been checked through destructive tests (see § 6.2.2.2);
 - It was demonstrated how the integration procedure is able to take care of low-frequencies errors and correct them through a phase of cold slumping: the results on the integrated plates suggest the potentiality to meet the final scope of the study: i.e. the realization of a prototype representative of the flight optical modules of IXO telescope by the end of spring 2012 (see § 6.2.4.2).

The valuable gained experience has been committed to propose solutions to the still open questions and to plan the follow up activities: some of them are already ongoing while others will start in the near future. In particular:

- Production of the slumped plates to be integrated in the prototypes;
- Production of numerous samples to test the glass strength after the thermal cycle;
- Assessment of Silicon as new material for mould;
- Assessment of new antisticking layer, other than Platinum, to overcome the necessity of antisticking coating re-deposition after several thermal cycles;
- Further reduction of thermal gradients during slumping;
- Modification in the application of pressure through a new kind of pressing membrane and cylindrical muffle to avoid local deformations in the slumped glasses due to wrinkles in the metal sheet;
- Cutting of slumped glass edges to eliminate perimetrical areas and to relax potential internal stresses;
- Improvements in the hot wire cutting system.

The performed activities have been published in a number of paper, lists on page 209.

8 Annex A: Surface morphology parameters

To evaluate the results of the slumping process, the *intrinsic shape*²⁰ and the *micro-roughness* of the obtained segments, and those of the moulds for comparison, have been considered. The two parameters are of fundamental importance to describe the performances and the imaging capacity of mirrors [132], [133], [134]: the intrinsic shape traces the path of the reflected rays to the focus, while the micro-roughness accounts for scattering effects. Both have effects on the resolution at the focus, i.e. on the performances of the mirrors in producing sharp images on the focal plane. Different numerical parameters can be used for their description, the most important being:

- The height of scan profiles and their local slopes rms;
- The roughness rms and its distribution over the frequency window (the PSD -Power Spectral Density-);
- The angular resolution of the produced mirrors (expressed in terms of HEW -Half Energy Width-).

These main parameters considered throughout the entire work, are hereafter briefly described, together with the basic theory behind them. Each surface can be completely described by a function $z(x,y)$, which gives the height values for every position on the surface. Let's consider the 1D case of surface profiles for which the profile height is given by $z=f(x)=z(x)$; the bi-dimensional case is simply the mathematical extension of it. Each profile shows height variations with respect to a reference theoretical/mathematical profile: in fact, even the best polished surface shows "noisy" features when observed at microscopic levels. The distances between two adjacent picks (or valley) represent the spatial wavelength while the amplitudes of the variations are usually expressed, depending on the spatial wavelength being considered, in terms of shape errors or roughness (or micro-roughness). Fig. 8.1 and 8.2 clearly explain the difference while Table 8.1 summarized formulae and definitions. Both shape errors and roughness have important consequences on the performances of a reflecting

²⁰ The adjective "intrinsic" indicate the "real" shape of the considered surface with no deformations introduced by gravity effects. It particularly applies to the floppy glass surface considered during the study, which are affected by support and gravity deformations.

surface since they cause the reflected beam not to follow the wanted path to the focus. In particular, in case of shape errors the effects can be analyzed with the application of geometrical optics formulas while, the effects of micro-roughness have to be considered through the scattering theory. Its consequences are different in dependence on the radiation wavelength: the shorter the wavelength the higher the effects. X-rays lie in the wavelength range of 0.01 – 10 nm (corresponding to an energy range of 120 eV – 120 keV): the mirror surface finishing should be good at a comparable level, since surfaces roughness with height in the order of the incident wavelength causes out-of-focus scattering of the reflected beam up to 20% at Grazing Incidence angle of 2°. It is immediately clear from this example how the surface topography of an X-ray mirror is of extreme importance and should meet stringent requirements in terms of micro-roughness to ensure sharp images in the focus. Between shape errors and micro-roughness errors lays a range of frequencies in which the effects are contemporarily present, normally referred to as waviness area. Another way to describe surface profiles is through a sum of Fourier components of different spatial wavelength. The square modules of the Fourier transformation of the profile height ($Z(f_x, L)$) normalized to the scan length represent the Power Spectral Density, PSD. This mathematical function is used in the field of surface metrology to correlate the profile height amplitudes $z(x)$ with the corresponding spatial frequencies f_x . The 1D PSD has the dimension of a cubic length [nm^3]. Slope errors and roughness data can be directly calculated also starting from the PSD. However, the square of the module in the PSD formula erases the information on the wave phase: the PSD only contains statistical information but does not allow to reconstruct univocally the profile morphology. The PSD is a geometrical property of the surface and is independent from the measuring technique employed for its evaluations. Different characterization instruments should give the same results in the same spatial frequencies regions (in the limits of instruments error bars): this allows for a cross checking of data acquired with different techniques. It is possible to demonstrate that the PSD is the Fourier Transform of the Self-Correlation Function and vice-versa (as both are real and even):

$$C(x) = \int_{-\infty}^{+\infty} PSD(f_x) e^{2\pi i f_x x} df_x$$

The autocorrelation function $C(x)$ is sometimes used as an index on how much the height function is similar to a self-replication shifted by a factor y (multiple of the sample step in the discrete case). The autocorrelation function has a maximum for $y=0$ and then decreases, as quickly as the profile is different from its shifted replica, meaning it does not contain periodic features. The shift at which the function decreases by a factor of $1/e$ is called correlation distance. Slope errors and roughness can be derived from the autocorrelation function. The knowledge of the surface morphology, acquired with different metrological instruments depending on the considered spatial frequencies, allows the

evaluation of its effect on the focal spot, described in terms of HEW, i.e. in terms of the angular diameter including the 50% of focused photons. This is done by ray-tracing codes and scattering simulations.

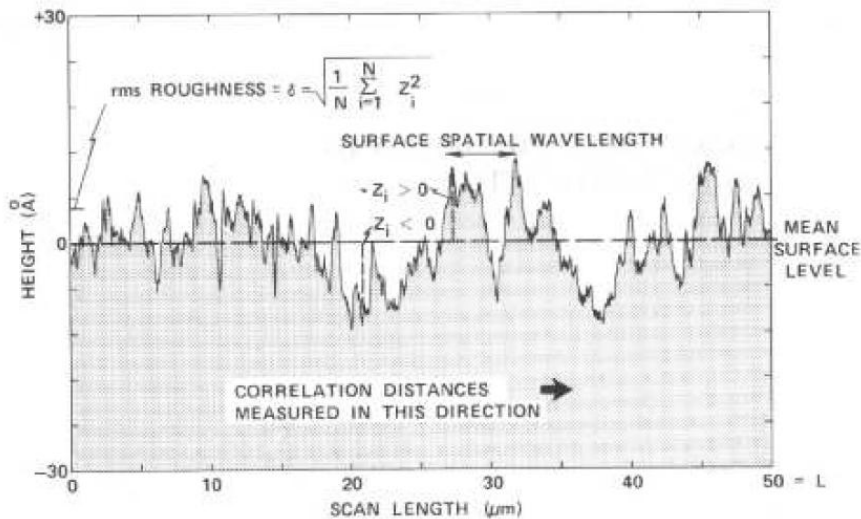


Fig. 8.1: Mono-dimensional profile of a real surface: even the best polished surface, when observed at microscopic level, shows “noisy” features whose amplitudes depend on the considered spatial wavelength.

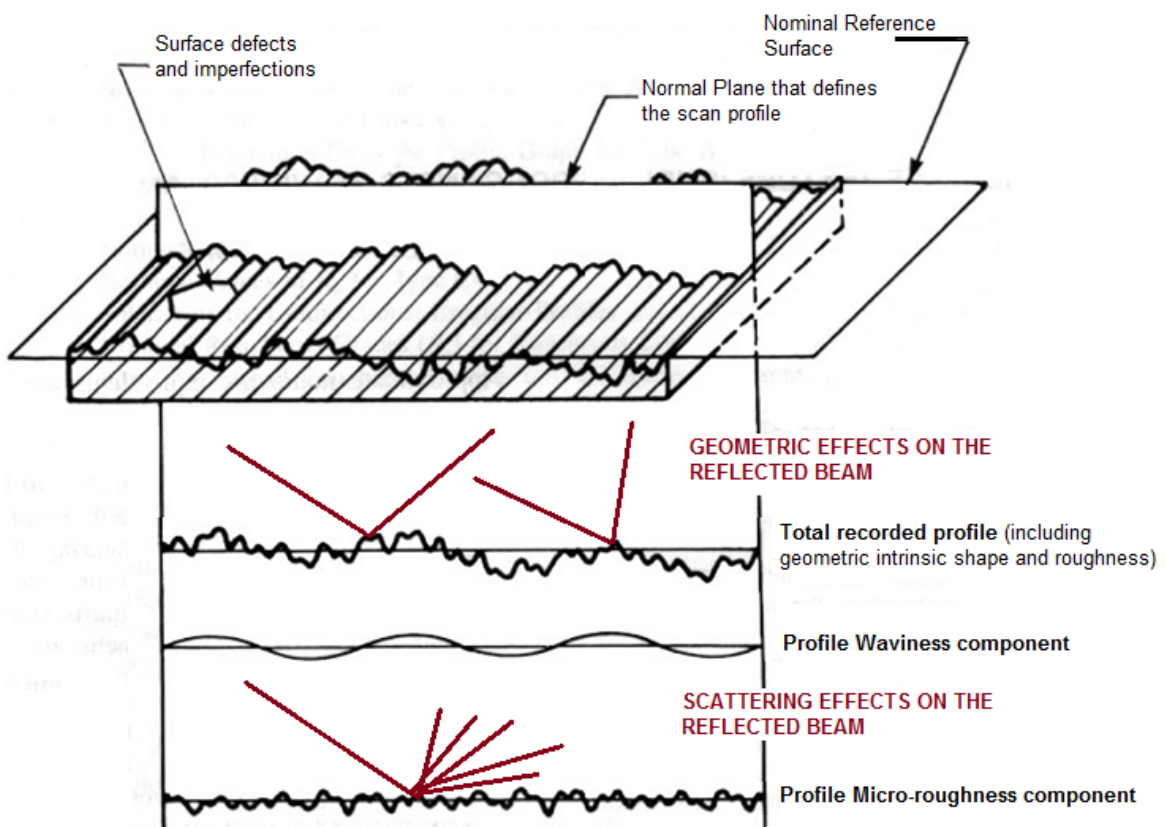


Fig. 8.2: Geometric and scattering effects on a reflected beam caused by the surface finishing at different spatial frequencies. Low-frequency components are referred to as “shape”; high-frequency components are referred to as “micro-roughness”. Between shape and micro-roughness features, lays a range of frequencies whose geometrical and scattering effects are contemporarily present, referred to as “waviness” or “mid-frequency” range.

Table 8.1: Basic parameters for surface characterization and analysis adopted during this study

Parameter	Formula°	Discrete case*
Reference profile* It corresponds to the average profile	$\bar{z}(x) = \lim_{L \rightarrow \infty} \frac{1}{L} \int_{-L/2}^{L/2} z(x) dx$	$\bar{z} = \frac{1}{N} \sum_{n=1}^N z(x_n)$
Roughness The roughness** represent a deviation of the real profile wrt the reference profile and can be expressed in term of average value or as standard deviation (rms)**	$\sigma_a = \lim_{L \rightarrow \infty} \frac{1}{L} \int_{-L/2}^{L/2} z(x) - \bar{z} dx$ $\sigma_{RMS} = \sqrt{\lim_{L \rightarrow \infty} \frac{1}{L} \int_{-L/2}^{L/2} z(x) - \bar{z} ^2 dx}$	$\sigma_{RMS} = \sqrt{\frac{1}{N} \sum_{n=0}^N z(x_n)^2}$ Considering $z = 0$
Slope of the reference profile Reference profile first derivative	$\bar{z}'(x) = \frac{d\bar{z}}{dx}$	$\bar{z}'_n = \frac{\Delta Z}{\Delta x} = \frac{z_{n+1} - z_n}{z_{n+1} - z_n}$
Slope error The same evaluation as roughness applied to profile slope**. It describes the distribution of profile tangents slope along the scan length.	$m_a = \lim_{L \rightarrow \infty} \frac{1}{L} \int_{-L/2}^{L/2} \left \frac{dz}{dx} - \bar{z}' \right dx$ $m_{RMS} = \sqrt{\lim_{L \rightarrow \infty} \frac{1}{L} \int_{-L/2}^{L/2} \left \frac{dz}{dx} - \bar{z}' \right ^2 dx}$	$m_{RMS} = \sqrt{\frac{1}{N} \sum_{n=1}^N \left(\frac{z(x_n) - z(x_{n-1})}{z(x_n) - z(x_{n-1})} \right)^2}$
Self-Correlation function Describes the randomness of the surface	$C(x) = \lim_{L \rightarrow \infty} \frac{1}{L} \int_{-L/2}^{L/2} z(x)z(x+y) dx$	$K(x_n) = \frac{1}{N} \sum_k z(x_{n-k}) - z(x_k)$
PSD Power Spectral Density	$PSD(f_x) = \lim_{L \rightarrow \infty} \frac{ Z(f_x, L) ^2}{L}$	$PSD(f_k) = \frac{L}{N^2} \left \sum_{n=0}^N z_n e^{-2\pi i k \frac{n}{N}} \right ^2$

*The case of surface is the mathematical extension to the 2D case of the formulas.

*Real profile measurements foresee a discrete sampling of the surface under test. The range of evaluated spatial frequencies is determined by the maximum scan length (L) and the sampling step (d, which determine the number of acquired value $N = L/d$) through the Nyquist-Shannon sampling criterion; they are comprised in $[1/L \div 1/2d]$.

**Both the roughness and the slope depend on the spatial wavelength. Two surfaces might show the same roughness values although if their morphology is completely different; the slope error parameter is used to distinguish the cases.

**The roughness rms is normally utilized in the optical processes field, while the averaged σ_a is adopted for mechanical processes. In the following the RMS will be considered.

° All definitions are to be intended with L tending to infinite as the surface features are much smaller than the surface sides.

Table 8.2: Slope error and roughness can be derived from the autocorrelation function and the PSD.

	Derived from correlation function	Derived from PSD
Slope error	$m_{RMS} = \sqrt{\left(\frac{d^2 C(y)}{dy^2}\right)_{y=0}}$	$m_{RMS} = \sqrt{\int_{f_{min}}^{f_{max}} (2\pi f)^2 PSD(f_x) df_x}$ $m_{RMS} = \sqrt{\sum_{k=-N/2}^{+N/2} (2\pi f_k)^2 PSD(f) \Delta f}$
Roughness	$\sigma_{RMS} = \sqrt{C(0)}$	$\sigma_{RMS} = \sqrt{\int_{f_{min}}^{f_{max}} (2\pi f)^0 PSD(f_x) df_x}$ $\sigma_{RMS} = \sqrt{\sum_{k=-N/2}^{+N/2} PSD(f_k) \Delta f}$

9 Annex B: Characterization instruments

Annex B provides a brief description of the operative principles of the characterization instruments used during the study.

Shape characterization instruments

Long Trace profilometer (LTP)

The Long Trace Profilometer, LTP, is a non-contact measuring instrument sensitive to surface local slopes, whose functioning is based on interferometric principles [135], [136]. Its dynamical range of detectable slopes is limited to ± 5 mrad, making it the ideal instrument to detect tangential slope errors and get mono-dimensional profiles of Grazing Incidence optics. Its measurement principle is indeed simple: two pencil Ne-He laser beams scan the surface of the mirror under measurement and the reflected beam direction changes according to the local surface slope. A Fourier transform lens converts the angle variation of the reflected beam in a variation of position in its focal plane. Meanwhile two beams are focused on a reference surface, in order to evaluate and then subtract the tilting and rotation of the optical head. The focused laser beam position is recorded by a linear array detector and, after a proper fit, the local slope of the mirror under test is obtained. The LTP set-up foresees the positioning of the sample under measurement in horizontal position under the movable carriage. A suitable sustaining of the sample has to be individuated to reduce the gravity induced deformations. With proper environmental conditions (mainly temperature stability and air turbulence control along the laser beam path) and periodic and precise calibration, the LTP instrument is able to measure slope profiles with accuracy better than 1 mrad rms. The characteristic range of spatial frequencies seen by the instrument goes from around 10^{-6} to 10^{-3} μm^{-1} . The carriage has a movable range that allows the measurement of samples up to 1 m in the scan direction and 600 mm in height. The minimum scan step is 0.1 mm, but normally a scan range of 1 mm is adopted to make the measure faster: with this scan step, the typical linear dimension of glass and mould (about 200 – 250 mm) requires 3-4 minutes of time, plus alignment time that can require up to a hour. During the scan, the detector pixels record a profile of beam intensity that is opportunely converted in information of local slope and profile by the LTP software, taking into account eventual correction for carriage tip-tilt movement. The final output of this instruments is a

double columns file containing the x (position) and z (height) of the one-dimensional scan profile from which the PSD and HEW can be evaluated.

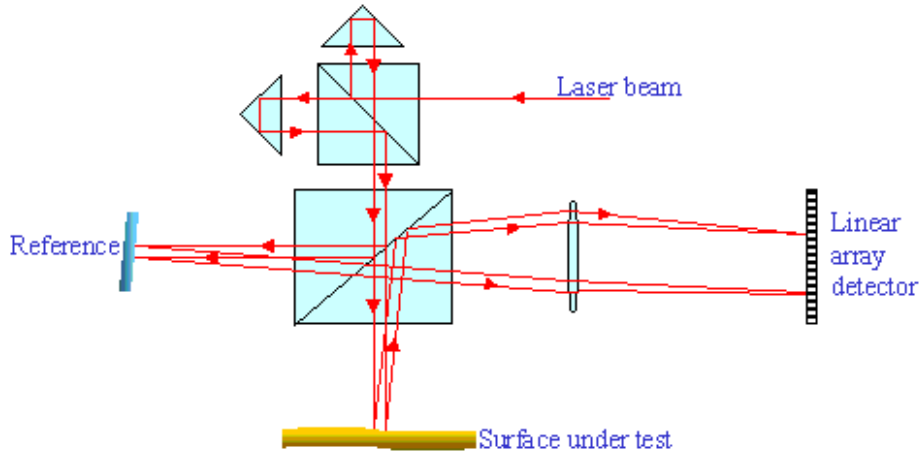


Fig. 9.1: Scheme of the LTP optics head [135]: red arrows represent the optical path followed by the laser beam employed for the measurement.

LTP has been used during this project for the characterization of moulds longitudinal profiles. Unfortunately, it could not be directly employed for measurements on thin glass plates because of the laser reflection on the two surfaces of the sample resulting in a perturbed signal on the detector. To overcome these limitations, two types of solutions were possible:

- Act on the glass plate to eliminate the second spurious reflection of the back surface; for example applying a dark paint or positioning the sample in water, or depositing a reflective layer on the optical surface. The drawback with these procedures resides in the potentially induced deformations on the sample that are not easy to separate from the intrinsic profile;
- Use other type of sensor instead of the LTP laser beam; for example, equip the LTP movable stage with an optical sensor.

Only the second option gave reliable results and was diffusively employed for the characterization of slumped segments; it was implemented by positioning the CHRcodile optical sensor on the precise translational stage of LTP, as described in the following paragraph.

Optical sensor on a translational stage

An optical sensor has been mounted on the LTP linear stage to obtain profile scans of the glass plate without problem of spurious signal. Two optical sensors by Precitec have been used: the CHRocodile 660, and the CHRocodile 3300. Also in this configuration, the characteristic range of spatial frequencies seen by the instrument goes from around 10^{-6} to 10^{-3} μm^{-1} , although if the instrumental noise is higher: in fact in this configuration, the precise correction for carriage tip-tilt movement cannot be applied. However, it has been demonstrated that following a suitable measurement procedure (i.e. subtracting from the measurements the error due to the stage oscillation previously characterized with calibrated samples and averaging on more than four consecutive scans) the results is within a ± 0.5 microns error, acceptable for the first characterization of the samples.

The results of this measurement is a double columns file containing the x (position) and z (height) of the one-dimensional scan profile. It is worth noting that this file might require additional elaboration before extracting the information on HEW, as explained in the following. Also in this configuration, the measurement set-up foresees the positioning of the sample under measurement in horizontal position under the movable carriage. A suitable sustaining of the sample has to be adopted not to induce any deformation. This is relatively easy for a stiff structure, like for example the moulds (usually it is enough to simply laying them on the instruments table or sustain them on three equally spaced point at 120° to reduce the deformation introduced by gravity). The situation is in general trickier in the case of glass foils: because of their low thickness, their rigidity is very low and they behave as floppy structures, easily subject to any kind of deformations introduced by gravity or support friction. While analyzing the data, deformation effects have to be carefully considered to be sure that the recorded profile is the glass intrinsic one. Astatic supports appositely designed in the past for other applications, cannot be considered because of the lack of circular symmetry in the shape of the glass or because they will require to many sustaining points.

In the case of thin cylindrical segments, to subtract from the measured data the deformation introduced by gravity, two ways were followed:

- The adoption of a sustaining system whose behavior is reliably modeled by FEM simulation;
- The subtraction of two measurements of the same glass profile, taken with the glass in exactly the same sustaining condition but taken with the gravity acting in opposite direction.

The first solution was initially adopted during the evaluation of longitudinal profiles of slumped glasses: since the cylindrical slumped glass have always the same dimensions (200 mm x 200 mm or 180 mm x 180 mm) and Radius Of Curvature (1 m), one single FEM model allows the evaluation of gravity effects when the glass is sustained in its center of mass, as shown in Fig. 9.2. The particular supporting mode was selected to be simulated in a reliable way and empirically reproducible for all the measurements.

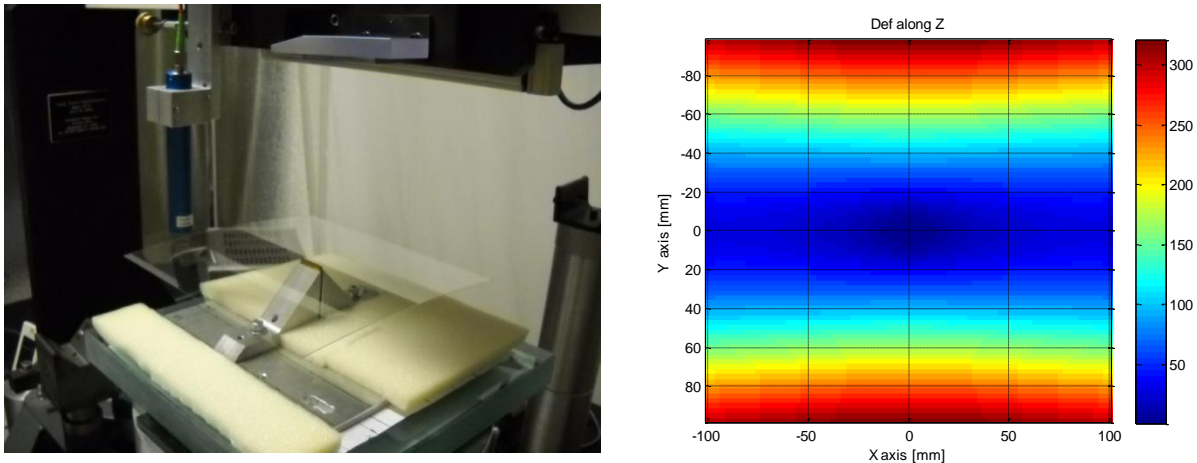


Fig. 9.2: (Left Side): Cylindrical slumped glass being measured with the CHRcodile optical sensor mounted on the LTP stage. (Right Side): Gravity effects simulated by FEM analyses: they must be subtracted from the scan data to obtain the intrinsic profile of the glass.

The second solution has been primarily adopted to characterize glass intrinsic shape before slumping. It has then preferred also for the cylindrical segments since it allows the elimination of systematic errors of the carriage movement. The CHRcodile sensors permit also the measurements of thickness variations in the glass. It is worth noting that in this case the supporting system was not important since the deformations induced by gravity have only effect on the intrinsic shape of the glass but not on its thickness. CHRcodile sensor 3300 was also used for the measurement of azimuthal profiles. The cylindrical shape considered during this project (Radius Of Curvature of 1 m) has a sagitta of 5-6 mm on 200-250 mm chord. The range of 3300 sensors (3.3mm) allows azimuthal scans by sticking together three consecutive measurements (the 660 will require more than 8).

Characterization Universal Profilometer (CUP)

The Characterization Universal Profilometer (CUP) is a metrological tool that has been developed in the contest of the IXO contract activities with the aim of mapping the entire figure of concave or convex elements, i.e. moulds used for glass foils slumping and slumped plates themselves. The CUP allows a 3D measurement of the surface, not only single profiles as in the case of LTP. Its working principle is sketched in Fig. 9.3. The CUP maps the position and distance of a mesh of points of the

surface under characterization from a rigid known optical flat taken as reference. It is based on the coupling of two non-contact sensors: the CHRcodile optical device and the SIOS triple beam interferometer. They are aligned each other and mounted on x-y-z translation system in order to allow the scan of the surface under test. The use of non-contact sensors is fundamental to avoid any risk of deforming the surface being measured or damaging it. The CHR sensor looks at the surface being measured working as a null lens, in such a way to avoid any non-linearity issues of the sensor response at the edges of its measurement range. The SIOS triple-axis interferometer allows measuring the distance of the cavity between the sample and the optical reference within few nanometers accuracy. The collected data are used to reconstruct the surface of the sample (in the considered case the mould or the integrated glass plate) with a potential accuracy of 20 nm [137]. The final output of the CUP is a matrix of x-y position on the sample and z value for the surface height of each point.

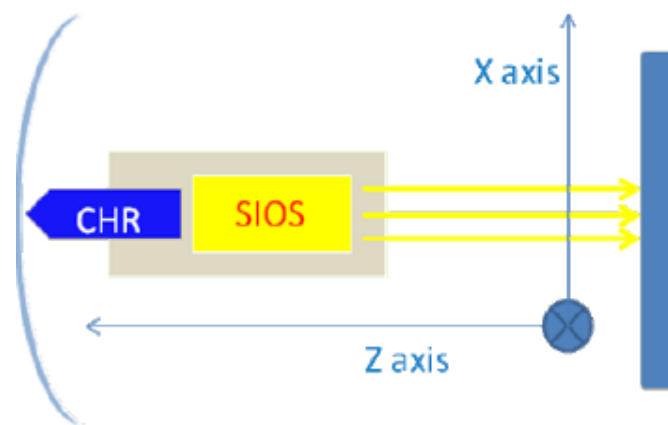


Fig.9.3: Scheme of the working principle of the CUP profilometer.

Sodium lamp for qualitative shape evaluation through interference fringes

Sodium lamps have been used in the laboratory to visually check progress in the obtained results. Two lamps are available: one portable and one fix. The portable one generates a beam of intense monochromatic light that makes more visible any surface imperfection or the presence of dust and contaminants, because of the light scattering. The fix one is assembled in a structure to form a classical Fizeau interferometer arrangement, which makes visible the interference fringes generated by the reflection from two surfaces, due to a different optical path followed by the photons [138]. If the two surfaces are the front and the back surface of a glass foil, then the fringes pattern is representative of the thickness variations. If the two surfaces are that of the glass and the mould, the fringes pattern gives indication on the difference in their shape.

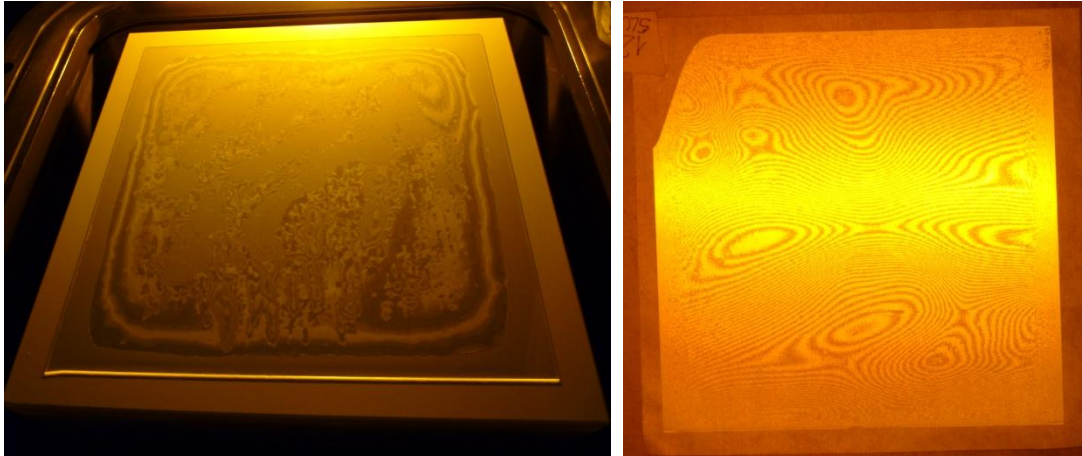


Fig.9.4: Example of qualitative information coming from the portable sodium lamp. (Left Side): Interference fringes indicating the shape difference between the mould and the glass. It is immediately visible how the main deformations are concentrated on the glass edges areas. (Right Side): Example of thickness variation visualized by interference fringes from the two surfaces of a glass foil.

Surface roughness characterization

The direct measurements of roughness are performed using topographic instruments (like WYKO profilometer and AFM) and Bede X-ray Diffractometer. All the topographic instruments return direct information on the 1D or 2D profiles of the surface: they are usually designed to have a high precision level in a limited frequency range. The sampled area at each scan is only a small fraction of the whole surface. For this reason, the typical procedure for surface characterization consists in taking a number of measurements (usually at least more than five) on different points of the sample surface and then averaging the information in terms of PSD. Each instrument is equipped with its own software for preliminary data analyses and interpretation. Raw data can be recorded for further analyses with ad-hoc developed codes.

WYKO Optical Profilometer

The WYKO topo-2D is an optical profilometer used for topographic measurements of surfaces in the range of spatial frequencies comprised from 3 μm up to 2.5 mm. The instrument available at INAF-OAB possesses two optical heads: one at 20X and one at 2.5X magnification. The WYKO instrument returns a mono-dimensional profile of the sample: it always scans 1024 point on a length of 0.66 mm for the 20X head and 5.25 mm for the 2.5X head, resulting in a sample bin of respectively 0.61 micron or 5.1 micron. The 20X head provides information on the lowest frequencies involved in the X-rays reflection, going from hundreds of microns up to 1 micron (Nyquist's limits), with a few angstroms height accuracy. The instrumental noise limits the effective lowest wavelength to 3 μm . The 2.5X provides information on higher spatial frequencies, normally referred to as mid-frequencies, up to

few mm resulting comparable with the information coming from other instruments, i.e. CHRcodile sensor, LTP or CUP (depending on the set scan step). Fig. 9.5 shows a scheme of the possible instrument heads that are based on interferometric principles: they make use of visible polychromatic light to generate interference fringes between the test surface and an internal reference. For the available instrument, the polychromatic light source is split by a Mirau interferometer mounted inside the instrument objective: one beam is sent to a known reference surface, the other is focused on the sample under characterization. From the fringes pattern the instrument records the phase shift while scanning the sample surface so to return its mono-dimensional profile. The output of the instrument is a two-column file containing the scan position on the surface (in mm) and the sample profile (in nm) after a suitable elaboration to eliminate eventual error in the sample alignment and the influence of the reference surface. The resultant data are utilized for the evaluation of PSD. The setup of the instruments foresees the placing of the sample in vertical position, in such a way not to introduce deformations in the sample and not to experience vibrations. While this was relatively easy in the case of mould characterizations, more attention had to be paid in the case of thin glass foils: in the majority of the cases they were measured with WYKO only after their integration on the stiffening back plates or by laying them on the back plate itself to sustain them in a safe way.

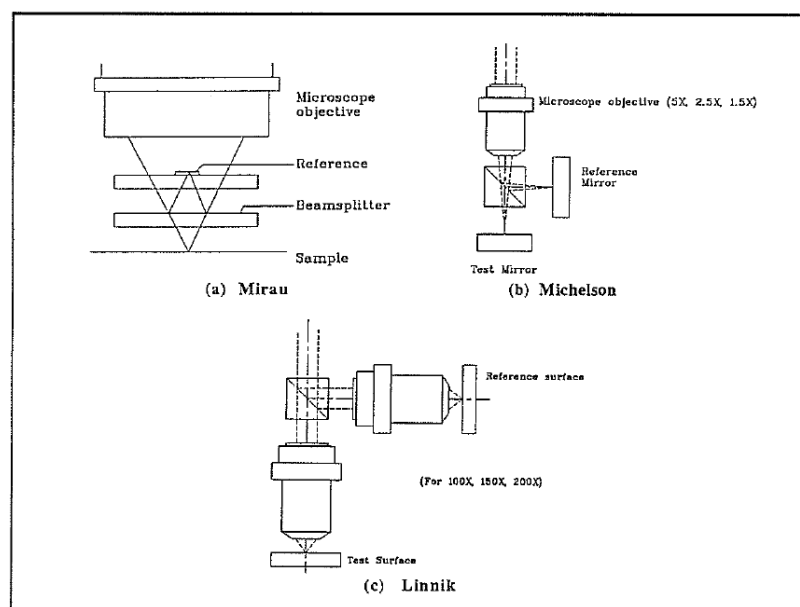


Figure D-1. Interference arrangement for (a) Mirau, (b) Michelson, and (c) Linnik objectives.

Fig.9.5: Scheme of the WYKO instrument possible head objectives: in general the polychromatic light source is collimated and filtered; then it is divided in two coherent beams, one going on the surface under test and the other on an internal reference surface; after they are reflected, they are combined internally to the interferometer and the fringe pattern is recorded by a position-sensitive CCD. Its analysis returns the sample surface profile [139].

Atomic Force Microscope (AFM)

The Atomic Force Microscope (AFM) is aimed at the micro-topographic characterization of surfaces at very high spatial frequencies, corresponding to a wavelength range from 0.01 to 50 μm . It returns 3D maps of the surface under test in square scan areas whose side ranges from 1 μm up to 100 μm . Operatively, since the surface under test is seen only in very small area, to avoid interpreting local defects as data regarding the entire surface, several points (at least more than five) are measured on the surface to have a statistical vision. The obtained data are averaged and elaborated to extract the PSD of the surface under tests.

Fig. 9.6 shows the operative principle of the instrument: a small probe of few microns is mounted on a cantilever structure at the bottom of the instrument scan head. During the measurement phase, it is approached to the surface under test by means of dedicated computer control. The probe feels the interaction force with the atoms of the surface; this small force, in the order of nN, causes a deflection of the cantilever that supports the probe. By means of a laser beam incident on the lever, its deflection and oscillation can be amplified and recorded during the scan. From this information, the AFM software reconstructs the surface map, with a few angstroms accuracy in height, and a horizontal accuracy up to 20-30 \AA . The AFM can work either in "contact mode" (the interaction of the tip to the surface is stronger and the instrument has a better resolution but the surface can be damaged) or in "non-contact" (*tapping*) mode. The AFM available at INAF-OAB lab is the Explorer model, by Veeco. It is equipped with two scan heads, one suitable for scans from 10 μm x 10 μm to 100 μm x 100 μm , the other used for scans from 200 nm x 200 nm to 2 μm x 2 μm . Every scan covers a 400 x 400 pixel area, so that the scan resolution varies between 5 \AA and 0.25 μm . It is usually operated in non-contact mode to minimize the interaction of the surface with the probe so to avoid the introduction of any degradation or imprinting on the sample surface. Its reduced dimensions allow to position it directly on the sample to be characterized. It has been widely used to characterize the surfaces of the mould and the glass at every step of the project. While the characterization of the mould surface is relatively simple (since the instrument is laid on the surface of a stiff element), the characterization of thin glass elements required little attention: the glass needs to be suitably sustained during the measurement. It was found that AFM characterization of slumped segments after the integration in the stiffening structure of the back plate was not possible because of the vibration felt by the instrument. The only possibility is to measure slumped glass micro-roughness with AFM before the integration step, by laying it on a support with the same Radius Of Curvature. This implies that the AFM characterizations on curved glasses have to be completed before the integration onto in the stack. Luckily this is good since it allows checking the compliance of the slumped foils to the roughness specification before they are integrated.

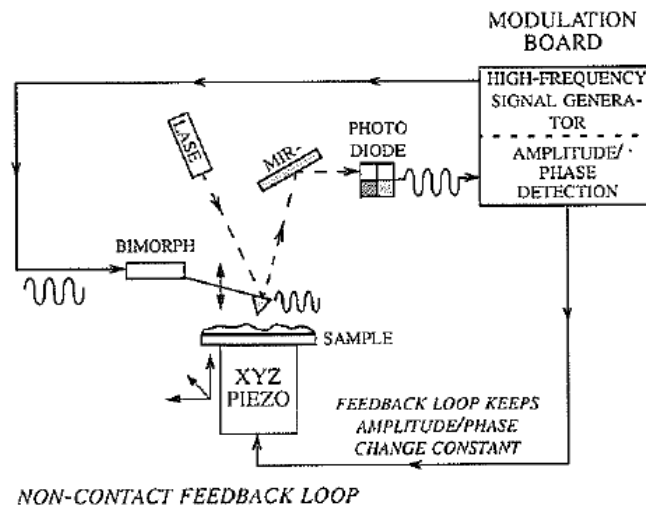


Fig.9.6: Scheme of the operative principle of AFM [140].

BEDE-D1 X-ray Diffractometer

The BEDE-D1 X-ray Diffractometer is a general purpose instrument that allows X-ray diffraction, reflectance, and scattering measurements [141]. It is mainly used to indirectly investigate the microroughness of optical surfaces. The other topographic instruments give direct measurements on small areas of the sample; while the X-ray investigation performed with the diffractometer allows checking bigger areas of the surface under test. Fig. 9.7 shows a schematic representation of the instrument. It consists of a suitable-shield X-ray apparatus containing three main blocks: an X-ray generator stage (formed by X-ray tube, a Si crystal monochromator (Channel-Cut-Crystal -CCC-) and slits), a sample carrier and an X-ray detector. The two last stages are both equipped with precision goniometers for precise movement during the measurement, with a resolution of 1". All of these elements are positioned and moved by micrometric motors driven by an external computer code, for precise alignment before the measurements. Once the X-ray beam is generated inside the tube by Breinstrahlung, the CCC and the systems of slits collimate it to improve the angular resolution; the beam width can be reduced to 0.07 mm (at expenses of the photon flux), so that the reflectivity of short samples (some cm) can also be measured. The emerging beam arrives on the sample, mounted on the sample carrier, in Grazing Incidence. The reflected and/or scattered rays are collected by a photoelectric detector. The angles of the sample and of the detector are measured and recorded by the goniometers, as well as the corresponding reflected and/or scattered beam. In dependence on the data to be recorded (reflected beam or scattered beam), two kind of set up measurements are foreseen, as depicted in Fig. 9.8. During X-ray Reflectivity (XRR) at Grazing Incidence, the X-ray detector is maintained at an angle twice the incidence angle of the beam on the sample (that is the

parameter that varies during the scan); for X-ray Scattering (XRS) measurements, the detector scans over a wide range of scattering angle for a fix incidence angle of the beam on the sample.

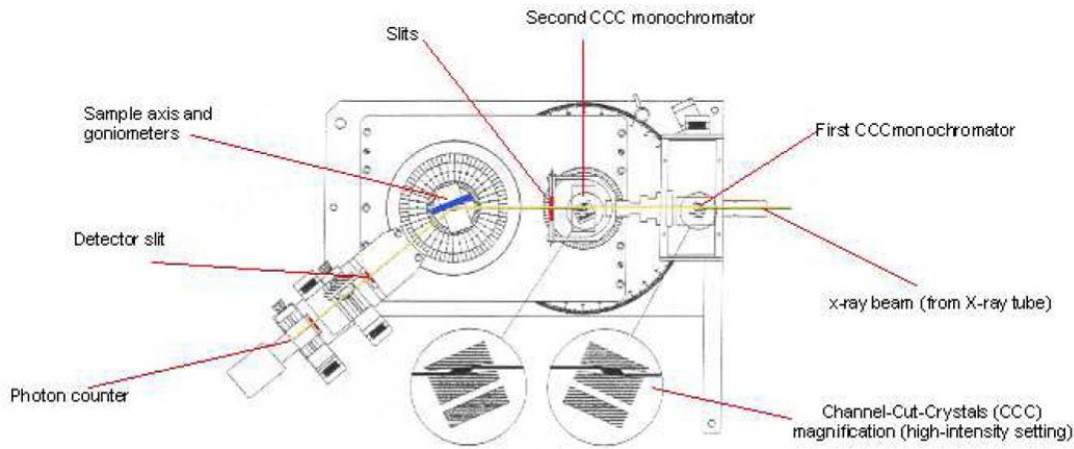


Fig.9.7: Scheme of the BEDE-D1 Diffractometer (credits: BEDE Scientific).

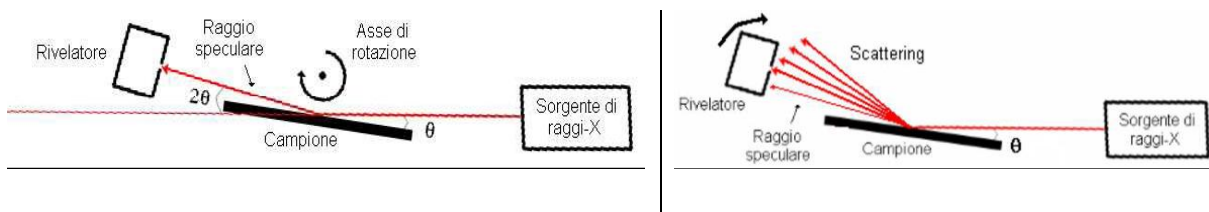


Fig.9.8: Schematics of the BEDE-D1 X-ray Diffractometer set ups. (Left Side): Configuration employed during XRR measurement. (Right Side): Detector-scan configuration employed during XRS measurement.

For the purposes of this project, XRR and XRS measurements were performed with the BEDE Diffractometer in monochromatic setup at 8.045 keV (the Cu-K α line), scanning over a wide range of incidence and scattering angles. The machine set up requires the positioning of the sample in vertical position: only slumped glasses integrated in the stiffening back plate structure have been characterized. The results allow the determination of PSD in a spectral range of 10-1 μ m, so overlapping the range obtained by AFM but measured on bigger areas. In general, a good agreement between the measurements of the two instruments was obtained, confirming the reliability of single results.

Phase Contrast Nomarski Microscope

The Nomarski microscope returns images of the surface under test giving qualitative indication on its topography. Although it does not permit roughness quantitative measurements, it is widely used to visually check the surface of the samples and to understand the size and origin of eventual defects or

periodic patterns. The instrument employs polarized white light to make visible surface details enhancing their relative contrast. Fig. 9.9 shows the operative principle: the Nomarski microscope produces a polarized, polychromatic light beam, which is split by a Wollaston Prism, producing two correlated beams with perpendicular polarizations. A lens focuses the two beams at two positions on the surface under test, separated by one-micron distance. The two beams are reflected by the surface, pass again through the Wollaston Prism that combines them to form an image. If a surface defect is present (meaning a variation in heights, slopes, or optical constants), the two beams will be reflected with two different phase changes. The phase variation appears in the variable brightness of the image, returning a surface map with a sensitivity of 1 nm. Many magnifications are selectable (from 5X up to 100X) and the phase difference may be shifted in order to highlight the features. The space resolution is closed to 0.22 μm . The output of this instrument is a picture of the surface (or a digital video if necessary). The qualitative images show features in the spatial frequency ranges of AFM and WYKO instruments. The Nomarski microscope has been widely used for the qualitative check of the surface of the mould (both before and after the deposition of the eventual antisticking layer) and of the glasses (both before and after the slumping process).

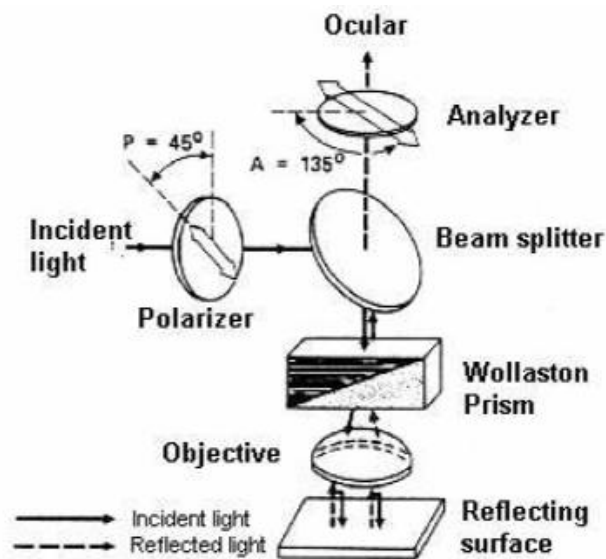


Fig. 9.9: The Nomarski phase contrast microscope: schematic representation of the operating principle of the Nomarski phase contrast microscope.

Table 9.1: The qualitative images obtainable with the Nomarski microscope visually show the features in the spatial frequency ranges of WYKO and AFM instruments.

Magnification	5X	10X	20X	50X	100X
Image dim.	750 μm	375 μm	187.5 μm	75 μm	35 μm
Spatial Freq. range	WYKO	WYKO	WYKO/AFM	AFM	AFM

Summary of the characterization instruments

The following plot and table summarized the main characteristics of the metrological instruments, widely used during the presented study, for the surface characterization of both the moulds and the produced slumped plates.

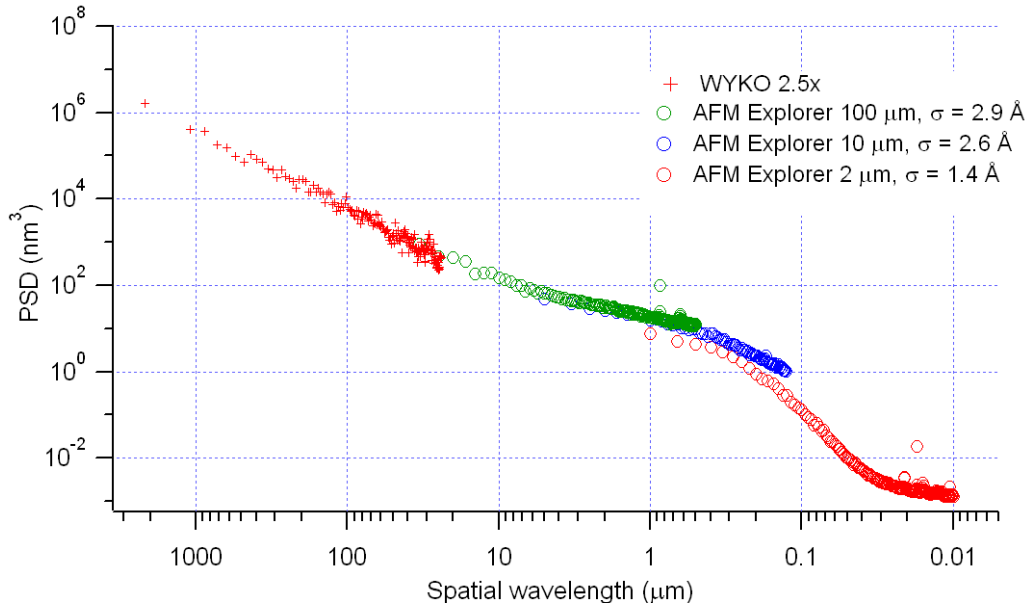


Fig. 9.10: Each instrument is sensitive only to a particular window of spatial frequencies. The Power Spectral Density that provides a global description is obtained combining the data of several instruments. In the plot, the WYKO and AFM data are reported. BEDE data overlaps the spatial wavelength of AFM, while CUP and LTP data goes in the left side of the plot, at higher wavelength.

Table 9.2: Summary of all the measurement instruments adopted for the evaluation of the slumping process

Instruments	Spatial Wavelength	Accuracy
CUP	From 0.1 mm up to 300 mm	20 nm accuracy (design) 1 μ m currently
LTP	1 m to 0.2 mm	1 mrad rms (on the detected slope)
CHR on LTP	1 m to 0.2 mm	$\pm 0.5 \mu$ m on the height data due to instrumental noise
SODIUM LAMP	~ 0.5 m (sample dimension)	Two consecutive fringes are $\lambda/2$ distant, ~ 300 nm
WYKO	1.2 μ m – 2.5 mm (3 μ m effective for instrumental noise)	Few \AA height accuracy
AFM	wavelength range from 0.01 to 50 μ m	Few \AA height 20-30 \AA horizontal

10 Annex C: List of experiments

Table 10.1: List of all the experiments performed during the study with their main aim.

Test Nomenclature	Description and Main aim
PS-IXO-1	Slumping of D263 glass on Fused Silica with different surface coating to test the behaviour of several antisticking materials.
PS-IXO-2	Slumping of D263 glass on Fused Silica with different surface coating to test the behaviour of several antisticking materials.
PS-IXO-3	Slumping of D263 glass on Fused Silica with different surface coating to test the behaviour of several antisticking materials.
PS-IXO-4	Slumping of D263 glass on Fused Silica with different surface coating to test the behaviour of several antisticking materials.
PS-IXO-5	First small cylindrical slumping with glass D263 and Fused Silica mould to test the behaviour of the process on curved sample.
PS-IXO-6	Slumping of D263 glass on Fused Silica with different surface coating to test the behaviour of several antisticking materials.
PS-IXO-7	Slumping of D263 glass on Fused Silica with different surface coating to test the behaviour of several antisticking materials.
PS-IXO-8	First small cylindrical slumping with glass D263 and Fused Silica mould to test the behaviour of the process on curved sample.
PS-IXO-9	Annealing of coating layers on glass to check the effects on coating surface roughness of the application of a thermal cycle.
PS-IXO-10	Annealing of antisticking layer on Fused Silica moulds to test the behaviour in terms of layer adhesion and roughness modification.
PS-IXO-11	Slumping of D263 glass on Fused Silica mould with Pt layer on the glass to check its behaviour as antisticking.
PS-IXO-12	Annealing of antisticking layer on Fused Silica moulds to evaluate the effects on the layer itself of the thermal cycle.
PS-IXO-13	Annealing of coating layers on glass to check the effects on surface roughness of the application of a thermal cycle.
PS-IXO-14	Fused Silica mould and D263 glass with no antisticking layer to check the sticking behaviour.
PS-IXO-15	Slumping of D263 glass on Fused Silica after the annealing of the Pt antisticking layer applied on the mould.
PS-IXO-16	Annealing of antisticking layer on Fused Silica moulds to find the optimum annealing thermal cycle.
PS-IXO-17	Annealing of antisticking layer on Fused Silica moulds to check for contamination problems.
PS-IXO-18	Slumping of D263 glass on Fused Silica after the annealing of the Pt antisticking layer applied on the mould to evaluate eventual glass roughness modification.
PS-IXO-19	Annealing of antisticking layer on Fused Silica mould to check for contamination problems.
PS-IXO-20	Annealing of antisticking layer on Fused Silica mould to check for contamination problems.
PS-IXO-21	Annealing of antisticking layer on Fused Silica mould to find the optimum annealing thermal cycle.
PS-IXO-22	Annealing of antisticking layer on Fused Silica mould to have a mould on which perform several slumping cycles.

PS-IXO-23	Slumping of D263 glass on Zerodur K20 with no antisticking layer to check the sticking behaviour in the case of this mould material.
PS-IXO-24	Slumping of D263 glass on Fused Silica after the annealing of the Pt antisticking layer applied on the mould to evaluate the slumping results in terms of shape and roughness and start optimized the parameters.
PS-IXO-25	Slumping of D263 glass on Zerodur K20 with no antisticking layer to check the sticking behaviour in the case of this mould material.
PS-IXO-26	Cylindrical slumping of D263 glass on MCX1 with the antisticking layer on the glass to start getting experience on cylindrical slumping.
PS-IXO-27	Slumping of glass D263 on Fused Silica mould with Cr+Pt antisticking layer to check the presence of Cr layer on the release coating.
PS-IXO-28	MCC1 Annealing (concave mould for the German colleagues).
PS-IXO-29	Cylindrical slumping of D263 glass on MCX1 with the antisticking layer on the glass to characterize the coated glass roughness after the process.
PS-IXO-30	Cylindrical slumping of D263 glass on MCX1 with the antisticking layer on the glass to characterize the coated glass roughness after the process.
PS-IXO-31	Slumping of glass D263 on flat Fused Silica mould with Pt antisticking layer to evaluate the effect of a different thermal cycle.
PS-IXO-32	CVI2 CVI3 ED2 Annealing (flat fused silica sample to be used for slumping parameters optimization).
PS-IXO-33	CVI2 1° slumping to evaluate the behaviour of the mould after repeated thermal cycle.
PS-IXO-34	CVI2 2° slumping to evaluate the behaviour of the mould after repeated thermal cycle.
PS-IXO-35	CVI2 3° slumping to evaluate the behaviour of the mould after repeated thermal cycle.
PS-IXO-36	D263 glass slumped on Fused Silica with no antisticking to test the sticking behaviour at high temperature in dependence of p application.
PS-IXO-37	MCX1 Annealing thermal cycle.
PS-IXO-38	E2 Annealing thermal cycle.
PS-IXO-39	MCX1 1° slumping to test several process parameters in order to select the optimal.
PS-IXO-40	MCX1 2° slumping to test several process parameters in order to select the optimal.
PS-IXO-41	MCX1 3° slumping to test several process parameters in order to select the optimal.
PS-IXO-42	E3 Annealing to have a flat mould to use for parallel tests.
PS-IXO-43	E3 Second Annealing to have a flat mould to use for parallel tests.
PS-IXO-44	MCX1 4° slumping to test several process parameters in order to select the optimal.
PS-IXO-45	MCX1 5° slumping to test several process parameters in order to select the optimal.
PS-IXO-46	MCX1 6° slumping to test several process parameters in order to select the optimal.
PS-IXO-47	MCX1 RE-slumping of the forth slumped glass to check the behaviour of a second thermal cycle on the same glass.

List of slumping experiments

PS-IXO-48	MCX1 7° slumping to test several process parameters in order to select the optimal.
PS-IXO-49	E3 1° slumping to test several process parameters in order to select the optimal.
PS-IXO-50	E2 1° slumping to test several process parameters in order to select the optimal: in particular the pressure concentration on glass edges.
PS-IXO-51	E2 2° slumping to test several process parameters in order to select the optimal.
PS-IXO-52	ED5 Annealing thermal cycle.
PS-IXO-53	MCX2 Annealing thermal cycle.
PS-IXO-54	ED5 1° slumping to test several process parameters in order to select the optimal.
PS-IXO-55	Slumping of glass D263 on Zerodur K20 mould to test the thermal condition on the glass during slumping with a different material.
PS-IXO-56	MCX2 1° slumping → D1 the aim was to produce a representative glass to be employed in integration tests.
PS-IXO-57	ED5 2° slumping to test several process parameters in order to select the optimal.
PS-IXO-58	MCC2 Annealing (concave mould for German colleagues).
PS-IXO-59	MCX2 2° slumping → D2 the aim was to produce a representative glass to be employed in integration tests.
PS-IXO-60	ED5 3° slumping to test several process parameters in order to select the optimal.
PS-IXO-61	C3 Annealing + CVI6 Pressure experiment.
PS-IXO-62	MCX2 3° slumping → D3 the aim was to produce a representative glass to be employed in integration tests.
PS-IXO-63	CVI6 with 4 triangular ECO glass.
PS-IXO-64	MCX2 4° slumping → D4 the aim was to produce a representative glass to be employed in integration tests.
PS-IXO-65	K20 RoC 5m to check the behaviour, mainly in terms of mid-frequency, on the slumping on a spherical shape.
PS-IXO-66	MCX2 5° slumping → D5 the aim was to produce a representative glass to be employed in integration tests.
PS-IXO-67	MCX2 6° slumping → D6 the aim was to produce a representative glass to be employed in integration tests.
PS-IXO-68	MCX2 7° slumping → D7 the aim was to produce a representative glass to be employed in integration tests.
PS-IXO-69	K20 cylinder + 4 moulds (CVI4, CVI5, E2, E3) No p. From here K20 remachined by Andalò and polished in house.
PS-IXO-70	ED5 4° slumping to test several process parameters in order to select the optimal.
PS-IXO-71	K20 cylinder No p + K20 138mm flat 1° slumping No p.
PS-IXO-72	MCX2 8° slumping → D8 the aim was to produce a representative glass to be employed in integration tests.
PS-IXO-73	Zerodur K20 138mm flat 2° slumping (first with pressure).
PS-IXO-74	MCX2 9° slumping → D9 the aim was to produce a representative glass to be employed in integration tests.
PS-IXO-75	K20 138mm flat 3° slumping (second with pressure).
PS-IXO-76	C4, C5, E2, E3 annealing back surfaces.

PS-IXO-77	C4, C5, E2, E3 slumping 4 flat without pressure.
PS-IXO-78	Cylindrical slumping on MCX2 and glass T21 → D10 the aim was to produce a representative glass to be employed in integration tests.
PS-IXO-79	Zerodur K20 cylinder and glass T107 to optimized the parameters of the process in the case of a new mould material.
PS-IXO-80	Zerodur K20 cylinder and glass T101 to optimized the parameters of the process in the case of a new mould material.
PS-IXO-81	Zerodur K20 cylinder and glass T125 to check First Contact efficiency in cleaning surfaces.
PS-IXO-82	Zerodur K20 cylinder and glass ECO12 to optimized the parameters of the process in the case of a new mould material.
PS-IXO-83	Si wafer+Pt and Si wafer+Cr+Pt (no annealing) and ECO glass to test a mould made by Silicon.
PS-IXO-84	Zerodur K20 cylinder and glass ECO3 to optimized the parameters of the process in the case of a new mould material.
PS-IXO-85	Si wafer+Pt and Si wafer+Cr+Pt: annealing cycle
PS-IXO-86	Zerodur K20 cylinder and glass ECO37 to optimized the parameters of the process: in particular, test the presence of glass frame near glass edges.
PS-IXO-87	Zerodur K20 cylinder and glass ECO32 to optimized the parameters of the process.
PS-IXO-88	Si wafer+Pt and Si wafer+Cr+Pt (annealed) and ECO glass to test a mould made in Silicon.
PS-IXO-89	ED6 / ED1 / Si wafer annealed 1° slumping and D263 glass to compare Fused Silica and Silicon moulds.
PS-IXO-90	Zerodur K20 with thermocouples inside the muffle to calibrate new thermocouples.
PS-IXO-91	Si wafer+Cr+Pt (3° slumping) and Fused Silica with sputtered annealed Pt (no pressure) to compare Fused Silica and Silicon moulds.
PS-IXO-92	Zerodur K20 cylinder: fast-low T (570°C) cleaning cycle to eliminate contaminants on the mould.
PS-IXO-93	Zerodur K20 cylinder: slow-high T (750°) cleaning cycle to eliminate contaminants on the mould.
PS-IXO-94	Zerodur K20 and D263ECO glass #8: X° slumping with the aim of produce representative sample to be integrated into the prototypes.
PS-IXO-95	Slumping of D263 glass on Zerodur K20 mould: different process set up.
PS-IXO-96	Slumping of D263 glass on Zerodur K20 mould: different process set up, in particular smaller glass foil to check edges deformations.
PS-IXO-97	Slumping of D263 glass on Silicon mould with Pt antisticking layer to test the sticking behaviour.
PS-IXO-98	Slumping of D263 glass on Silicon mould with Pt antisticking layer to test the sticking behaviour.
PS-IXO-99	Annealing large mould 310mmx310mm in Fused Silica for the production of sample to test glass strength.
PS-IXO-100	Slumping of D263 glass on Zerodur K20 mould: different process set up, in particular small oven to test thermal behaviour.
PS-IXO-101	Slumping of D263 glass on Zerodur K20 mould: different process set up, in particular small oven to test thermal behaviour.
PS-IXO-102	Slumping of D263 glass on Zerodur K20 mould: different process set up, in particular no pressure application to check for mid-frequencies in the plate.

List of slumping experiments








PS-IXO-103	Slumping of D263 glass on Zerodur K20 mould: different process set up.
PS-IXO-104	Slumping of D263 glass on Zerodur K20 mould: different process set up.
PS-IXO-105	Slumping of D263 glass on Zerodur K20 mould to produce representative sample to be integrated into the prototypes.
PS-IXO-106	Slumping of D263 glass on Zerodur K20 mould: different process set up, in particular evaluation of the thermal effects introduced by the presence of the pressing membrane.
PS-IXO-107	Production of flat samples to tests the glass strength.
PS-IXO-108	Production of flat samples to tests the glass strength.
PS-IXO-109	Production of flat samples to tests the glass strength.
PS-IXO-110	Thermocouples re-calibration and muffle re-generation and cleaning.
PS-IXO-111	Slumping of D263 glass on Zerodur K20 mould: different process set up.
PS-IXO-112	Slumping of D263 glass on Zerodur K20 mould: different process set up.
PS-IXO-113	Test on the production of flat glasses in stack.
PS-IXO-114	Test on Silicon with different antisticking layers: in particular, annealing thermal cycle of the Silicon Nitride coating on 100 mm diameter Silicon wafer.
PS-IXO-115	Slumping of D263 glass on Zerodur K20 mould: different process set up.
PS-IXO-116	Slumping of D263 glass on Zerodur K20 mould to test eventual contamination introduced by a new type of graphite sealant.
PS-IXO-117	Slumping of D263 glass on Silicon mould with annealed Silicon Nitride release layer.
PS-IXO-118	Slumping of D263 glass on Zerodur K20 mould to produce representative sample to be integrated into the prototypes.
PS-IXO-119	Slumping of D263 glass on Zerodur K20 mould: different process set up, in particular first test on the cylindrical muffle.
PS-IXO-120	Slumping of D263 glass on Zerodur K20 mould: different process set up, in particular test on the cylindrical muffle configuration.
PS-IXO-121	Stack of 4 glasses for the production of sample necessary to test the glass strength.
PS-IXO-122	Stack of 4 glasses for the production of sample necessary to test the glass strength.
PS-IXO-123	Slumping of D263 glass on Zerodur K20 mould: different process set up, use of the cylindrical muffle.
PS-IXO-124	Slumping of D263 glass on Zerodur K20 mould: different process set up, in particular a thicker pressing membrane was employed.
PS-IXO-125	Slumping of D263 glass on Zerodur K20 mould: different process set up, in particular a thicker pressing membrane was employed.
PS-IXO-126	Annealing MCX2_B after its re-conditioning.
PS-IXO-127	Annealing of large mould 310mmx310mm in Fused Silica for the production of sample to test glass strength.
PS-IXO-128	MCX2_B and 240mmx240mm glass foil. To have a slumped sample to test the cutting of its edges. (B1)
PS-IXO-129	MCX2_B and 240mmx240mm glass foil. To have a slumped sample to test the cutting of its edges. (B2)
PS-IXO-130	MCX2_B and 240mmx240mm glass foil. To have a slumped sample to test the cutting of its edges. (B3)

PS-IXO-131

MCX2_B and 240mmx240mm glass foil. To have a slumped sample to test the cutting of its edges. (B4)

11 Annex D: Slumping procedure

Table 11.1: Direct slumping operative procedure developed during the study.

1	A mould with the required shape and microroughness is procured. Thin glass sheets are procured and laser cut to the required dimension.	
2	The mould is coated with an anti-sticking layer (if needed, depending on the mould material). Present used antisticking layer, working in the case of Fused Silica and Silicon moulds, is composed by 50 nm of evaporated Pt. 5 nm interlayer of Cr might be used in order to increase the antisticking layer adhesion on the mould.	
3	Everything is prepared in the clean environment to execute the entire procedure. The deionization system is switched on to eliminate electrostatic charges in the environment. Metal pressing membrane is cleaned with alcohol and acetone. Muffle is cleaned with alcohol and three supports are positioned inside it at the right height to sustain the mould.	
4	The mould is cleaned and positioned in the muffle. Bi-distilled water, amber clean, a flow of Nitrogen, acetone and optical paper are used for this scope. Sodium light lamp is used to check dust absence.	
5	The glass sheet is cleaned with amber clean and bi-distilled water and is dried with N flow. The last cleaning step is done with acetone and optical paper. The glass is placed above the mould and its position is adjusted with the help of vacuum tweezers and calibrated spacers. The Pressing membrane is positioned and the muffle is closed.	
6	The muffle is placed in the center of the big oven and thermocouples are applied to control the effective temperature. Pipes are connected and oxygen is evacuated from the muffle where Ar atmosphere is established. The thermal cycle is started and at temperature between the annealing point and the softening point, a uniform pressure is applied on the glass in order to push it against the mould and obtain its shape replication.	
7	After the cooling down of the oven, the muffle is opened and the slumped glass plate is released, ready to be characterized and integrated.	

List of publications

[p1] **Production of the IXO glass segmented mirrors by hot slumping with pressure assistance: tests and results**, [Laura Proserpio](#), Mauro Ghigo, Stefano Basso, Marcos Bavdaz, Oberto Citterio, Marta M. Civitani, Paolo Conconi, Francesco Martelli, Riccardo Negri, Giuseppe Pagano, Giovanni Pareschi, Giancarlo Parodi, Daniele Spiga, Lorenzo Raimondi, Bianca Salmaso, Luca Terzi, Erik Wille, Alberto Zambra, Proceedings of SPIE Vol 8147, 8147-20 (2011)

[p2] **IXO glass mirrors development in Europe**, Giovanni Pareschi, Mauro Ghigo, Oberto Citterio, Marta M. Civitani, [Laura Proserpio](#), Paolo Conconi, Gianpiero Tagliaferri, Alberto Zambra, Stefano Basso, Daniele Spiga, Giancarlo Parodi, Francesco Martelli, Daniele Gallieni, Matteo Tintori, Marcos Bavdaz, Erik Wille, Proceedings of SPIE Vol 8147, 8147-19 (2011)

[p3] **Design of the IXO optics based on thin glass plates connected by reinforcing ribs**, Mauro Ghigo, Stefano Basso, Marcos Bavdaz, Oberto Citterio, Marta M. Civitani, Paolo Conconi, Francesco Martelli, Giovanni Pareschi, Giancarlo Parodi, [Laura Proserpio](#), Bianca Salmaso, Daniele Spiga, Erik Wille, Alberto Zambra, Proceedings of SPIE Vol 8147, 8147-24 (2011)

[p4] **The integration machine: design, development and validation of an alternative process for the integration of slumped-glass segments into an x-ray module**, Marta M. Civitani, Stefano Basso, Oberto Citterio, Paolo Conconi, Mauro Ghigo, Giovanni Pareschi, [Laura Proserpio](#), Daniele Spiga, Gianpiero Tagliaferri, Alberto Zambra, Daniele Gallieni, Matteo Tintori, Francesco Martelli, Giancarlo Parodi, Marcos Bavdaz, Erik Wille, Proceedings of SPIE Vol 8147, 8147-25 (2011)

[p5] **Progress on precise grinding and polishing of thin glass monolithic shell (towards WFXT)**, O. Citterio, M. M. Civitani, J. Arnold, S. Campana, H. Combrinck, P. Conconi, V. Cotroneo, R. Freeman, E. Mattaini, R. Morton, G. Motta, G. Pareschi, G. Parodi, [L. Proserpio](#), S. Schuler, P. Simpson, G. Tagliaferri, D. Walker, , Proc. Of SPIE 8147 (2011)

[p6] **Thermal shaping of thin glass foils for segmented grazing incidence**, [Laura Proserpio](#), Marta Civitani, Mauro Ghigo, Giovanni Pareschi, Proceedings of SPIE Vol 7803, 78030K (2010)

[p7] **3-D characterization of thin glass segmented X-ray mirrors via optical profilometry**, Marta M. Civitani, Mauro Ghigo, Oberto Citterio, [Laura Proserpio](#), Daniele Spiga, Giovanni Pareschi, Proceedings of SPIE Vol 7803, 78030L (2010)

[p8] **Design and Development by Direct Polishing of the WFXT Polynomial Mirror Shells**, Proserpio, L.; et al., ICSO 2010 International Conference on Space Optics, Rhodes 2010

[p9] **Hot slumping glass technology for the grazing incidence optics of future missions with particular reference to IXO**, Ghigo, M., Basso, S., Bavdaz, M., Conconi, P., Citterio, O., Civitani, M., Friedrich, P., Gallieni, D., Guldemann, B., Martelli, F., Negri, R., Pagano, G., Pareschi, G., Parodi, G., Proserpio, L., Salmaso, B., Scaglione, F., Spiga, D., Tagliaferri, G., Terzi, L., Tintori, M., Vongehr, M., Wille, E., Winter, A., Zambra, A., Proceedings of SPIE Vol. 7732, 77320C (2010)

[p10] **Design and development of thin quartz glass WFXT polynomial mirror shells by direct polishing**, Proserpio, L., Campana, S., Citterio, O., Civitani, M., Combrinck, H., Conconi, P., Cotroneo, V., Freeman, R., Langstrof, P., Mattaini, E., Morton, R., Oberle, B., Pareschi, G., Parodi, G., Pels, C., Schenk, C., Stock, R., Tagliaferri, G., Proceedings of SPIE Vol. 7732, 77320D (2010)

[p11] **IXO x-ray mirrors based on slumped glass segments with reinforcing ribs: optical and mechanical design, image error budget, and optics unit integration process**, Civitani, M., Basso, S., Bavdaz, M., Citterio, O., Conconi, P., Gallieni, D., Ghigo, M., Guldemann, B., Martelli, F., Pagano, G., Pareschi, G., Parodi, G., Proserpio, L., Salmaso, B., Spiga, D., Tagliaferri, G., Tintori, M., Wille, E., Zambra, A., Proceedings of SPIE Vol. 7732, 773242 (2010)

[p12] **A wide field X-ray telescope for astronomical survey purposes: from theory to practice**, Paolo Conconi, Sergio Campana, Gianpiero Tagliaferri, Giovanni Pareschi, Oberto Citterio, Vincenzo Cotroneo, Laura Proserpio, Marta Civitani, Monthly Notices of the Royal Astronomical Society Main Journal, MN-09-2625-MJ.R1 (2010)

[p13] **Development of hot slumping technique and last optical performances obtained on a 500mm diameter slumped segment prototype for adaptive optics**, Ghigo, M., Basso, S., Canestrari, R., Proserpio, L., Proceedings of SPIE Vol. 7439, 74390M (2009)

[p14] **Design optimization and trade-off study of WFXT optics**, Conconi, P., Pareschi, G., Campana, S., Citterio, O., Civitani, M., Cotroneo, V., Proserpio, L., Tagliaferri, G., Parodi, G., Proceedings of SPIE Vol. 7437, 74370D (2009)

[p15] **Hot slumping glass technology and integration process to manufacture a grazing incidence scaled prototype for the IXO telescope modules**, Ghigo, M., Basso, S., Canestrari, R., Conconi, P., Citterio, O., Civitani, M., Dell'Orto, E., Gallieni, D., Pareschi, G., Parodi, G., Proserpio, L., Spiga, D., Proceedings of SPIE Vol. 7437, 74370P (2009)

[p16] **Investigation of a novel slumping technique for the manufacturing of stiff and lightweight optical mirrors**, R. Canestrari, M. Ghigo, G. Pareschi, S. Basso, and L. Proserpio, Proceedings of SPIE 7018, 70180D (2008)

[p17] **Lightweight optical segment prototype for adaptive optics manufactured by hot slumping**, R. Canestrari, M. Ghigo, S. Basso, D. Spiga, and L. Proserpio, Proceedings of SPIE Vol. 7015, 70153S (2008)

[p18] **Slumped glass option for making the XEUS mirrors: preliminary design and ongoing developments**, M. Ghigo, R. Canestrari, L. Proserpio, E. Dell'Orto, S. Basso, O. Citterio, G. Pareschi, and Giancarlo Parodi, Proceedings of SPIE Vol. 7011, 70111F (2008)

Bibliography

OVERVIEW ON X-RAY ASTRONOMY

- [1] WALLACE H. TUCKER, The X-Ray Universe, Beam Line 1995 <http://www.slac.stanford.edu/pubs/beamline/25/2/25-2-tucker.pdf> (1995)
- [2] Riccardo Giacconi, *History of X-ray telescopes and astronomy*, Springer editor, DOI 10.1007/s10686-009-9139-8, Exp Astron (2009)
- [3] http://www.nobelprize.org/nobel_prizes/physics/laureates/2002/giacconi.html
- [4] Riccardo Giacconi, Herbert Gursky, Frank R. paolini, Bruno B. Rossi, *Evidence for X-rays from sources outside the solar system*, Physical review letters, Vol. 9, Num. 11, December 1, (1962)
- [5] Giacconi, R., Reidy, W.P., Zehnpfennig, T.F., Lindsay, J.C., Muney, W.S., *Solar X-ray image obtained using grazing incidence optics*, Astrophys. J. 142, 1274 (1965)
- [6] Hale V. D. Bradt, *X-ray Astronomy Missions*, Annual Reviews Astronomy Astrophysics 1992.30:391-427 (1992)
- [7] Philip A. Charles, Frederick D. Seward, *Exploring the X-ray Universe*, Cambridge University press (1995)
- [8] <http://heasarc.gsfc.nasa.gov/docs/uhuru/uhuru.html>
- [9] <http://heasarc.gsfc.nasa.gov/docs/einstein/heo2.html>
- [10] <http://heasarc.gsfc.nasa.gov/docs/exosat/exosat.html>
- [11] <http://heasarc.nasa.gov/docs/rosat/taps.html>
- [12] <http://www.asdc.asi.it/bepposax/> & <http://heasarc.gsfc.nasa.gov/docs/sax/saxgof.html>
- [13] M.C. Weisskopf, The Chandra X-Ray Observatory: An overview, Advances in Space Research, Volume 32, Issue 10, 2003, Pages 2005-2011
- [14] O. Citterio, P. Conconi, M. Ghigo, F. Mazzoleni, H. Brauninger, W. Burkert, N. Shulz, P. Gondoin, K. Vankatwijk, R. Laurence, Results of X-ray measurements on electroformed mirror shells for the XMM project, Proc. of SPIE 1742, (1992)
- H. Eggel, R. Lainè, D.H. Lumb, A. Peakock, ESA XMM mission, Proc. Of SPIE 2808-32 (1996)
- [15] <http://heasarc.gsfc.nasa.gov/docs/astroe/astroe2.html>
- [16] Joachim E. Trümper, Günther Hasinger (Eds.), *The Universe in X-Rays*, Springer – Verlag Berlin Heidelberg (2008)
- [17] <http://ixo.gsfc.nasa.gov/technology/index.html>

[18] Roger J. Brissenden et al., *The Generation-X mission: benefits of a heavylift capability*, IAC-08-D2.8.8 (2008)

X-RAY FOCUSING SYSTEMS

[19] Bernd Aschenbach, *Realization of X-ray telescopes – from design to performance*, Exp Astron (2009) 26:95-109 DOI 10.1007/s10686-009-9163-8

[20] <http://www.springerimages.com/search.aspx?val=keyword%3aX-ray+telescopes> (image downloaded from this site)

[21] http://henke.lbl.gov/optical_constants/

[22] Bernd Aschenbach, *Realization of X-ray telescopes – from design to performances*, Exp Astron DOI 10.1007/s10686-009-9163-8 (2009)

[23] Brian D. Ramsey, *The development of focusing optics for the hard X-ray region*, Advances in space research (a COSPAR publication), Vol. 38, 2985-2988 (2006)

[24] Wolter, H., *Verallgemeinerte scawarzschildsche spiegelsysteme streifender reflexion als optiken für röntgenstrahlen*, Ann. der Phys. **10**, 286–295 (1952) –published in german–

Wolter, H., *Spiegelsystem streifenden Einfalls als abbildende Optiken für Röntgenstrahlen*, Ann. Phys. **10**, 94–114 (1952) –published in german– (Grazing incidence mirror systems as imaging optics for X-rays)

[25] Daniele Spiga, *Development of multilayer-coated mirrors for future X-ray telescopes*, PhD Thesis, Università degli studi di Milano-Bicocca, (2004-2005)

[26] <http://solar.bnsc.rl.ac.uk/>

[27] Peter Z. Takacs, *X-ray mirror metrology*, Brookhaven National Laboratory Upton, New York , Hand book of optics, (2010)

[28] D. Spiga, L. Raimondi, *From X-ray mirror surface metrology to the Point Spread Function: a self-consistent approach*, ACTOP (2011)

STATE OF THE ART IN X-RAY TELESCOPE MANUFACTURING TECHNIQUES

[29] Paul B. Reid, *X-ray telescopes*, Encyclopedia of Astronomy and Astrophysics, Natur Publishing Group 2001

[30] http://heasarc.nasa.gov/docs/einstein/hea02_about.html#instrument

[31] ROSAT mission description, ROSAT Scientific Data Center and Max-Planck-Institut für Extraterrestrische Physik, NRA 91-OSSA-3, Appendix F, Jan. 1991.

[32] Giacconi et al., *Solar X-ray images obtained using grazing incidence optics*, American Astronomical Society, 1965ApJ-142.1274G (1965)

[33] Citterio, O., Conti, G., Mattaini, E., Santambrogio, E., Sacco, B., *Optics for X-ray concentrators on board of the Astronomy Satellite SAX*, Proceedings of the Meeting, Cannes, France, December 2-4, 1985 (A87-19722 07-35). Bellingham, WA, Society of Photo-Optical Instrumentation Engineers, 1986, p. 102-110. (1986)

- [34] L. Proserpio, S. Campana, O. Citterio, M. Civitani, H. Combrinck, P. Conconi, V. Cotroneo, R. Freeman, P. Langstrof, E. Mattaini, R. Morton, B. Oberle, G. Pareschi, G. Parodi, C. Pels, C. Schenk, R. Stock, G. Tagliaferri, *Design and development of thin quartz glass WFXT polynomial mirror shells by direct polishing*, Proc. SPIE 7732-12 (2010)
- [35] O. Citterio, P. Conconi, M. Ghigo, F. Mazzoleni, G. Pareschi, L. Peverini, *Development of Soft and Hard X-ray optics for astronomy*, Proceedings of SPIE Vol. 4138 (2000)
- [36] Serlemittos, P. J. et al. 1995, "The X-ray Telescope with ASCA", Publ. Astron. Soc. Japan, 47, 105
- [37] Kei Itoh et al., Ground-based X-ray calibration of the Astro-E2 X-ray telescope II. With diverging beam at PANTER, Proc. of SPIE, vol. 5488 (2004)
- [38] Schnopper H W, Ingram R, Silver E, Barbera M, Candia R, Christensen F, Carlsen, Jensen P, Romaine S, Vernani, Cotroneo V, Varisco S, Artale M, Madsen K K and Calura A, *Thin shell plastic lenses for space and laboratory applications*, SPIE Proc. 5488, (2004)
- [39] Derived from: http://www.u.phys.nagoya-u.ac.jp/uxge/r_e/r_e6_6.html

IXO MISSION OVERVIEW

- [40] <http://sci.esa.int/science-e/www/object/index.cfm?fobjectid=37710>
- [41] <http://sci.esa.int/science-e/www/area/index.cfm?fareaid=100>
- [42] <http://ixo.gsfc.nasa.gov/news/index.html>
- [43] <http://sci.esa.int/science-e/www/area/index.cfm?fareaid=103>
- [44] <http://sci.esa.int/science-e/www/area/index.cfm?fareaid=103>
- [45] *The International X-ray Observatory (IXO) Mission Concept*, presented at IXO meeting (2009) <http://constellationx.nasa.gov/resources/presentations/PDFs/IXOMissionDescription.pdf>
- [46] K.Wallace, *IXO Silicon Pore Mirror Technology Development Plan (TDP)*, ESA unrestricted distribution, reference TEC-MMO/2009/044 (2009)
- [47] ESA, *Cosmic vision: space science for Europe 2015-2025*, BR-247
- [48] <http://www.astronet-eu.org>
- [49] European Space Agency, *IXO – Revealing the physics of the hot Universe, Assessment Study Report*, ESA/SRE(2011)2, (2011)
- [50] Nandra, presentation at IXO Science Meeting, Rome 2011

IXO SCIENCE CASE

- [51] J. Bookbinder, *The International X-ray Observatory – Activity submission in response to the Astro2010 Program Prioritization Panel RFI*, (2010)
- [52] Emanuele Berti, Marta Volontari, *Cosmological Black Hole Spin Evolution By Mergers and Accretion*, The Astrophysical Journal, 684:822-828, 2008 September 10 (2008)

- [53] Philip J. Armitage, Christopher S. Reynolds, *The variability of accretion on to Schwarzschild black holes from turbulent magnetized discs*, MNRAS 341, 1041-1050 (2003)
- [54] J. Cottam, F. Paerelst, M. Mendez, *Gravitational redshifted absorption lines in the x-ray burst spectra of a neutron star*, Nature, 420, 51 (2002)
- [55] James M. Lattimer, Maddapa Prakash, *Neutron Star Observations: Prognosis for Equation of State Constraints*, Phys.Rept.442:109-165,2007
- [56] [Diehl et al. 2010], presentation at <http://www.iasf-roma.inaf.it/IXO/IXOProgramme3.htm>
- [57] Jelle S. Kaastra, *Feedback and enrichment from SNR to LSS*, presentation given at the IXO science meeting, Rome CNR, March 2011 (2011)
- [58] animation available on <http://www.google.it/imgres?q=ixo+perseus+cluster&um=1&hl=it&sa=N&biw=1280&bih=799&tbm=isch&tbnid=GVIeSE2ETL8HIM:&imgrefurl=http://ixo.gsfc.nasa.gov/resources/posters2009.html&docid=HpxJOa9KerXrWM&w=573&h=600&ei=5RBtTvSwGYHT4QTt2NX9BA&zoom=1>
- [59] David A. Buote, Fabio Gastaldello, Philip J. Humphrey, Luca Zappacosta, James S. Bullock, Fabrizio Brighenti, 2, 3 and William G. Mathews, *The X-ray concentration-virial mass relation*, The Astrophysical Journal, 664:123 Y 134, (2007)
- [60] G.W. Pratt, M. Arnaud, E. Pointecouteau, *Structure and scaling of the entropy in nearby galaxy clusters*, 2006, A&A, 446, 429
- [61] M. Sun, G. M. Voit, M. Donahue, C. Jones, W. Forman, A. Vikhlinin, *Chandra studies of the X-ray gas properties of galaxy groups*, arXiv:0805.2320v2 [astro-ph] 21 Nov 2008
- [62] Andreon S. et al., *JKCS041: a colour-detected galaxy cluster at $z_{phot}=1.9$ with deep potential well as confirmed by X-ray data*, arXiv0812.1699 (2008)
- [63] W. Kapferer, T. Kronberger, J. Weratschnig, S. Schindler, W. Domainko, E. van Kampen, S. Kimeswenger, M. Mair, and M. Ruffert, *Metal enrichment of the intra-cluster medium over a Hubble time for merging and relaxed galaxy clusters*, A&A 466, 813-821 (2007)
- [64] Arnaud. M. et al., *The evolution of Galaxy Clusters across cosmic time*, A science working paper for the 2010 decadal survey, http://ixo.gsfc.nasa.gov/decadal_references/ (2010)
- [65] Renyue Cen and Jeremiah P. Ostriker, *Where Are the Baryons? II. Feedback Effects*, The Astrophysical Journal, 650:560-572, (2006)
- [66] Dvali, G., Gabadadze, G., Porrati, M., *4-D gravity on a brane in 5-D Minkowski space*, Phys.Lett. B485:208-214 (2000)
- [67] D. Huterer and M.S. Turner, *Probing Dark Energy: Methods and Strategies*, Phys. Rev. **D 64**,123527 (2001).
- [68] K. Kifonidis, T. Plewa, H.-Th. Janka, and E. Müller, *Nucleosynthesis and Clump Formation in a Core-Collapse Supernova*, The Astrophysical Journal, 531:L123-L126, (2000)
- [69] A. M. Khokhlov, P. A. Höflich, E. S. Oran, J. C. Wheeler, L. Wang, and A. Yu. Chtchelkanova, *Jet-induced Explosions of Core Collapse Supernovae*, The Astrophysical Journal, 524:L107-L110, (1999)

[70] G. C. Jordan IV *et al.*, Three-Dimensional Simulations of the Deflagration Phase of the Gravitationally Confined Detonation Model of Type Ia Supernovae, *ApJ* 681 1448 doi:10.1086/588269, (2008)

[71] Jelle S. Kaastra, *Feedback and enrichment from SNR to LSS*, presentation given at IXO science meeting, Rome (2011)

[72] Julia C. Lee, Randall K. Smith *et al.*, Solid State Astrophysics: Probing Interstellar Dust and Gas Properties with X-rays, A White Paper Submitted to the Astro2010 Decadal Survey for Astronomy and Astrophysics, arXiv:0902.4671v1 [astro-ph.HE] 26 Feb (2009)

[73] N. S. Brickhouse, S. R. Cranmer, A. K. Dupree, G. J. M. Luna and S. Wolk, *A deep Chandra X-ray spectrum of the accreting young star TW Hydrae*, *ApJ* 710 1835 doi:10.1088/0004-637X/710/2/1835, (2010)

IXO OPTICAL PAYLOAD MANUFACTURING CHALLENGE

[74] Abe Kazuhiro, Kaneko Hitoshi, Kunieda Hideyo, Ishida Manabu, Maeda Yoshitomo, *Development of Extensible Optical Bench for next generation X-ray astronomy satellite*, Uchu Kagaku Gijutsu Rengo Koenkai Koenshu Journal, Vol. 49, pag. 2G08, (2005)

[75] Jay Bookbinder *et al.* on behalf of the IXO Team, *An Overview of the IXO Observatory*, Proc. of SPIE Vol. 7732 77321B-1 (2010)

[76] L. Proserpio, S. Campanaa, O. Citterio, M. Civitani, H. Combrinck, P. Conconi, V. Cotroneo, R. Freeman, P. Langstrof, E. Mattaini, R. Morton, B. Oberle, G. Pareschi, G. Parodi, C. Pels, C. Schenk, R. Stock, G. Tagliaferri, *Design and development of thin quartz glass WFXT polynomial mirror shells by direct polishing*, Proc. of SPIE 7732-12, (2010)

[77] M. Bavdaz, E. Wille, K. Wallace, B. Guldemann, D. Lumb, D. Martin, N. Rando, *ESA Optics Technology Preparation for IXO*, Proc. of SPIE (2010)

SPO BASE-LINE TECHNOLOGY

[78] A. L. Mieremet and M. W. Beijersbergen, *Fundamental spatial resolution of an X-ray pore optic*, Applied Optics, vol. 44, no. 33, pp. 7098-7105, (2005)

[79] M. Bavdaz, *IXO System Studies and Technology Preparation – ESA*, presentation at the TWG at AXRO meeting, 09-Dec-2009, available on line at <http://axro.cz/axro09/> (2009)

[80] Kotska Wallace, Marcos Bavdaz, Philippe Gondoin, Maximilien J. Collon, Ramses Günther, Marcelo Ackermann, Marco W. Beijersbergen, Mark Olde Riekerink, Marko Blom, Bob Lansdorp, Lennart de Vreede, *Silicon Pore Optics Development*, Proc. of SPIE Vol. 7437 74370T-1, (2009)

Marcos Bavdaz, Max Collon, Marco Beijersbergen, Kotska Wallace, and Eric Wille, *X-Ray Pore Optics Technologies and Their Application in Space Telescopes*, X-Ray Optics and Instrumentation Vol. 2010 Article ID 295095 (available at: <http://www.hindawi.com/journals/xroi/2010/295095/>) (2010)

[81] Silicon Pore Optics brochure, http://cosine.nl/pdf/brochure_spo.pdf

[82] M. J. Collon, R. Günther, M. Ackermann, R. Partapsing, G. Vacanti, M.W. Beijersbergen, M. Bavdaz, E. Wille, K. Wallace, M. O. Riekerink, B. Lansdorp, L. de Vreede, C. van Baren, P. Müller, M. Krumrey, M. Freyberg, *Silicon Pore X-ray Optics for IXO*, proc. of SPIE Vol. 7732 77321F-1 (2010)

SGO BACK-UP TECHNOLOGY

- [83] M. Ghigo, S. Basso, O. Citterio, F. Mazzoleni, D. Vernani, Manufacturing of lightweight glass segments for adaptive optics, Proc. of SPIE Vol. 6272, 62720X (2006)
- [84] ESA, STATEMENT OF WORK Back-up IXO (former XEUS) Optics Technology, Phase 1, Reference: TEC-MMO/2008/109 Issue: 1 (2008)
- [85] <http://sci.esa.int/science-e/www/object/index.cfm?fobjectid=42369>
- [86] G. Parodi, F. Martelli, S. Basso, O. Citterio, M. Civitani, P. Conconi, M. Ghigo, G. Pareschi, L. Proserpio, D. Spiga, A. Zambra, "Design of the IXO optics based on thin glass plates connected by reinforcing ribs", Proc. Of SPIE Vol. 8147-24 (2011)
- [87] Marta Civitani for the IXO team, *XOU-BB requirement specification*, document number IXO-OAB-SP-001 of ESA contract #22545 "Back up IXO Optics Technology"
- [88] M. Civitani, P. Conconi, A. Zambra, *P.O.C. requirement specification*, document number IXO-OAB-SP-003 of ESA contract #22545 "Back up IXO Optics Technology"

THE SLUMPING TECHNOLOGY FOR MAKING MIRRORS

- [89] Percival Marson, Glass and Glass Manufacture, Sir Isaac Pitman & Sons Ltd -1992- (available on line at <http://bookdome.com/science/Glass-Manufacture/index.html>) (1992)
- [90] L.A.B. Pilkington, *The float glass process, Review Lecture*, Proc. Roy. Soc. Lond. A. 314, 1-25-1969- (available on line at <http://www.jstor.org/pss/2416528>) (1969)
- [91] FLABEG, Solar Brochure, -2006- (available on line at www.flabeg.com)
- [92] P. Baillon, A. Braem, T. Ekelöf, G. Gendre, A. Hallgren, G. Muratori, C. Nichols, T. Rydqvist, S. Walles, *Production of 300 paraboloidal mirrors with high reflectivity for use in the barrel rich counter in Delphi at LEP*, European Organization for Nuclear Research, CERN-EP/88-169 -1988- (Submitted to Nucl. Instr. And Methods in Physics Research) (1988)
- [93] P. Baillon, A. Braem, G. Gendre, G. Muratori, C. Nichols, *An improved method for manufacturing accurate and cheap glass parabolic mirrors*, European Organization for Nuclear Research, CERN-EP/88-157 -1988- (available on line at <http://cdsweb.cern.ch/record/192714/files/198812051.pdf>) (1988)
- [94] O. Citterio, M. Ghigo, F. Mazzoleni, G. Pareschi, B. Aschenbach, H. Braeuninger, P. Friedrich, G. Hasinger, G. Parodi, *Large light X-ray optics: basic ideas and concepts*, Cospar publication, Advances in Space Research 34 -2637–2645- (2004)
- [95] Ghigo et. al., *The manufacturing of the XEUS X-Ray glass segmented mirrors: status of the investigation and last results*, Proceedings of SPIE Vol. 5168 (2004)
- [96] M. Ghigo, S. Basso, O. Citterio, F. Mazzoleni, D. Vernani, *Manufacturing of lightweight glass segments for adaptive optics*, Proc. of SPIE Vol. 6272 62720X-1 (2006)
- [97] R. Canestrari, M. Ghigo, S. Basso, D. Spiga, L. Proserpio, Lightweight optical segment prototype for adaptive optics manufactured by hot slumping, Proc. SPIE 7015, 70153S (2008)
- [98] R. Canestrari, G. Motta, G. Pareschi, S. Basso, M. Doro, E. Giro, L. Lessio, *Composite panels for optical mirrors for Cherenkov telescopes: development of the cold glass slumping technology*, Proc. of SPIE Vol. 7739, 77390H · 2010

- [99] R. Canestrari, M. Ghigo, G. Pareschi, S. Basso, L. Proserpio, *Investigation of a novel slumping technique for the manufacturing of stiff and lightweight optical mirrors*, Proc. of SPIE Vol. 7018 (2008)
- [100] <http://www.brera.inaf.it/?page=attivita>
- [101] Marta M. Civitani, Stefano Basso, Oberto Citterio, Paolo Conconi, Mauro Ghigo, Giovanni Pareschi, Laura Proserpio, Daniele Spiga, Gianpiero Tagliaferri, Alberto Zambra, Daniele Gallieni, Matteo Tintori, Francesco Martelli, Giancarlo Parodi, Marcos Bavdaz, Erik Wille, The integration machine: design, development and validation of an alternative process for the integration of slumped-glass segments into an x-ray module, Proceedings of SPIE Vol 8147, 8147-25 (2011)
- [102] M. Bavdaz, Max Collon, M. Beijersbergen, K. Wallace, and E. Wille, *X-ray Pore Optics Technologies and Their Application in Space Telescopes*, Hindawi Publishing Corporation – X-ray Optics and Instrumentation, Vol. 2010, Article ID 295095 (2010)
- [103] The Constellation-X Project Team, *Constellation-X Reference Mission Description Document*, CX-7402-00003 Baseline February 25, (2000)
- [104] Roger Brissenden, Generation_X technology development program, Activity submission in response to the Astro2010 PPP RFI
- [105] F. A. Harrison, S. E. Boggs, A. Bolotnikov, F. E. Christensen, W. R. Cook, W. W. Craig, C. J. Hailey, M. Jimenez-Garate, P. H. Mao, S. E. Schindler, D. L. Windt, *Development of the High_Energy Focusing Telescope (HEFT) balloon experiment*, Proc. of SPIE Vol. 4012 (2000)
- [106] <http://www.srl.caltech.edu/HEFT/>
- [107] <http://www.nustar.caltech.edu/about-nustar/instrumentation/optics>
- [108] Jason E. Koglin, C. M. Hubert Chen, Jim C. Chonko, Finn E. Christensen, William W. Craig, Todd R. Decker, Charles J. Hailey, Fiona A. Harrison, Carsten P. Jensen, Kristin K. Madsen, Michael J. Pivovarov, Marcela Stern, David L. Windt, Eric Ziegler, *Hard X-ray Optics: from HEFT to NuSTAR*, Proc. of SPIE Vol. 5488, Bellingham, WA (2004)
- [109] Jason E. Koglin et al., *Hard X-ray Optics: from HEFT to NuSTAR*, Proc. of SPIE Vol. 5488 (2004)
- [110] Kai-Wing Chan, William Zhang, Tyler Evansc, Ryan McClelland, Melinda Hong, James Mazzarella, Timo Saha, Lalit Jalota, Lawrence Olsen, Glenn Byron, Mounting and alignment of IXO mirror segments, Proc. of SPIE Vol. 7732, 7732Q-1 (2010)
- [111] Peter Friedrich, Bernd Aschenbach, Heinrich Bräuninger, Günther Hasinger, Oberto Citterio, Mauro Ghigo, Francesco Mazzoleni, Giovanni Pareschi, Udo Dinger, Wilhelm Egle, Axel Matthes, *Recent Results on Manufacturing of Segmented X-Ray Mirrors with Slumped Glass*, Proc. of SPIE Vol. 5900 5900W-1 (2005)
- [112] Peter Friedrich et al., *Manufacturing of Wolter-I Mirror Segments with Slumped Glass*, Proc. of SPIE Vol. 6266 62661G-1 (2006)
- [113] Anita Winter*, Monika Vongehr, Peter Friedrich, *Light weight optics made by glass thermal forming for future X-ray telescopes*, Max-Planck-Institute for extraterrestrial Physics, Giessenbachstr., 85748 Garching, Germany, Proc. of SPIE Vol. 7732 77320B-1 (2010)
- [114] R. Hudec, L. Pina, V. Semencova, A. Inneman, M. Skulinova, L. Sveda, M. Mika, J. Sik and M. Lorenc, *Space optics with Silicon wafers and slumped glass*, ICSO Conference (2008)

[115] http://altamira.asu.cas.cz/xray_xeus1.php

[115p] private communication by Renè Hudec at AXRO meeting in Prague, December (2010)

[116] M. Ghigo, R. ragazzoni, N. Hubin, European Extremely Large Telescope Design Study – Slumped shell test progress review, ELT-TRE-INA-09300-0007, 11 October 2006 – *internal report* –(2006)

[117] R.N. Wilson, *Reflecting Telescope Optics II*, Springer edition (2001)

[118] Thorsten Döhring*, Ralf Jedamzik, Peter Hartmann, Hauke Esemann, Clemens Kunisch, *Forming mandrels for X-ray telescopes made of modified Zerodur*, Proceedings of SPIE Vol. 5168 (2004)

[119] Rodolfo Canestrari, M. Ghigo, S. Basso, D. Spiga, G. Pareschi, L. Proserpio, *Hot Press Direct Slumping: an option to manufacture deformable optics*, ACTOP08 – Synchrotron Elettra – Trieste – October, 9-11 (2008)

[120] Schott, *Optical glass: description of properties*, Pocket catalogue – <http://www.schott.de/>

[121] Ohara Optical Glass, *Technical information*, Optical glass catalogue – <http://www.ohara-gmbh.com>

[122] Hoya Corporation Usa Optics Division, *Optical glass*, Catalogue Technical Note – <http://www.hoyaoptics.com/>

EXPERIMENTS AND RESULTS

[123] <http://www.teknokilns.it/prodotti.php?id=12&lang=ita>

[124] Thorsen Doring, Ralf Jedamzik, Peter Hartmann, Hauke Esemann, Clemens Kunisch, *Forming mandrels for X-ray telescopes made of modified Zerodur*, Proc. of SPIE Vol 5168, pag. 180 (2004)

[125] Schott glass D263 brochure, http://abrisa.com/specs/D263_Glass.pdf

[126] Joshua Schneider, “Vibration testing of the constellation x spectroscopy x-ray telescope reflector mounting design”, Thesis submitted to the School of Engineering and Applied Science of The George Washington University, September (2005)

[127] Ye-Sul Jeong, Hyun-Uk Lee, Sang-A Lee, Jong-Pil Kim, Hyun-Gyu Kim, Se-Young Jeong, Chae-Ryong Cho, *Annealing effect of platinum-based electrodes on physical properties of PZT thin films*, Current Applied Physics Volume 9, Issue 1, January 2009, Pages 115-119 (2009)

[128] D. Hulsenberg, A. Harnisch, A. Bismarck, “Microstructuring of Glasses”, Springer Series in Material Sciences, ISBN 978-3-540-26245-9

[128p] private communication by MPE colleagues

[129p] private communication by MDI Schott staff

[130] Glass in building. Procedures for goodness of fit and confidence interval for Weibull distributed glass strength data

Standard Practice for Reporting Uniaxial Strength Data and Estimating Weibull Distribution Parameters for Advanced Ceramics

Standard Practice for Reporting Uniaxial Strength Data and Estimating Weibull Distribution Parameters for Advanced Ceramics

[131] L. Proserpio and IXO team, Technical note: Analysis of methods for forming thermally slumped glass plates for an X-Ray optic, IXO-OAB-TN-001 document, ESA contract # 22545, (2010)

ANNEX

[132] J. M. Bennett and L. Mattsson. *Introduction to Surface roughness and scattering*, (1999)

[133] J.C. Stover, *Optical Scattering: measurement and analysis*, SPIE Optical Engineering Press, (1995)

[134] E.L. Church, *Role of surface topography in X-ray scattering*, SPIE Proc. Vol. 184 Space Optics / Imaging X-ray Optics Workshop (1979)

[135] Soft X-Ray Optics Group, *The Long Trace Profiler (LTP)*, ELETTRA Synchrotron, Trieste (available online at http://www.elettra.trieste.it/organisation/experiments/laboratories/soft_xray/LTP.html)

[136] P. Z. Takacs and S. N. Qian. *Design of a long trace surface profiler*. In Metrology: Figure and finish. Edited by Bruce E. Truax. Proc. SPIE Vol. 749, January 1987.

[137] M. Civitani, M. Ghigo, O. Citterio, D. Spiga, G. Pareschi, L. Proserpio, *3D characterization of thin glass X-ray mirrors via optical profilometry*, Proc. of SPIE Vol. 7803 78030L-1 (2010)

[138] Edmund Manual, *Optical Techniques for measuring flatness*, available online at www.edmundoptics.com

[139] Wyko Corporation, *TOPO-2D Two-Dimensional Surface Profiles – user's manual*, version 4.40 (1988)

[140] Thermomicroscopes, *Explorer™ Instrument Operation Manual*, 85-10244 rev. C

[141] N. Locksley, B.K. Tanner, D.K. Bowen, *A novel beam conditioning monochromator for high-resolution X-ray diffraction*, J. Appl. Cryst. 28, 314 (2005)
